UNIVERSITÀ DEGLI STUDI DI MILANO

FACOLTÀ DI SCIENZE E TECNOLOGIE

PhD course in Environmental Sciences

Valorization of secondary metal resources through hydrometallurgical processes

Supervisors: Prof. Stefano Trasatti

Dr. Edoardo Guerrini

Dr. Massimo Maccagni

Head of the PhD course: Prof. Francesco Ficetola

PhD Thesis of:

Andrea Stefano Grassi

Cycle XXXIV

Academic year 2021

Acknowledgements

Thanks to the supervisors for their help and valuable advice during the PhD period.

Thanks to all the Engitec staff for their availability.

Thanks to Professor Monica Santamaria, Department of Engineering UniPa, and her collaborators, Francesco Di Franco and Andrea Zaffora, for their support during the period spent at their laboratories.

Summary

Foreword

This PhD project is the result of a collaboration between the Università degli Studi di Milano and Engitec Technologies S.p.a.; it is an executive PhD where most of the time has been spent directly in the Engitec laboratory and on pilot plants.
This research work allowed a strong interaction between the private and the academic worlds considering the needs of both.

A close contact between the private sector and academic world should not be an optional, too often these two have difficulty understanding the needs of the other part. Privates usually do not understand the needs of basic research because it appears as an investment with a high grade of risk; on the other side, the academic world lacks the right instruments to communicate the importance and usefulness of the research done. One of the objectives of this PhD project, in addition to the scientific aspect, was also the establishment of a collaboration between private industry and university to fully exploit the potential of both that, too often, remains hidden.

From a scientific point of view, the purpose of this work was to deepen the knowledge of two innovative hydrometallurgical processes developed and patented by Engitec. Initially the technology in question has been analyzed on the basis of the information and experience retained by the company, then the main problems and key points to focus on were defined. The experimental part was planned and conducted both in Engitech and in university laboratories. It was possible to spend time working on the pilot plant installed in Cape Gate, South Africa, where the opportunity to experience the technology first-hand helped identify further possibilities for improvement.

Many topics were addressed, and the work done has led to some congress presentations and one patent. Compared to the beginning of the project, the two technologies have certainly made progress in terms of process knowledge thanks to the systematic approach adopted to address existing issues; room for improvement still exists and can be filled by continuing along the line taken.

Introduction

In a world that is going straight towards a circular economy approach, it is of fundamental importance to focus efforts on the development of more environmentally sustainable processes. Engitec Technologies is an Italian engineering company that is focusing its attention on the development of processes capable to recover non-ferrous metals from secondary sources while overcoming the environmental problems of available technologies.

Nowadays the recycling concept is becoming increasingly important for our future. Recycling is the process by which used materials and industrial waste are converted into new products. If used materials are not recycled, new products must be made by extracting fresh raw material from the Earth through mining and forestry. Recycling helps to conserve important raw materials and to protects natural habitats for the future. The use of recycled materials in the manufacturing processes uses considerably less energy than that required for producing new products from raw materials; costs like extraction, refining, transport and processing can be partially reduced. Recycling also reduces air and water pollution associated with mining, quarrying, logging and refining processes with a consequent reduction of greenhouse gas emission.

This work focuses on the recovery of zinc and lead with two patented hydrometallurgical technologies that operate in compliance with the most stringent environmental regulations.

Zinc

Zinc is currently the fourth most widely consumed metal in the word; it finds its main application in the galvanizing process of steel to protect it from corrosion. It is also used for cathodic protection, production of zinc-based alloy, like brass and zamac, and in pharmaceutical industries, Figure 1.

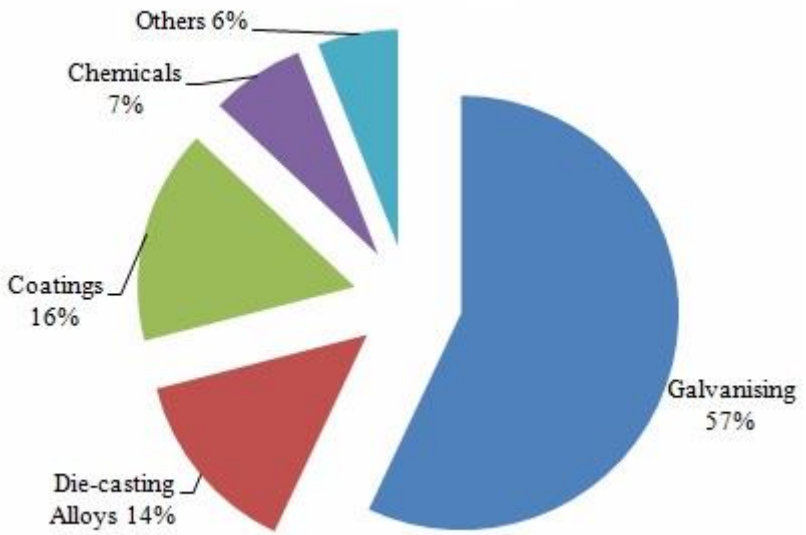

Figure 1: Global zinc consumption[1]

According to a recent LCA analysis[2], special high-grade zinc (*SHG zinc* 99.995%) has a primary energy demand of 37,500 MJ/t and a climate change impact of 2600 kg CO_2-eq./t, where around 65 % of the burden is associated with smelting, 30% with mining and concentration, and 5 % with transportation of the concentrate.

Currently, over 13 Mt of refined zinc of various grades are produced annually from ores, concentrates, and recycled materials[3]. In 2017, zinc prices increased almost 30 percent on the back of supply concerns. Despite this increase, zinc prices are not likely to drop significantly in the next year since zinc demand, particularly from China, remains high. Natural zinc deposits are running out[4] ,Figure 2 , and recycling technologies are becoming increasingly important as they will be the only alternative to zinc production in the close future.

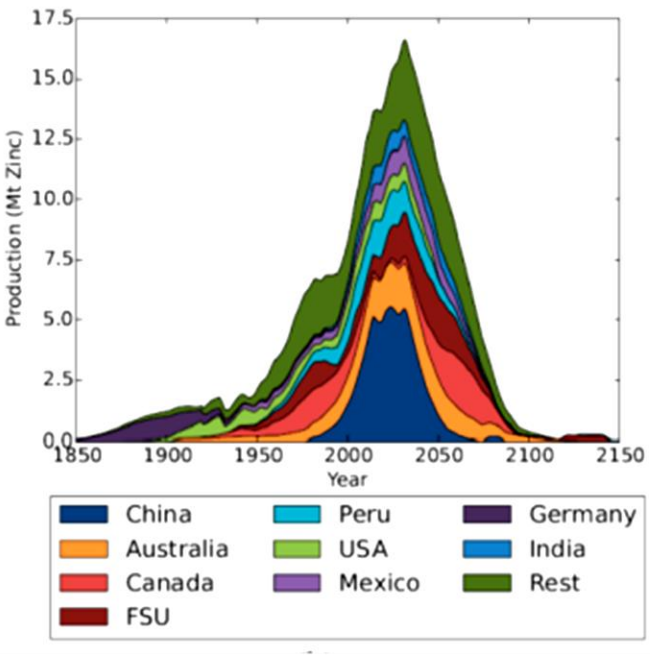

Figure 2: Zinc production forecast.[4]

Zinc production

Nowadays zinc, from primary sources, is produced by two methods[5] (Appendix C): the pyrometallurgical, based on the thermal reduction (Appendix A) of zinc oxides and the hydrometallurgical process, based on electrolytic processes in sulfuric acid solutions. Both routes require roasting and sulfuric acid recovery plants. The blast furnace requires a refining unit to make *SHG zinc*, whereas the electrolytic plant requires a higher-grade feed as compared to that utilized in the blast furnace. Pollution poses special problems in both processes; extreme care must be taken to work with existing environmental regulation[6]. In the case of the hydrometallurgical process, air pollution is relatively easy to control, but liquid effluents and iron residues are more onerous than blast furnace wastes. The main waste produced by the blast furnace (furnace slag) is stable and can be dumped safely without affecting surface water, but since the blast furnace is also a lead smelter, stringent precautions for limiting lead emission must be observed.

Zinc is contained in many wastes and secondary raw materials, however, only parts of these are currently processed. Most of them are landfilled with or without previous stabilization processes. The major secondary source of zinc is the dust produced in the

manufacturing of steel. The production of steel in electric arc furnace (*EAF*) plants uses scrap galvanized steel, containing zinc, as part of the starting material. The high temperatures involved in EAF plants produce vapors that, after condensation, result in a dust material with a zinc content ranging from 2 to 47%[7]. The amount of *EAF* dust generated varies between 15 and 20 kg per ton of steel produced, while the global quantity is estimated at about 3.7 Mt/year[8].

Currently, the treatment of these wastes is based mainly on the use of a Waelz Kiln[9] (Appendix D), in which the zinc is vaporized and re-oxidized producing crude zinc oxide (*C.Z.O.*) which also contains relatively high concentrations of heavy metals and halides. Many potential *C.Z.O.* sources, such as *EAF* dust, galvanizing ashes, brass foundry, and converters fumes, contain chlorides, fluorides, and alkali metals that will then be found in the produced *C.Z.O.* This *C.Z.O.* must then be transformed into zinc metal and it is done with two processes: the sulfate leaching followed by a hydrometallurgical process in sulfuric acid electrolyte and the Imperial Smelting Process (*ISP*) (Appendix C, blasting furnace).

In the case of the *ISP* process, the presence of chloride causes the clogging of the zinc condenser compromising its working ability.

In the sulfuric acid hydrometallurgical process, chlorides, usually present as alkali chlorides in the range of 8-12%, can induce corrosion of lead anodes taking Pb^{2+} in the solution which can be incorporated in the zinc deposit reducing its purity. Chlorides lead also to the production of chlorine gas at the anode that must be treated with additional costs. Fluorides, usually present in range of 0.2-0.4 %, cause a very strong adhesion of the zinc deposit to the aluminum cathode, making it not easily removable. Ni and Co, usually present in range of 100-300 mg/L, depolarize the hydrogen discharge at the cathode decreasing current efficiency related to zinc deposition. For both processes, the removal of these impurities is necessary, so a pre-treatment is required. It consists in a wash with some chemicals but is very expensive and impacts negatively on the operating costs.

Lead

Lead is a dense, soft, low-melting metal. It is an important component of batteries, about 75% of the world's lead production is consumed for their production[10]. Lead is the densest common metal; this quality makes it effective for its application in sound barriers and as X-rays shield material. Due to its corrosion resistance in water, it has long been used in the plumbing industry. It is also added to paints, and it makes a long-lasting roofing material.

Lead is also commonly used in glass[11] and enamel. In television picture tubes and computer video display terminals, lead helps block radiation, and the inner portion of the common light bulb is made of leaded glass. Lead also increases the strength and brilliance of crystal glassware and is used to make bearings and solder; it is also important in rubber production and oil refining.

Lead is a health hazard to humans if it is inhaled or ingested, interfering with the production of red blood cells. Its use must be carefully controlled, and several formerly common uses of lead are now restricted. Many old buildings have been internally painted with lead paints, but it is now mostly used on outdoor steel structures such as bridges, to improve their weatherability. A lead compound called tetraethyl lead was used as gasoline additive because it prevented the "knocking" problem of high-compression automobile engines. However, most gasoline are now lead-free, because lead from car exhaust was a major source of air pollution.

Nowadays, the main application of lead is the production of lead acid batteries, the single largest class of batteries used today. They are essential for application ranging from starting automobile engines, providing emergency back-up power for data centers, and powering industrial and recreational vehicles such as forklift trucks and golf carts. Unlike any other battery type, lead acid batteries, are almost 100% recycled and this feature puts lead as the single most recycled commodity. While the production of this kind of batteries is increasing at an average rate of about 6% per year globally, Figure *3*, production of new lead from ore is becoming increasingly difficult as lead rich ore deposits as depleted[12]. In nature lead can be found in the form of ores, generally associated with zinc, copper and

silver. The most important one is galena, PbS, with a lead content of 86.6%, other common ores are $PbCO_3$, $PbSO_4$ and $PbMoO_4$. The main extraction points are in Australia which own 19% of World lead production, followed by USA, China, Peru, Canada, Mexico and Germany[13].

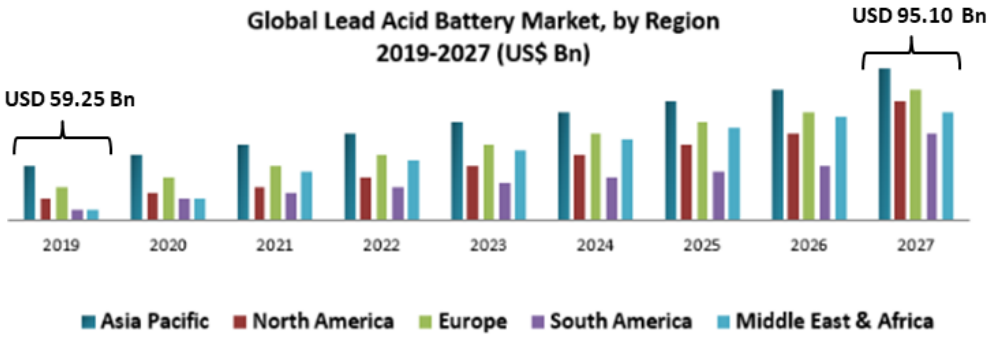

Figure 3: Global lead-acid battery market 2019-2027. [10]

Lead production

Lead production dates back at least 8,000 years. It was used in Egypt as early as 5,000 B.C., and in the time of the Pharaohs it was used in pottery glazes and as solder. It was also cast into ornamental objects. A white lead paint was also used in ancient Egypt, Greece, and Rome. Ancient Rome used lead pipes for its extensive water works. Some of the toxic effects of lead were also noted as early as the Roman era, though lead was also thought to have positive medical qualities. In the 15th and 16th centuries, builders used lead as a roofing material for cathedrals, and lead was also used to hold together the different panels of colored glass in stained glass windows. The first lead battery is credited to a French physicist, Gaston Plante, who invented it in 1859[14]. By 1889, so-called lead-acid storage batteries of the modern type were being commercially produced.

Modern lead mines produce about 4 million tons of lead annually[15]. This is only about half the lead used worldwide; the remainder is obtained by recycling. The top producer of lead is China, followed by Australia, United States, Peru, and Canada (Figure 4). Other countries with major lead deposits are Mexico, Russia, and Kazakhstan.

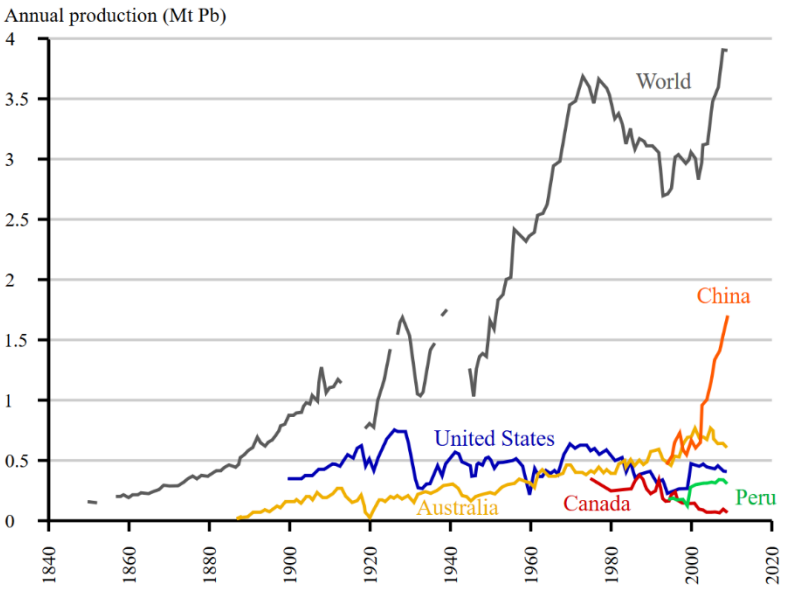

Figure 4: Primary production of lead since 1840.[16]

The World lead production is 10.5 Mt per year, around 50 % comes from the refining of primary source and 50% from secondary source[17]; both are processed by pyrometallurgical plants that exploit the possibility of reducing lead oxides and sulfides by the addition of a reducing agent at high temperature (Appendix A).

Lead production from primary sources, through pyrometallurgical processes (Appendix B), is associated with several critical issues. Large quantities of fumes, powders and toxic gases are generated[18]; in particular, sulfur dioxide gas is released when the ore is roasted at the sinter plant and large amount of CO_2 is produced. The sulfur dioxide is collected at a separate acid plant and converted to sulfuric acid. Moreover, this process is highly energy demanding[19], the consumed energy is mainly associated to mining and high temperature required by smelting. Lead refining produces also several solid byproducts. Most of the solid waste produced is a dense, glassy substance called slag. This contains traces of lead as well as zinc and copper. The slag is toxic and must be stored securely and monitored so that it does not escape into the environment or come in contact with populations.

Nowadays lead, from secondary source, is produced using pyrometallurgical processes, up to now hydrometallurgical processes have only been used at a preliminary stage[20].

The pyrometallurgical processes are subdivided in three steps: battery breaking and processing, smelting of battery scrap materials and refining.

In contrast to secondary zinc and copper production, which use a great variety of secondary
materials, the recycling of secondary lead materials is concentrated on the processing of scrap batteries, which accounts for about 80% of secondary lead recycling globally. Metal sheets, pipe scraps, sludge, dross and dusts play only a minor role as secondary raw materials. The reason for this is that most of the lead is used for manufacturing batteries.
In general, to produce secondary lead from battery scraps, two basic process routes are possible. One route is based on breaking up and dismantling old batteries, and separating the paste, metals and organic substances. Melting and reduction is carried out afterwards in different types of furnaces with an additional refining step. The other route is characterized by the direct treatment of complete and non-dismantled batteries with or without sulfuric acid inside in various smelting furnaces, followed by a refining step.
In detail, in the various stages of pyrometallurgical processing the following technologies are used worldwide[21]:
For battery scrap preparation various processes are possible, which can be differentiated by the degree of separation of single battery components. On an industrial scale, the Penneroya process, the MA process, the Tonolli-CX, and Contibat process are used. Generally heavy metal emissions from battery scrap preparation play a minor role compared to the smelting operation.
The Varta and the Bergsoe processes are smelting processes carried out without an initial separation, so that the batteries are directly smelted in a furnace in presence of sulfuric acid.

For the industrial production of secondary lead, various kinds of smelting furnaces are employed. The short rotary furnace is the most extensively used furnace for smelting separated battery scrap materials, while long rotary kilns and reverberatory furnaces are only used in a few applications. In contrast to the short rotary kiln, the long rotary kiln is operated continuously. Reverberatory furnaces may also be used for smelting a lead-rich slag, which has been recovered in a primary furnace. Shaft furnaces are typically used for smelting unprepared battery scrap, together with lead cable scrap, furnace slag and filter dusts. The lead bullion from secondary lead production contains various impurities, mainly copper, antimony and tin, which may require elimination or adjustment by refining. Generally, the operations necessary for secondary lead refining are limited compared to

those necessary for primary lead refining. Pre-decopperising is not necessary and only final decopperising is carried out. In addition, a removal and adjustment of antimony and the elimination of tin may be necessary.

From battery scrap preparation, only small amounts of particulate heavy metals are emitted as direct emissions. The smelting process emissions depend on the types of furnaces and the types of fuels are used. Generally short rotary furnaces and long rotary kilns are equipped with natural gas/air burners or sometimes with oxy-fuel burners, while shaft furnaces use coke as fuel. For refining and alloying, several kettles are installed depending on the required lead quality; in all these processes, various amounts of heavy metals in particulate and gaseous form are emitted. The amount and composition greatly depend on the process configuration and operation mode[22].

As in many plants, direct emission sources are preferably equipped with emission reduction measures and fugitive emissions released into ambient air, in secondary lead production, are usually much higher than direct emissions.

The most important SO_2 and NO_x emission source, during secondary lead production, are the smelting furnaces. The amount of SO_2 formed is mainly determined by the amount of sulfur contained in the raw materials and in the fuel used. Although a major part of the sulfur remains in the slag formed during the smelting process, a considerable share is also converted to SO_2.

All these pollution issue have forced the closure of many smelters which have transferred their activities in less regulated countries without solving the environmental related concerns[23]. In addition, the obtainment of permissions for lead smelters has become increasingly difficult, and smelting plants are generally expensive to build and operate. As profitable operation of smelters is a function of scale, this has brought to the enlargement of smelter plants which has generated a centralized production of recycled lead. Transport of recycled lead to lead acid batteries production sites further increases the generation of pollution.

Innovative hydrometallurgical processes based on ammonium chloride solutions

According to the concept of circular economy, sustainability and environmentally friendly processes, in the last twenty years, Engitec Technologies S.p.A has developed an innovative hydrometallurgical technology based on ammonium chloride (NH_4Cl) electrolyte[24–30].

This technology aims to solve the current problems related to lead and zinc recycling both from a purely technical point of view and from what concern environmental emissions.

In the past, several attempts have been made regarding the possibility of producing lead by electrolysis, but any process has proven to be satisfactory. The first review on the hydrometallurgy of lead was published in 1924[31]. The most important process that was operating on a small industrial scale was based on brine electrolyte[32-33]; this process, however, was not successful and the plant was dismantled. The failure of the process seems to have been in the electrolytic step since chlorine was formed and was not disposed properly with consequent corrosion problems. In addition, the obtained lead powder was not satisfactorily handled and was contaminated by silver. Intensive research on the hydrometallurgy of lead was undertaken in 1970s and 1980s, when environmental problems due to lead smelters became of much more concrete. However, no viable process resulted.

Current hydrometallurgical technology for zinc production/recovery is based on sulfuric acid solution but, as previously described, the feeding material must be purified by expensive and polluting processes.

With the hydrometallurgical technology based on ammonium chloride electrolyte, lead can finally be recovered from aqueous solution, and problem related to the impurity of *C.Z.O* can be avoided. Emissions related to lead smelting and *C.Z.O* purification can also be eliminated.

Both plants, F.A.S.T. and EZINEX®, share the same basic configuration, as shown in the

block diagram reported in Figure 5, and differ mainly in the electrolysis step.

A brief description of the main chemical aspects of the hydrometallurgical technology, as it was at the beginning of this project, is here reported.

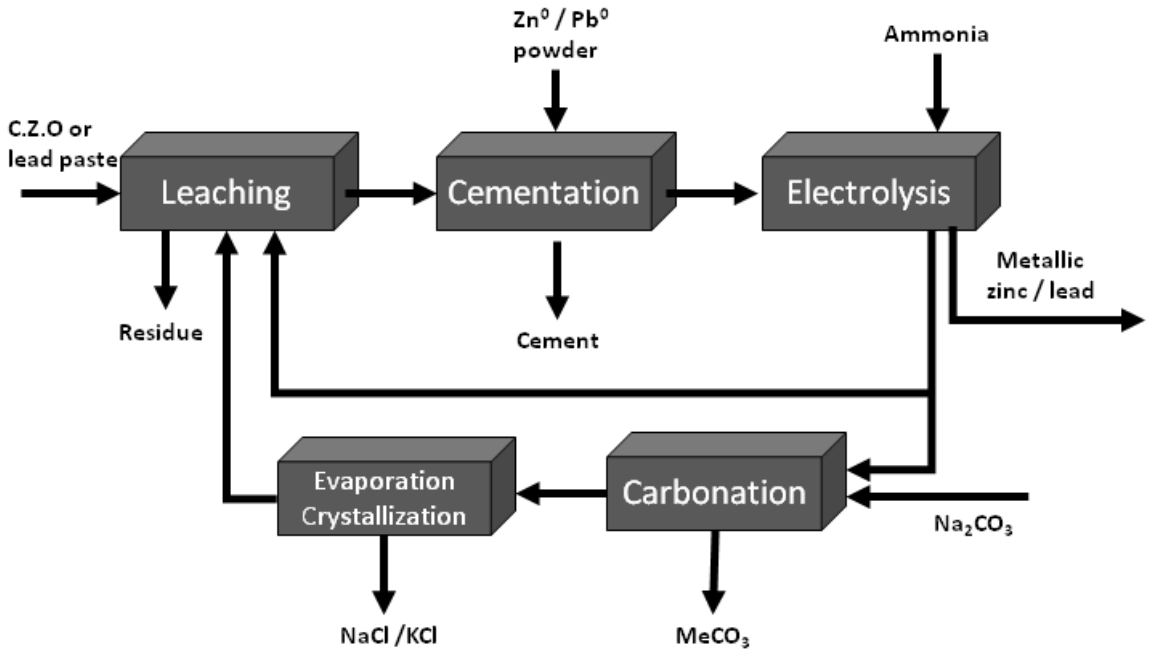

Figure 5: Block diagram of hydrometallurgical processes.

Leaching

The first step is the leaching where the feed material, desulfurized lead pastel obtained from batteries or *C.Z.O/EAFD*, is put in contact with hot ammonium chlorides solution. Temperature is between 70 and 80°C, while ammonium chloride concentration is 300 g/L. In this environment lead, zinc and other metals are easily leached and taken in solution as cations, together with alkaline chlorides and part of the alkaline-earth salts. The leaching mechanism is as follows:

$$MeO_{n/2} + nNH_4Cl \rightarrow Me(NH_3)_nCl_n + {}^n/_2H2O \qquad (Me = Zn^{2+}, Cu^{2+}, Ag^{+} \ldots)$$

$$PbCl_2 + nXCl \rightarrow (X)_nPbCl_{(2+n)} \qquad (X = Na^{+}, K^{+}, NH_4^{+})$$

The neutral pH of the leaching solution, in the case of *C.Z.O/EAFD* treatment, has the advantage of not leaching iron present in the feed material.

Cementation

Before the electrolysis step, the solution must be purified from metals nobler than zinc or lead. If not removed, these can be co-deposited at the cathode lowering the purity of the final product. The depuration is achieved by adding zinc powder or lead granules which causes the precipitation of these metals in metallic form. Most common impurities are copper, silver and lead; the latter is an impurity only for the EZINEX® process. The general redox reaction, in the case of zinc ($E^0_{Zn^{2+}/Zn}$=−0.76 V) powder addition, is the following:

$$Me^{n+} + {}^{n}/_{2}\, Zn^0 \rightarrow Me^0 + {}^{n}/_{2}\, Zn^{2+} \qquad (Me = Cu^{2+}, Ag^{+}, Pb^{2+}, \ldots)$$

The presence of ammonia leads to the formation of metal complex. Accordingly, the reactions for silver ($E^0_{Ag^+/Ag}$=+0.81 V) and copper ($E^0_{Cu^{2+}/Cu}$=+0.34 V) are:

$$Ag(NH_3)_2Cl + Zn^0 \rightarrow Ag^0 + Zn(NH_3)_2Cl$$

$$Cu(NH_3)_2Cl_2 + Zn^0 \rightarrow Cu^0 + Zn(NH_3)_2Cl_2$$

Lead ($E^0_{Pb^{2+}/Pb}$=−0.13 V) does not form a complex with ammonia and its reduction reaction is:

$$PbCl_2 + Zn^0 \rightarrow Pb^0 + ZnCl_2$$

Metallic lead or zinc dissolution, at the operative pH, is kinetically slow, being, for this reason not a serious competitive reaction for the cementation step. The complete removal of these impurities is fundamental for the quality of the final lead or zinc deposit. Multiple cementation stages are needed to achieve an almost complete depuration. Depending on the feeding material composition, notable quantities of silver and copper are recovered from the formed cement.

Electrolysis

The core, and the real novelty, of these hydrometallurgical processes is the electrolysis step. As anticipated, the presence of chlorides is an important issue in the electrolytic processes, based on sulfuric acid, currently used to produce zinc. This has also blocked the development of a hydrometallurgical lead recovery technology. Chlorine anions are oxidized at the anode according to the following reaction:

$$2Cl^- \rightarrow Cl_2 + 2e^-$$

Chlorine gas is a strong oxidant and cannot be released freely in the atmosphere; its presence requires a complex cell design and an abatement system. The use of ammonium chloride solution solves these problems due to the quickly chemical reaction between chlorine and ammonia:

$$Cl_2 + \tfrac{2}{3}NH_3 \rightarrow 2HCl + \tfrac{1}{3} N_2$$

which leads to the following overall anodic reaction:

$$2Cl^- + \tfrac{2}{3} NH_3 \rightarrow 2HCl + \tfrac{1}{3} N_2 + 2e^-$$

Because of the possible formation of chloro-amines, the electrolyte pH must be maintained in the range 5.3-7. The pH is adjusted by addition of ammonia solution to replace what is consumed by the chemical reactions reported.

The reduction of the metal takes place at the cathode, made of titanium grade 1, according with the following general reactions:

$$Me^{n+} + ne^- \rightarrow Me^0 \quad (Me = Zn^{2+}, Pb^{2+}, \ldots) \text{ (general reaction)}$$

$$Zn(NH_3)_2Cl_2 + 2e^- \rightarrow Zn^0 + 2NH_3 + 2Cl^-$$

$$PbCl_2 + 2e^- \rightarrow Pb^0 + 2Cl^-$$

The overall reactions are:

$$Zn(NH_3)_2Cl_2 + \tfrac{2}{3} NH_3 \rightarrow Zn^0 + \tfrac{1}{3}N_2 + 2NH_4Cl$$

$$PbCl_2 + \tfrac{2}{3} NH_3 \rightarrow Pb^0 + \tfrac{1}{3}N_2 + 2HCl$$

During the electrolysis, the temperature is maintained between 70 and 80°C to avoid

crystallization of ammonium chloride.

The design of the electrolytic cell and the separation of the final product from the solution are different for the F.A.S.T. and the EZINEX® process.

The F.A.S.T. electrolysis cell is composed of vertical compartments where the solution flows in ascending direction at a speed of 2 m/s. The electrodes are located on the walls of these compartments. Using a high current density, 10.000 A/m^2, lead is deposited on the cathodes with a sponge like morphology. Once the deposit has reached a certain size, the solution flow strips it from the cathode. Lead flakes, coming out from the cell head, are separated from the solution by a centrifuge.

The EZINEX® electrolysis cell is composed by a tank in which the electrodes are immersed. By applying a current density of 300 A/m^2, the zinc is deposited at the cathode in the form of foil. Reached a certain thickness, the cathode is extracted from the solution and the formed deposit is detached. The cell is also provided with an air sparging system which optimizes the diffusion rate and provides a very effective mixing of the solution. The cathodic hydrogen evolution, the real competitor of zinc plating in the sulfuric acid process, is practically absent. The cell voltage of the EZINEX® process is lower than that used in the sulfuric acid electrolysis and, at neutral pH, the overpotential of hydrogen evolution is higher.

This issue is practically inexistent in the F.A.S.T. process, titanium and lead present an extremely high overpotential for the hydrogen evolution reaction.

The ammonia eventually released in the plant is scrubbed and recycled back to the process.

Evaporation /crystallization

The main impurities building up in the leachate are alkali chlorides and fluorides, calcium and magnesium. They are not affecting the metal deposition but, apart from the fact they can slightly modify the electrolyte conductivity reducing the ohmic drop, they must be removed to avoid unwanted crystallization of salts in the process. This unit has two main goals: the evaporation of the water fed to the plant and the elimination of alkaline chlorides from the electrolyte. The mother liquor containing zinc or lead and ammonium chloride, is recycled back to the plant.

Carbonation

Calcium and magnesium, build up in solutions, likely interfere with the zinc migration to the cathodic surface and, if present in high concentration, can lead to unwanted crystallization. To avoid these problems, Ca and Mg are precipitated and filtered by adding Na_2CO_3 / $NaHCO_3$ according to the following mechanism:

$$NaHCO_3 + MeCl_2 \rightarrow MeCO_3 + NaCl + HCl \qquad (Me = Ca, Mg, Mn, \ldots)$$

$$Na_2CO_3 + MeCl_2 \rightarrow MeCO_3 + 2NaCl \quad (Me = Ca, Mg, Mn, \ldots)$$

The technology described has still room for improvements, some were analyzed while others will be object of future studies; Figure 6 schematizes all the problems already known and those that emerged after the experience on the Cape Gate pilot plant.

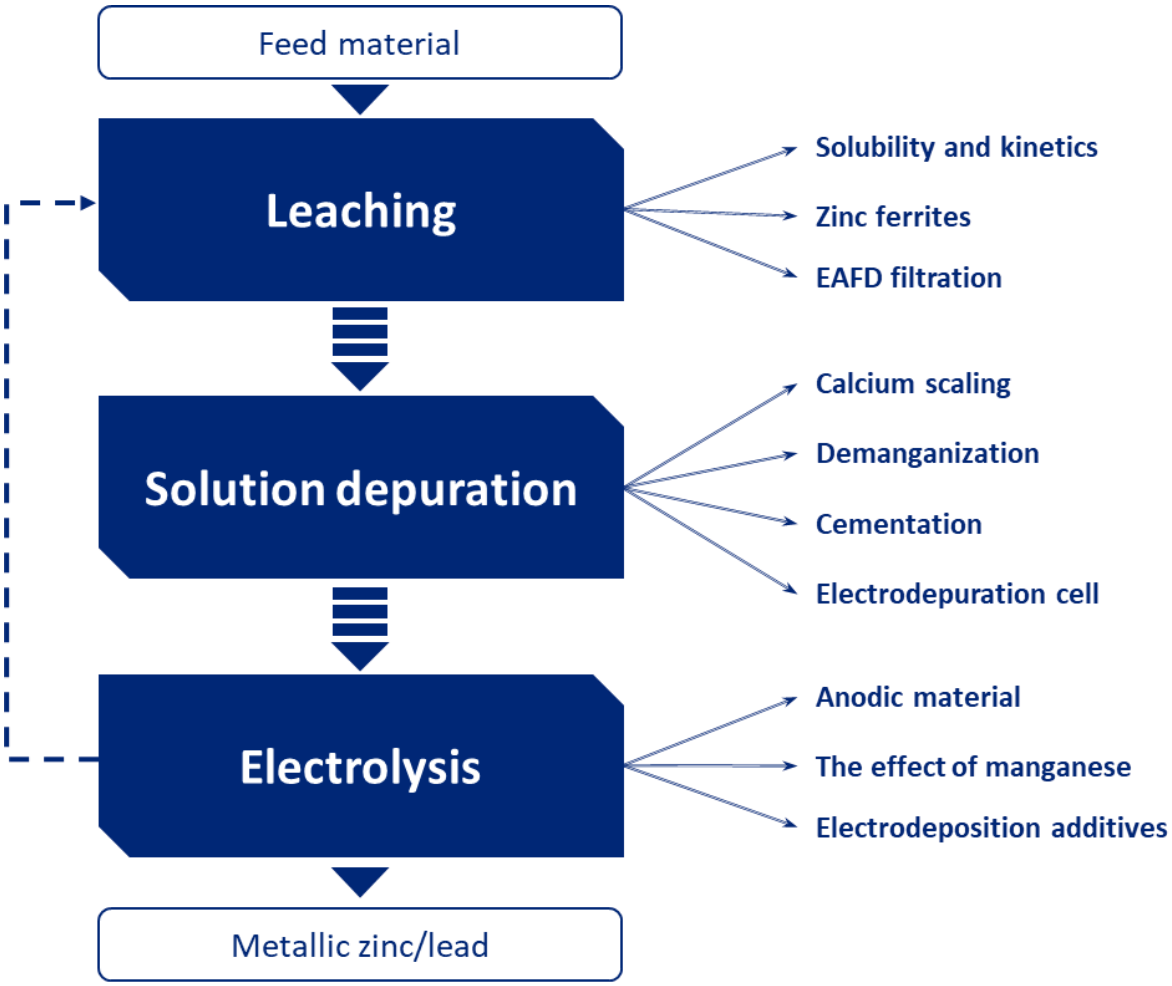

Figure 6: Scheme of the ammonium chloride technology and relative issues.

For each problem a specific experimental approach was adopted and, for fluent reading of this elaborate, the discussion of the results obtained and the description of the methods used has been structured as follows.

The hydrometallurgical technology has been divided into three macro sections, these have been addressed individually by deepening the various criticisms and reporting the most relevant results obtained from experimentation. The complete documentation related to the various studies is reported in the Appendix and includes, in addition to the detailed description of the problem, the description of the instruments, methods used and tests carried out, as well as all the data obtained and the discussion of the results.

As mentioned earlier, the two processes share the same scheme and differ only in the design and operating conditions of the electrolysis cell; therefore, most of the knowledge gained is applicable to both.

However, during the period in which the research was carried out, the EZINEX® process was a priority for Engitec Technologies so much of the work carried out was focused on this process.

Research work

Leaching

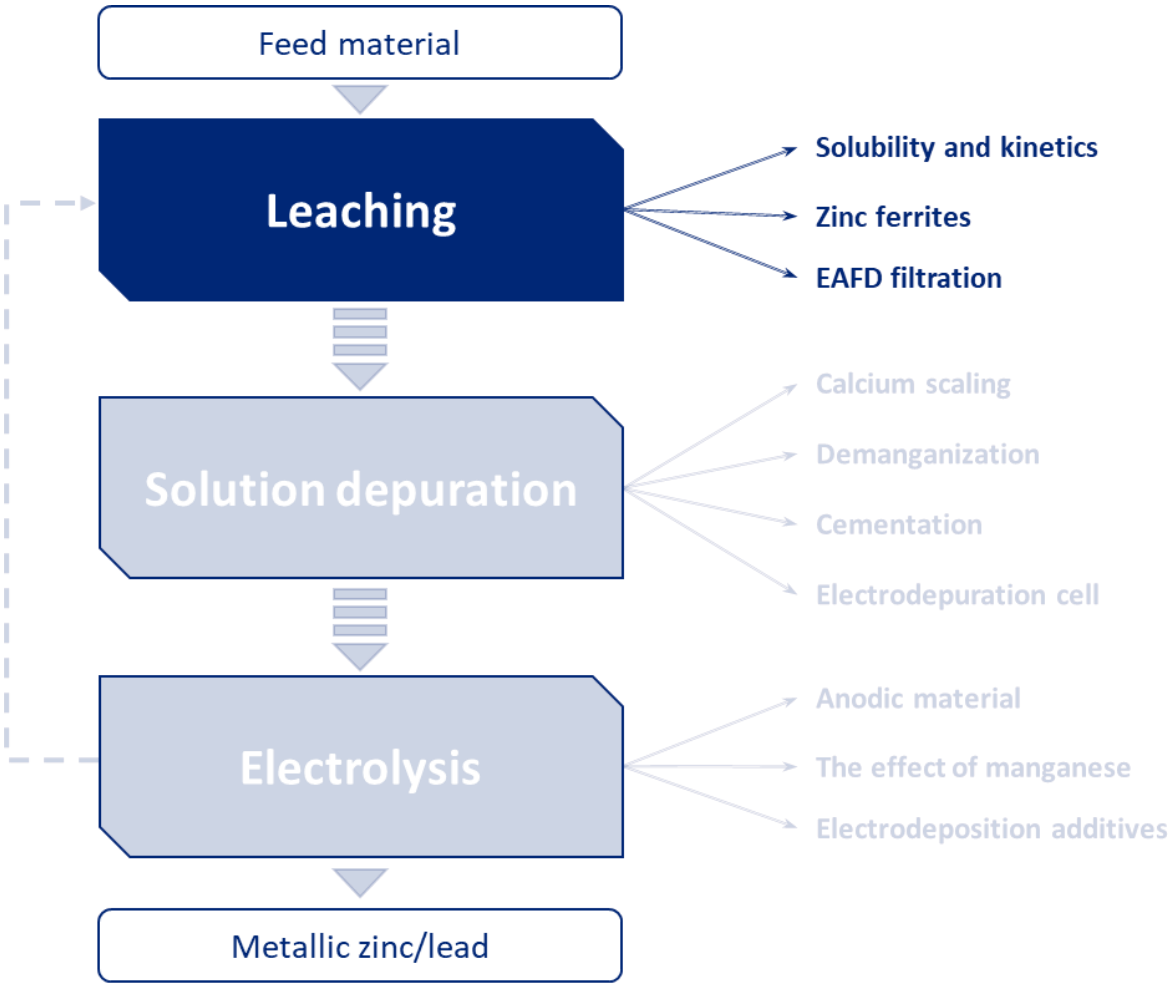

The leaching step represents the beginning of the zinc and lead recovery cycle, it is basically an extraction process that aims to enrich the process solution as much as possible in terms of the content of the metal cation of interest. It is critical to know the timing with which the process takes place, whether there are factors that increase the extraction yield, and how to separate the process solution from the unleached residue.

Solubility and kinetics

Knowledge of the solubility limits of the two metal cations, Zn^{2+} and Pb^{2+}, as a function of temperature and ammonium chloride content is a useful parameter in order to properly dose the feed material; the following are some important consideration emerged from the analysis possessed by Engitec. In ammonium chloride, zinc form a complex with ammonia, $[Zn(NH_3)_4]^{2+}$, while lead is solvated as a negatively charged chlorinated anion, $PbCl_4^{2-}$.

The engitec know-how on solubility and leaching kinetics is briefly given below in order to summarize the key points of this step.

The experimental solubility curves of the two metal complexes, obtained starting from ZnO and PbO, as function of temperature and ammonium chloride concentration are shown in Figure 7 and Figure 8. As the temperature and the ammonium chloride content increase, the solubility of the two metal cations increases, however, it must be considered that working with sulutions close to the solubility limit could be risky; a slight decrease in temperature, at any point in the system, would lead to the precipitation of salts and subsequent clogging of the pipes.

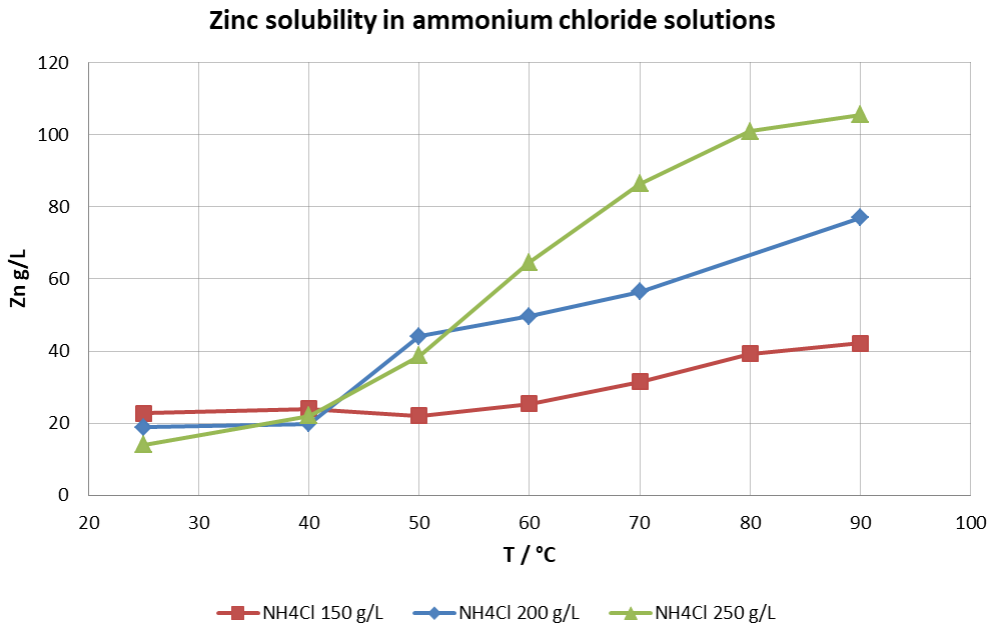

Figure 7: Zinc solubility in ammonium chloride as function of T and NH_4Cl concentration.

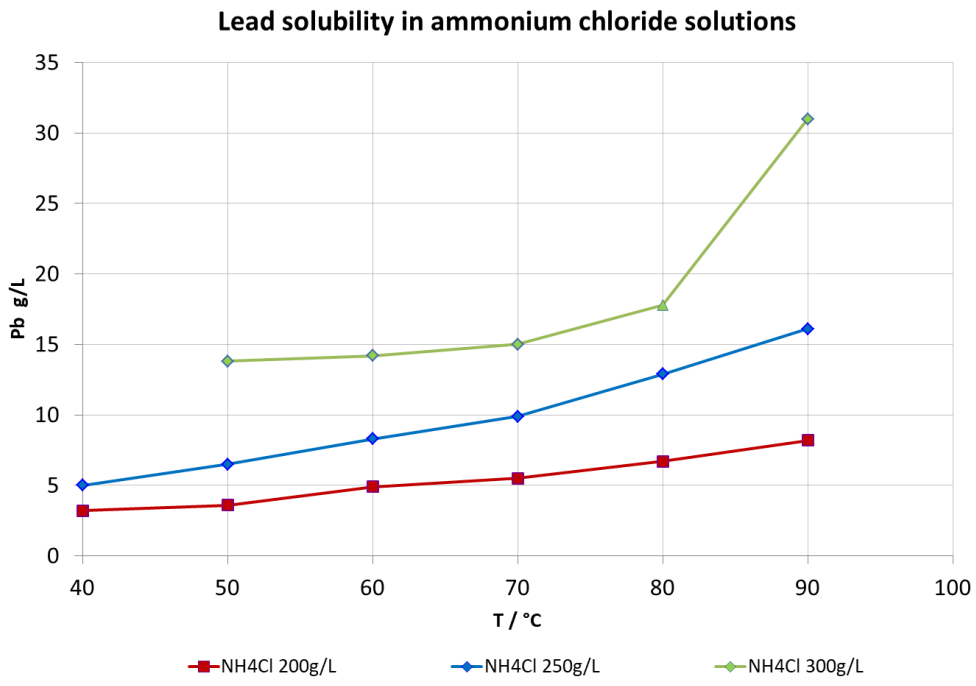

Figure 8 Lead solubility in ammonium chloride as function of T and NH_4Cl concentration.

Another important parameter to consider in order to optimize the leaching process is the dissolution kinetics of the two metals from the two different starting materials, EAFD for zinc and lead acid battery paste (*LAB*) for lead.

Not all the zinc contained in eafd is soluble, extraction of the soluble part, ZnO, is fast and temperature plays a marginal role, Figure 9, while the zinc ferrite fraction remains unleached even at long leaching time; this topic is addressed in detail in the following section.

In LAB paste, the feed material for the F.A.S.T. process, lead is present in several forms: $PbCO_3$, PbO, PbO_2, $PbSO_4$, and metallic. Pb(II) compounds are dissolved by ammonium chloride in less than 15 minutes, as shown in Figure 10, but represent only 50-60% of the lead content. To achieve a better extraction yield, it has been found that several strategies can be used. The over-oxidized lead compound, PbO_2, can be reduced by adding H_2O_2 into the solution, Figure 11, or it can be air roasted, Figure 12, to convert PbO_2 to PbO and then leached. Metallic lead must be oxidized to be solubilized, hydrogen peroxide can do the job but is slow, oxygen in the air seems to act quite well. All of these options for increasing

lead extraction are subject to economic factors rather than chemical feasibility.

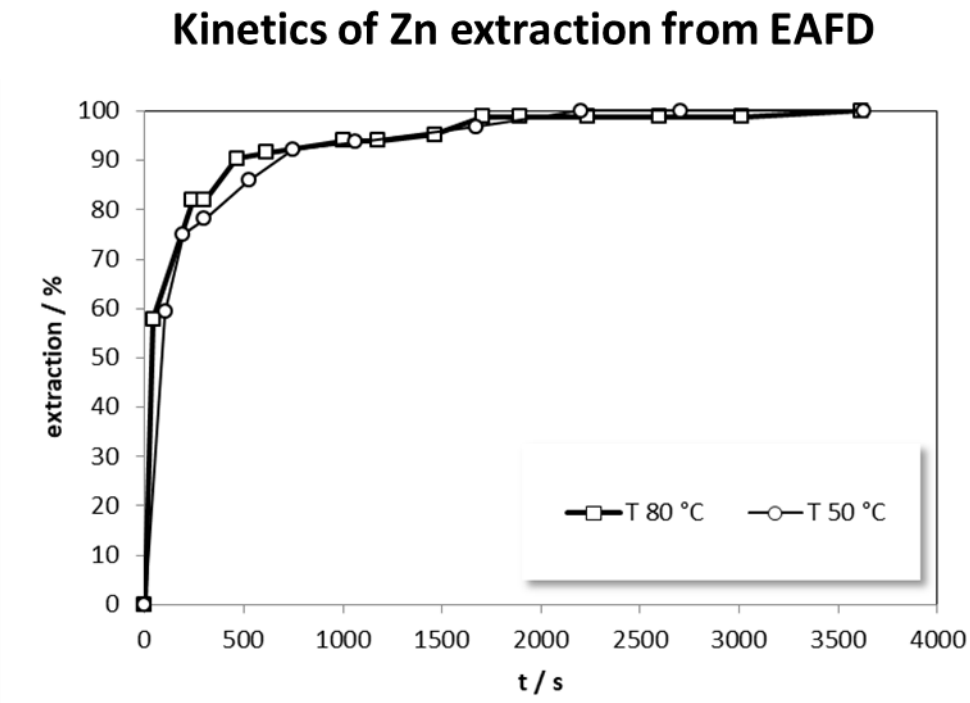

Figure 9: Kinetics of zinc extraction from EAFD, refers to extractable zinc.

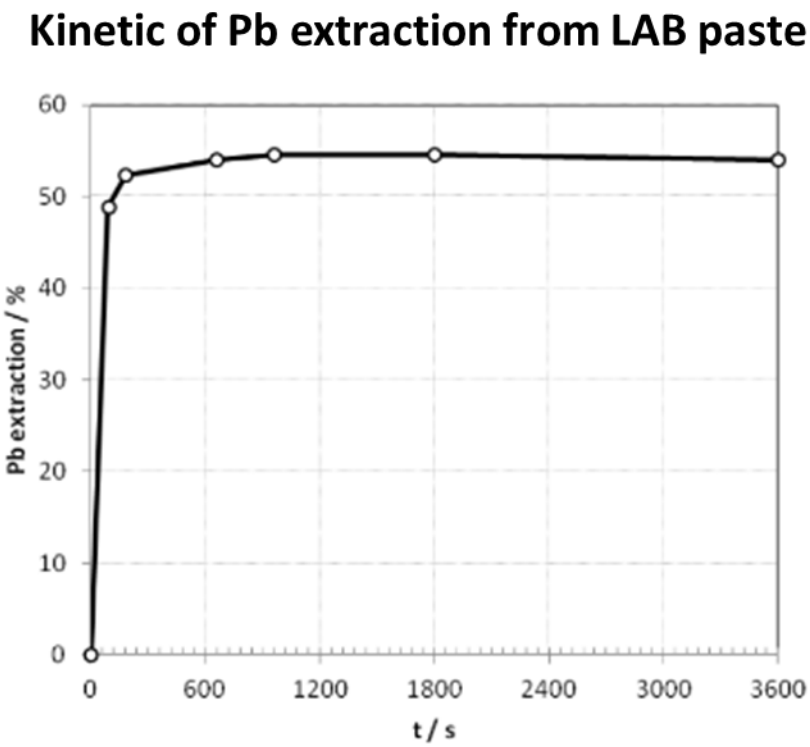

Figure 10: Kinetic of lead extraction from LAB paste.

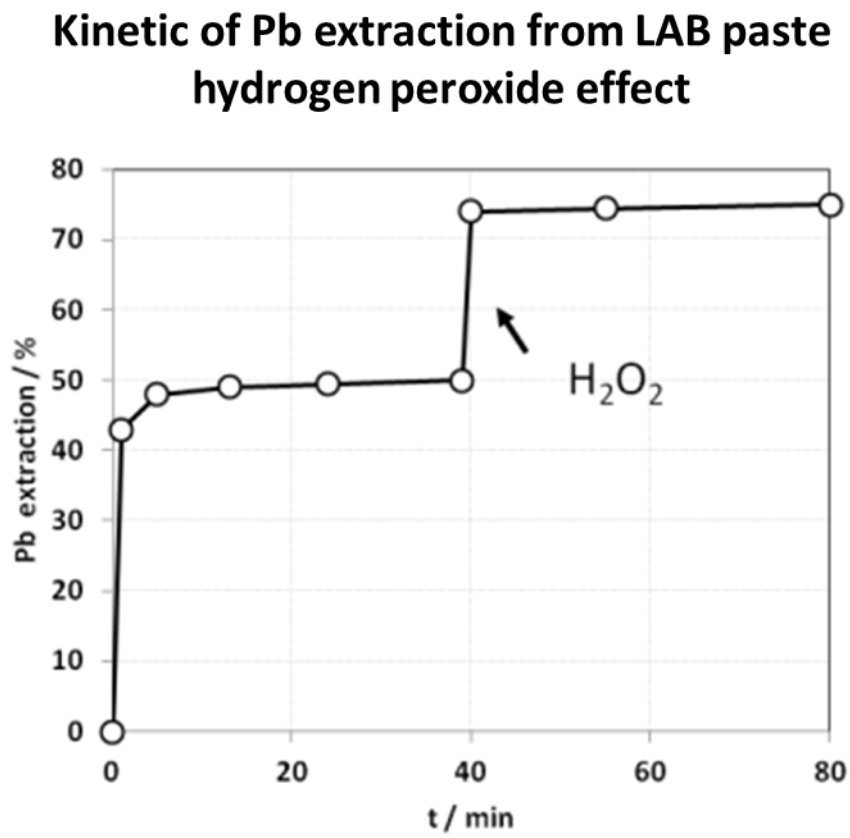

Figure 11: Kinetic of lead extraction from LAB paste, effect of hydrogen peroxide.

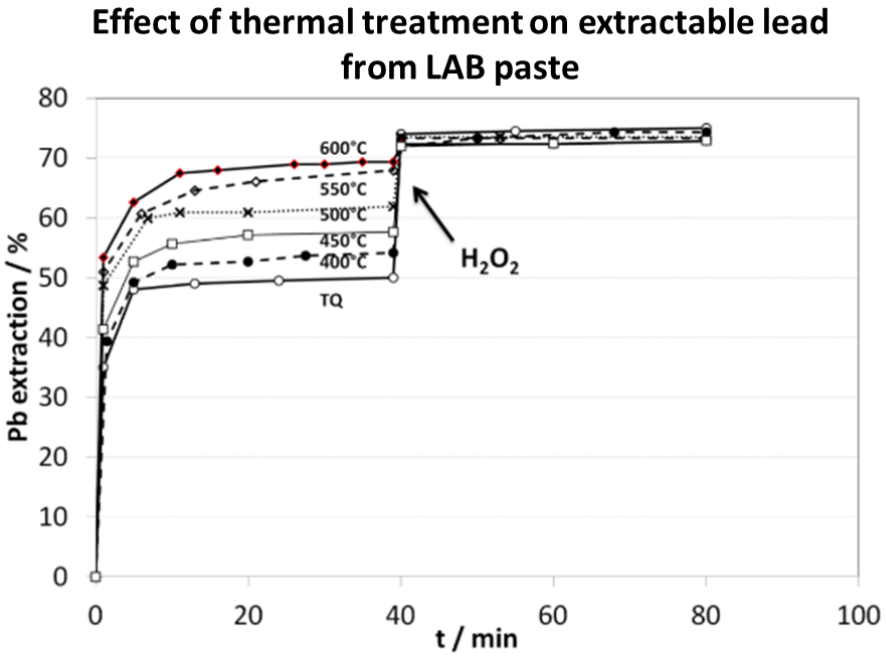

Figure 12: Effect of thermal treatment, 300-600°C, on extractable lead from LAB paste.

Zinc ferrites problem

Appendix 1

EAFD, fed to the EZINEX® pilot plant installed at Cape Gate, are characterized by a content of zinc around 50% w/w, however, a leaching in hot ammonium chloride solution, pH 6, is not able to dissolve all the zinc. The soluble fraction of zinc is bonded to an oxygen atom forming zinc oxide, ZnO, but a relevant part that depends on Fe content, is in the form of zinc ferrites, that are insoluble in ammonium chloride. Unrecovered zinc, along with all other insoluble components of the EAFD mixture, is removed through filtration and represents waste as well as a lost profit.

Zinc ferrites are a family of inorganic compound of iron and zinc with the general formula $Zn_xFe_{3-x}O_4$; they are particularly stable to heat, oxidation and practically insoluble in ammonium chloride. A possible route to convert zinc ferrites in a soluble zinc compound is rosting in presence of reducing agents[34] however, this implies a pretreatment of the dust.

To increase the zinc extraction capability of the EZINEX® process, leaching tests were performed with the addition of reducing agents, potentially capable of reducing iron freeing zinc from the crystalline structure of zinc ferrite. Three reducing agents were chosen and tested: sodium sulfite, hydrazine, and sucrose. Leaching tests were performed and the residue was analyzed by atomic absorption, after mineralization, and SEM-EDX. None of the reducing agents tested had the desired effect, even the one with the highest reducing power, hydrazine.

Other reducing agents could be tried, however the thermal route in the presence of reducing agents seems to be the only alternative for complete recovery of zinc content from EAFDs for the moment.

Filtration of EAFD leaching residue

Appendix 2

The filtration of EAFD leach residue is not without its problems; tests on the pilot plant installed in Cape Gate, South Africa, showed some issues related to clogging of the filter cloth then filtration tests with alternative fabrics were planned.

The particle size distribution of the EAFD leaching residue was determined, Figure 13, and several filter fabrics were proposed by the experienced supplier and tested. Tests were performed using a jacketed laboratory filter operating under pressure. Two types of solutions were tested to simulate an output suspension from a leaching process made with a fresh ammonium chloride solution and one made with a process solution containing chemical species that accumulate during the plant cycle.

The average particle size varies from 0.3µm to 1200µm, 90% have a size smaller than 2µm.

The relevant data in a filtration test is the average permeability, the hourly flow rate per square meter of filter area measured after the formation of a residue cake. The adhesion of the cake to the filter fabrics, its moisture content, and its thickness were also measured.

The different filter fabrics tested did not show large differences; the average permeability, Figure 14, did not vary significantly, only the PVDF cloth showed slightly lower performance. The data obtained were made available to those involved in defining parameters and process specifications in norder to select the most suitable filtering cloth.

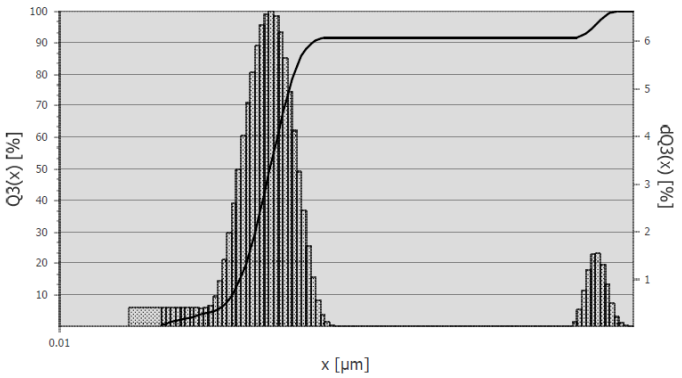

Q3(x) %	x [µm]
5	0.3
10	**0.4**
25	0.6
50	**0.9**
75	1.3
90	**2.2**
95	883.4
99	1'201.2

Figure 13: Particle size distribution of a leached EAFD suspension.

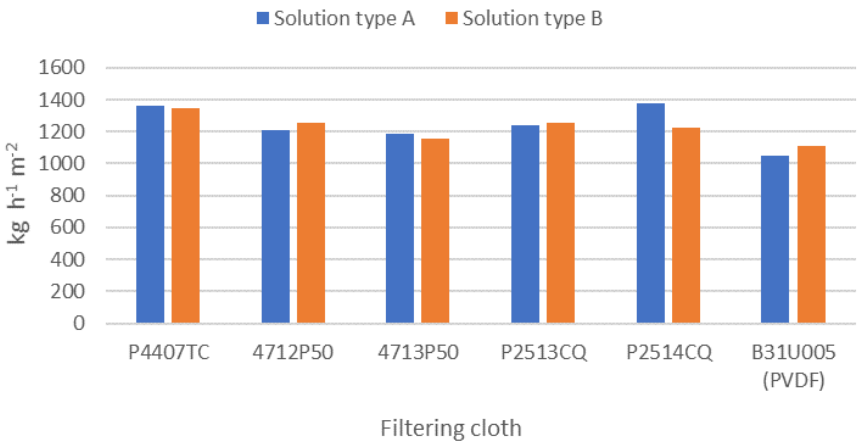

Figure 14: **Filtration of leached EAFD suspension; average permeability of different commercial filter cloths (provided by DrM, Dr.Muller AG).**

Solution depuration

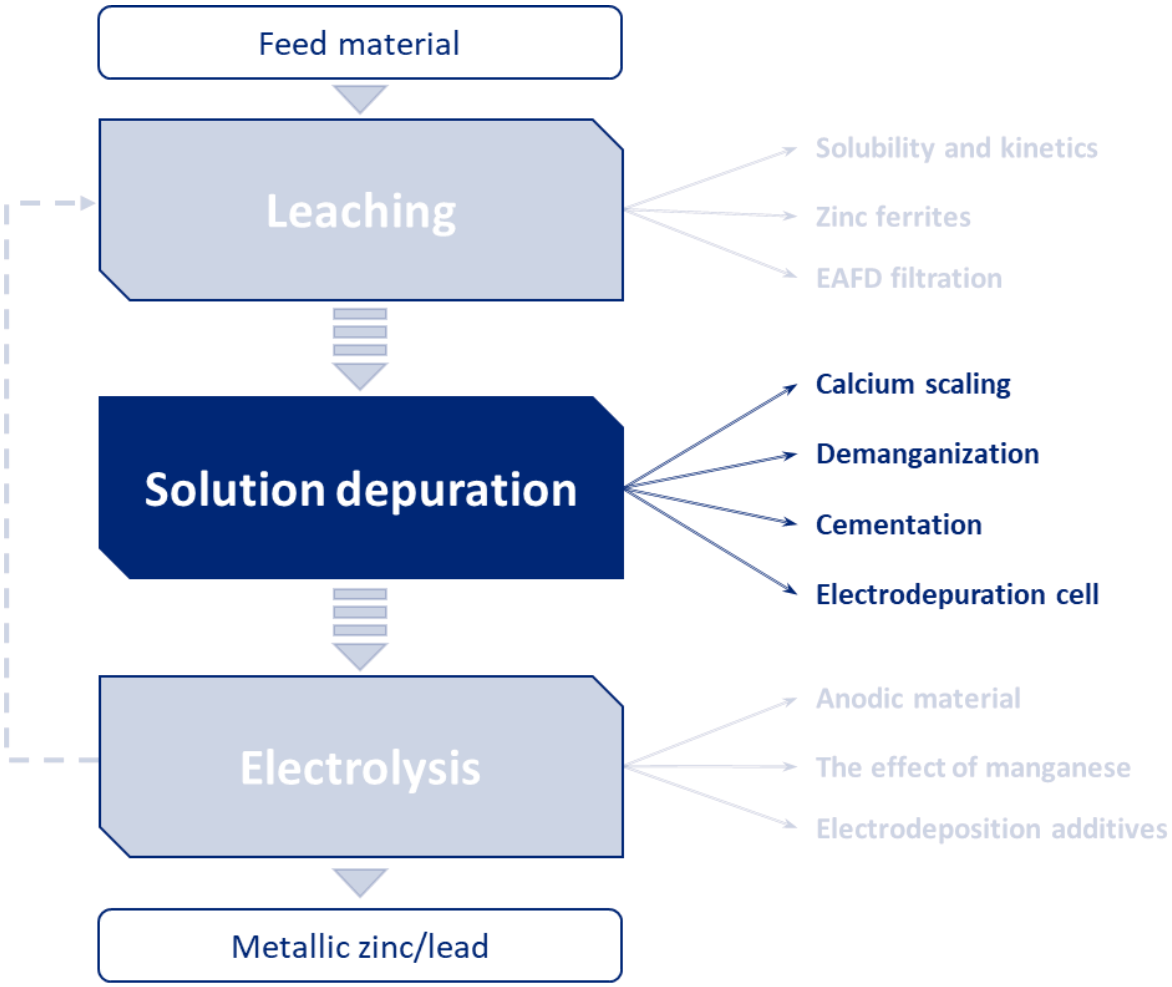

The purification of the solution leaving the leaching phase is of fundamental importance to obtain a high pure final deposit, to avoid problems of precipitation of salts, reduction of the faradic efficiency during the electrolysis phase and deactivation of the catalytic electrodes. The different issues have been addressed and from the results obtained some possible alternatives to the current process have been derived.

Solution depuration: calcium scaling

Appendix 3

Calcium, present in the EAFD, is leached by ammonium chloride solutions and, if not removed, it builds up and precipitate as calcium sulphate. In the EZINEX® pilot plant, the lack of calcium control had led to the precipitation of calcium sulphate in the heat exchangers, reducing their performances.

The F.A.S.T. process

Calcium is not an issue for the F.A.S.T. technology, secondary sources of lead usually contain sulphates, so calcium is continuously kept under control and precipitate as calcium sulphate in the leaching phase.

To control the calcium concentration in the process solution, the possibility to add ammonium sulfate in the leaching tank was investigated. Ammonium sulfate is generated in the scrubber by the reaction of scrubbed ammonia and sulphuric acid used as neutralizing agent; the idea resides behind the fact that, in the process solution, solubility of calcium sulphate is low and its precipitation in the leaching tank allow calcium removal by filtration together with the leaching residue.

Tests were done to determine the maximum amount of calcium that can be precipitated by addition of sulfate ions.

From results shown in Figure 15, it can be seen that even additions of sulfate ion stoichiometrically in excess respect to calcium do not increase the amount of precipitable calcium; the solubility of calcium sulfate in ammonium chloride, under the conditions tested, is 3 g/L.

In order to assess the possibility of the problems encountered occurring again, the amount of water to be evaporated before obtaining a precipitation of calcium sulfate from a solution containing 3 g/L of calcium was determined. The volume of water to evaporate was found to be around 30-40%, this allows to work with these calcium concentrations without scaling the heat exchangers.

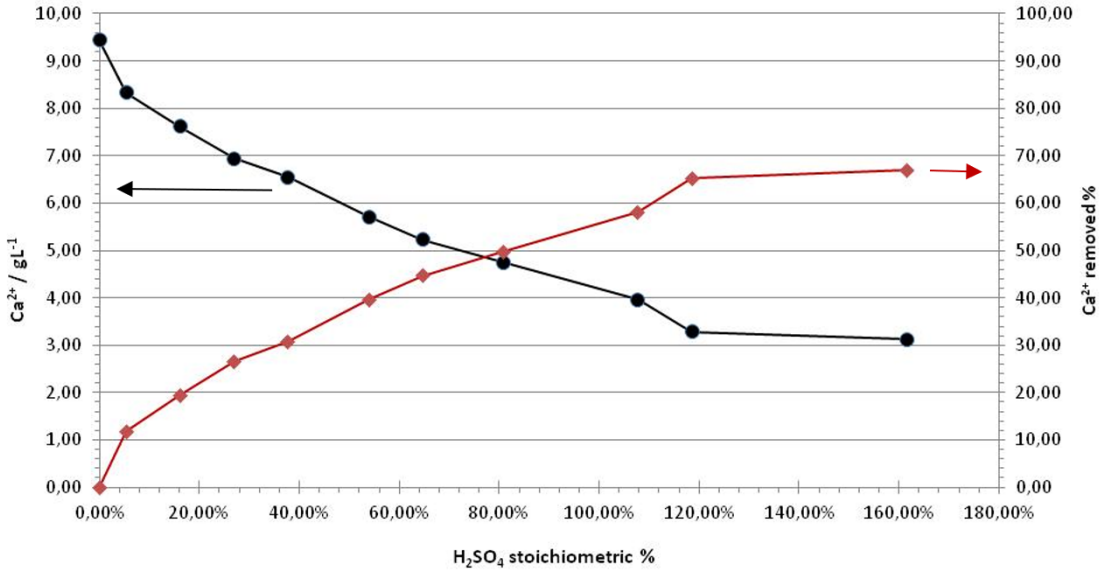

Figure 15: Calcium content as function of the stoichiometric percentage of sulfuric acid added.

Purging part of the ammonium sulfate from the scrubber is therefore a valid method to keep the amount of calcium under control, avoiding the clogging of the heat exchangers and promoting the reuse of a plant waste. Figure 16 shows the appearance of an exchanger after a few hours of operation in the presence of different concentrations of Ca^{2+}.

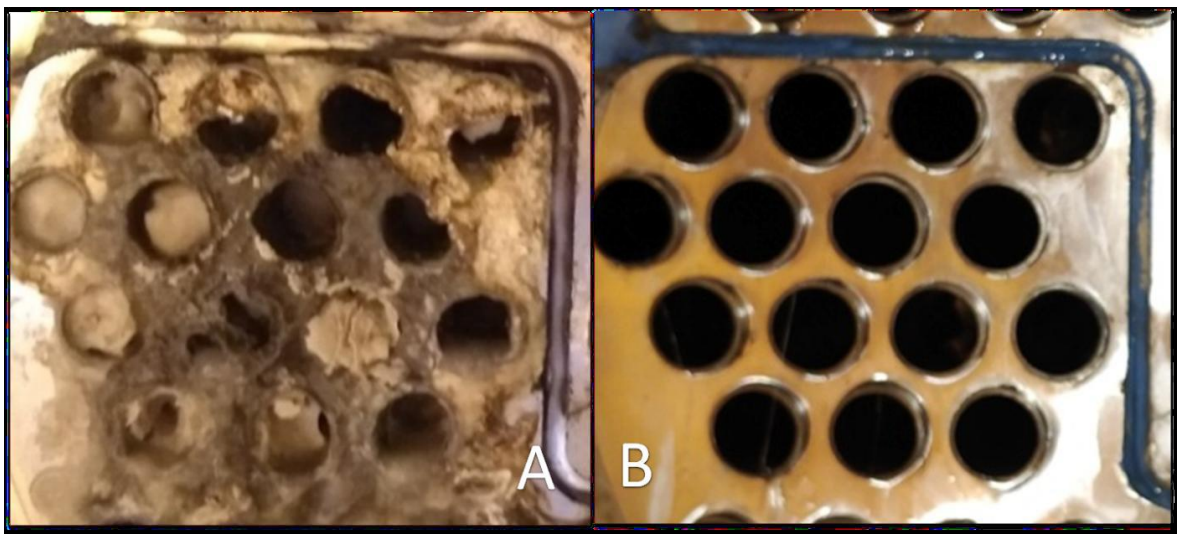

Figure 16: Heat exchanger with Ca^{2+} (A) and without Ca^{2+} (<3g/L) (B) in the solution.

Solution depuration: Demanganization

Manganese is usually present in EAFD, around 2% w/w, and is leached in ammonium chloride solution. It is nobler than zinc, however, cannot be cemented by the addition of zinc powder as is the case with other metallic impurities such as lead, cadmium, copper and silver. Manganese is present in the form of bivalent cation and, if present during electrolysis, it is oxidized to Mn^{4+} that precipitate as a brwown solid. Removal of such impurity is mandatory for the good operation of the whole EZINEX® system.

The demanganization operation consists in the addition of potassium permanganate, a strong oxidant that undergoes a comproportionation reaction with bivalent manganese to produce an insoluble compound of Mn^{4+}.

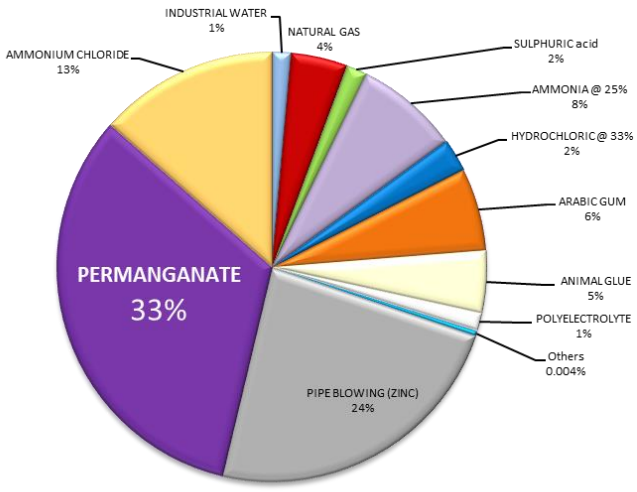

Figure 17: Cost of chemicals the EZINEX® technology Data from cape gate test run.

The F.A.S.T. process

Some secondary sources of lead contain manganese, in these cases demanganization is necessary also for the F.A.S.T. process. It should be done in the same way described for the EZINEX® process and all consideration reported in this section are to be considered valid for both technologies.

The end point of the reaction is controlled with an ORP electrode, which can measure the solution potential. During the EZINEX® test run at Cape Gate facility, this reaction end point control showed some issues. Permanganate was added in the leaching tank and the ORP electrode was inserted in the EAFD-ammonium chloride slurry. The addition made in this way brings permanganate in direct contact with EAFD containing potentially oxidizable compounds, in addition the electrode was immersed in a sidestream of the leaching reactor that was prone to clogging.

The addition of concentrated permanganate was controlled by a software-driven pump that, during periods of clogging, incorrectly dosed the reagent causing excessive permanganate consumption or pollution of the solution due to unremoved manganese.

Furthermore, the equilibrium potential of the redox reaction in question is dependent on pH and temperature, not considering these variables can lead to over-consumption of permanganate or underestimating the amount needed. Permanganate accounted for over 30% of operating costs during the Cape gate test run, Figure 17.

Learning from this field experience, a more accurate way of determining the ORP set point was explored by considering the pH and temperature of the solution. A dedicated packaging unit for the demanganization reaction was suggested to increase the control of the reaction and to have the ability to recover and recycle the manganese instead of leaving it in the EAFD residue.

The reaction rate of the demanganization reaction is essential to determine the reactors volumes and their retention time. Kinetics of the comproportionation reaction between Mn^{2+} and MnO_4^{2-} were determined in different conditions. The produced precipitate must finally be separated from the liquid, solutions can be different and include filtration, flocculation and centrifugation; investigations were carried out to define the most suitable.

Finally, an attempt was made to define the chemical formula of the recoverable manganese precipitate as a byproduct of the EZINEX® technology.

Demanganization: ORP set point

Appendix 4

To obtain a good quality zinc deposit the amount of metallic impurities in the electrolysis solution must be less than 1 ppm. Manganese must be removed by the addition of permanganate that is capable to oxidize Mn^{2+} to Mn^{4+} leading to the precipitation of manganese, probably dioxide (MnO_2), that can be removed by filtration. Reactions that occur are shown in Equation 1; the first represents the desired demanganization reaction while the second is an undesired side reaction that occurs kinetically slowly and transforms

the excess of permanganate in MnO_2 by consuming ammonium.

$$2MnO_4^- + 3Mn^{2+} + 2H_2O \rightarrow 5MnO_2 + 4H^+$$

$$2MnO_4^- + 2NH_4^+ \rightarrow 2MnO_2 + 4H_2O + N_2$$

Equation 1: Permanganate reactions in presence of Mn^{2+} and NH_4Cl.

The addition of permanganate anion, as a saturated $KMnO_4$ solution, can be done in three different points: to the leaching solution, to the filtered leaching solution and to the cemented solution. This addition is made automatically, the software continuously controls the permanganate pump and attempts to maintain the ORP at the established set point.

The ORP set point value represents the point at which the demanganization reaction is finished, exceeding it is a sign of excessive permanganate addition resulting in ammonium consumption.

The influence of solution type, temperature and pH on the ORP set point of the manganese-permanganate reaction was evaluated with potentiometric titrations. The knowledge of the behaviour of these factors can lead to the determination of an equation that can determine the proper ORP set point depending on the solution conditions.

Determination of the equivalence point, to which the equivalent volume and inflection point ORP correspond, was performed following a mathematical analysis of the obtained curves. A tipical potentiometric titration curve is reported in Figure 18.

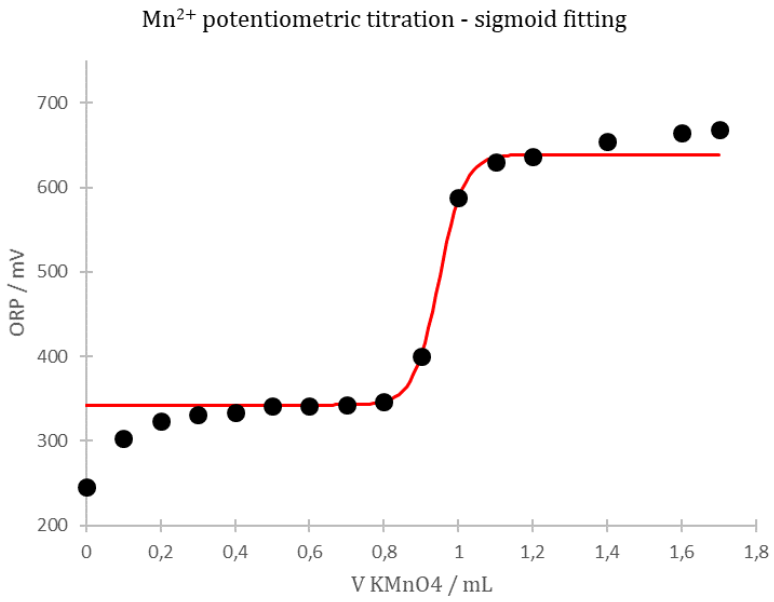

Figure 18: Demanganization reaction titration curve.

Obtained ORP inflection point values were plotted against pH for each different solution and temperature, Figure 19 shows the linear correlation between ORP and pH on filtered EAFD leach solutions.

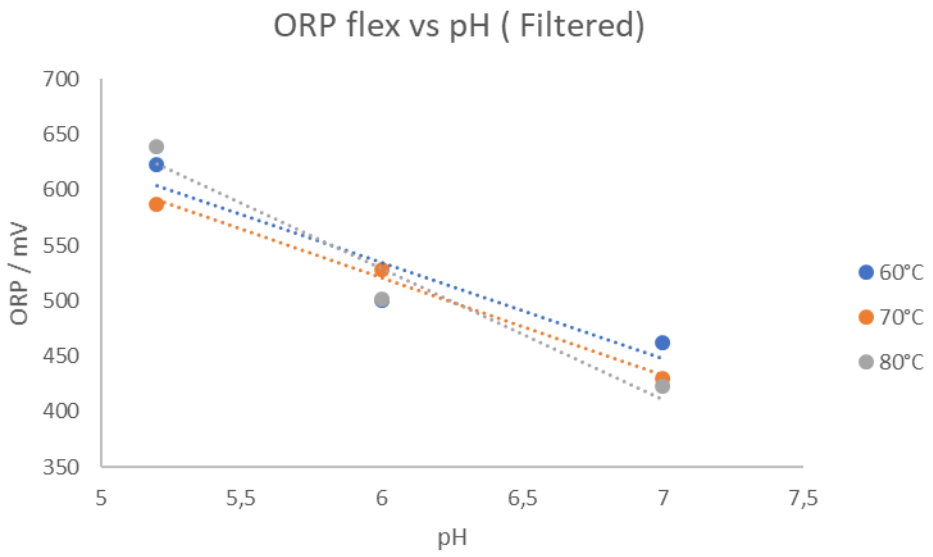

Figure 19: ORP inflection points vs pH at different temperature, filtered solution.

From the analysis of correlations obtained on filtered leach solutions, cemented solutions, and unfiltered leach solutions, the influence of temperature and solution type seems minimal. The data obtained were averaged and a linear correlation between ORP and pH was determined.

The correlation found plotted on manganese Pourbaix diagram, Figure 20, helps to understand the concept behind the redox end point. If the solution potential, read with an ORP probe, is below the dashed red line, the Mn^{2+} species is still present, if it its above, manganese will have been oxidized and will be in the form of a precipitate oxide. With the correlation found, is possible to establish the correct ORP set point according to the solution pH optimizing permanganate consumption.

Note that the ORP electrode used referred to an Ag/AgCl electrode, the pourbaix diagram report E-pH equilibrium vs hydrogen electrode.

In addition, increased permanganate consumption was observed during titrations of solutions containing EAFD, approximately +11%.

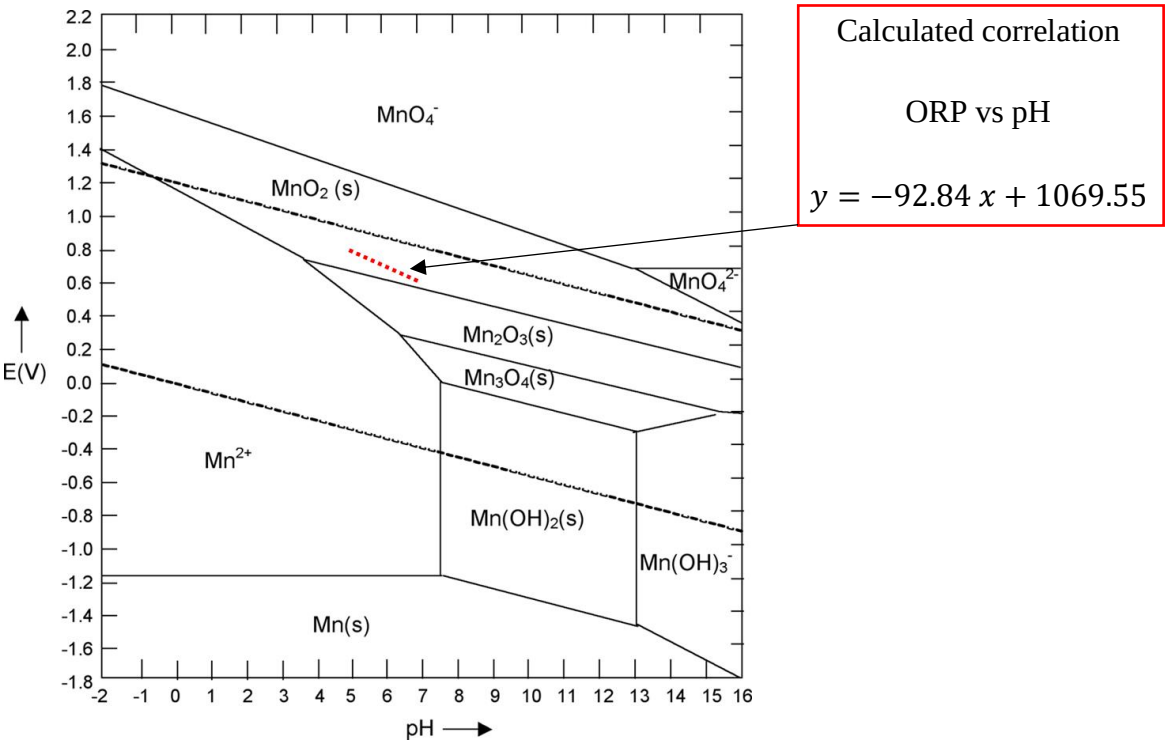

Figure 20: ORP vs pH correlation and manganese pourbaix diagram. Note: the ORP electrode used referred to an Ag/AgCl electrode; in the pourbaix diagram the E-pH correlation is reported vs hydrogen electrode.

Demanganization reaction: kinetic study

Appendix 5

As mentioned above, permanganate added to an EZINEX® solution can react in three different ways: with the Mn^{2+}, with ammonium or oxidable compounds present in EAFDs. The first one is the desired reaction while the others are side reactions.

More than 30% of the costs of the chemicals required by the EZINEX® process are related to permanganate consumption and these side reactions represents a possible waste of such reagent; a better understanding of the kinetics of these in different conditions could lead to optimization of permanganate consumption.

The demanganization reaction is a very fast reaction, it can be defined instantaneous, while the reaction of permanganate and ammonia proceeds on a slower time scale.

Reaction kinetics were determined using two different techniques: UV-Vis spectroscopy for the slow reaction and oxidation reduction potential monitoring for the fast reaction.

Permanganate absorbs in the visible range, and its concentration can be monitored over time (@ 525nm), Figure 21, allowing the derivation of kinetics laws, Figure 22.

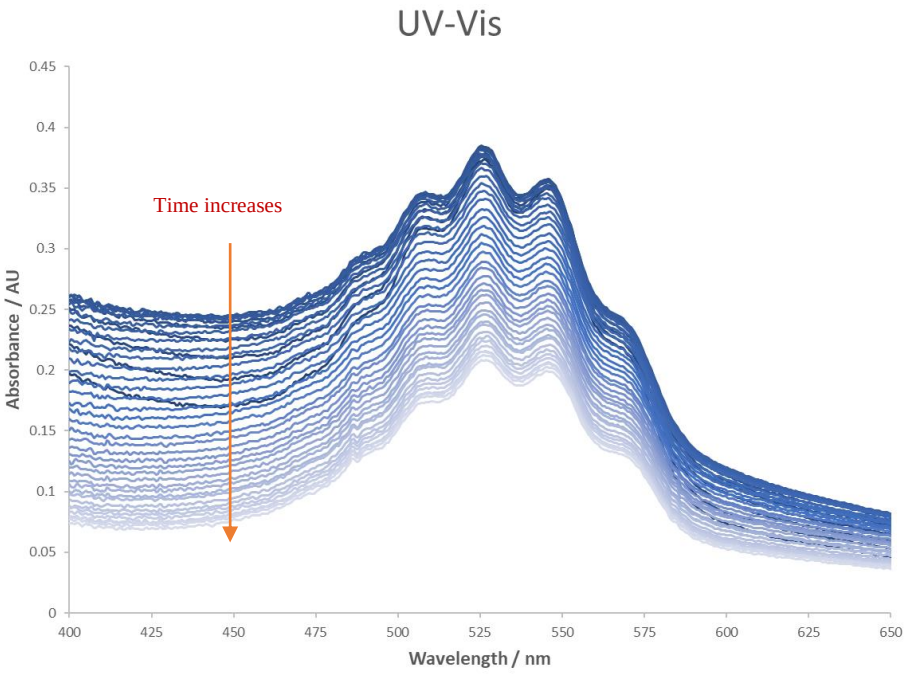

Figure 21: Series of UV-Vis spectra of permanganate in ammonium chloride solution at different times.

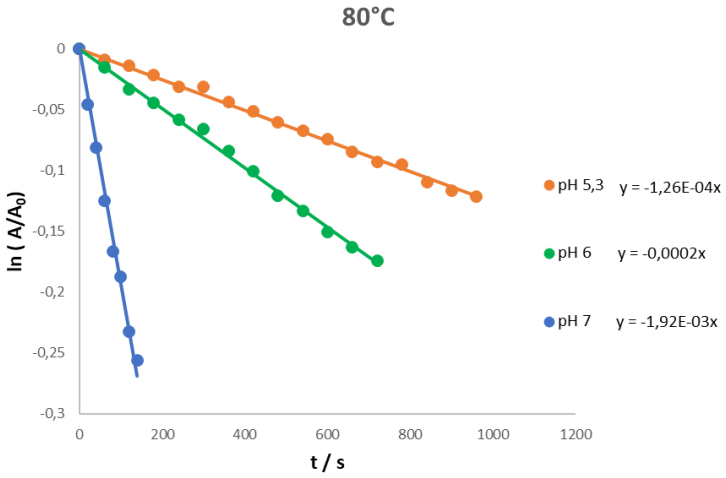

Figure 22: Kinetics of permanganate in NH_4Cl 200 g L^{-1} @ 80°C.

The reaction between permanganate and manganese on the other hand is very fast; kinetics were obtained by monitoring the solution ORP, Figure 23. Results are shown in Figure 24; in both cases the increase of pH and temperature increases reactions kinetics.

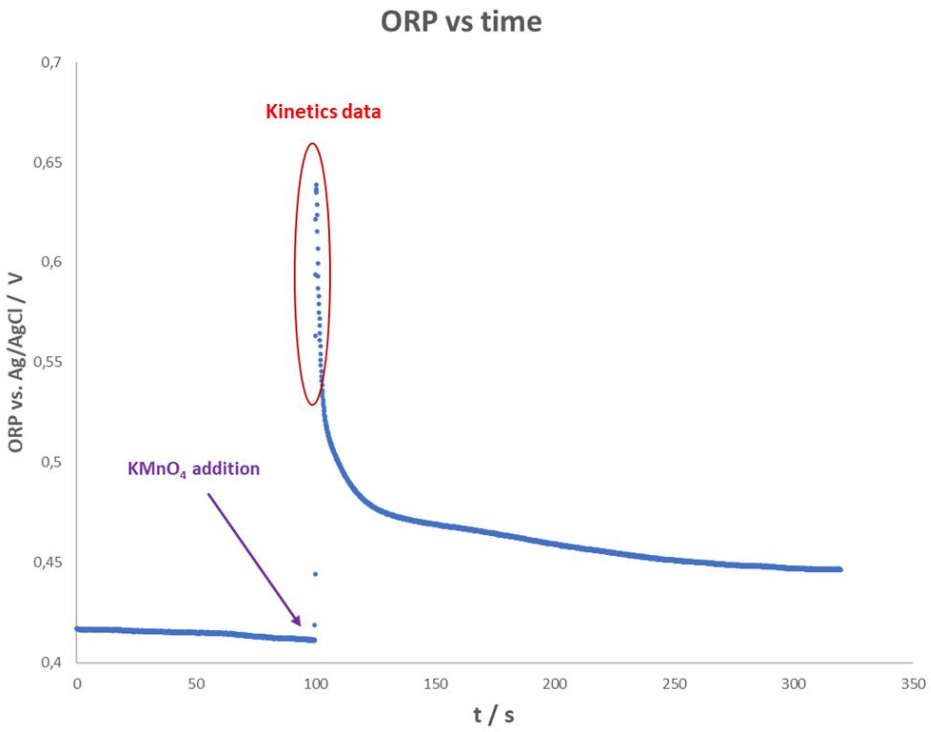

Figure 23: ORP behavior after permanganate addition.

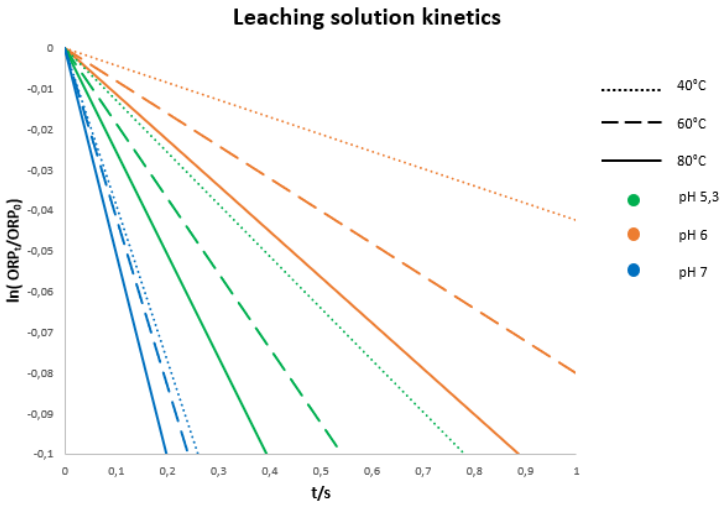

Figure 24: kinetics of permanganate in leaching solutions, the hatching of lines represent the temperature while colors are relative to diffent pH values.

Furthermore, the influence of EAFD on permanganate consumption was evaluated; experimental reaction half-lives are summarized in Figure 25 and Figure 26. The reaction between ammonium and permanganate is much slower than the reaction that occurs

between permanganate and manganese, both proceeding faster the higher the temperature and the more basic the pH. Permanganate consumption by its side reaction with ammonium can therefore be considered irrelevant even if it should be taken into consideration that, preparing permanganate concentrated solution using wash water will lead to a consumption of reagent due to the presence of ammonium.

In addition, the kinetic test conducted in the presence of EAFD shows faster kinetics than the same test performed on filtered leach solution under the same conditions. As noted above, the addition of permanganate to the process solution, if done in the leaching tank will lead to excessive permanganate consumption, it would be better to do the addition after removing EAF; this would also allow the precipitate to be separated from the leach residue giving added value to the process.

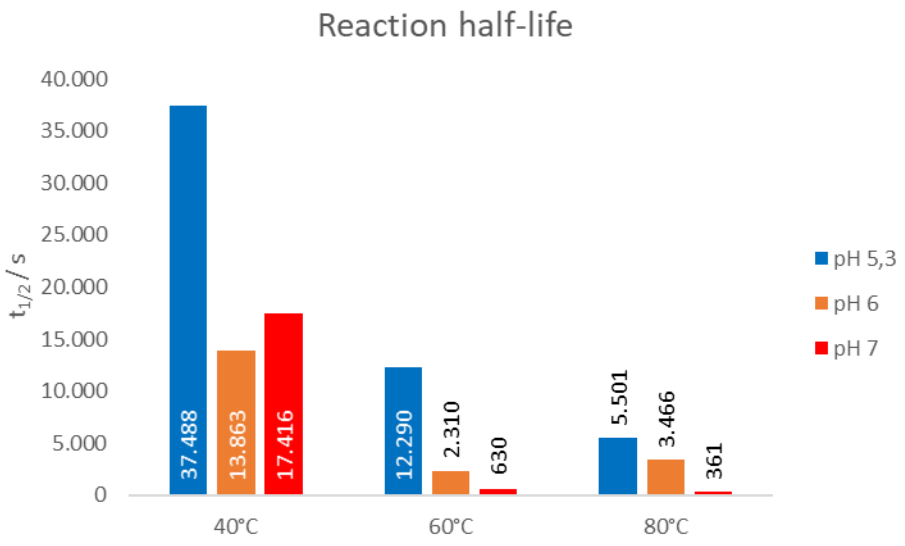

Figure 25: Permanganate- ammonium reaction half-lives in different conditions.

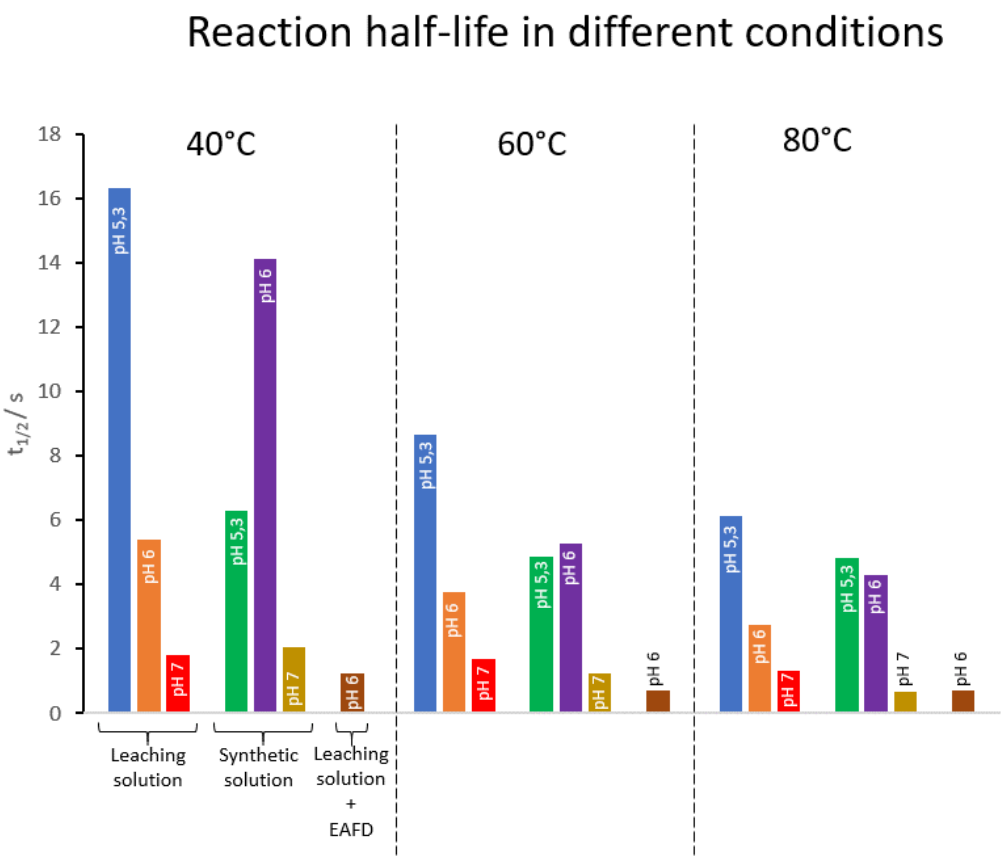

Figure 26: permanganate reaction half-life in different conditions.

Demanganization: particle size distribution

Appendix 6

The product of the demanganization reaction must be removed from the process solution, a series of static light scattering (SLS) measurements were performed to determine the particle size distribution of the product of the demanganization reaction.

The demanganization reaction was performed at different pHs and temperatures to cover the full spectrum of conditions possible within the plant.

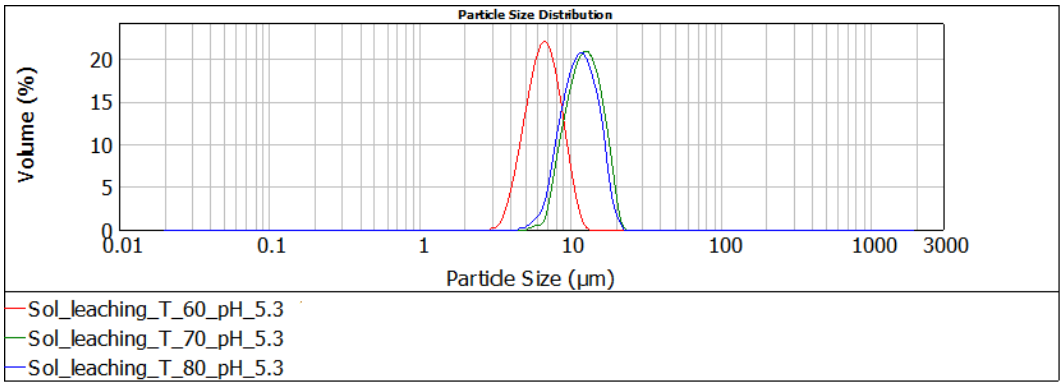

Figure 27: Manganese oxide particle size distribution, pH 5.3 -60/70/80 °C.

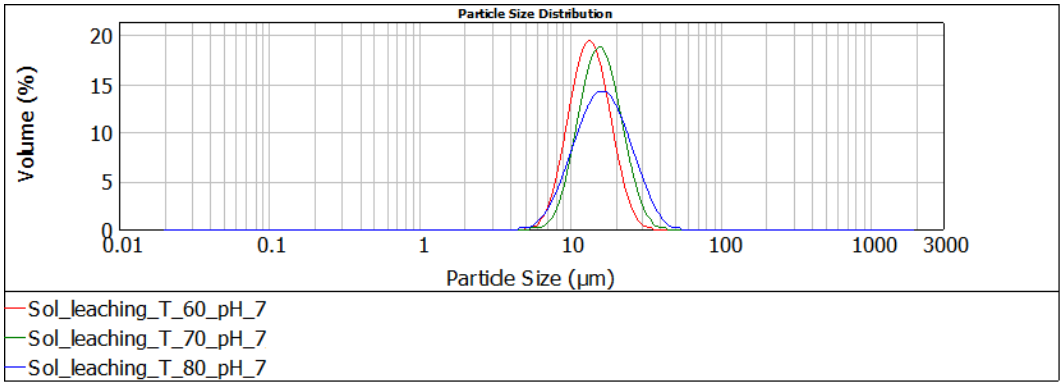

Figure 28: Manganese oxide particle size distribution, pH 7 - 60/70/80 °C.

pH seems to influence the particle size distribution, the particles increase in size as this parameter increases, from 6 µm to 13 µm. When this process is conducted at a higher temperature, the influence of pH is no longer evident, the average size of the precipitate being 15 µm, Figure 27 and Figure 28.

Demanganization reaction: flocculation

A possible method for the separation of manganese oxide obtained after a demanganization reaction is flocculation. The fine particles in solution are usually charged and repel each other, the addition of flocculating agents neutralizes this electrostatic charge allowing the aggregation of the particles into heavier flocs which, due to their higher mass, have a higher sedimentation rate than the initial particles. The settled particles can then be removed by filtration of the thickened fraction.

Several types of flocculating agents, both anionic and cationic, were compared; Figure 29 shows the effect of some after 25 seconds. The supernatant solution was sampled and

FTUs were measured to have a yardstick for comparison. The most promising, DRYFLOC 971, was used for a sedimentation rate test and compared to a demanganized solution without flocculant, Figure 30. The two sedimentation rates do not differ much, even in the solution without the addition of the flocculant agent, large particles able to sediment rapidly are present, however the finer portion of the solid remains in suspension for a long time and only the addition of the flocculant is able to aggregate and deposit it.

Summarizing the knowledge obtained regarding the behavior of flocculants on the demanganized reaction product, the best results were obtained with anionic flocculants. Manganese oxide is probably positively charged, and it is possible to settle the suspended solid obtaining a completely clear solution by adding a flocculating agent. The settled solid can then be separated from the liquid without treating the entire plant flow rate, which can range from a few hundred to several thousand liters per hour.

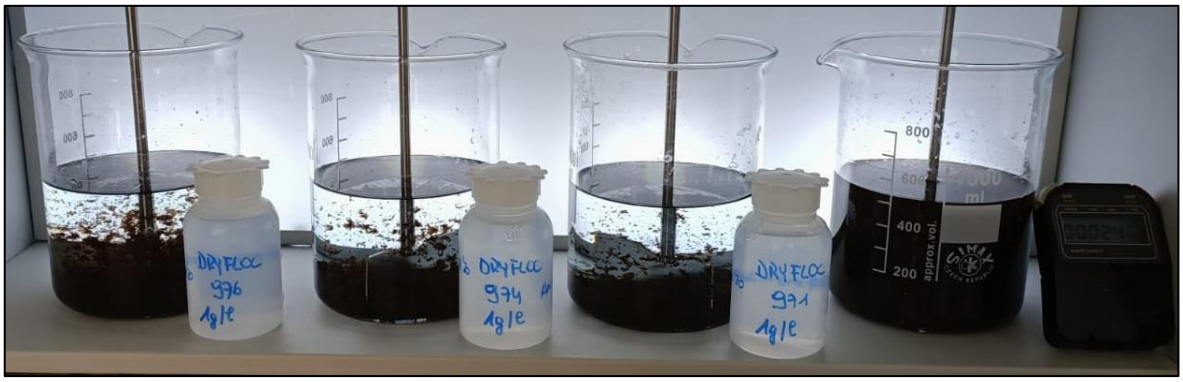

Figure 29: appearance of a demanganized solution in presence of different flocculating agents after 25 second, as it is solution on the right for comparison.

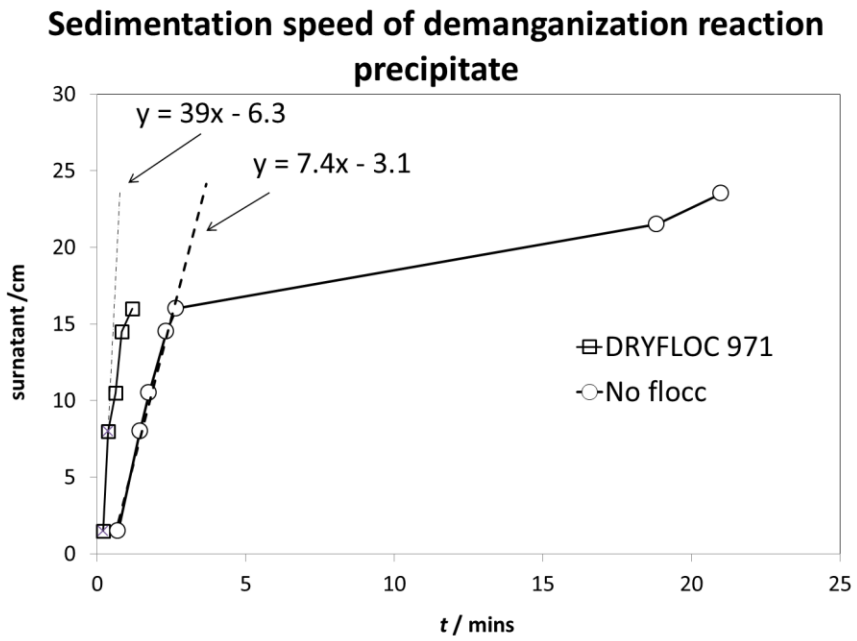

Figure 30: Sedimentation speed with and without flocculating agent.

Demanganization reaction: Solid-liquid separation, filtration

Filtration is the most common solid-liquid separation technique; tests on a freshly demanganized solution were performed to evaluate its effectiveness. First, a correlation between FTU, turbidimetric analysis, and manganese concentration was determined, Figure 31. A freshly demanganized solution was then filtered through a vacuum filtration system repeating this operation without removing the formed filter panel until a zero-manganese concentration was reached in the filtered solution. The manganese concentration in the filtrate was checked by turbidimetric analysis and the results obtained are shown in Figure 32.

The correlation between manganese concentration in the filtrate and the number of filtrations is expontetial, asymptotic to zero for an infinite number of filtrations; this means that even though the panel becomes thicker and more packed, the smallest particles are very difficult to stop by filtration.

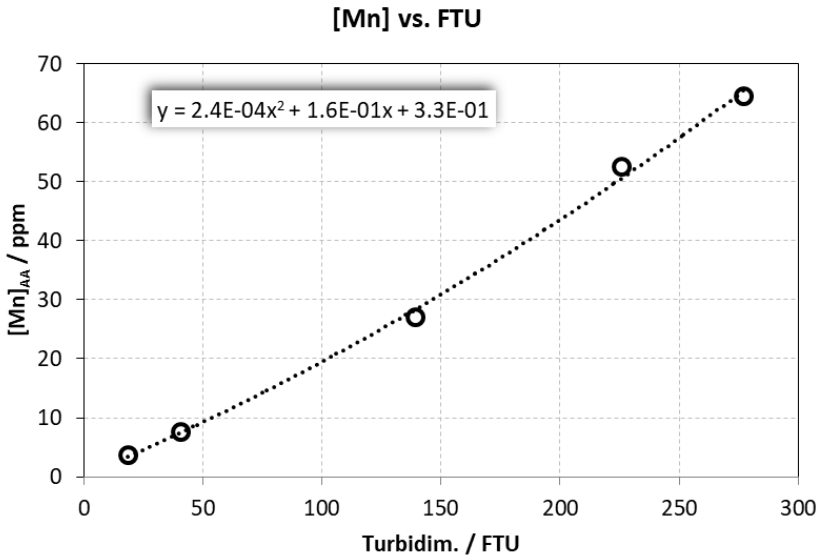

Figure 31: Correlation between FTU and manganese concentration determined with atomic absorption analysis.

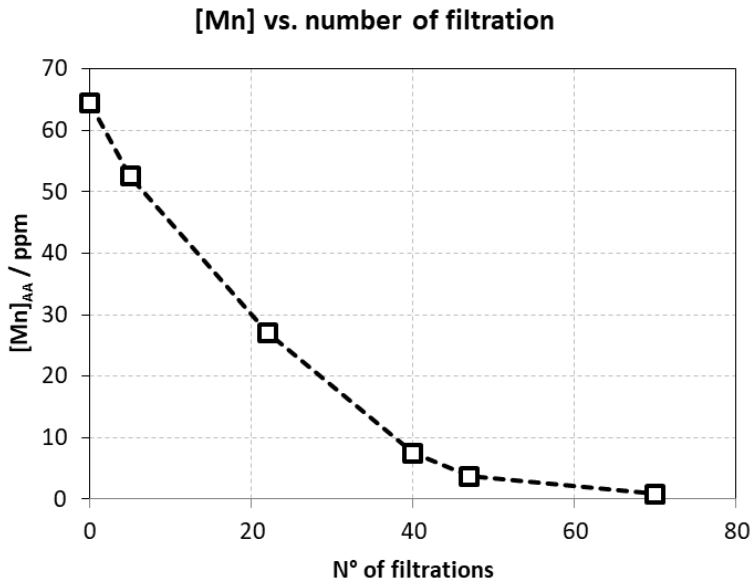

Figure 32: Manganese concentration in the filtrate vs number of filtrations.

Demanganization reaction: Solid-liquid separation, centrifugation

Centrifugation is a solid-liquid separation method that separates the mixture by applying a centrifugal force; it works on the principle of sedimentation but with a higher g-force. To explore the possibility of removing the manganese oxide produced by the demanganization reaction, tests were performed using a laboratory centrifuge. An array of tests was made on

a freshly demanganized solution by changing the centrifugation time and speed, the degree of separation of each test was evaluated by turbidimetric analysis of the supernatant.

As shown in Figure 33, centrifugation was shown to be able to separate even the finest solid, which was less likely to settle. A 3D plot that can provide a correlation between centrifugation time, g-force applied, and degree of separation in terms of ppm Mn in the supernatant is shown Figure 34. With this experimentation was proved that there is an alternative to filtration, the data obtained will be useful to evaluate the possibility of implementing this separation process

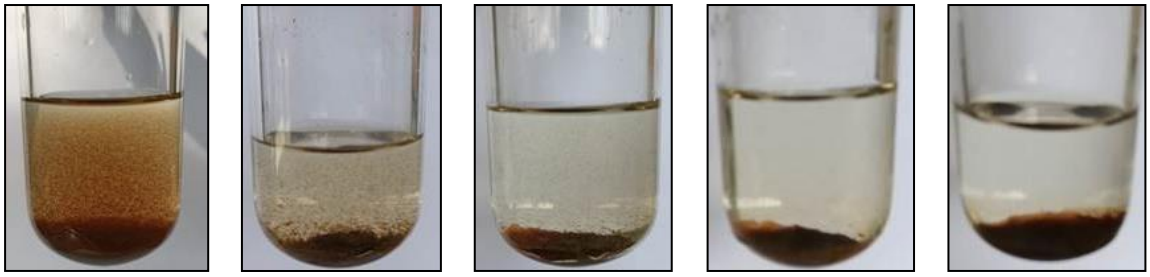

Figure 33: Centrifugation tests on a freshly demanganized solution; time 10 min, rpms 500-1000-2000-3000-4000 (from left to right respectively).

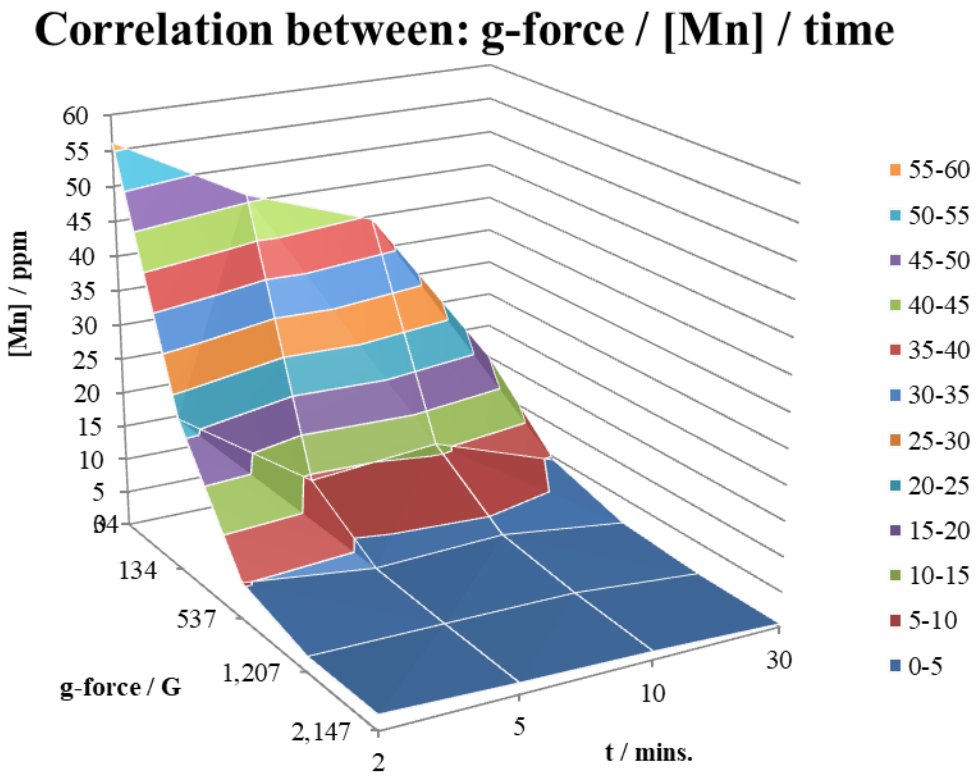

Figure 34: Centrifugation tests: g-force, [Mn] and time correlation.

Demanganization reaction: Manganese oxide formula determination

Appendix 7

If the demanganization reaction is carried out in a dedicated reactor, the manganese oxide obtained could represent resalable byproduct of the two hydrometallurgical technologies. Knowing the chemical formula of the manganese oxide extracted from the plants would lead to a more accurate selection of potential buyers.

Therefore, an attempt was made to determine the chemical formula of the compound. Manganese oxide was produced in the laboratory under various conditions and analyzed using XRD and XPS techniques.

The XRD spectra, Figure 35, show a good correlation between the peaks of the $HMnO_2$ species with those of the compound obtained by demanganization of a synthetic solution but do not match that obtained from an EAFD leaching solution. The spectrum of the latter does not have enough characteristic peaks to be solved.

Through an XPS analysis it is possible to obtain information on the oxidation state of the elements. The oxidation state of manganese can be distinguished using Mn 3s peak; splitted Mn 3s peak is caused by coupling of non-ionized 3s electron with 3d valence band electrons. The splitting width is diagnostic of the oxidation state of Mn[1,3]. Figure 36 shows the high-resolution spectra of Mn 3s peak, the difference between the two splitted peaks is in both cases near the value of 5.4 eV which is diagnostic of Mn (III) specie. The sample obtained from the leaching solution present a central peak overlapped to a two peaks system, this is attributed to the presence of zinc which interfere with the manganese identification. The average oxidation state of Mn results 3.02 for the synthetic sample and 3.01 for the leaching one.

Considering the above, presence of MnO_2 can be excluded and most probable compounds are Mn_2O_3 and $HMnO_2$.

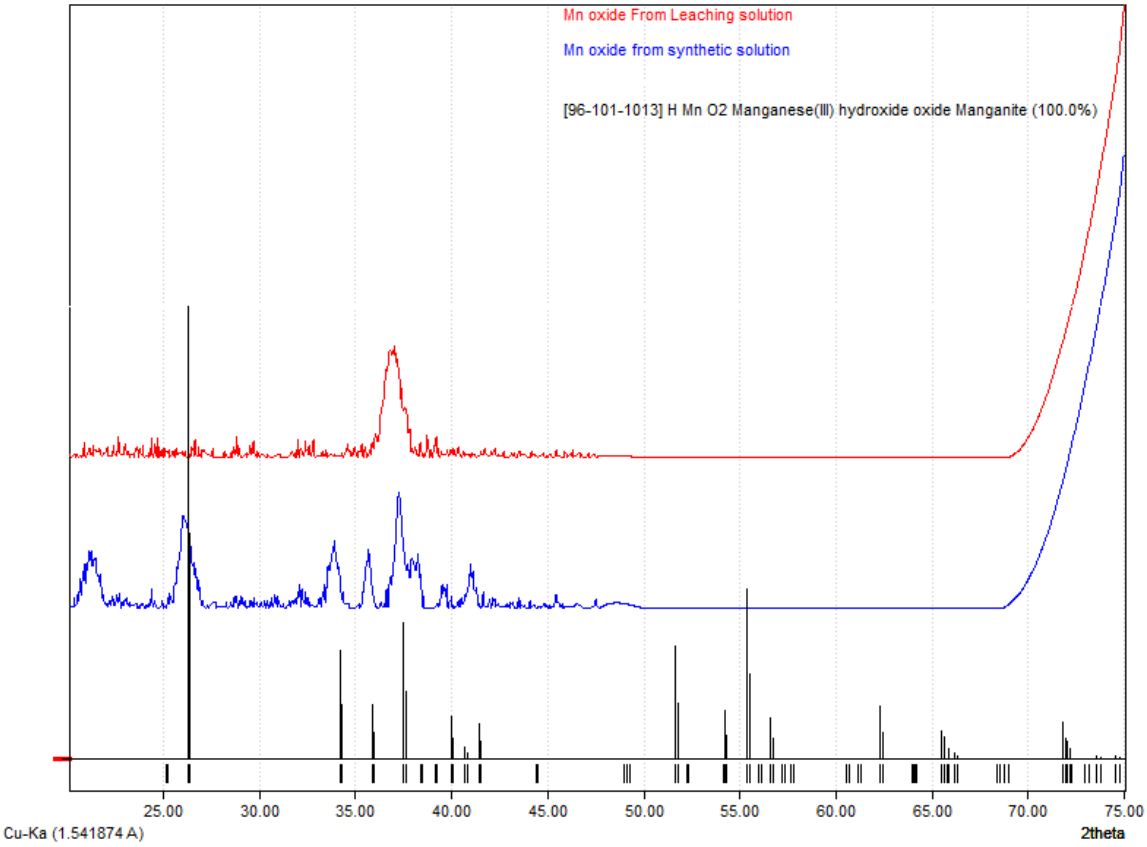

Figure 35: XRD pattern of manganese oxide obtained from synthetic and leaching solutions.

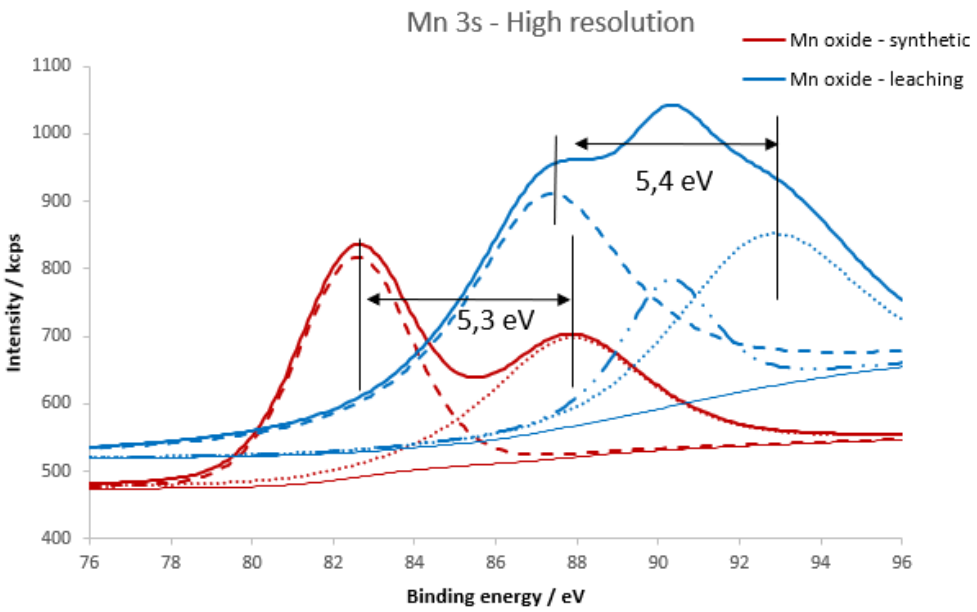

Figure 36: Manganese oxide xps spectra, detail of Mn 3s peaks.

Solution depuration: cementation

Secondary sources of zinc and lead contain, in addition to the two metals of interest, other metallic elements that are leached into ammonium chloride solutions; if they are not removed, they are reduced together with zinc or lead in the electrolysis cell and decrease the purity of the final deposit. Cementation is the step in which the spontaneous electrochemical reaction between an active metal and an electrolyte containing ions of a more noble metal is exploited. The active metal undergoes oxidation while the nobler ion is reduced; in practice, taking an EZINEX® solution as an example, the addition of metallic zinc powder causes part of the zinc to dissolve and silver, copper, lead and cadmium are reduced to their metallic form so that they can be removed from the process solution. For the F.A.S.T. process metallic lead must be added instead of zinc, but cementation in this case is practically an unexplored topic.

The following discussion is therefore related to the cementation of an EZINEX® solution and does not apply to the F.A.S.T. process for which additional aspects must be considered.

Currently, cementation in the EZINEX® process is carried out using the two-stage design; the concept is to perform a first stage of cementation with a partially spent zinc powder and then proceed with a second stage where a fresh zinc powder is used. This exploit the facte fact that the partially spent powder encounters a solution rich in impurities and greatly reduces its content, the total abatement is then carried out with a fresh more active zinc powder. Once the process is underway the fresh zinc powder is introduced into the second stage, removed and then added to the first stage; after it is finally removed from the process and forms so-called cements, a mixture of zinc and all the impurities.

In order to obtain a deeper understanding of the cementation reaction carried out in the presence of metallic zinc, the cementation kinetics for each impurity were determined and an alternative cementation reactor was tested.

Cementation: reaction kinetics

Appendix 8

Cementation tests were conducted on EZINEX® solutions using zinc metal pellets and the influence of temperature was evaluated. From the kinetic laws obtained, Figure 37 and Figure 38, the activation energies were extrapolated using Arrehenius equation, Table 1. According to Peters[35], activation energies lower than 10 kJ/mol, for cementation reactions, are to be attributed to processes under diffusive control while values above 40 kJ/mol are typical of chemically or electrochemically controlled reactions. Although the experimental apparatus used for the test was optimized to have as much diffusion as possible, the cementation reaction was still under diffusive control.

This experimental evidence indicates that the key to efficient solution purification through the addition of zinc metal powder lies in the hydrodynamics of the system, and a simple stirred vessel with baffles is not an optimized solution.

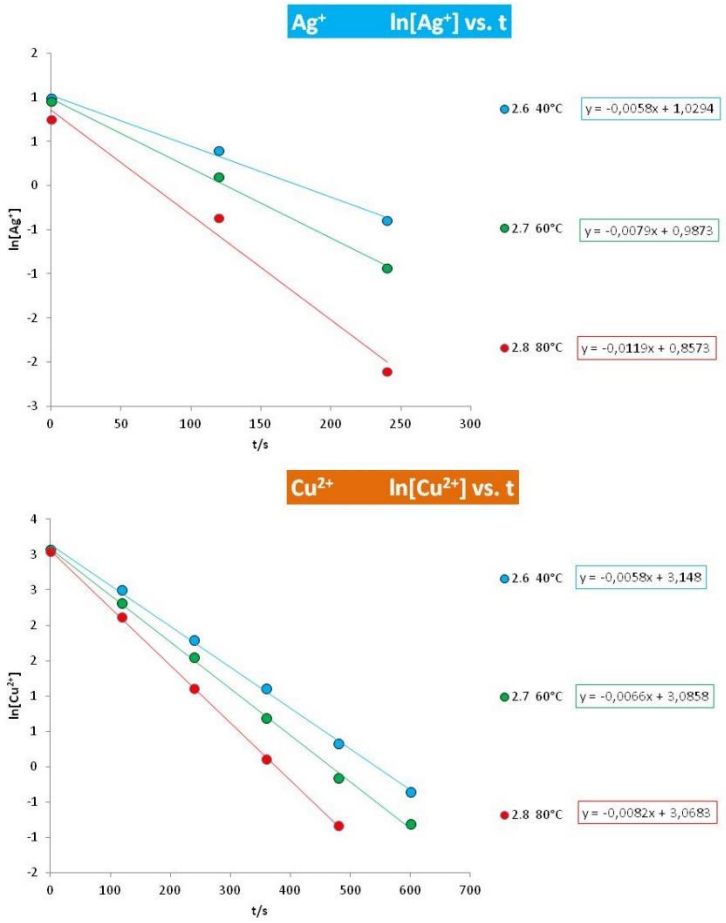

Figure 37: Cementation reaction kinetics.

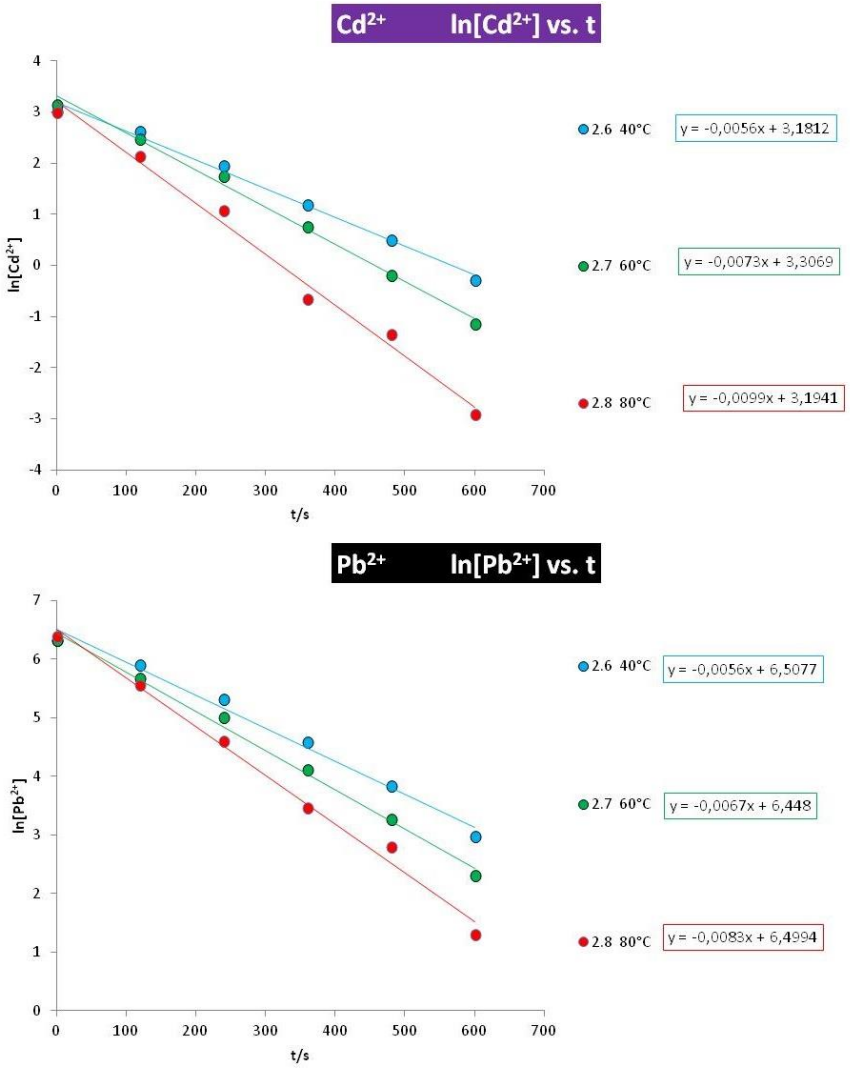

Figure 38: Cementation reaction kinetics.

	$Ag^{+}+e^{-}\rightarrow Ag^{0}$	$Cu^{2+}+2e^{-}\rightarrow Cu^{0}$	$Cd^{2+}+2e^{-}\rightarrow Cd^{0}$	$Pb^{2+}+2e^{-}\rightarrow Pb^{0}$
Ea (kj/mol)	16.44	6.78	13.04	9.004

Table 1: Cementatation reactions, extrapolated activation energy.

Cementation: rotary cylindrical reactor loaded with zinc pellet

Appendix 9

The possibility of performing the cementation reaction in an alternative way was evaluated. A cylindrical reactor loaded with zinc pellets was designed and tested, Figure 39.

The reduction reaction of the metal cations in the solution takes place on the surface of the metallic zinc particles that, once coated, stop being active. The use of a rotating reactor loaded with metallic zinc implies that the cements formed on the surface are removed due to the rubbing of the pieces thus renewing the surface and promoting the progress of the reaction. The detached cements will remain in suspension as very fine particles, the flow of the solution exiting the reactor should carry them away with it. The main advantage lies in the fact that the need for a reagent can be eliminated since the load of the cementation reactor is self-generated by the plant; a small portion of the zinc produced can be used to sustain the solution purification process.

Tests were conducted to evaluate the influence of various parameters such as rotational speed, temperature, solution flow rate, and the amount of metallic zinc loaded into the cylinder. A solution containing typical impurities found in an EZINEX® system was used for the tests.

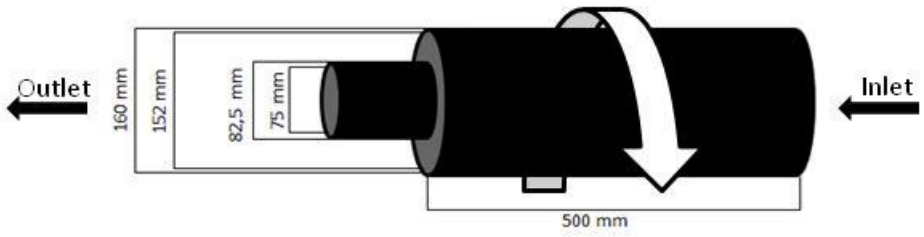

Figure 39: Rotary cylindrical reactor with dimensions.

The concentration of impurities was monitored by atomic absorption on samples taken from the reactor outflow; as an example, Figure 40 shows the concentration of lead in the outflow at different times. From the analysis of all the tests performed, all the variables considered affect the efficiency of the process, however those that increase the solution

residence time and surface renewal of the zinc pellets are the most influential.

This means that a low solution flow rate, a high static zinc load and a high rotation speed work best; temperature is also important but not for a kinetic point of view but to avoid precipitation of zinc salts.

Starting from a solution containing 20-25 ppm of cadmium and copper and 400-500 ppm of lead, it was possible, under the best working conditions, to reduce their concentration below 1 and 2 ppm respectively.

Laboratory-scale experiments did not allow sufficient material to be cemented to evaluate the removal of cements through the cylinder exit. This latter aspect needs to be evaluated in a larger scale series of tests.

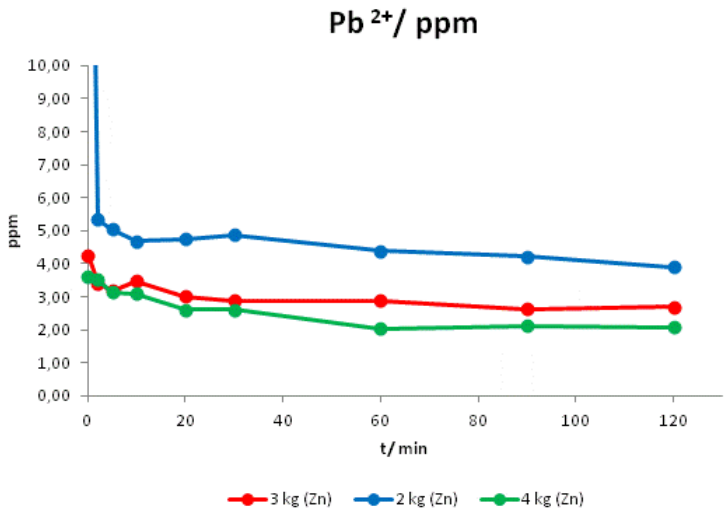

Figure 40: Influence of zinc load on the rotary cementation vesse. Lead initial concentration ~400 ppm.

Solution depuration: electrodepuration cell

An alternative way, compared to cementation, to remove metal impurities from the process solution could be an electrodepuration cell. The concept is based on an electrochemical cell operating at a potential at which everything, but zinc or lead is selectively reduced and deposited on the cathode. Subsequently, the resulting deposit is removed from the solution which is now free of metallic impurities. Initially, the energetics related to the deposition reaction of all the metal cations involved in the process were evaluated. The efficiency of different cell designs was then assessed.

Electrodepuration cell: polarization curves

Cathodic polarization curves were recorded in the presence of all possible metal cations present in the leachate solution to determine the energetics of the reduction reactions.

Silver is the noblest metal, its reduction begins at -0.2 V, Figure 41, followed by copper, -0.45 V, lead, -0.59 V, cadmium, -0.86 V, and finally zinc, -1.1 V. All potentials refer to an Ag/AgCl reference electrode, pH and cations concentrations are the one typical of an EZINEX® solution. The hydrogen evolution reaction is an undesirable reaction and depending on the substrate, which can catalyze or inhibit the reaction, it can start at different potentials. It should be kept in mind that when copper and silver are present, hydrogen evolution begins at about -1V Ag/AgCl. Considering the results, the electrodepuration of a F.A.S.T. leachate solution cannot be done because the cadmium reduction starts at a lower potential than the one related to the lead reduction. The situation is different in the case of an EZINEX® process solution; zinc is the least noble metal in this group and an electrode polarized at -0.9 vs Ag/AgCl might be able to reduce all metallic impurities.

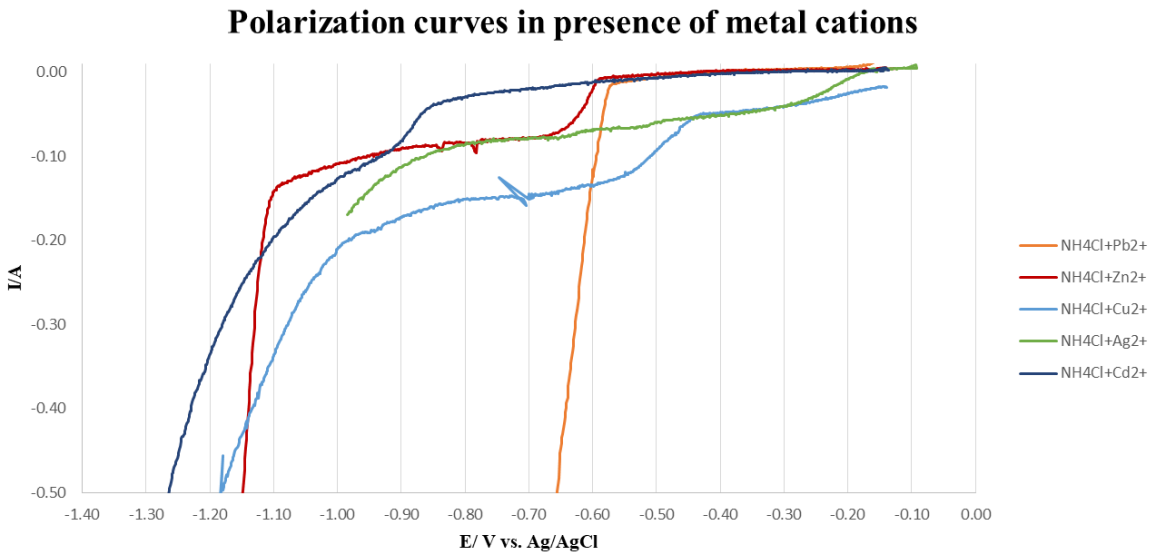

Figure 41: polarization curves in presence of different metal cations.

Electrodepuration cell: Packed electrodes design

The first design tested was a packed cell in which an array of titanium nets was compressed between two titanium frames, Figure 42. The cathodes were polarized at different potentials, -0.2/-0.4/-0.6/-0.8/-1/-1.2 V vs Ag/AgCl, and the cell was tested under one-through and recycle conditions using a typical EZINEX® solution. For the one-through conditions, meaning a single passage of solution into the cell, three flow rates were used. By changing the potential, it was possible to selectively remove impurities while leaving the zinc content unchanged, however even at -1.2 V complete lead removal was not observed. Recycling conditions gave better results, an example of the results obtained on the cell output flow is shown in Figure 42.

This design had some problems: it was difficult to remove the deposit from the cathodes and the residence time of the solution was low. However, it was realized that the efficiency increases as the metal deposit increases its surface area and based on these considerations, a second design was tested.

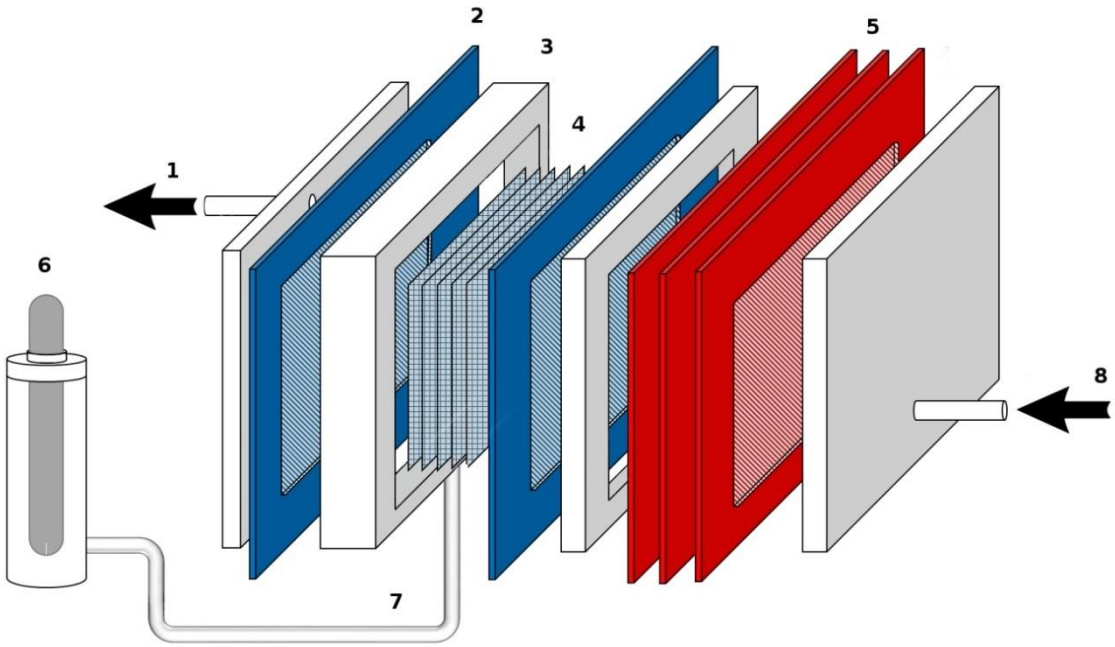

Figure 42: Electro-depuration cell: 1 outlet flow, 2 titanium cathode, 3 PVC-C frame to hold the titanium mesh pack, 4 titanium mesh pack, 5 activated titanium anodes, 6 reference electrode holder, 7 Luggin capillary, 8 inlet flow.

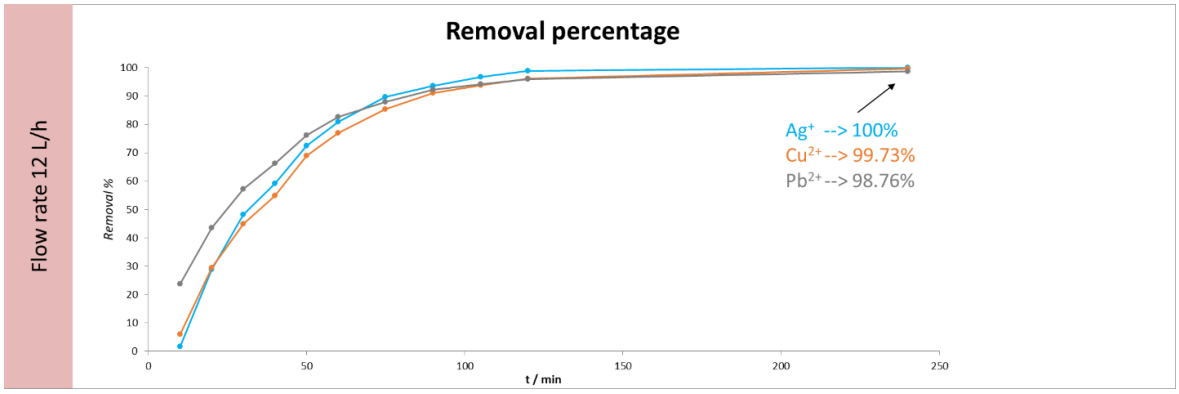

Figure 43: Removal percentage of silver lead and copper, applied potential -1V vs Ag/AgCl.

Electrodepuration cell: “snake-like path” design

Lead is the most prevalent impurity, it is solvated as a negatively charged chlorinated anion and rejected by the cathode that is positively charged. To mitigate this effect, a cell was designed to force the solution to come in contact with the cathodes as much as possible.

This cell consisted of alternating anodes and cathodes in which the solution is constrained to follow a snake-like path and become in contact with the cathodes surfaces as much as possible during a single passage in the cell, Figure 44 and Figure 45. This design was not as efficient as expected, due to the laminar motion of the solution, a channel is created between each electrode where the solution proceeds faster in the center and slows down on the walls. As the cell works, the concentration of lead in the immediate vicinity of the cathodes decreases more and more and the solution in laminar motion is unable to replenish it.

To overcome this, titanium nets were soldered onto the surface of the titanium cathodes, Figure 46 and Figure 47, and the performance of the cell was tested. As an example, tests performed under recycled conditions on both cells are shown in Figure 48. The effect of the increased surface area and turbulence created by the nets is evident on the lead concentration, however this design also presented a problem; the formed lead sponge caused a short circuit.

The spongy lead deposit, Figure 49, causes the deposit itself to act as an electrode with a very high surface area. When lead anions pass through this sponge-like deposit, they have a high contact probability with the electrode surface and the removal rate increases drastically. A new design that takes full advantage of the above will be the target of future studies.

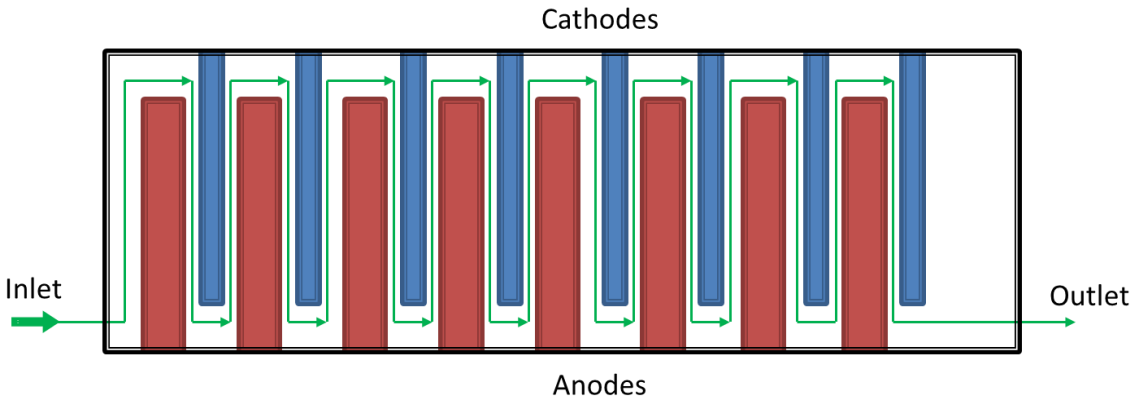

Figure 44: Snake path electrodepuration cell, schematized top view and solution path (green).

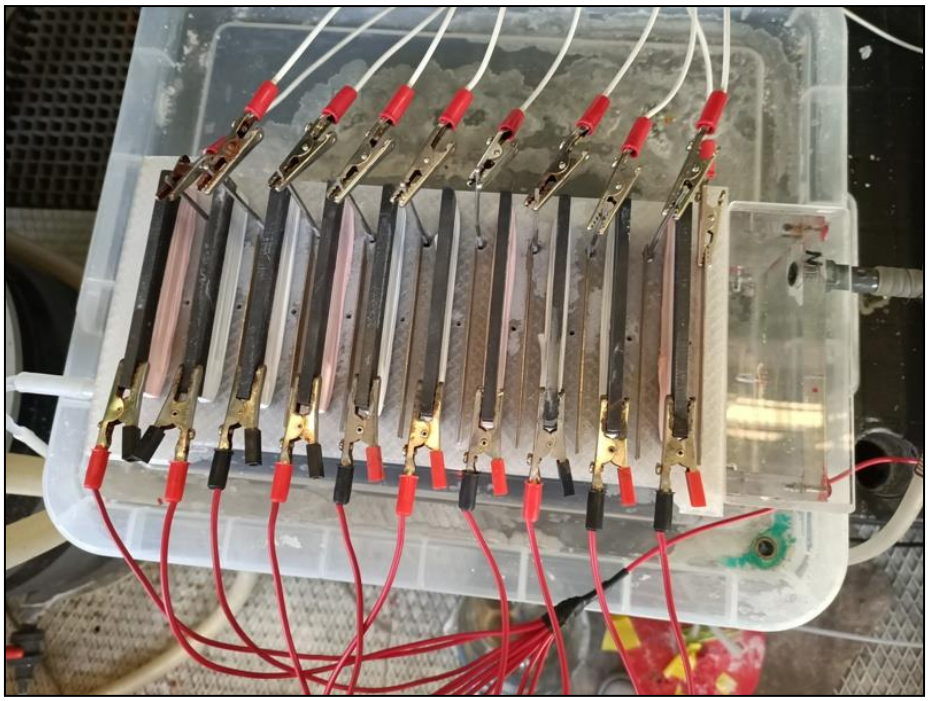

Figure 45: Snake path electrodepuration cell, top view.

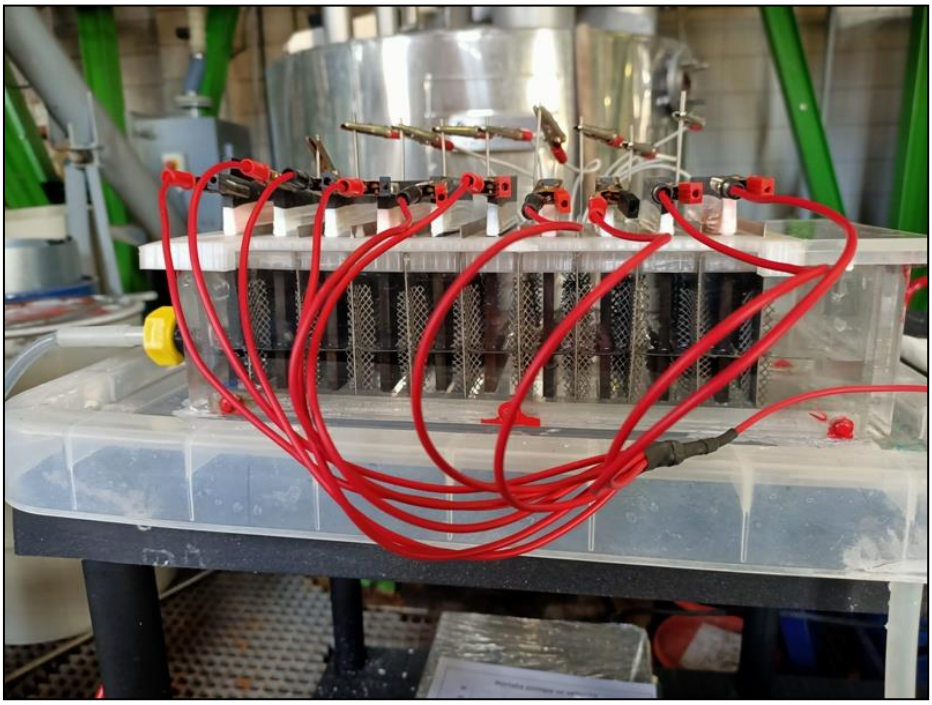

Figure 46: Snake path electrodepuration cell, side view.

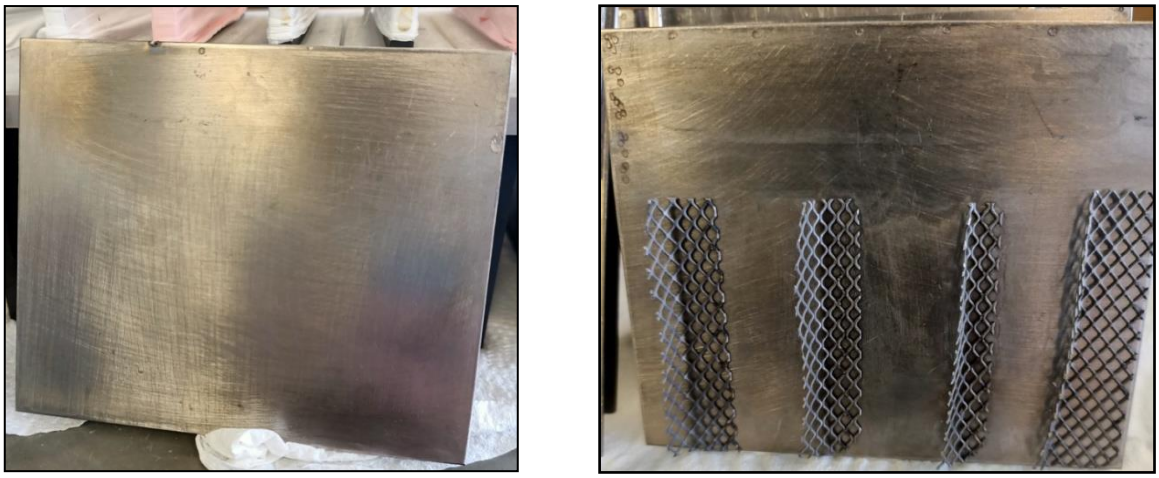

Figure 47: catodes before and afte the addition of titanium nets.

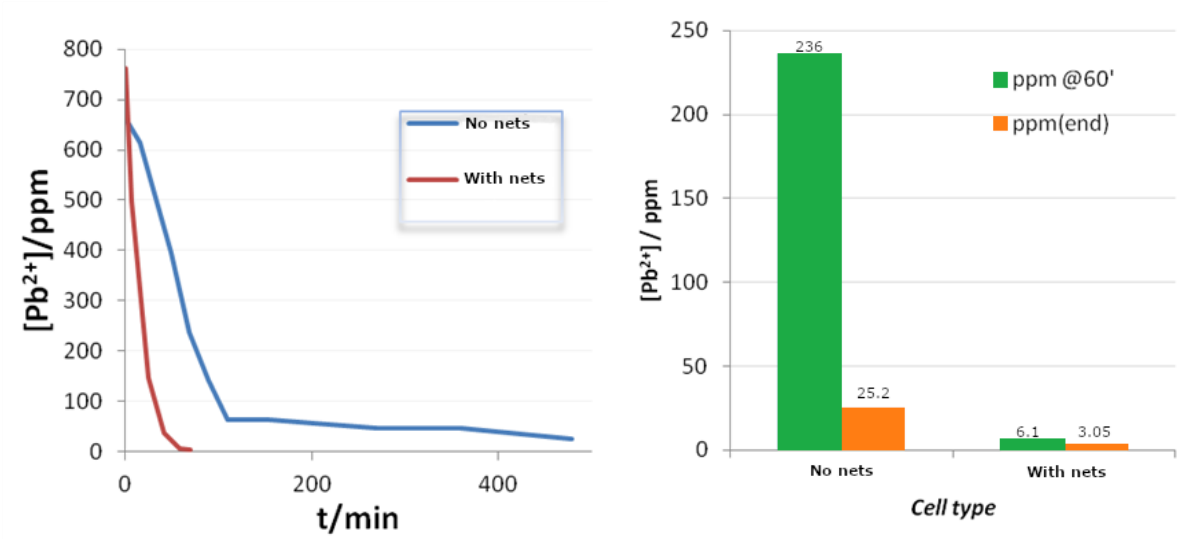

Figure 48: Comparison of performances before and after the addition of titanium nets.

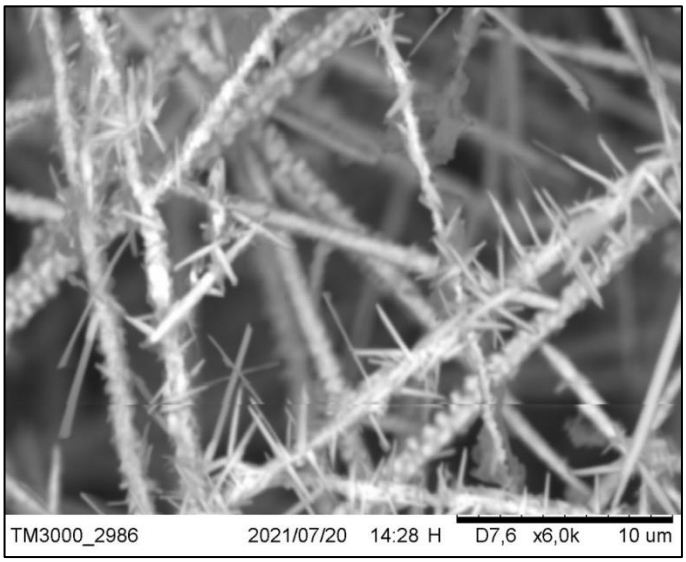

Figure 49: lead deposit, acicular deposit with high surface area.

Electrolysis cell

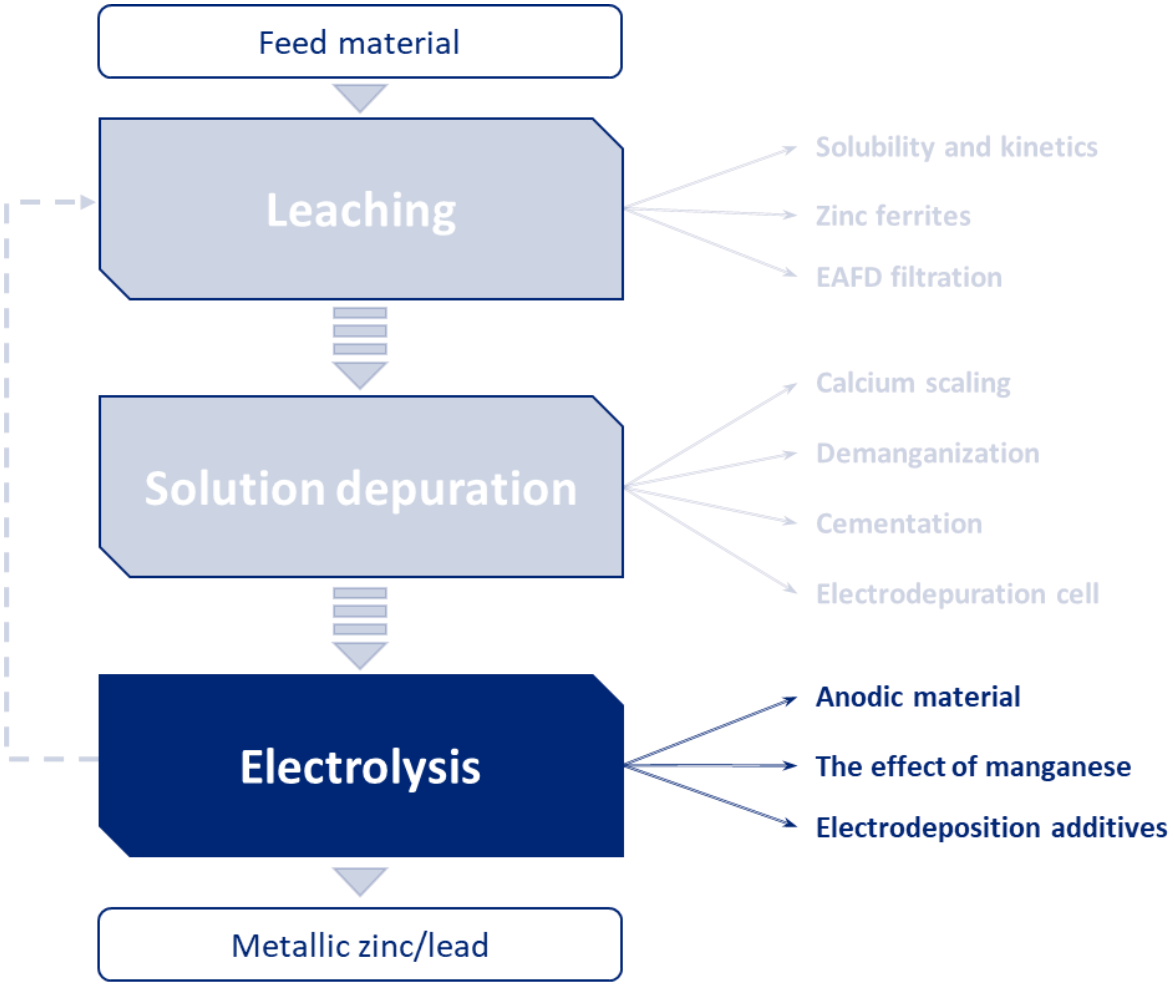

The electrolysis cell represents the heart of the two hydrometallurgical technologies, here the reduction of lead or zinc occurs on the surface of the cathodes giving origin to the final product.

The energy applied, in the form of electric current, contributes to the cost of the refined metal so it is important to ensure that the process works in the most favorable conditions possible. The choice of the anodic material is one of the main points on which it is possible to act in order to make the process less energy demanding.

The most performing electrode materials however can suffer from the presence of some species such as manganese, its effect on their service-life has been analyzed.

In the case of the EZINEX® process, the quality of the zinc sheets is measured not only in terms of purity but also in terms of appearance. This does not refer purely to the appearance of the plate but also to its structure; the more compact the deposit, the safer is the subsequent melting process. Among the factors that contribute to influencing this characteristic is the effect of additives, substances that can modify the growth of the deposit due to specific interactions between their functional groups and the electrode surface.

Therefore, the effect of different additives on the morphology of the zinc deposit was evaluated to produce a deposit as compact as possible.

Electrolysis cell: anodic material

During an electrolytic process, two half-reactions take place, the anodic and the cathodic; the combination of the two gives the complete reaction. These take place on the surface of the two electrodes called anode and cathode, which must be carefully chosen according to the reactions taking place. In ammonium chloride solutions, the two half-reactions are the evolution of Cl_2 at the anode and the reduction of lead or zinc at the cathode. The cathode must be a material that does not corrode in ammonium chloride and on which zinc and lead can be deposited and stripped easily, the only one is titanium and it is the one currently used for both processes.

The F.A.S.T. process

At the F.A.S.T. operative current density, 10 kA/m^2, the oxygen evolution reaction can not be excluded. In these conditions graphite undergoes oxidation then the use of activated titanium as anodic material is mandatory.

The anode is a somewhat complicated question, metal alloys undergo oxidation or passivation when polarized at positive potentials and are unable to sustain an oxidation current. Graphite could be a viable anodic material, but it has a high overpotential for the chlorine evolution reaction and this represents a high operational cost. Therefore, the choice should fall on catalytic materials that are able to sustain the oxidation current for a long time and have a low overpotential for the desired reaction. Furthermore, research should not be extended to exotic catalysts because the electrode must be commercially available to be applied to an industrial process. The only alternative are the so-called activated titanium anodes, a titanium substrate coated with metal oxides, usually Ru and Ir, that can sustain high anodic current densities with relatively low overpotentials.

To evaluate the benefits of replacing graphite with activated titanium, polarization tests were performed to determine the difference in energy required by the process[36]. Tafel straight lines, Figure 50, were extrapolated potential difference required by the anodic process was evaluated, Figure 51. The use of activated titanium instead of graphite can provide a theoretical gain in cell potential of about 0.45V at 300 A/m^2. Considering that the cell potential in the EZINEX® process is around 2.6-2.8 V, the use of activated titanium can reduce the energy requirement of the electrolysis step by about 16-17%.

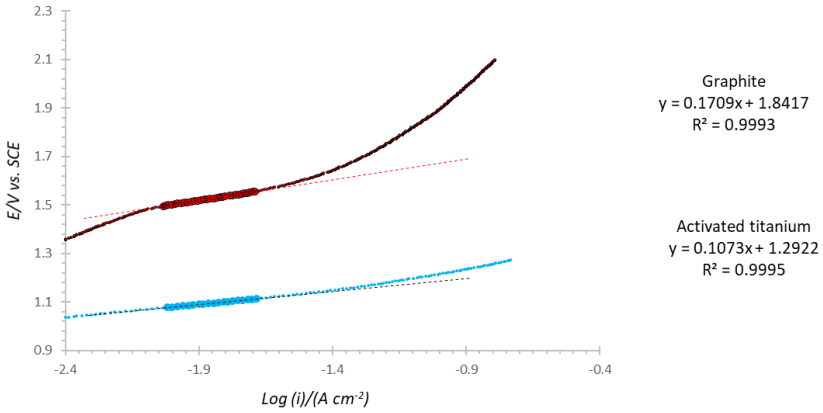

Figure 50 Tafel's straight line extrapolation.

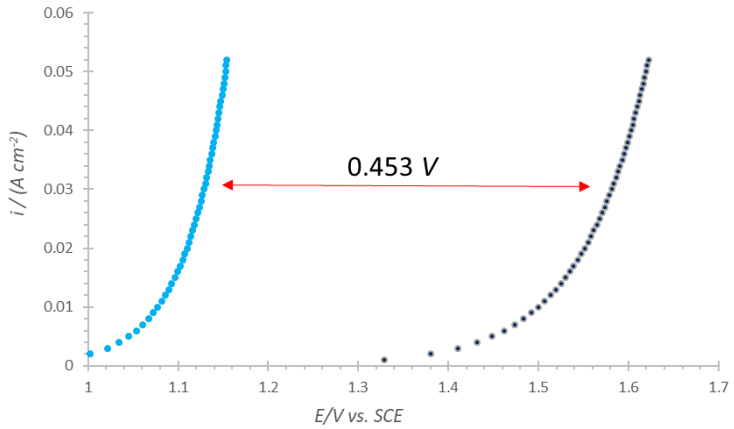

Figure 51: Evaluation of anodic potential difference at 300 A/m^2.

Electrolysis cell: the effect of manganese

Appendix 10

Manganese is removed from the process solution in the demanganization step but, if this is not conducted properly, it can get into the electrolysis cell. If this happens, manganese II is oxidized to manganese IV by the anode forming a fine solid that partly covers the electrode and partly goes into solution. When this solid touches the cathodes, it is reduced to its soluble form, Mn^{2+}, and can be oxidized again; this redox cycle consumes electrons decreasing the Faradaic efficiency of the electrolysis.

This happens regardless of the type of anodic electrode used but, in the case of the activated titanium, the presence of manganese poses another problem: deactivation of the catalytic coating. Activated titanium electrodes have a mud-like structure with deep cracks,

the formation of solid manganese oxide inside these cracks can mechanically stress the coating by detaching it from the substrate. At some point, the remaining coating is not sufficient to sustain the applied current and the electrode potential begins to rise increasing operating costs. The final step is the complete removal of the catalytic coating leaving the titanium substrate fully exposed.

This is a theoretical explanation of what might happen, however the time scale at which this process takes place is unknown. Tests have been done to get an idea of the behavior of this anodic material in an ammonium chloride solution containing manganese.

At the beginning of electrolysis, the solution appears transparent, but after a few minutes it begins to become increasingly turbid as the manganese oxidizes, Figure 52.

Figure 52: Ammonium chloride solution with manganese before electrolysis, A, and after 5, 15, 60 min, B, C, D.

The reading of the cell potential during electrolysis is an indication of the state of the electrode; as shown in Figure 53, in tests conducted in the presence of manganese, this value began to increase after one day of electrolysis while electrodes immersed in ammonium chloride, without manganese, showed a stable response.

Contrary to all expectations, the electrodes were found to be completely worn out, Figure 54, and not only without catalytic coating.

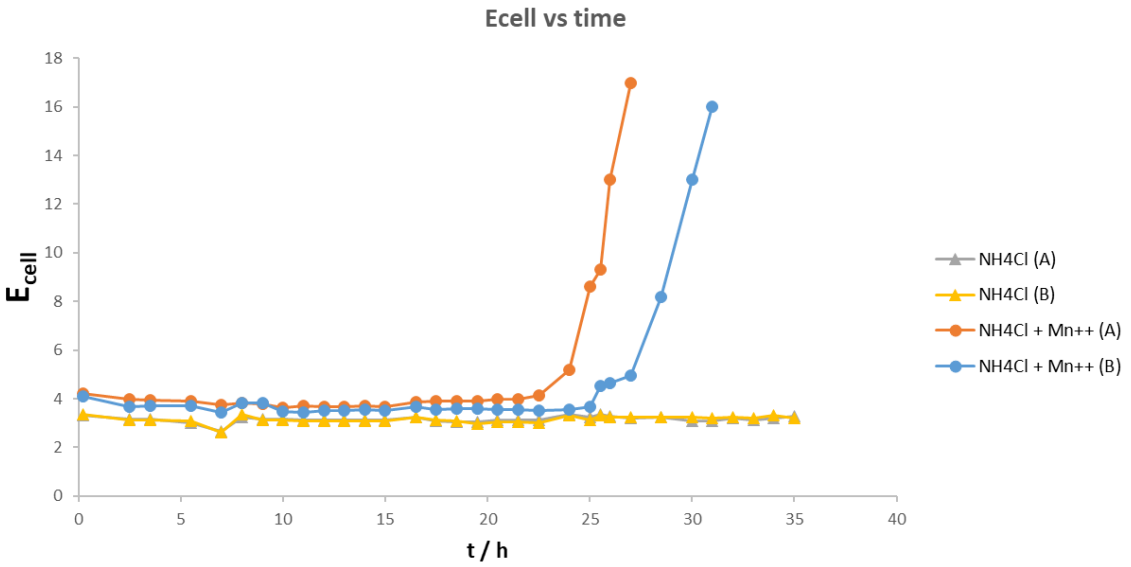

Figure 53: Cell potential vs time.

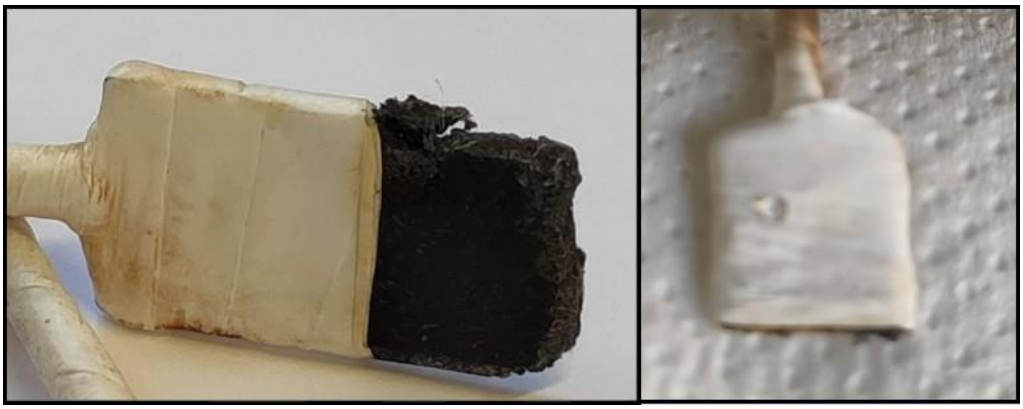

Figure 54: Detail of activated titanium electrode after 25 (left) and 27 hours of electrolysis (right).

The tests were replicated to try to understand the mechanism of deactivation with the help of a scanning electron microscope (SEM-EDX) and X-ray photoelectron spectroscopy (XPS) analysis.

When the cell potential of an electrode working in the presence of manganese began to rise, it was removed for analysis. Surface magnification, Figure 55, shows a noticeable difference between the electrode that worked in ammonium chloride and the one stressed by the presence of manganese, the latter appearing more cracked as if the manganese oxide

formation had mechanically opened the cracks already present. EDX analysis, Figure 56, shows a decrease in ruthenium and an increase in manganese on the surface of the partially deactivated electrode. In addition, traces of ruthenium, probably in its metallic form, were found on the surface of the cathodes that worked in the manganese-containing solution. This indicates that deactivation in presence of manganese could occur not only due to mechanical action but also due to chemical dissolution of the catalytic coating.

XPS analysis, done on new and nearly deactivated electrodes, does not show any particular changes in ruthenium oxidation states, but shows that its depletion starts in a certain area and then spreads to the whole coating,Figure 57.

The mechanism of depletion is still unclear, but evidence of both mechanical and chemical effects has been found. The consumption of the titanium substrate was not expected, it could be attributed to the high anodic potential reached after deactivation of the electrode which led the titanium to transnpassivation conditions. However, the possibility of using titanium-activated electrodes when manganese is present in the electrolyte solution must be carefully evaluated as this drastically reduces electrode lifetime and increases operating costs due to electrode replacement.

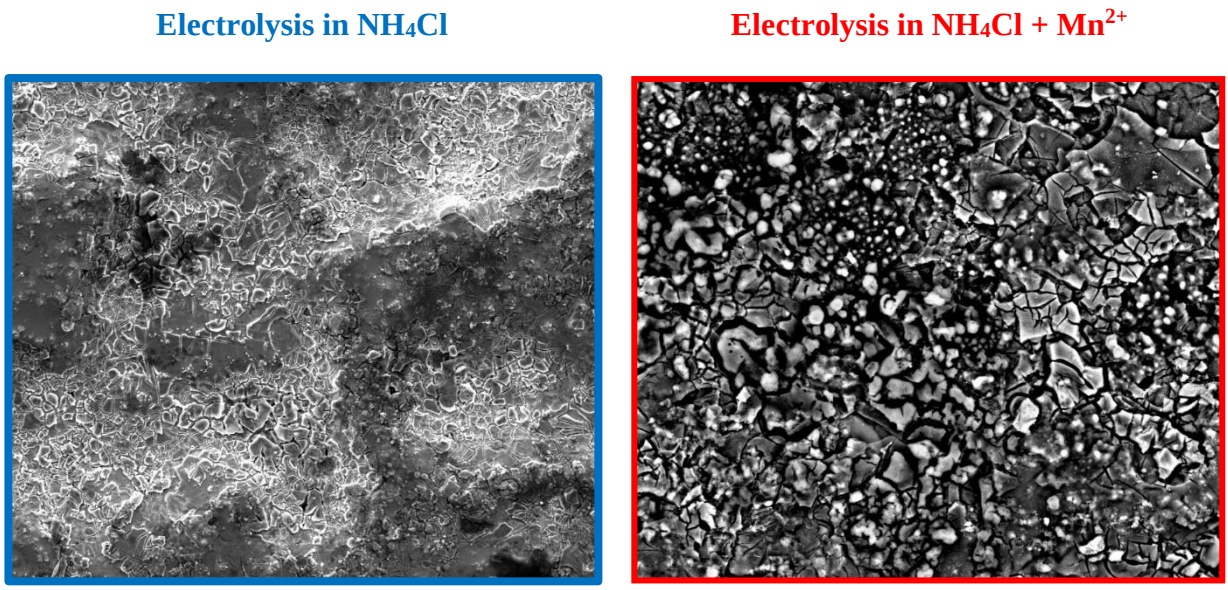

Figure 55: Surface morphology of activated titanium ruthenium coating before and after electrolysis, 500X.

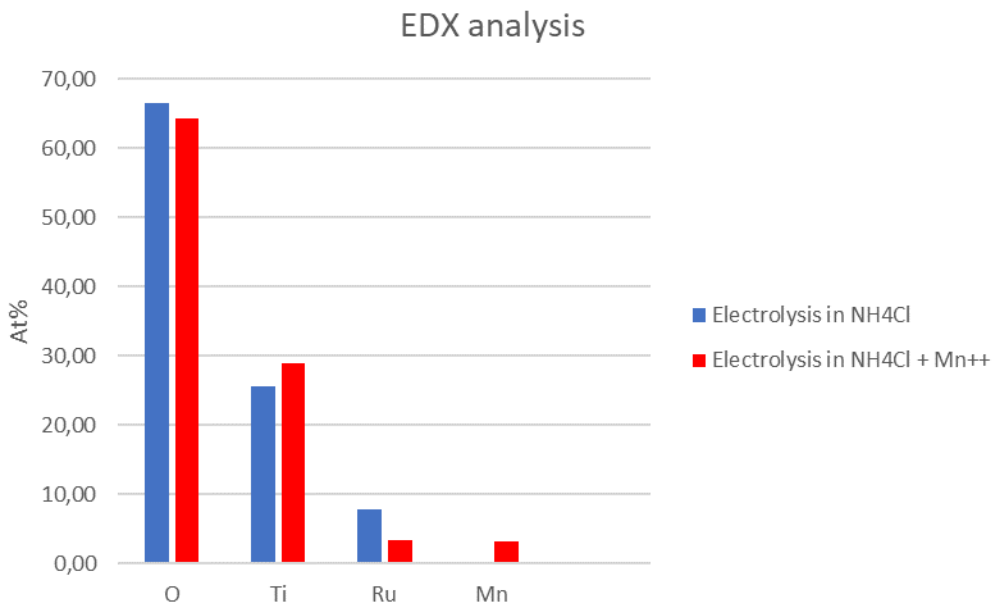

Figure 56: **EDX analysis on titanium activated electrodes.**

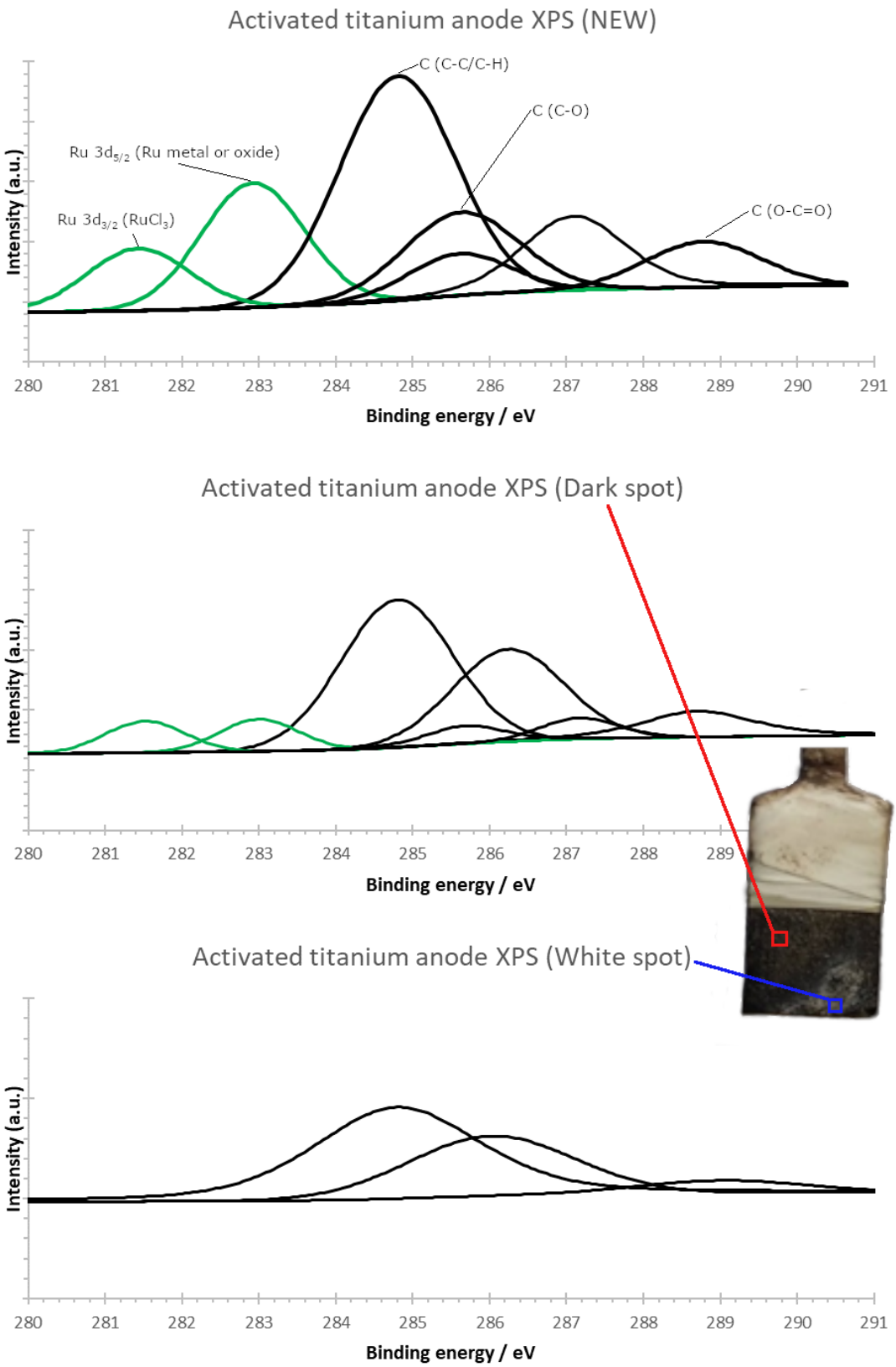

Figure 57: XPS of activated titanium, both new and semi exhausted.

Electrolysis cell: electrodeposition additives

Appendix 11

Metals refined using the electrodeposition technique have less environmental impact than the conventional pyrometallurgical method and high purities can be easily achieved. However, obtaining compact deposits without porosity and dendritic structure is not easy.

The aim of the EZINEX® process is to obtain zinc sheets with the highest possible purity. These are then destined to be melted in hot dip galvanizing baths or cast into ingots. From the Cape Gate experience, Figure 58, it was found that by immersing the zinc cathodes produced, the release of air present in the porosity made the process unsafe. In addition, the formation of dendrites on the surface of the cathodes has been noted; dendrites are dangerous because, if allowed to grow, they could lead to cell shorting.

The F.A.S.T. process

The F.A.S.T. process takes advantage of the dendritic growth mechanism. Lead is deposited on the cathode in the form of flakes, and stripped due to the high velocity of the electrolyte flow. The lead flakes are then agglomerated in a decanter, separated from the solution, and finally briquetted.

Many factors influence how metals are electrodeposited; some of them are current distribution, concentration of metal species, temperature, and presence of additives.

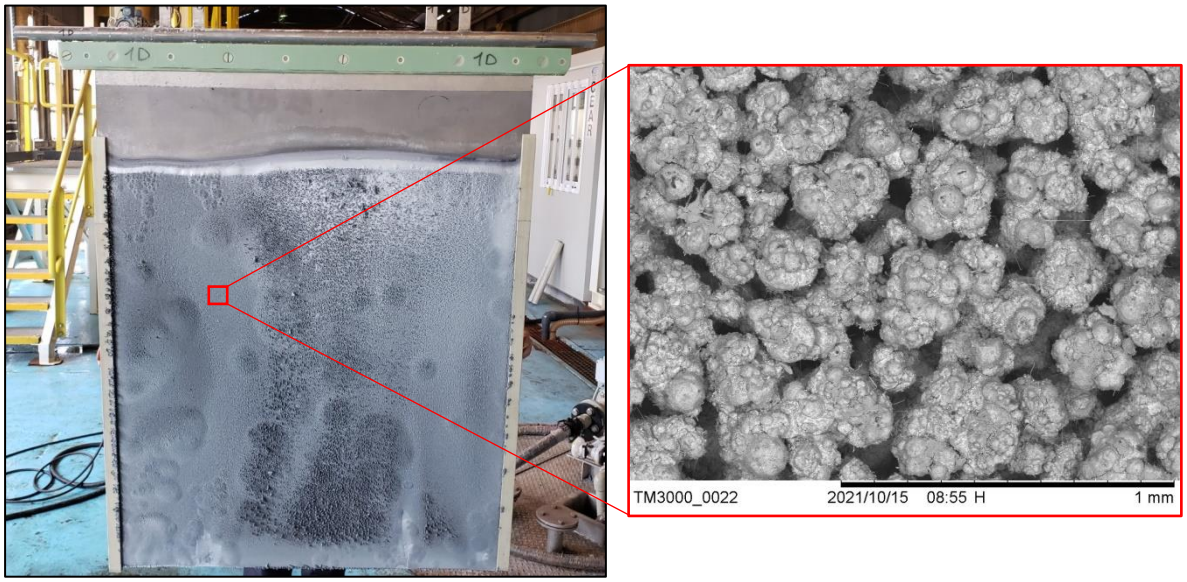

Figure 58: Electrodeposed zinc, Cape Gate pilot plant.

The efforts were focused on the effect of some additives on the electrodeposition of zinc in ammonium chloride electrolyte. Additives used in metal electrodeposition induce changes in the morphology of the deposit by adsorption onto active growth sites. At the same time, structural modifications of the deposit take place affecting the texture, internal tensions, dislocations etc.

Additives can significantly alter the nucleation and growth processes by changing the type of nucleation, the competition between nucleation and growth, or between different types of growth mechanisms of the electrodeposited layers. The growth process by nucleation depends not only on the nature of the additive, but also on the nature of the substrate and experimental conditions such as additive/metal ion concentration ratio, applied overpotential, temperature, electrolyte, pH, etc.

The literature lacks experimental data regarding the electrodeposition of zinc in ammonium chloride solutions, the characteristic electrolyte of the EZINEX® process. Therefore, several classes of additives were considered and tested using a Hull cell. Cell potential, adhesion, fracture type, surface morphology, and cross-sectional appearance were the parameters considered for additive evaluation. Theoretically, the best additive is one that does not increase the cell potential, produces an adherent, smooth and compact deposit free of pores and dendrites, with good adhesion to the cathode during electrodeposition, and is easily stripped.

Additives: effect on deposit morphology

The experimentation began with 15 additives tested individually; the best were then tested in combination with each other and finally in groups of three.

The tests were conducted in the Hull cell, a special cell designed to test different current densities simultaneously; for each test, the zinc plate produced was detached from the titanium cathode and prepared for morphological analysis, Figure 59.

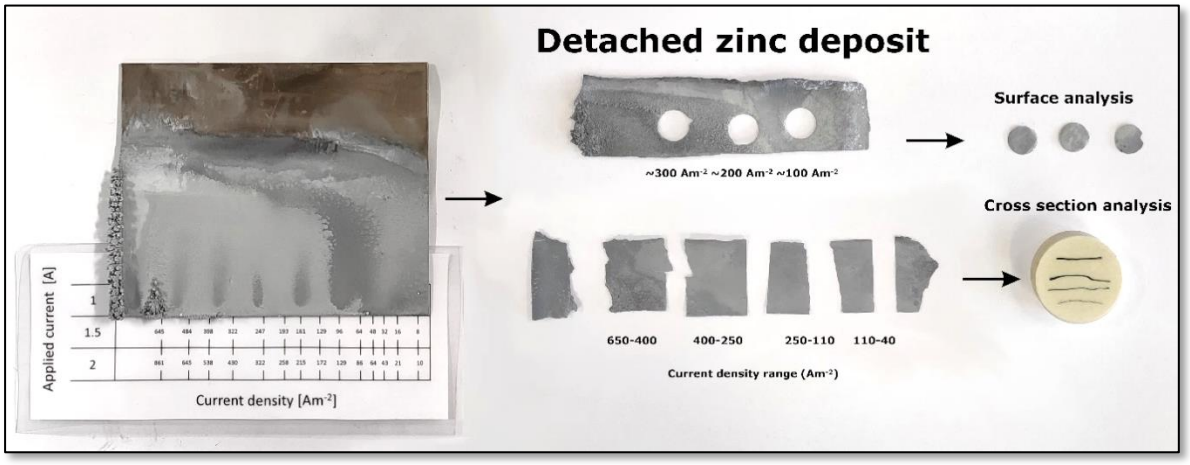

Figure 59: Sample preparation. From left: obtained zinc deposit, horizontally cut deposit, samples ready for SEM analysis.

To have a basis for comparison of the results, a first test was conducted in the absence of additives, Figure 60. At high current density, the presence of dendrites can be seen and although the deposit appears smooth at first glance, SEM images reveal microporosity that should be avoided.

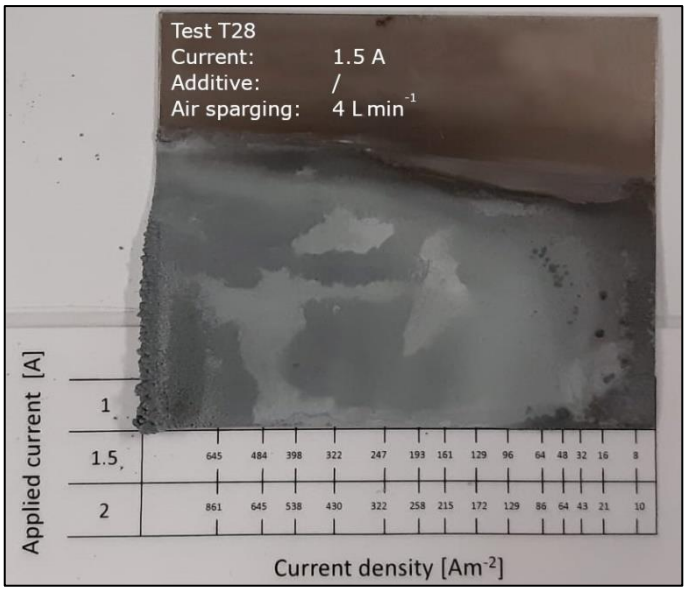

Zinc sheet

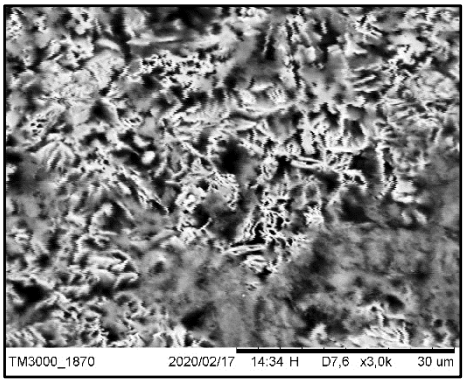

Surface and cross section at 300 A/m^2

Figure 60: Zinc deposit obtained without additives.

Some additives produced a beneficial effect on deposit morphology while others had the opposite effect, for example, isonicotinic acid was found to promote dendritic growth while thiourea produced a sponge like deposit, Figure 61. Otherwise, some were found to be effective in terms of surface smoothing and compactness of the deposit, two of these were lignite sulfonate and aesculus hippocastanum extract; the former was able to produce a very smooth surface while the latter acted on the compactness of the deposit, Figure 62 and Figure 63.

Based on the results obtained in the first screening, six of the fifteen additives were selected to be tested in combination to exploit their effects in a synergistic manner.

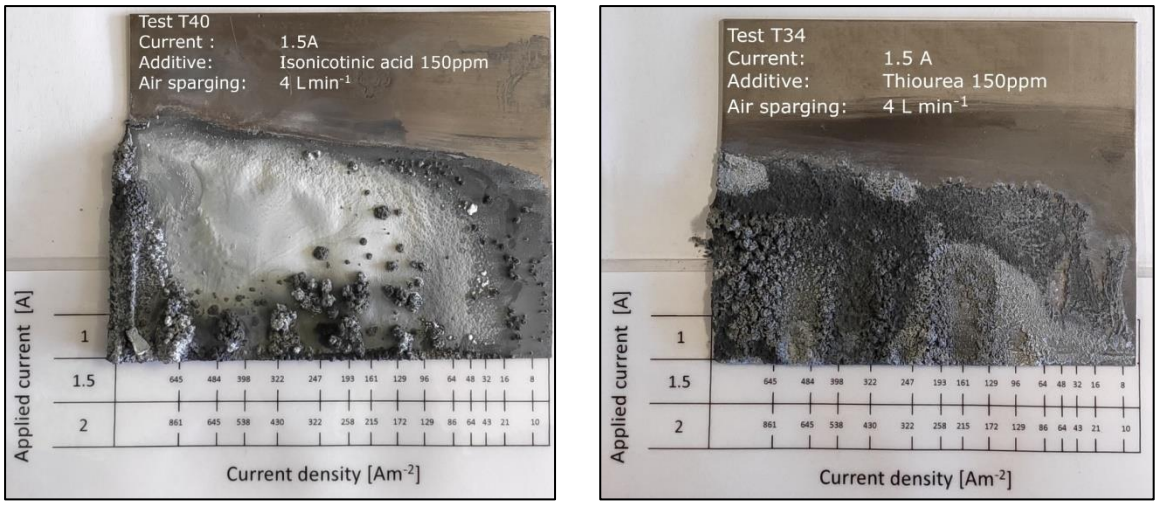

Figure 61: Two additives with harmful effects on zinc deposit.

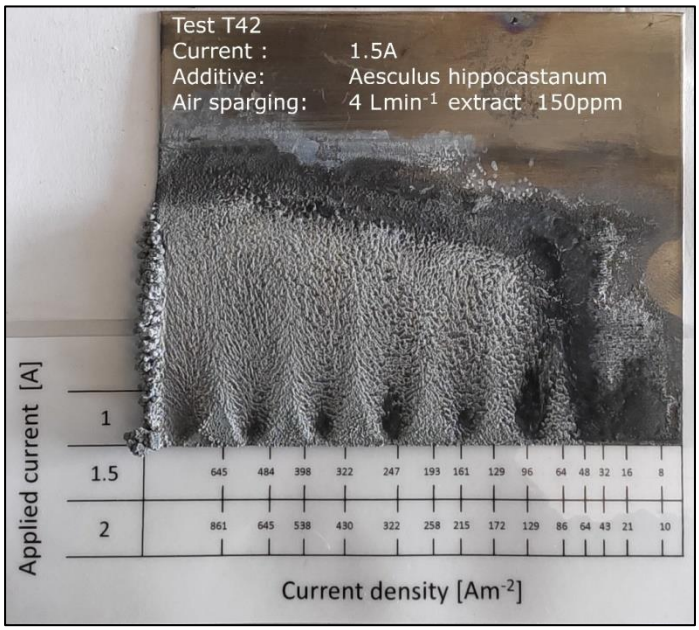

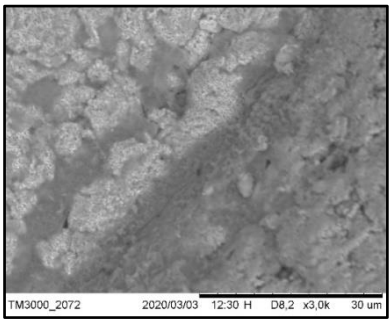

Surface at 300 A/m^2

Figure 62: Effect of aesculus hippocastanum on zinc deposit.

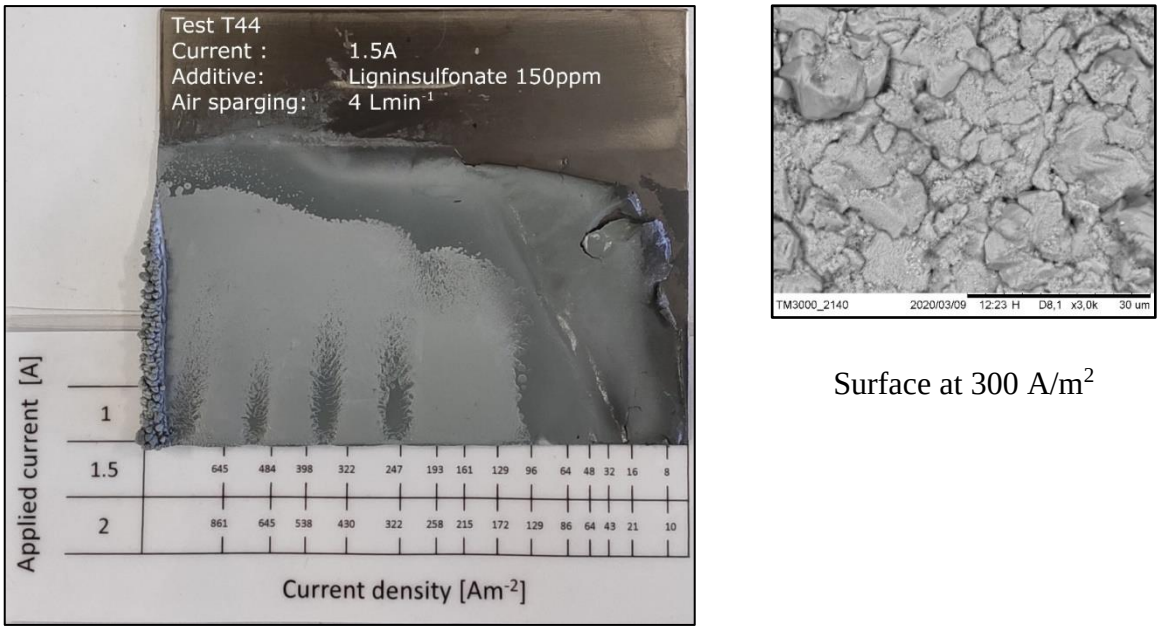

Figure 63: effect of lignin sulfonate on zinc deposit.

A test array to cover all possible combinations was then planned; again, some combinations of additives gave good results while others did not. Good results were obtained, for example, combining agar and lignin sulfonate resulted in a smooth surface with a relatively compact deposit, Figure 64.

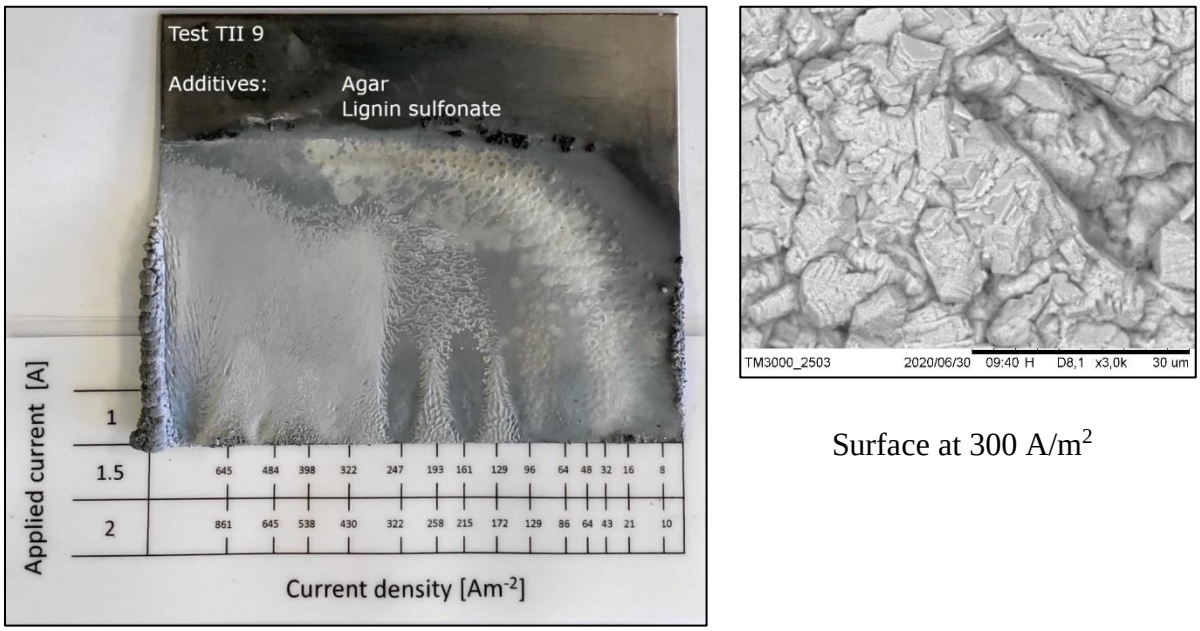

Figure 64: effect of the combination of agar and lignin sulfonate on zinc deposit.

Finally, four additives were chosen for a series of tests using mixtures of three. The best combination was found to be the mixture of agar, aesculus hippocastanum extract, and gum Arabic, Figure 65.

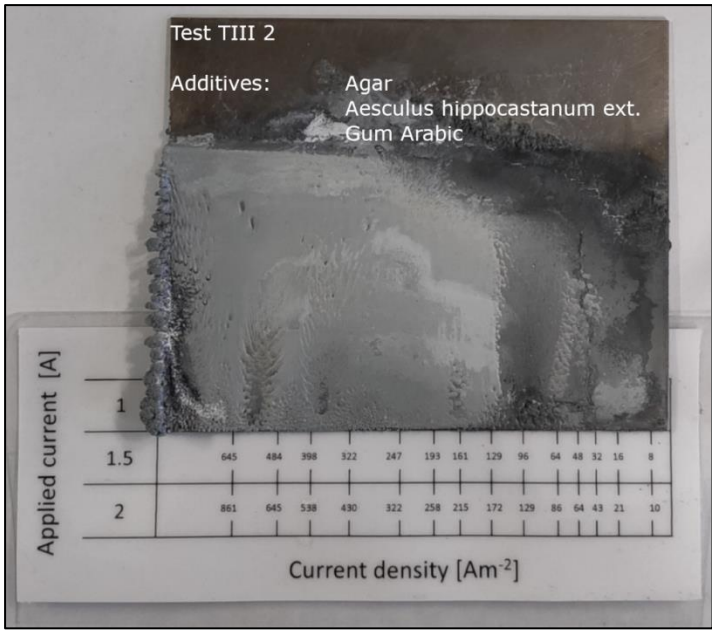

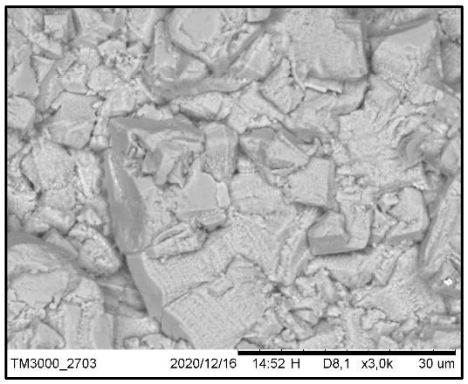

Surface at 300 A/m^2

Figure 65: effect of agar-aesculushippocastanum-gum Arabic mixture on zinc deposit.

Additives: effect on cell potential

The introduction of a new molecule into an electrolysis process could affect cell potential. The molecule may hinder reactions or may be reduced/oxidized producing undesirable effects. To get a first idea of the effect of the tested additive on the electrolysis process, cell potentials were recorded during each experiment and compared to the potential of an electrolysis conducted on a solution without additives, baseline.

The deviation from the baseline, represented by the zero value, is shown in Figure 66; a positive deviation represents an increase in energy consumption, a negative deviation is the opposite.

However, their effect on cell potential is not additive, in fact, the final part of the screening where mixtures of three were tested revealed that during the test of the TIII 2 mixture,

which was found to be the best, the potential was practically at the same level as the baseline, Figure 67. This means that, theoretically, the use of this combination of additives does not affect the energy requirements of the system.

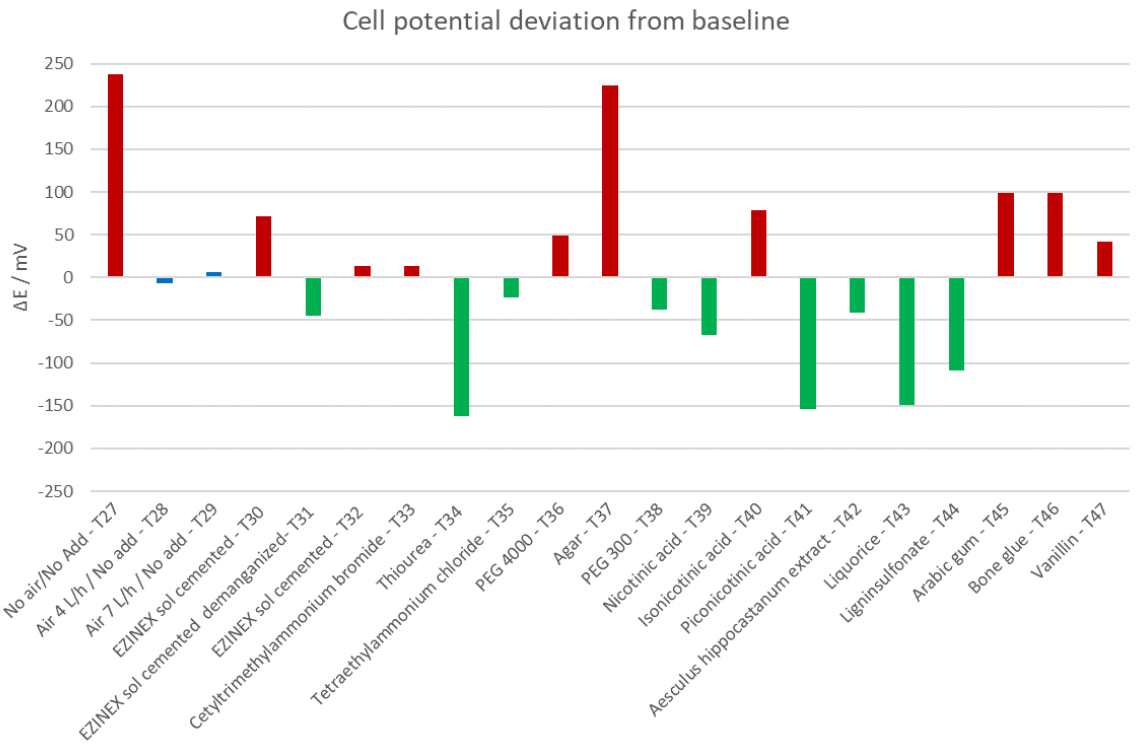

Figure 66: cell potential deviation from baseline.

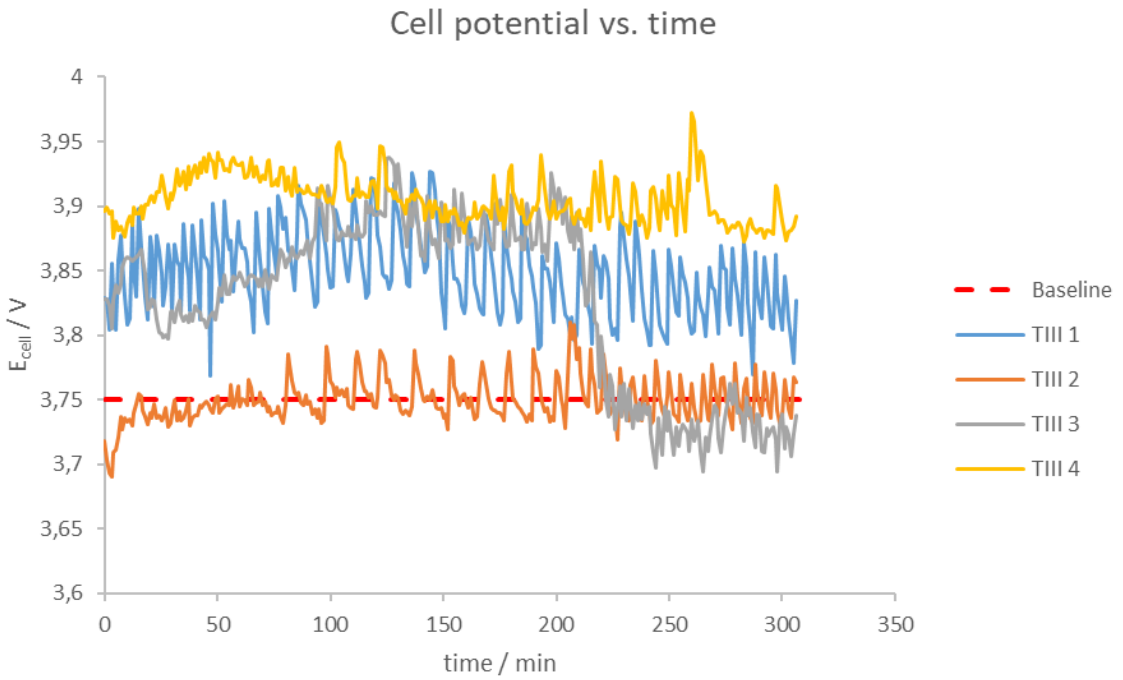

Figure 67: Cell potential of three additives mixtures.

Additives: effect on current efficiency

The current efficiency, or Faradic efficiency, indicates the percentage of the passed charge that was used for zinc deposition. This can take values less than 100% when other cathodic reactions take place; for this experiment, the only two cathodic side reactions are oxygen reduction and additive reduction. Oxygen reduction is always present since the air sparging system was used, so a current efficiency of 100% cannot be expected. As shown in Figure 68, no significant variation in current efficiency was observed; values above 90% were recorded in all cases; deviations are in the range of experimental error.

The efficiency calculated in the presence of the best mixture of additives was also above 90%; significant current waste was not observed in the presence of additives.

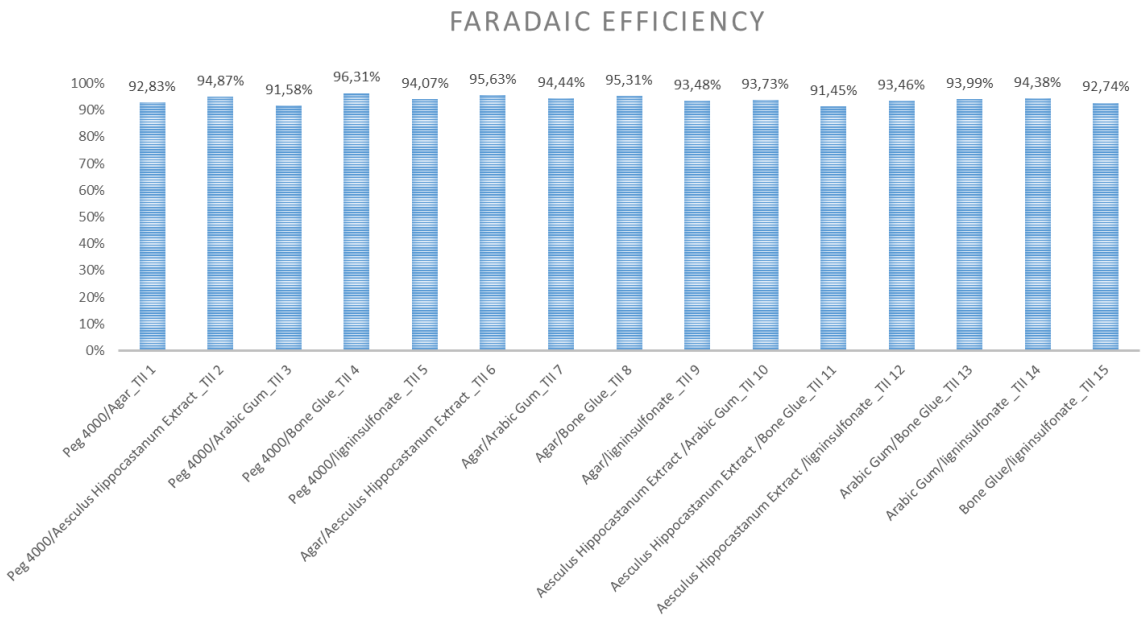

Figure 68 Faradaic efficiency.

Additives: concentration monitoring

Additives are basically surfactants that change the surface tension of solutions, this parameter was therefore measured on the electrolysis solution after and before the test to assess the possibility of determining their concentration or assessing their consumption. In some cases, the additives increased the surface tension while in others it decreased; it is difficult to tell if electrolysis consumed or degraded the additives in the smaller molecules and the variations are small, Figure 69.

Surface tension measurement was not found to be a valid method for rapidly monitoring additive concentration.

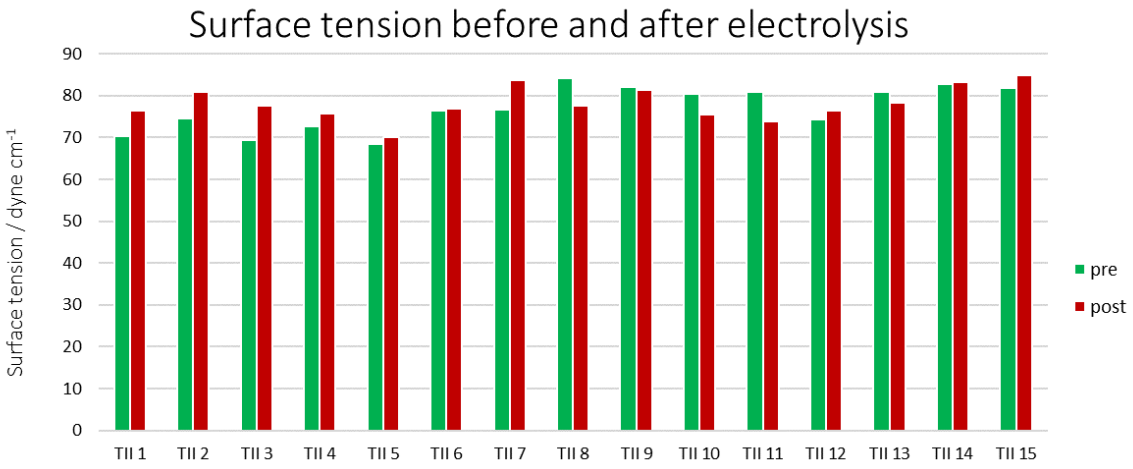

Figure 69: **Surface tension of electrolytic solution in presence of additives, after and before 5h of electrolysis.**

Conclusions

In this study many aspects of the two hydrometallurgical technologies, F.A.S.T. and EZINEX®, were considered; the attention was mainly focused on the possibilities of improvement of EZINEX® technology as it represented a major need for Engitec. In agreement with the company, a line of research that touched on the main issues was started. The experience on the pilot plant installed in South Africa has allowed to test on field some alternative solutions and to verify advantages and disadvantages. Moreover, other problems which are difficult to identify in laboratory tests, have emerged.

The following is a summary of the results obtained starting from the step of leaching to finally arrive at the electrolysis cell.

The leaching process is the first step of the two technologies. The obtained extraction times and the solubility limits of the metal species of interest are of fundamental importance in order to proceed to a correct scale up of the leaching reactor and dosage of the material to be treated. The possibility of increasing the extraction yield from the EAFD directly in the leaching, without the need to treat the powders in advance, has not found a solution. Following the problems encountered in the filtration of the leaching residue, an experimental campaign was conducted to evaluate the operational characteristics of alternative filter cloths, concluding that the type of cloth does not seem to have any particular effect on the performance of filtration. However, parameters have been obtained useful for the sizing of filter surfaces.

One of the problems discovered thanks to the pilot plant was related to calcium, the presence of this element caused the precipitation of gypsum in the heat exchangers, thus decreasing their efficiency and causing their occlusion. It has been found that the addition of sulphate ions is able to precipitate and keep under control the calcium concentration. This addition could be done through the reuse of a waste product of the plant, that is the

ammonium sulphate that is formed in the scrubber.

The purification of the solution allows to obtain a final deposit of high purity; obviously the higher the quality of the deposit required, the greater the economic efforts to be put into the purification process. Manganese is generally present in EAFD; its removal is critical for the subsequent electrolysis process. Removal is accomplished by the addition of permanganate and following filtration of the solid formed. The pilot plant showed that permanganate heavily affects the cost of zinc produced; this leds to an in-depth study of the reaction in question. It was found that the permanganate dosage according to the redox potential of the solution must consider the solution pH. A relationship between pH and the redox value to be reached was derived in order to avoid waste. Permanganate reaction kinetics were determined, and the following conclusions were drawn:

- The reaction with manganese proceeds very quickly and could possibly be conducted in-line in a static mixer.
- The presence of EAFD increases permanganate consumption by about 11%, so demanganization should be done in a dedicated reactor.
- Ammonia is oxidized by permanganate, therefore the concentrated permanganate solution should not be prepared from plant wash water containing ammonia, otherwise part of the reagent will be consumed.

In order to allow the removal of the manganese oxide, several flocculants have been tested, one of which has proved to be particularly effective in clarifying the solution from the finer particles that are difficult to sediment. Filtration of this compound was particularly difficult, while the use of a centrifuge demonstrated the high degree of separation obtainable through this solid-liquid separation technique. A relationship between separation quality, g-force and time was then derived in order to provide guidance for the choice of an industrial centrifuge.

Finally, the manganese oxide produced was also found to be a mixture of different manganese compounds and not only MnO_2 as originally hypothesized.

In addition to manganese, other impurities include copper, silver, cadmium and, in the case of the EZINEX® process, also lead. In the EZINEX® process, the removal of these impurities is accomplished by the addition of zinc metal powder. In order to optimize the process a kinetic study of the cementation reactions was carried out which showed that the

limiting factor of the reaction is the diffusion of the species on the surface of the metallic zinc particles. With the aim to maximize diffusion, an alternative to the classical cementation process was tested. It consists of a cylinder placed horizontally, filled with metallic zinc and rotated on its axis. In this way the probability of contact between the active material and the impurities is increased and moreover, the surface of metallic zinc particles is kept constantly active thanks to the friction generated by the rubbing of the particles with consequent removal of cements from the surface. Several variables were analyzed and under the best conditions it was possible to obtain a solution containing less than 2 ppm of impurities in a single pass.

A second alternative, based on a different concept, is the electrodepuration cell. By polarizing the cell cathodes to a certain potential, impurities can be selectively removed from the solution without the need of reagents. Initially, the energy of the various reduction processes involved was evaluated and through experimentation with different designs, this cell was optimized more and more. It was concluded that the formation of a lead sponge increases the probability of contact between the metal ion and the electrode, and the key to developing a better performing cell lies in exploiting this feature.

The electrolysis cell is the heart of the two hydrometallurgical technologies. The choice of the correct anode material can lead to a decrease in its operating expenses with a consequent decrease in the cost of the final product. Activated titanium was compared to graphite to evaluate the energy benefits that its implementation in the EZINEX® process would have. It was found that if graphite is replaced by activated titanium, the reduction in energy consumption for electrolysis would be about 16-17%.

However, the use of activated titanium as an anode material is subject to one basic precaution: the solution must not contain manganese. Experiments have shown that the presence of manganese leads to premature deactivation of the catalytic coating, thus nullifying the benefits related to the reduction of energy consumption and leading to additional costs for their replacement

The zinc deposit obtained on the pilot plant was found to be very porous and unsuitable for melting in the molten zinc bath. Different classes of additives were taken into account and their effects on the deposit morphology were evaluated. Different mixtures were tried until

one, capable of producing a more compact deposit, was identified.

The effect of these additives on the energy consumption of the electrolysis process and on the current efficiency was also verified; the selected mixture of additives does not seem to have any particular effect on the energetics of the process and the faradaic efficiency is in line with what is expected from an electrolysis process.

In conclusion, with this work it was tried to enter as much as possible in the detail of the problems related to the two technologies, analyzing them from a new point of view respect to what has been done so far in Engitec. Alternative solutions to the existing ones have been proposed and some fundamental issues have been deepened. The two technologies still present several gaps that can be filled by continuing the lines of research set by this work.

Appendix

In this section there are some insights related to the technology currently used to produce lead or zinc, Appendix A through C.

In Appendix 1 through 11, there are complete reports describing all test conditions and experimental apparatus along with results and conclusions related to each experiment.

Appendix A: Thermodynamics of pyrometallurgical processes

Pyrometallurgical processes exploit the possibility of reducing metal oxides to metals. Ellingham diagram, Figure 70, describe the thermodynamics of a metal reduction reaction and helps to select the best reducing agent for various ores in the extraction process. The feasibility of a reaction depends on the sign of ΔG, the Gibbs free energy (ΔG=ΔH-TΔS). This diagram plots the ΔG^{o}, free energy of formation, change for each oxidation reaction as a function of temperature; for comparison, all ΔG^{o} values refer to the reaction of one mole of oxygen. Given the reaction:

$$2XM_{(s)} + O_{2(g)} \rightarrow 2M_xO_{(s)}$$

the gaseous amount of reactant decreases from left to right as the product formed is solid metal oxide. The change of ΔS is than negative and ΔG increase; so, for most of the reaction reported in the diagram, the relative curve has a positive slope. In addition, due to the same change in ΔS, these are roughly parallel. The lower the position of a metal's line, the greater is the stability of its oxide.

The most used reducing agent is carbon. The formation free energy of carbon dioxide (CO_2) is almost independent of temperature, while that of carbon monoxide (CO) has negative slope and crosses the CO_2 line near 700°C. Carbon monoxide is the dominant oxide of carbon at higher temperatures and its reducing power increase with it.

By comparing two curves, relative to two different metals, at a given temperature, the metal with the lower Gibbs free energy of oxidation will reduce the oxide with the higher one. The greater is the gap between the two values, the greater is the effectiveness of the reducing agent.

Applying the same concept to the line corresponding to carbon and to that relative to lead, it is possible to see that the carbon can reduce lead oxide to metallic lead at relatively low temperature.

The same concept can be applied to zinc with the difference that the reduction of zinc oxides by carbon proceeds spontaneously only above the zinc boiling point (907°C).

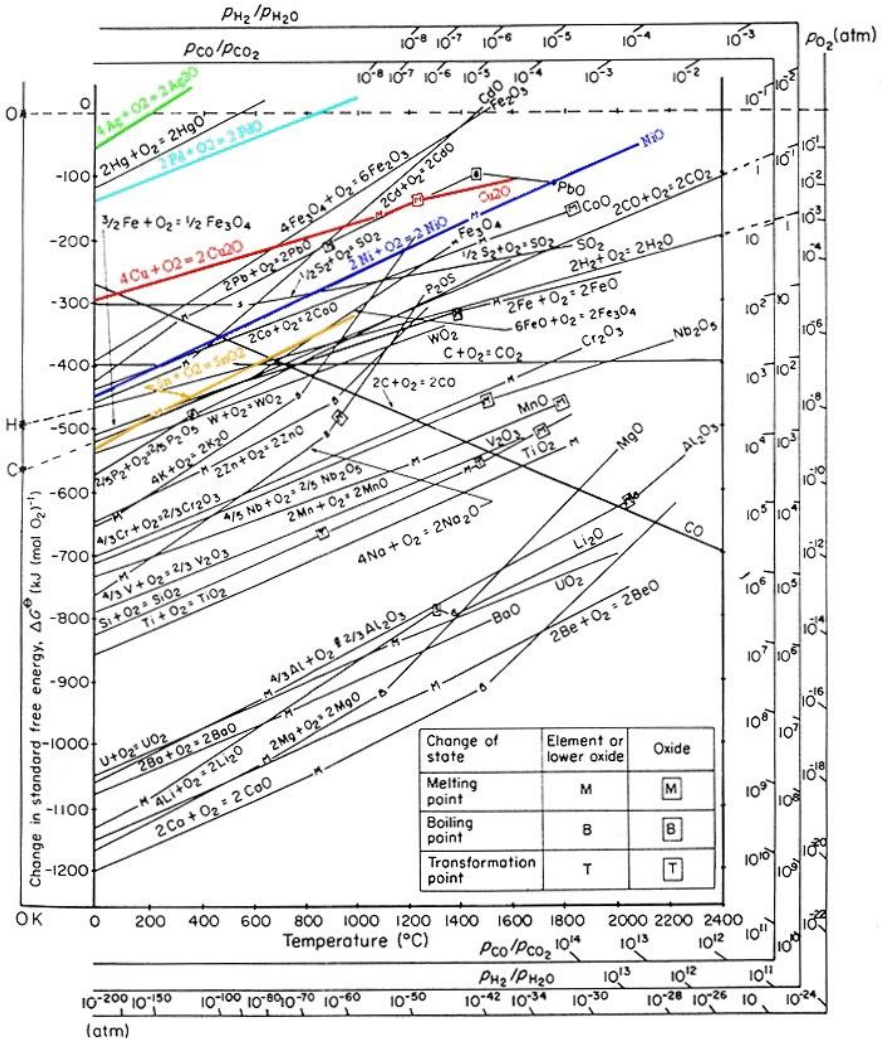

Figure 70: Ellingham diagram for several metals.[37]

Appendix B: Lead production from primary sources

The production of lead from primary sources, lead ores, is a complex process which involves several steps[38].

Mining

Lead is extracted from underground mines by drilling the rock with heavy machinery or blasting it with dynamite. When the ore is extracted from the rocks it is transported to the surface for further processing. The most used lead ores are Galena, Cerrusite and Anglesite. These three ores combine for 95% of the total lead mining production, however these deposits commonly contain other ores more prominently, such as silver and zinc. Lead is therefore usually a by-product of zinc and silver mining. Half of the worldwide refined lead comes from mining activity. When the lead ore is extracted to the surface, the process of extracting the actual lead from the ore, starts.

Concentrating the ore

After the ore is removed from the mine, it is treated at a concentrating mill. Concentrating means to remove the waste rock from the lead. Firstly, the ore must be crushed into very small pieces, it is ground at the mill, leaving it in particles with diameters of 0.1 millimeter or less.

Flotation

The next step involves flotation. The small particles of lead ore still consist of multiple types of chemicals such as sulfur. The flotation process collects the sulfur-bearing portions of the ore, which also contains the valuable metal. The finely crushed ore is diluted with water and then poured into a tank called a flotation cell. The ground ore and water mixture is called slurry. One percent pine oil, or a similar chemical, is then added to the slurry in the tank. The mixture than is stirred. The pine oil attracts the sulfide particles and air is bubbled through the mixture. This causes the sulfide particles to form an oily froth at the top of the tank. The waste rock, which is called gangue, sinks to the bottom. The flotation process is controlled by means of X-ray analyzers; the metal content of the slurry is the checked and, the aid of a computer, the proportion of the chemical additive is adjusted to optimize recovery of the metal. Other chemicals are also added to the flotation cell to help concentrate the minerals. Alum and lime aggregate the metal or make the particles larger. Xanthate is also added to the slurry, in order to help the metal particles float to the surface. At the end of the flotation process, the lead, zinc and copper has been separated from the rock.

After the ore is concentrated in the flotation cells, it flows to a filter, which removes up to 90% of the water. The concentrate at this point contains from 40-80% lead, with large amounts of other impurities, mostly sulfur and zinc. It is ready at this stage to be shipped to the smelter. The gangue, or rock that was not mineral bearing, must be pumped out of the flotation tank. It may be dumped into a pond resembling a natural lake, and when the pond

eventually fills, the land can be replanted.

Roasting

The lead concentrate needs to be further refined to remove the sulfur. After the concentrate is unloaded at what is called the sinter plant, it is mixed with other lead-bearing materials and with sand and limestone. Then the mixture is spread on a moving grate. Air which has been heated to around 1,400°C blows through the grate. Coke is added as fuel, and the sulfur in the ore concentrate combusts to sulfur dioxide gas. This sulfur dioxide is an important byproduct of the lead refining process. It is captured at a separate acid plant and converted to sulfuric acid. After the ore has been roasted in this way, it fuses into a brittle material called sinter. The sinter is mostly lead oxide, but it can also contain oxides of zinc, iron, and silicon, some lime, and sulfur. As the sinter passes off the moving grate, it is broken into lumps. The lumps are then loaded into the blast furnace.

Blasting

The sinter falls into the top of the blast furnace, along with coke fuel. A blast of air comes through the lower part of the furnace, combusting the coke. The burning coke generates a temperature of about 1,200°C and produces carbon monoxide. The carbon monoxide reacts with the lead and other metal oxides, producing molten lead, nonmetallic waste slag, and carbon dioxide. Then the molten metal is drawn off into drossing kettles or molds.

Refining

The molten lead as it comes from the blast furnace is from 95-99% pure. It is called at this point base bullion. It must be further refined to remove impurities, because commercial lead must be from 99-99.999% pure. To refine the bullion, it is kept in the Lead drossing kettle at a temperature just above its melting point, about 330°C. At this temperature, any copper left in the bullion rises to the top of the kettle and forms a scum or dross which can be skimmed off. Gold and silver can be removed from the bullion by adding to it a small quantity of zinc. The gold and silver dissolves more easily in zinc than in lead, and when the bullion is cooled slightly, a zinc dross rises to the top, bringing the other metals with it.

Casting

When the lead has been sufficiently refined, it is cooled and cast into blocks which may weigh as much as a ton. This is the finished product. Lead alloys may also be produced at the smelter plant. In this case metals are added to the molten lead in precise proportions to produce a lead material for specific industrial uses.

Appendix C: Zinc production from primary sources

Zinc is produced from primary source by two methods[5]: pyrometalurgical and hydrometallurgical.

The production of zinc from its ores by pyrometallurgical processes is much more difficult than with other metals such as lead, copper and iron. The reduction of zinc oxides by carbon proceeds spontaneously only above the zinc boiling point (907°C). The common zinc-containing minerals are zinc sulfide known as zinc blende or sphalerite (ZnS), marmatiti [(ZnFe)S] and zinc carmonates known as calamine or smithsonite ($ZnCO_3$). The zinc content of mined ore is usually between 3 and 10 percent; almost all ores contain the lead sulfide mineral, galena, and small quantities of cadminum sulfide. Chalcopyrite, a copper-iron sulfide, is often present.

Mining

Zinc ores are recovered by many mining techniques, the most common underground method of ore extraction is cut-and-fill stopping, in which tunnels are dug to moderate depths, branching away from the mine portals. Zinc is than concentrate by flotation separation; the ore initially is crished, combined with water, and ground to less than 0.1 millimetre in a ball mill. Fine particles and water form a slurry that flows from the mill to flotation cells or tanks, where, in the presence of selected chemical reagents that create a suspension of air bubbles, the slurry is agitatated. The mineral particles cling to the bubbles and float to the surface, forming an oily froth that is constantly skimmed, while the gangue is wetted by the action of the chemicals and sinks in the cell. The proper choice of frothing agents makes it possible to separate each constituent mineral of complex lead and zinc sulfides in a concentrated form.

Roasting and sintering

Both processes, pyrometallurgical and hydrometallurgical, for the production of zinc require the prior removal of sulfur in a highly exothermic oxidation reaction:

$$ZnS + 1.5\ O_2 \rightarrow ZnO + SO_2$$

For the electrolytic production of zinc, the roasting of concentrates is achieved in fluidized-bed roasters, in which finely divided and heated particles of concentrate are suspended in a rising stream of air. The sulfur content can be reduced to less than 0.5 percent; sulfur dioxide gas is forwarded to a sulfuric acid plant.

The process described above becomes difficult to operate if the lead content rises above 3 percent. For this reason, the zinc-lead blast furnace utilizes a sintering process to supply its oxidized feed. Fine concentrates are mixed with crushed returned sinter to give a material containing about 6.5 percent sulfur. This is fed onto a moving grate and fired in an updraft of air, and the sintered cake leaving the machine is broken into a convenient lump size. By virtue of its strength and hardness, sinter is an ideal feed for the blast furnace. A gas

containing 7.5 percent sulfur dioxide is passed to a sulfuric acid plant.

The zinc-lead blast furnace (also known as Imperial Smelting Process *ISP*)

Sintered zinc and lead concentrates, mixed with metallurgical coke, are charged into the top of a shaft furnace, into which preheated air is blown through nozzles. The major products of reduction are a zinc-bearing gas and liquid phases that separate in the furnace hearth and are tapped periodically.

The gas stream, containing 8 percent zinc, 10 percent carbon dioxide, and 20 percent carbon monoxide, is directed from the upper shaft to a lead-splash condenser, a chamber in which an intense shower of lead droplets is thrown up by rotors revolving in a pool of molten lead. The zinc vapour is absorbed into the lead, and, by withdrawing the lead continuously and cooling it, the saturation point of zinc in lead is reached and molten zinc separates as a distinct layer on the surface. The zinc-lead blast furnace has the flexibility to accept a wide range of mixed ores and residues in its feed. Complex sulfide ores have to be sintered, but oxidized residues such as zinc ashes and drosses recovered from galvanizing processes can bypass the sinter roasting process. The blast furnace produces an ordinary grade of zinc containing 1.2 percent lead. This can be used in general galvanizing, but an additional refining operation must be performed to produce special high-grade zinc. The refining operation is performed in two fractionating columns. In the first column, a large part of the zinc is vaporized and freed from impurities with higher boiling points, such as lead and iron. The distilled vapours are condensed and fed into the second column, where the liquid's remaining impurity, with a boiling point lower than that of zinc, is distilled. High-purity zinc is then run off from the bottom of the column.

Electrolysis

The basic steps in this process include the preparation of a zinc sulfate solution by leaching zinc oxide (produced by the roasting of sulfide concentrates) in dilute sulfuric acid and, purification of the resulting zinc solution and the electrolysis of the purified solution.

The theoretical voltage required to deposit zinc from zinc sulfate solution onto a cathode is about twice the voltage necessary to decompose water, so that, in theory, electrolysis should result in the production of hydrogen at the cathode and not the deposition of zinc. When a zinc cathode is used, however, overvoltage prevents the generation of hydrogen, and, hence, zinc is deposited. The hydrogen overvoltage depends crucially on the purity of the zinc sulfate electrolyte; the presence of certain impurities at even very low concentrations, like nickel and cobalt, can cause a drastic lowering of the overvoltage with the reduction of current efficiency related to zinc deposition. An extreme purification of the electrolyte is a critical necessity in the process and is accomplished in two stages. The first stage is the removal of iron as a solid residue, followed by cementation with zinc dust to remove other metallic impurities (like copper, nickel, cadmium, cobalt, and germanium) from the solution.

Electrolysis is performed in lead-lined concrete cells with anodes of lead dioxide and aluminum cathodes. The zinc deposit, which grow during time, is stripped from the

cathodes and remelted in an induction furnace before casting into ingots or pigs. The purification of the electrolyte ensures that the normal product will reach a purity of 99.99 percent or more.

Appendix D: The Waelz Klin process

The Waelz kiln[9] process is used in the treatment of zinc containing materials and residues. The feeding materials are provided in either dry compact-moist or pelletized form. These are fed to the Waelz kiln, a reactor typically 55 meters long with a four-meter diameter, that is slightly inclined 2-3% and has an approximate rotary speed of 1 rpm. As the moist material moves through the rotary kiln, it is dried and preheated by the kiln gas, flowing in a counter-current pattern. Reduction of the metal occurs around 1200°C as the zinc is vaporized as metal vapor into the fas cleaning system. Zinc is then re-oxidized in the kiln atmosphere that is operated with excess air, injected from the kiln end. Chlrotine and alkalis volatilize jointly with the heavy metals and the dust-landed off-gas is treated in a downstream off –gas system. The co-product, Waelz iron product, can be used directly in road construction, civil construction, cement manufacturing or can be reprocessed. Waelz Zinc Oxide, the main product of the process, is delivered to zinc recovery plant.

Appendix 1 - Influence of reducing agents on the leaching step

Electric arc furnace dust (EAFD) coming from Cape Gate contains around 50% wt. zinc, to recover the zinc through the EZINEX® process these are treated with a hot concentrated ammonium chloride solution. All the zinc that is present as zinc oxide, ZnO, is leached and brought into solution, however, a considerable amount of it is in the form of zinc-ferrites ($ZnFe_2O_4$) and remains in the residue. Zinc-ferrites are particularly stable to the action of ammonium chloride and cannot be attacked by oxidizing agents because zinc and iron are already in their maximum oxidation state.

The recovery of the highest as possible amount of zinc from EAFD is fundamental for the economics of the process. The possibility to increase the yield by adding reducing agents to in the leaching step was investigated; these, could reduce iron from +3 to +2 oxidation state freeing the zinc from the zinc-ferrite structure. Three reducing agents were selected for this experimentation: sodium sulfite, hydrazine, and sucrose.

Experimental part

Leaching tests were carried out in presence of the reducing agents in different concentrations. A 2L beaker was equipped with a mechanical paddle stirrer and bafflers to keep EAFD suspended. Ammonium chloride concentration was kept constants for all the tests, 250 g/L, and temperature was set at 70°C. Solution pH was adjusted in the range of 6.5-7 with 50% NaOH solution.

Each test was carried out using 50g of EAFD, from Cape Gate, previously sieved with an ASTM 500-micron sieve. The duration of leaching tests was 1 h. At the end of each test, the solution was filtered on a buckner filter, and the obtained cake was washed with 100 ml of hot ammonium chloride solution. The filtrate was then analyzed with atomic absorption technique (AA). The solid residue was dried overnight at 80°C and then weighted. It was then analyzed with a scanning electron microscope provided with EDX probe and XRD spectra were recorded. An aliquot of the dried residue was mineralized in aqua regia (HNO_3: HCL 1:3) until NO_2 fumes ceased and the obtained solution was filtered and analyzed with AA.

Results

EAFD characterization

Figure 71 shows the SEM-EDX analysis of the as received EAFD; the sample contains up to 50% of zinc and 15 % of iron. The presence of zinc ferrites is releavable from the XRD analysis, Figure 72, however their weight percentage is not precisely determinable because the spectrum is complex and not completely resolvable.

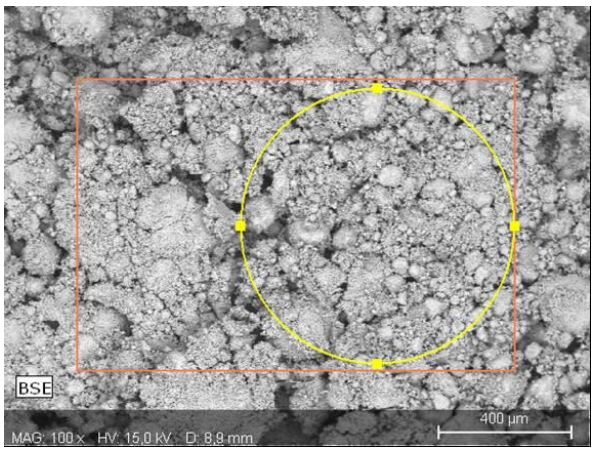

Element	AN	Series	norm. C [wt.%]	Atom. C [at.%]
Zinc	30	K-series	52,78	32,38
Oxygen	8	K-series	16,71	41,91
Iron	26	K-series	15,44	11,09
Calcium	20	K-series	3,16	3,17
Chlorine	17	K-series	2,82	3,19
Lead	82	M-series	2,64	0,51
Magnesium	12	K-series	2,04	3,37
Manganese	25	K-series	1,81	1,32
Potassium	19	K-series	1,34	1,37

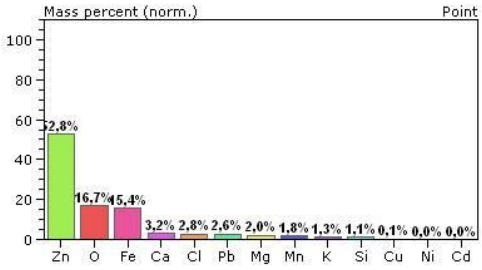

Figure 71: SEM-EDX analysis on as received EAFD (Cape Gate).

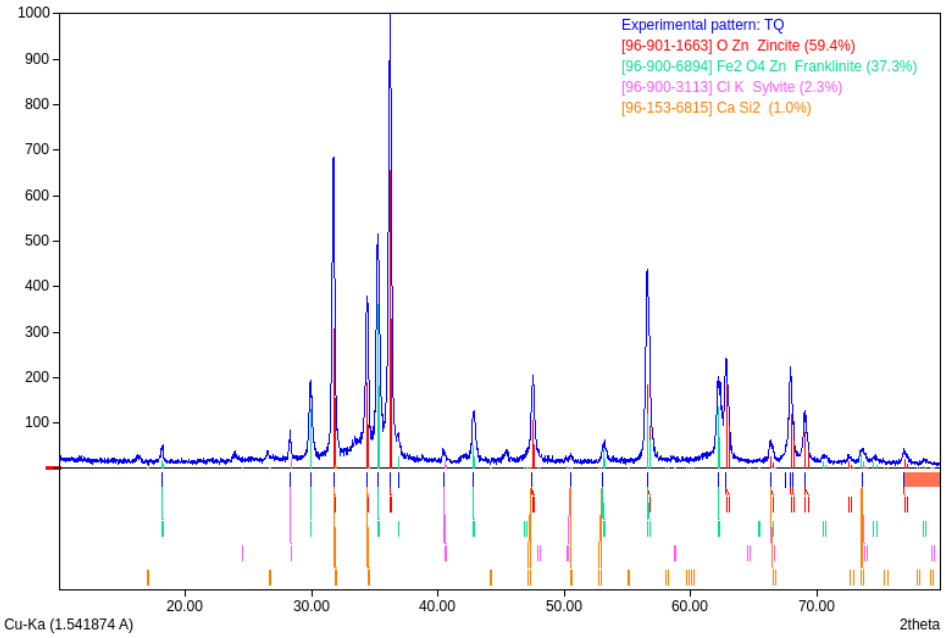

Figure 72: XRD spectrum of as received EAFD (Cape Gate).

Leaching tests

Figure 73 shows the amount of reducing agent used for each test, the bar graph reports the leached mass calculated on the dry residue. For comparison, a leaching test was conducted in absence of reducing agents, 4.1. Leached mass percentage increases in the case of sucrose and hydrazine while in the case of sodium sulfite remains unchanged respect to test conducted in just ammonium chloride.

Test ID		(g/L)	wt%*
4,1	/	/	
4,2	Na_2SO_3	2	4%
4,3	Na_2SO_3	5	10%
4,4	Na_2SO_3	10	20%
4,5	Saccarosio	1	2%
4,6	Saccarosio	3	6%
4,7	Saccarosio	5	10%
4,8	idrazina	1	2%
4,9	idrazina	2	4%
4,10	idrazina	4	8%

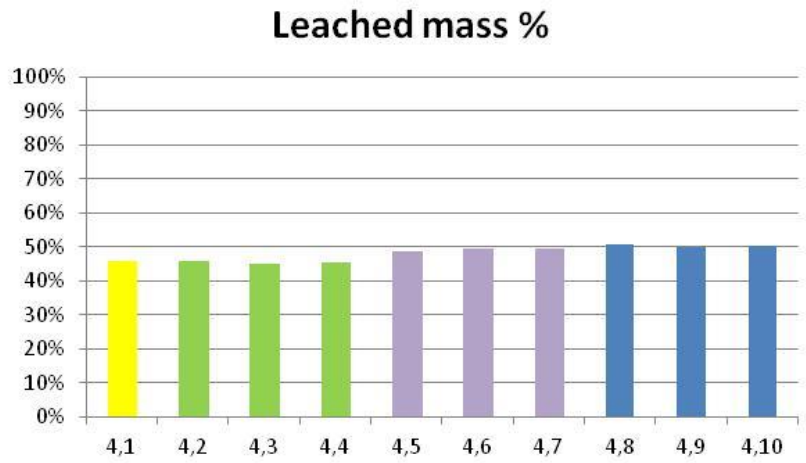

Figure 73 experimental conditions are reported in the table, bar graph report the leached mass in function of the reducing agent used. * Reducing agent weight percentage respect to the weight of the EAFD.

In Figure 74 the behaviour of zinc, iron, lead, copper, managanese and calcium in presence of the tested reducing agents is reported. Their amount in the leaching solution was determined with atomic absroption analysis while weight percentage in the residue was determined in two different ways. A part of the dried residue was mineralyzed and analyzed with AA while a part was analyzed with SEM-EDX analysis.

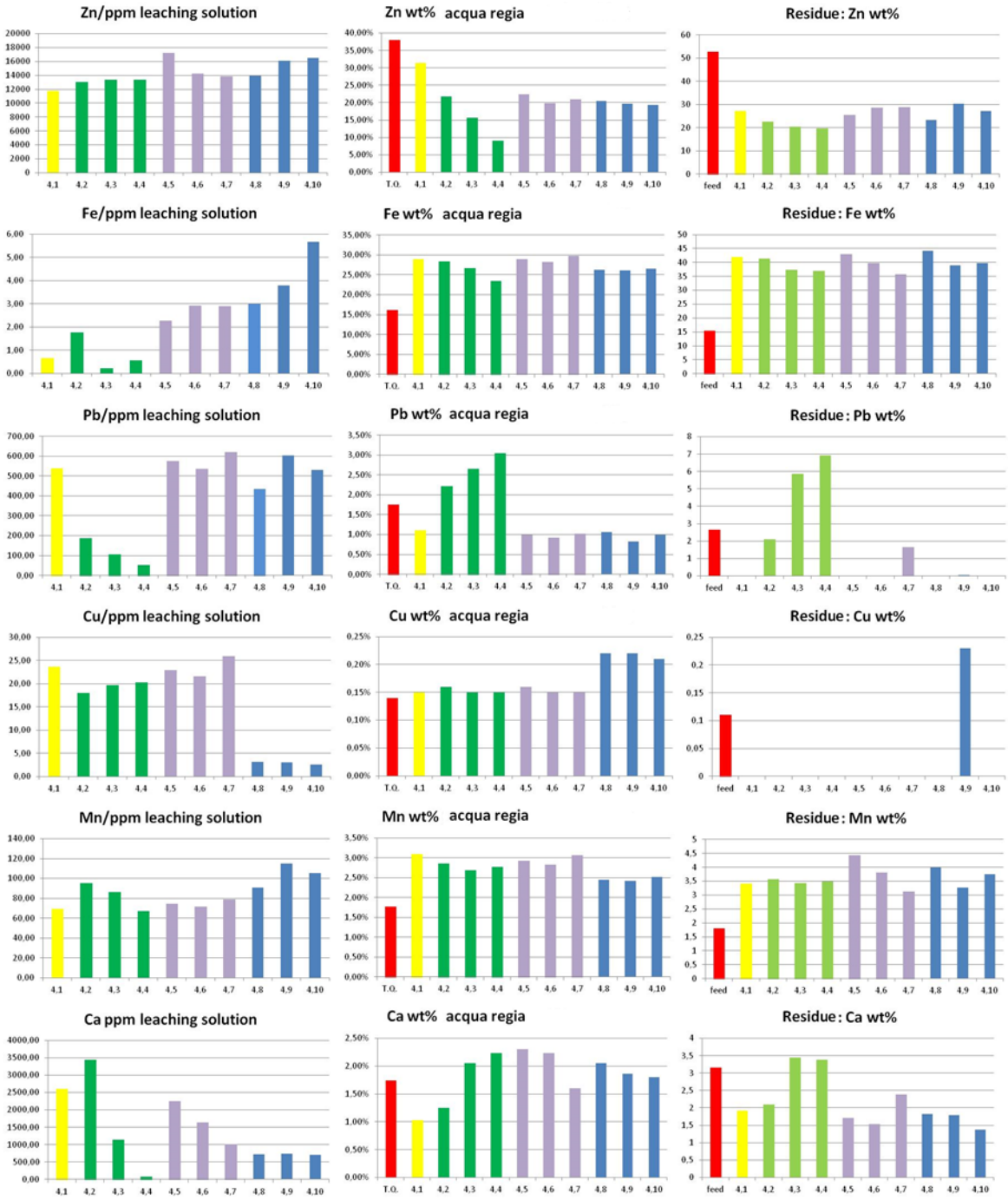

Figure 74: from left to right: concentration in the leaching solution, weight percentage in the residue calculated after mineralization in aqua regia and AA analysis, weight percentage in the residue from SEM-EDX analysis.

Zinc

All three reducing agents produces leaching solutions richer in zinc than what can be obtained using ammonium chloride alone. In the case of sucrose, zinc concentration does not increase as reducing agent concentration increases. Sucrose seems to have a benefical effect on zinc dissolution that is higher at low concentrations. The use of hydrazine shows an increase of zinc in the lecheate solution and a decrease in the residue, both proportional to the quantity added. It must be noted that the reduction of hydrazine generates ammonia

which is a complexing agent for zinc; the increase in zinc dissolution could be attributed to the increase in ammonia concentration and not to the effective reduction of zinc ferrites by hydrazine.

Iron

Hydrazine and, to a lesser extent, sucrose can increase the iron concentration in the leachate. This could be attributed to the presence of iron oxides that can be reduced to a soluble iron II form. Anyway, iron must not be present in the electrolyte and should be kept in concentration below 1 ppm occurs when leaching is carried out in ammonium chloride alone.

Lead

Lead, as other cations nobled than zinc, represents an impurity that must be removed before the electrolysis step. The addition of sulfite decreases its concentration in the leachate probably due to the formation of a poorly soluble lead compound. The addition of sucrose and hydrazyine did not produce significant effects on the lead concentration in the leaching solutions.

Copper

Copper represents another impurity in the EZINEX® process, analysis shows that the addition of hydrazine, regardeless of the amount used, decreases its concentration in the leaching solution. The cause is not clear, hydrazine could be able to reduce copper from +2 to +1 oxidation state forming an insoluble copper (I) specie. The increased amount of copper in the residue, when hydrazine is added, can be detected in the analysis of the mineralized residue, thus confirming its removal due to the formation of a precipitate that stays in the residue. SEM-EDX analysis are not accurate due to the low amount of copper in the dried residue.

Manganese

Manganese is another source of issues for the EZINEX® technology, all the tested reducing agents seems to increase the amount of manganese leached.

Calcium

Calcium does not affect the purity of the zinc deposit, however, as EZINEX® is a zero liquid discharge process, what is not consumed or removed tends to accumulate in the process solution. High concentration of calcium led to precipitation of calcium sulfate in the eheat exchangers. From the analysis of the obtained results, the addition of sodium sulfite seems to decrease its concentratioin in the leaching solution. Thi is due to the oxidation of sulfite to sulphate and consequent precipitation of calcium sulphate. Also sucrose and hydrazine are capable to reduce calcium concentration in the leaching solution.

XRD analysis

Figure 75 shows the XRD spectra of the as received EAFD and leaching residues. The disappearance of peaks related to zinc oxide, easily leachable, can be clearly seen. There is no significant difference between the residue obtained with and without the reducing agents; zinc ferrites characteristic peaks are present in all the spectra.

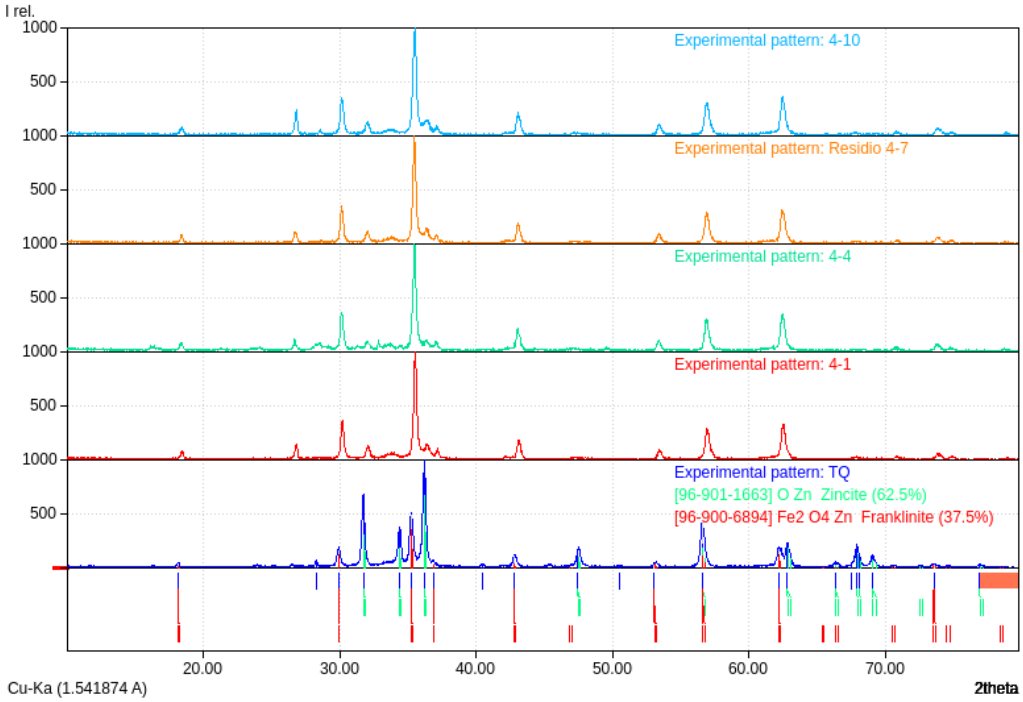

Figure 75: XRD spectra of as received EAFD and leaching residues.

Observations

The SEM-EDX analyzes carried out on the residues do not agree with the analyses performed on the solutions used for the mineralization of the same samples. This is probably due to the inhomogeneity of the residuem. The mineralization and subsequent analysis of the solution with AA technioque is belived to provide more accurate information on the elemental composition of the residue.

Conclusions

This study was conducnted to verify the possibility of recovering as much zinc as possible from EAFD by adding reducing agents during the leaching step. The main limitation in the recovery of zinc is the presence of zinc-ferrites. Previous studies have reported promising results relating to the use of various reducing agents in acicid environment, however the EZINEX® process makes the use of ammonium chloride and neutral pH leaching one of its strengths. It was therefore evaluated the effect of three different reducing agent on the EAFD in ammonium chloride solutions. None of the tested compound was able to increase the amount of zinc extractable from EAFD.

Appendix 2 - Leaching residue filtration

Filtration experiments were carried out in a 200 mL laboratory scale jacketed filter designed to be used with a 10 cm^2 filtering cloth disc. Six different types of filtering cloth, provided by DrM Dr.Muller AG, were tested and for each test a freshly new disc was used. Two types of EZINEX® solutions were prepared according to the following recipes:

Solution type A:

NH_4Cl	250 g/L
EAFD	50 g/L

Solution type B:

NH_4Cl	250 g/L
NaCl	20 g/L
KCl	20 g/L
$CaCl_2$	10 g/L
$MgCl_2$	5 g/L
EAFD	50 g/L

Each filtration test was conducted as follow:

solution was firstly heated up to 70°C then EAFD was added. After 30 minutes of leaching, at 70°C under stirring condition, the slurry was poured into the filter from the top and a constant pressure of 5 bar was applied using compressed air. The chronometer was started at the seeing of the first drop from the bottom of the filter and the amount of filtered solution was measured by weighing.

To avoid precipitation of salts during filtration, a thermostat was used to keep filter temperature at 70°C.

At the end of each test, the cake was blown with compressed air for 15 seconds then its thickness was measured with a caliper. It was then gently removed from the filtering cloth and weighted before and after an overnight drying in oven at 80°C to determine its moisture. A picture of the filtering cloth was also taken to evaluate the cake ease of removal.

Filtered solution pH was measured at the end of the filtration test.

In addition, a granulometric analysis of a leaching slurry (type A) was performed.

Utilized EAFD sample was from Cape Gate (South Africa).

Granulometric analysis

Granulometric analysis results are reported in Figure 76, 90% of the particles present after 30 minutes of leaching are below 2.2 µm.

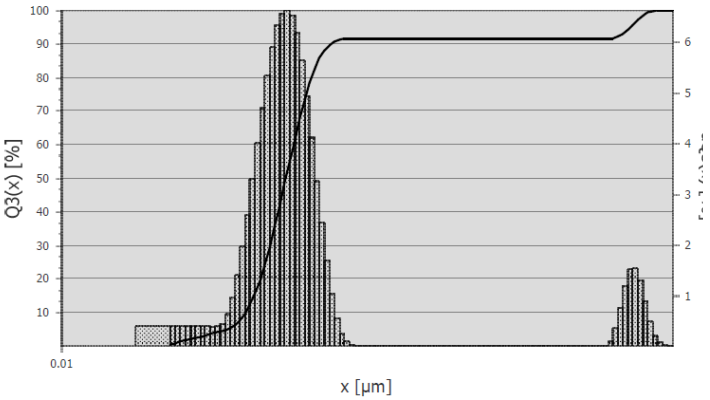

Q3(x) %	x [µm]
5	0.3
10	**0.4**
25	0.6
50	**0.9**
75	1.3
90	**2.2**
95	883.4
99	1'201.2

Figure 76: Granulometric analysis of a leaching slurry.

Filtration tests

For each filtering cloth type, instantaneous permeability is reported in the following charts with, on their side, pictures of the cloth after cake removal. Tests were not repeated in replica for all the filtering cloths due to good overlapping of the results obtained with the firstly tested samples.

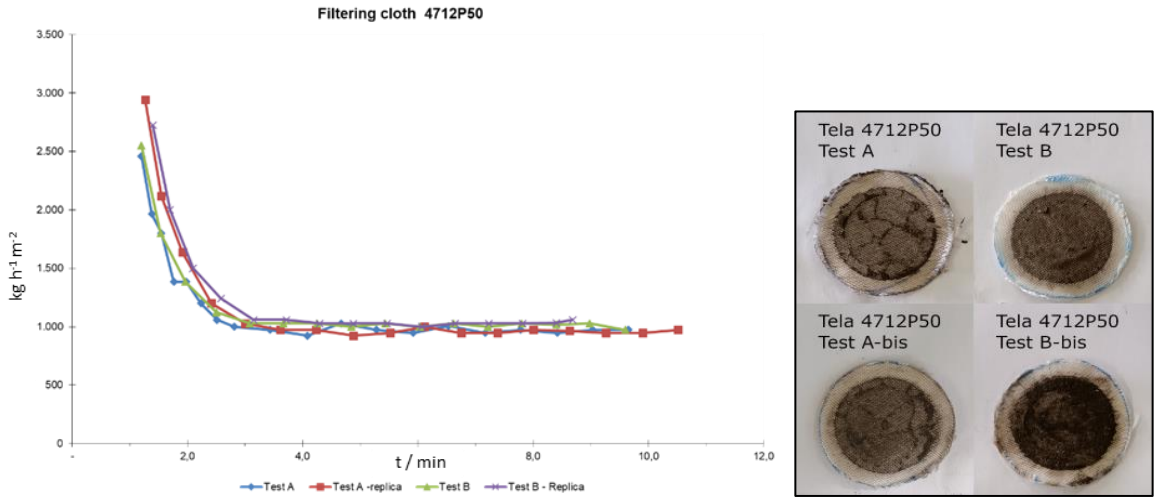

Figure 77: Filtering cloth 4712P50: Instantaneous filtration permeability (left) and appearance of the filtering cloth after cake blowing and removal (right).

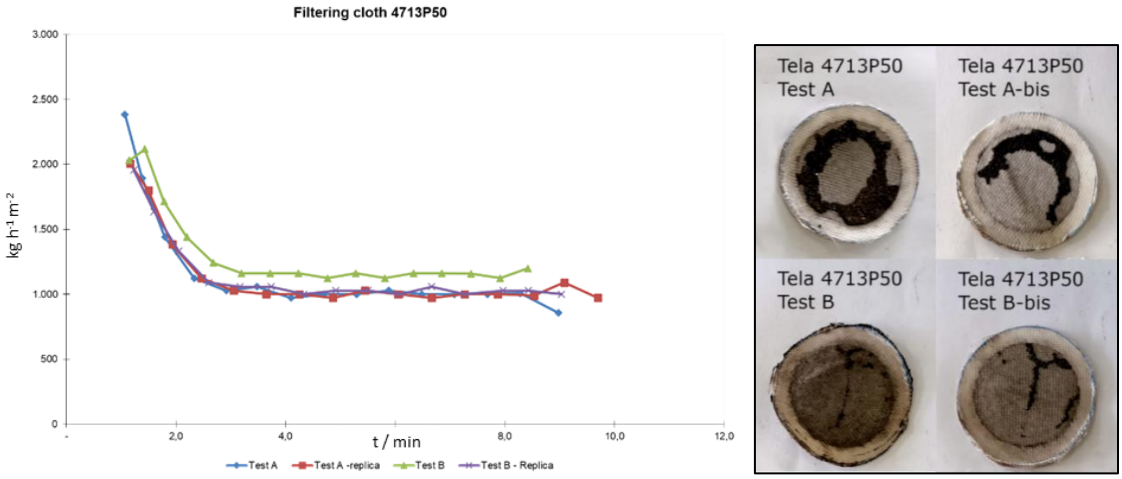

Figure 78: Filtering cloth 4713P50: Instantaneous filtration permeability (left) and appearance of the filtering cloth after cake blowing and removal (right).

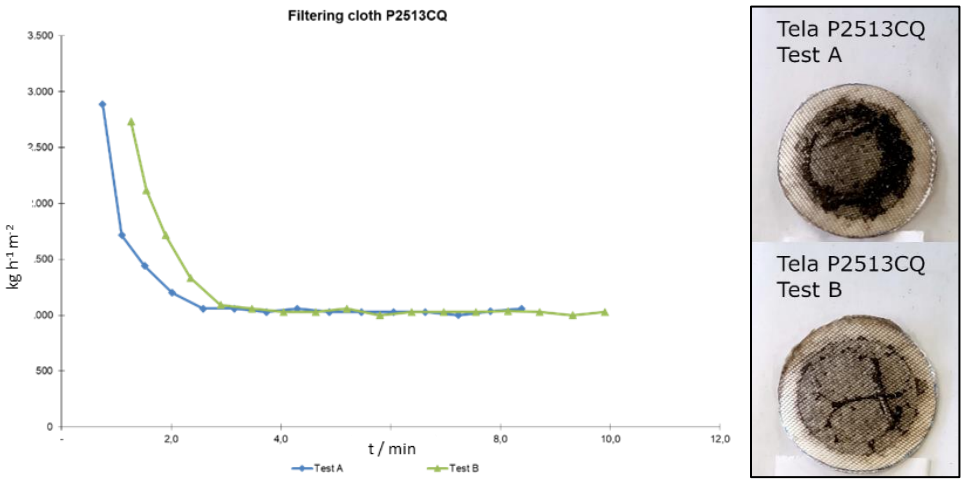

Figure 79: Filtering cloth P2513CQ: Instantaneous filtration permeability (left) and appearance of the filtering cloth after cake blowing and removal (right).

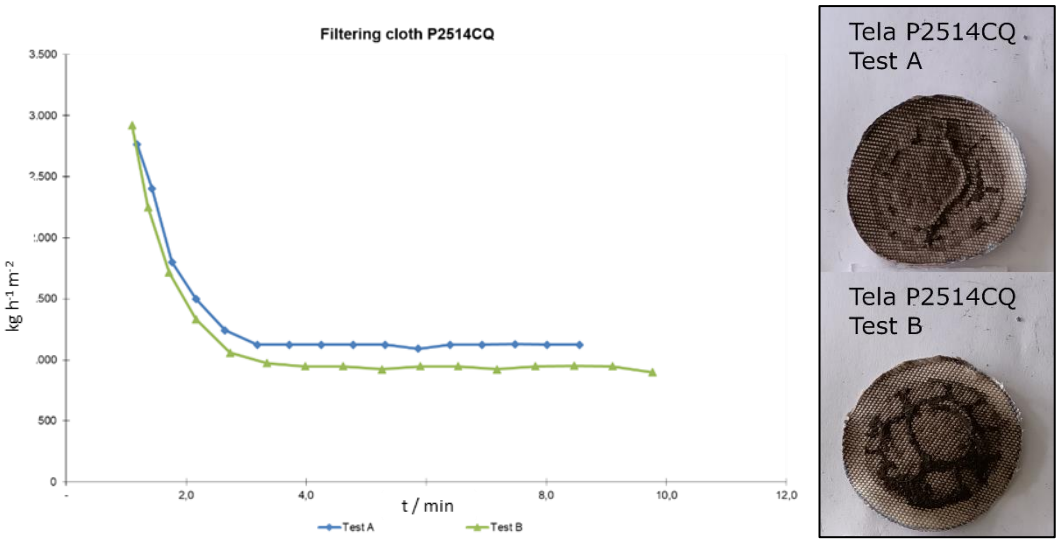

Figure 80: **Filtering cloth P2514CQ: Instantaneous filtration permeability (left) and appearance of the filtering cloth after cake blowing and removal (right).**

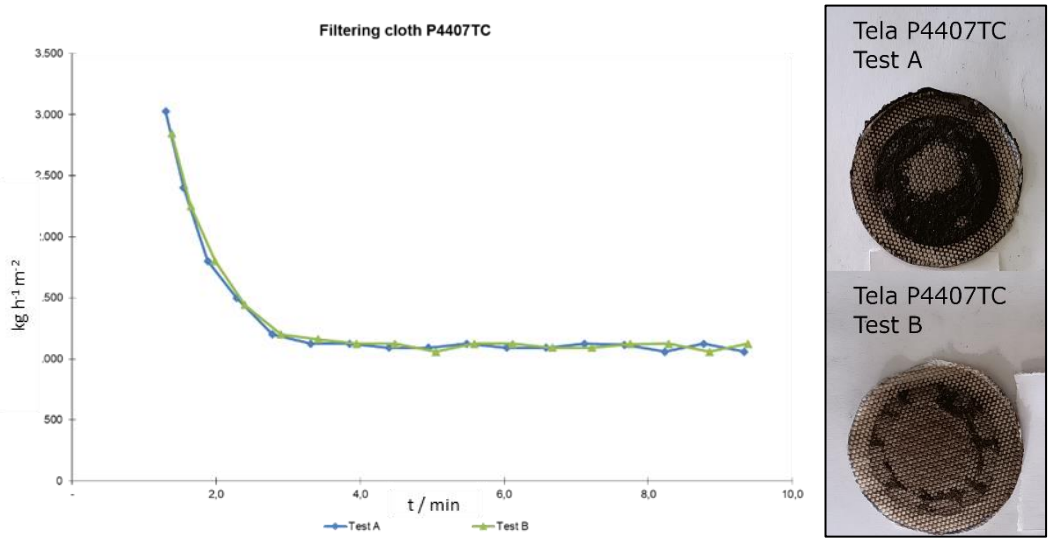

Figure 81: **Filtering cloth P4407TC: Instantaneous filtration permeability (left) and appearance of the filtering cloth after cake blowing and removal (right).**

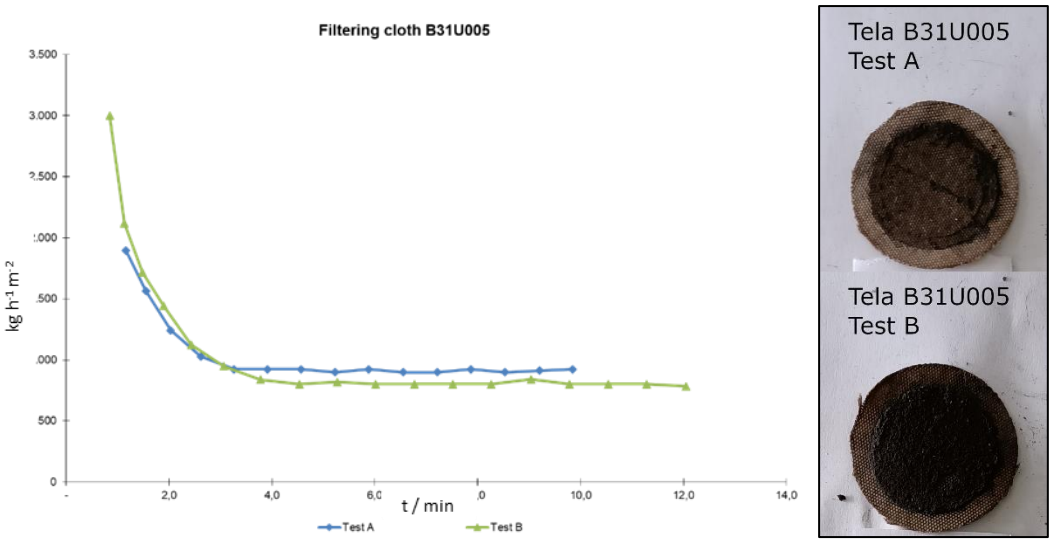

Figure 82: Filtering cloth B31U005: Instantaneous filtration permeability (left) and appearance of the filtering cloth after cake blowing and removal (right).

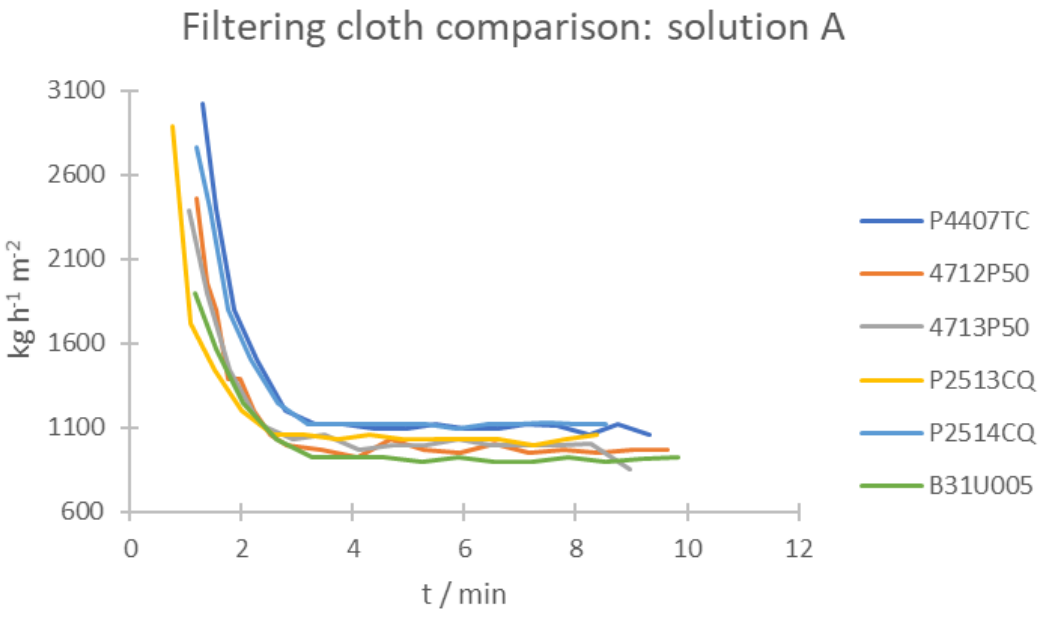

Figure 83: Instantaneous filtration permeability: solution A comparison.

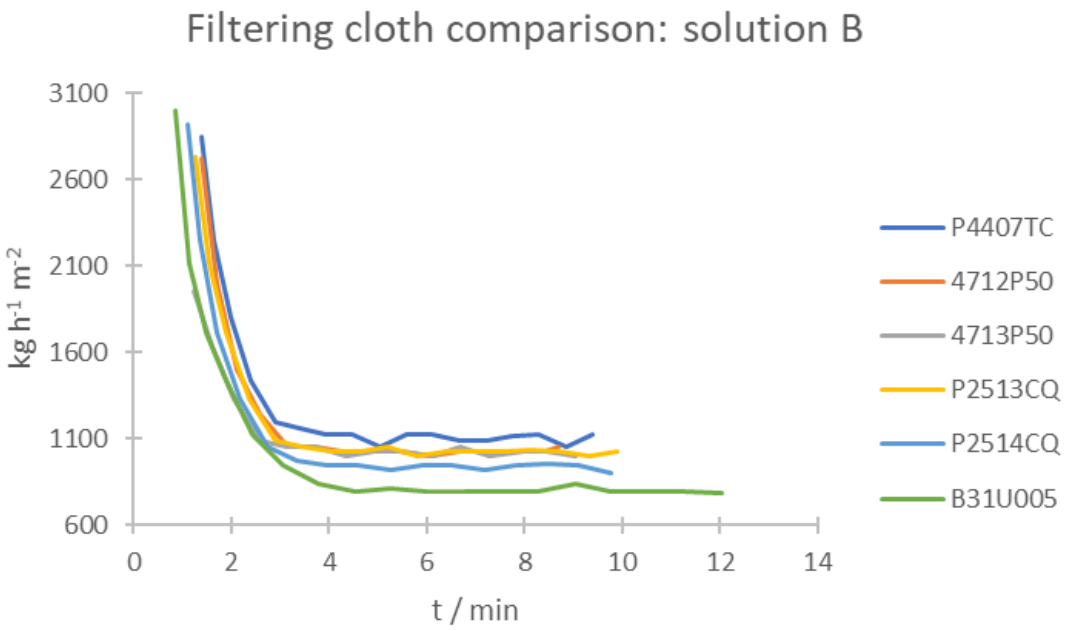

Figure 84 Instantaneous filtration permeability: solution B comparison.

The average instantaneous permeability relative to each filter cloth, both for the solution of type A and type B, is reported in Table 2 with the thickness of the panel and its moisture percentage. Figure 85 graphically shows the filtration parameters obtained with the tested filter chloths.

pH of filtered solution was comprised in the range 6.5-6.9.

	P4407TC		4712P50		4713P50		P2513CQ		P2514CQ		B31U005 (PVDF)	
Solution type	A	B	A	B	A	B	A	B	A	B	A	B
Average instantaneous permeability	1361,46	1345,35	1206,17	1256,22	1186,65	1153,88	1243,61	1255,46	1378,00	1227,14	1.052,0	1112,41
Cake thickness	3,46	3,54	3,3	3,6	3,73	3,58	3,48	3,48	3,45	3,58	3,44	3,44
Moisture	32,32%	18,78%	18,25%	17,08%	16,28%	17,31%	16,15%	20,71%	18,56%	18,07%	15,85%	13,56%

Table 2: Average instantaneous permeability, cake thickness and moisture percentage for each tested filtering media with both solution types.

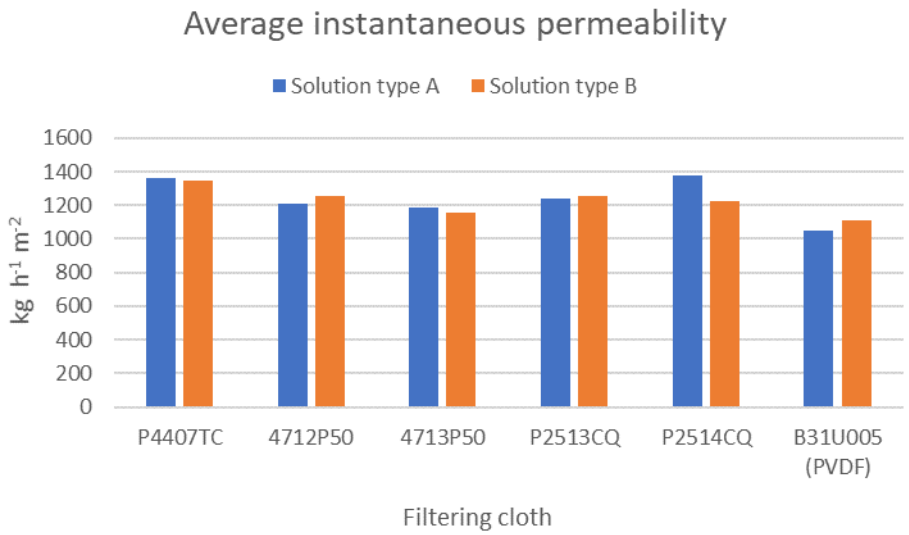

Figure 85: Average instantaneous permeability for each filtering cloth and both solutions type.

Observations and notes

In each test, a rapid clarification of the filtered solution was observed; no changes in the quality of the solution were detected during the entire filtration.

Filtering cloth B31UOO5 (PVDF): only one disc was available, already been used for other filtration tests.

For tests performed in replica, values reported in Table 2 are averaged.

Conclusions

No substantial differences were observed between the filtered fabrics, obtained instantaneous permeabiliy, obtained permeabilities can be used to size the filtering surface in function of the flow rate that must be treated.

Appendix 3 - Calcium sulfate precipitation

Calcium must be kept under control to avoid precipitation and subsequent scales in the heat exchangers. This study was carried out to investigate the possibility to remove Ca^{2+} cations from EZINEX® solutions through the addition of sulphate anions.

Experimental part

A solution containing ammonium chloride (250 g/L) and calcium (~10 g/L) was prepared and heated up to 60°C. 5 ml aliquots were withdrawn, and different amounts of sulfuric acid were added. Solution was allowed to react for 15 minutes and then centrifuged. The residual amount of Ca^{2+} left in the solutions was titrated with EDTA and eriochrome black T.

Calcium does not form a strong complex with eriochrome black T, so direct titration of Ca^{2+} by EDTA will not cause an abrupt color change at the end point (Red to Blue). The magnesium complex with EBT is more stable and its presence assure a net color change at the end point. Thus, a displacement titration of Ca^{2+} by EDTA in presence of a known quantity of Mg^{2+} was carried out. Titration were carried out in KCl/NaOH buffer solution (pH 12).

Results

Table 3 reports the concentration of chemicals used while obtained results are shown in Table 4. Calcium content as a function of the stoichiometric percentage of added sulfuric acid is shown in Figure 86.

EDTA / M	0,00497
Ca^{++} /g mol^{-1}	40
Vedta to titrate Mg^{++}/ ml	0,65
V sample/ ml	0,1
H2SO4 / M	0,636
V H2SO4 100% st / ml	1,86

Table 3: Concentration of chemicals and other analytic information.

V sample/ ml	H_2SO_4 0,636M /ml	H_2SO_4stoichiometric %	V EDTA /ml	Ca^{++} / g L^{-1}	Ca^{++} removed %
5	0	0	5,4	9,44	0,00
5	0,1	5,39%	4,84	8,33	11,79
5	0,3	16,16%	4,48	7,61	19,37
5	0,5	26,94%	4,14	6,94	26,53
5	0,7	37,72%	3,94	6,54	30,74
5	1	53,88%	3,52	5,71	39,58
5	1,2	64,66%	3,28	5,23	44,63
5	1,5	80,82%	3,04	4,75	49,68
5	2	107,76%	2,64	3,96	58,11
5	2,2	118,54%	2,3	3,28	65,26
5	3	161,64%	2,22	3,12	66,95

Table 4: Titration results.

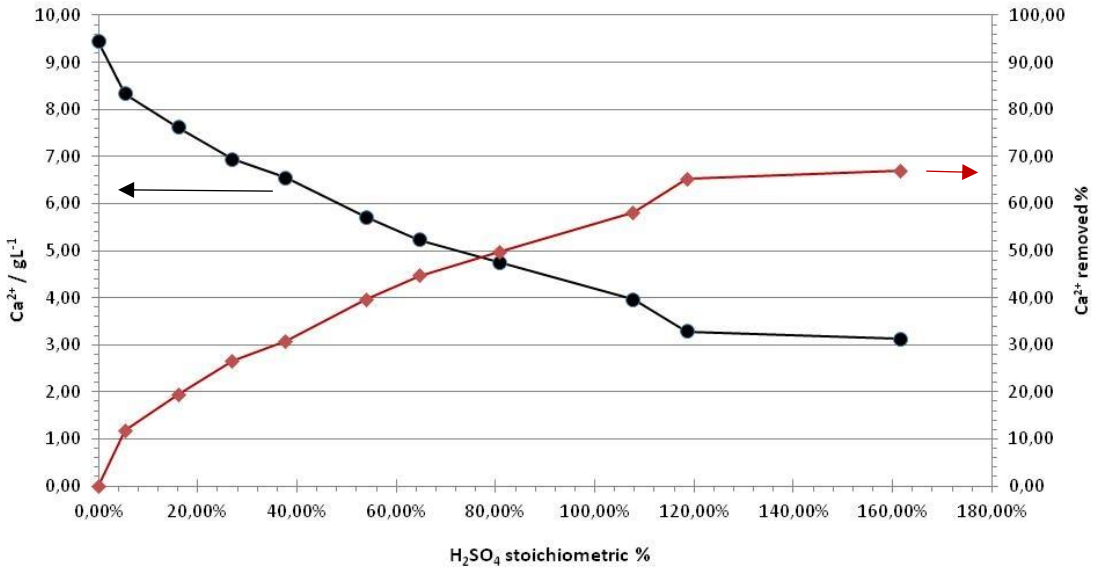

Figure 86: Calcium content in function of the stoichiometric percentage of sulfuric acid added.

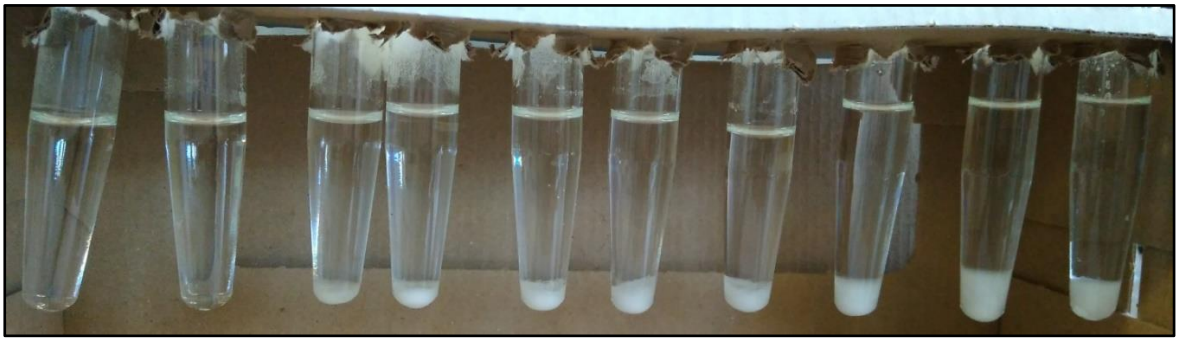

Figure 87: Different addition of sulfuric acid, 5.39% left to 161% right.

It is possible to notice that, even if sulfuric acid is in excess, complete precipitation of calcium cannot be achieved; further addition, over 100%, does not increase the amount of precipitated calcium sulfate.

Additional tests

To further reduce the calcium content, below the limit imposed by the solubility of calcium sufate, the effect of the addition of sodium hexametaphosphate (*SHMP*) was evaluated.

A solution with the following composition was used:

NH_4Cl 250 g/L, Ca^{2+} 3 g/L, $SO4^{2-}$ 20 g/L, Zn^{2+} 5 g/L (60°C).

Two different tests were carried out:

1) A volume of 75 ml was heated to 90 °C and evaporated until a solid white precipitate ($CaSO_4$) was formed. The percentage of volume reduction capable of causing precipitation of sodium sulfate was determined in the range of 40-50 %.

2) At three aliquots of 10 ml, SHMP was added in different amounts to precipitate calcium phosphate Figure 88.
   The white precipitate was than filtered, washed with 10ml of distilled water, dried in an oven (80°C) and analyzed with SEM-EDX.

Results are reported in Figure 88, the presence of zinc indicates that the SHMP is not selective for calcium, its use must therefore be excluded.

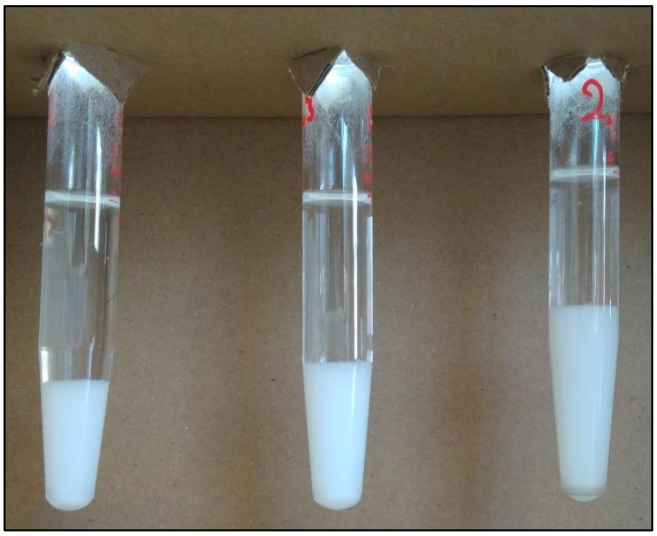

Figure 88: Different SHMP addition, 58.57% - 100% - 147.14% from left to right respectively.

SHMP/g	0,041	0,07	0,103
SHMP stoichiom. %	58,57	100,00	147,14

Spectrum: Point

Element	AN	Series	norm. C [wt.%]	Atom. C [at.%]
Oxygen	8	K-series	36,38	43,23
Carbon	6	K-series	22,10	34,99
Phosphorus	15	K-series	14,68	9,01
Chlorine	17	K-series	8,83	4,74
Zinc	30	K-series	7,84	2,28
Calcium	20	K-series	7,56	3,59
Sodium	11	K-series	2,61	2,16
Total:			100,00	100,00

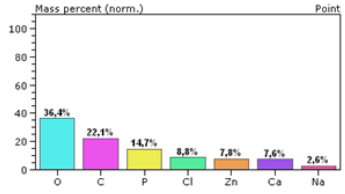

Spectrum: Point

Element	AN	Series	norm. C [wt.%]	Atom. C [at.%]
Oxygen	8	K-series	35,61	51,04
Phosphorus	15	K-series	21,81	16,15
Chlorine	17	K-series	11,50	7,44
Calcium	20	K-series	11,02	6,30
Zinc	30	K-series	10,04	3,52
Carbon	6	K-series	6,09	11,63
Sodium	11	K-series	3,93	3,92
Total:			100,00	100,00

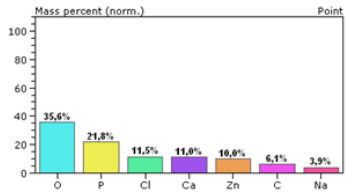

Spectrum: Point

Element	AN	Series	norm. C [wt.%]	Atom. C [at.%]
Oxygen	8	K-series	44,51	61,56
Phosphorus	15	K-series	21,18	15,13
Calcium	20	K-series	11,94	6,59
Chlorine	17	K-series	8,67	5,41
Zinc	30	K-series	7,06	2,39
Sodium	11	K-series	3,76	3,62
Carbon	6	K-series	2,88	5,30
Total:			100,00	100,00

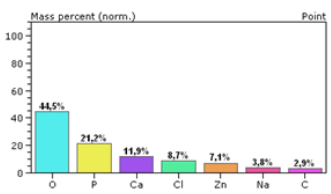

Figure 89: SHMP addition and SEM-EDX analysis.

Conclusions

The reaction between calcium cations and sulfate anions appears to be very slow, the fine precipitate begining to appear a few minutes after the addition of sulfuric acid. The addition of sulfate anion made it possible to obtain solutions with around 3 g/L of calcium. It is therefore possible to hypothesize the removal of calcium could be done by purging part of the ammonium sulphate solution, present in the the scrubber, directly in the leaching step. Precipitated calcium sulfate can then be filtered together with the leaching residue and calcium concentration will be kept under control

Appendix 4 - Demanganization of EZINEX® solution – Redox set point

Electric arc furnace dust consists, on average, of 2% by weight of manganese, mainly MnO, which is dissolved during the leaching step leading to a solution containing manganese in the form of bivalent cations (Mn^{2+}).

To obtain a good quality zinc deposit the amount of metallic impurities in the electrolysis solution must be less than 1 ppm. Unlike other metal cations nobler than zinc, manganese cannot be chemically cemented with the conventional cementation process, its removal is through the addition of permanganate which is capable of oxidizing Mn^{2+} to Mn^{4+} leading to the precipitation of manganese dioxide (MnO_2) which can be removed by filtration.

The reactions that occur in EZINEX® solutions are shown in Equation 2 and Equation 3; the former represents the desired demanganization reaction while the latter is a side reaction that occurs kinetically slowly and converts excess permanganate to MnO_2 by consuming ammonium. The combination of these reactions results in a solution that, after a suitable filtration step, should have a manganese content of less than 1 ppm.

$$2MnO_4^- + 3Mn^{2+} + 2H_2O \rightarrow 5MnO_2 + 4H^+$$

Equation 2.

$$2MnO_4^- + 2NH_4^+ \rightarrow 2MnO_2 + 4H_2O + N_2$$

Equation 3.

The addition of permanganate anion, such as a saturated solution of KMnO4, can be done in three different "points": to the leach solution, to the filtered leach solution and to the cemented solution. This addition is done automatically, the software continuously monitors the permanganate pump and attempts to maintain the ORP at the given set point. The ORP of the solution is monitored through an ORP electrode.

The ORP set point value should be the one at which the equivalence point of comproportionation reaction is reached without exceeding with permanganate leading to the reaction in Equation 3. The purpose of this study is to evaluate the influence of solution type, temperature, and pH on the ORP at the equivalence point of manganese-permanganate reaction.

Knowledge of the behavior of these factors can lead to the derivation of an equation that can determine the proper ORP set point depending on the solution conditions.

Typically, EAFD contains lead oxides that are partially leached in an ammonium chloride environment, leading to a solution with 200-400 ppm of $Pb2^+$. Theoretically, the oxidizing power of permanganate is sufficient to bring lead from a +2 to +4 oxidation state with

formation of insoluble PbO_2, this aspect was then analyzed.

Since pure MnO_2 may represent an added value, the composition of filtered solids obtained after permanganate addition was studied.

Moreover, the demanganization process is of interest also for the F.A.S.T. process in which lead is present in higher concentrations. An increased knowledge on the behavior of demanganization reaction would be useful also for the F.A.S.T. process.

Experimental part

Potentiometric titration

To reproduce the EZINEX® solution, a leaching was done on EAFD (Cape Gate).

Leaching conditions were:

Volume	4L
EAFD	20 g/L
NH_4Cl	250 g/L
T	70-80 °C
Time	1h

The resulting solution was divided into three portions to obtain an unfiltered solution, a filtered solution, and a cemented solution. Cementation was carried out with an excess of metallic zinc powder.

For each type of solution, potentiometric titration tests were performed at 60, 70, 80 °C and pH 5.2, 6, and 7. Titrations were done on 100 ml samples with 0.02M $KMnO_4$ solutions as titrant, while the pH was adjusted with a 36% HCl and 50% NaOH solution. The solutions were then analyzed with AAS after and before potentiometric titration to assess manganese content.

Filtered solids composition

To determine whether permanganate ion is capable of oxidizing Pb^{2+} to Pb^{4+} in ammonium chloride solution, a sample of filtered and cemented solution was titrated to the equivalence point with potassium permanganate (70°C pH 5.2). The solution was filtered, and the solid residue was washed, dried, and analyzed with a SEM-EDX.

Since the demanganization process is also of interest for the F.A.S.T. process, 20 mL of 0.02M potassium permanganate (70°C pH 6.2) was added to 300 mL of the actual F.A.S.T. solution. After 1h, the solution was filtered and the solid was washed, dried, and analyzed with a SEM-EDX.

Results

Potentiometric titration: ORP flex determination and ORP flex vs. pH law extrapolation

Determination of the equivalence point, to which the equivalent volume and the ORP of the inflection point correspond, was performed following a mathematical analysis of the obtained curves.

The titration curves presented a sigmoid-like shape, Figure 90 , which was fitted using Equation 4.

$$f(x) = \frac{a}{b + ce^{-d(x-f)}} + t$$

Equation 4: sigmoid function general form.

The root of the second derivative of the obtained sigmoid, Equation 6 and Equation 5, represents the equivalent volume that can be used in the sigmoid function to determine the ORP value at the flex point, Figure 91: Second derivative of the sigmoidal function.

$$f''(x) = -\frac{acd^2e^{d(x-f)}(be^{d(x-f)} - c)}{(be^{d(x-f)} + c)^3}$$

Equation 6: Second derivative.

$$\text{Root} \quad x = \frac{df + \ln\frac{c}{b}}{d}$$

Equation 5: Second derivative root.

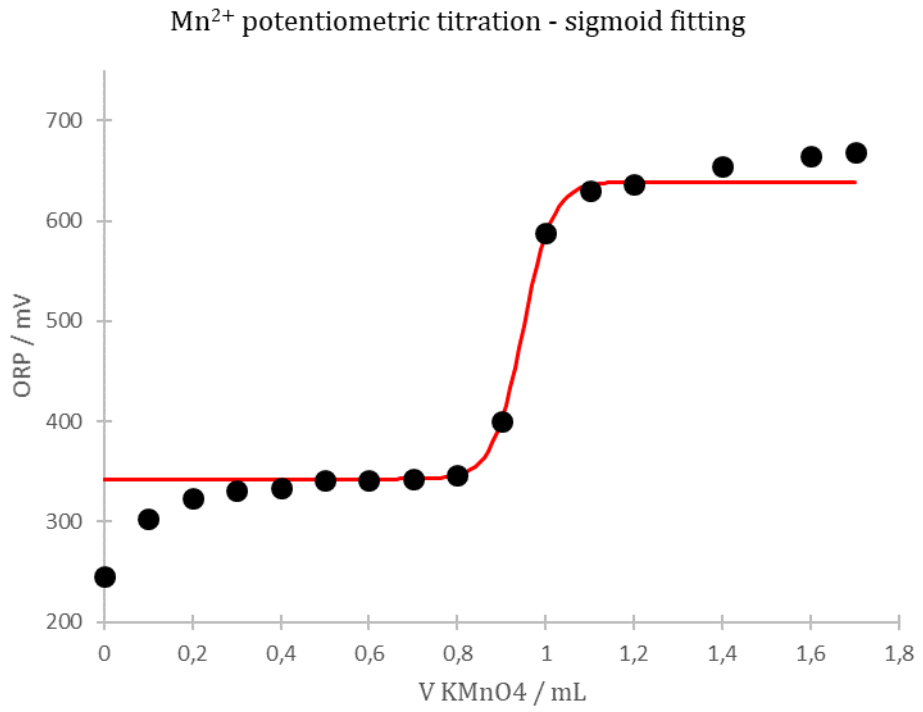

Figure 90: Potentiometric titration of EZINEX® solution and sigmoid fitting, Unfiltered solution 70°C pH 6.

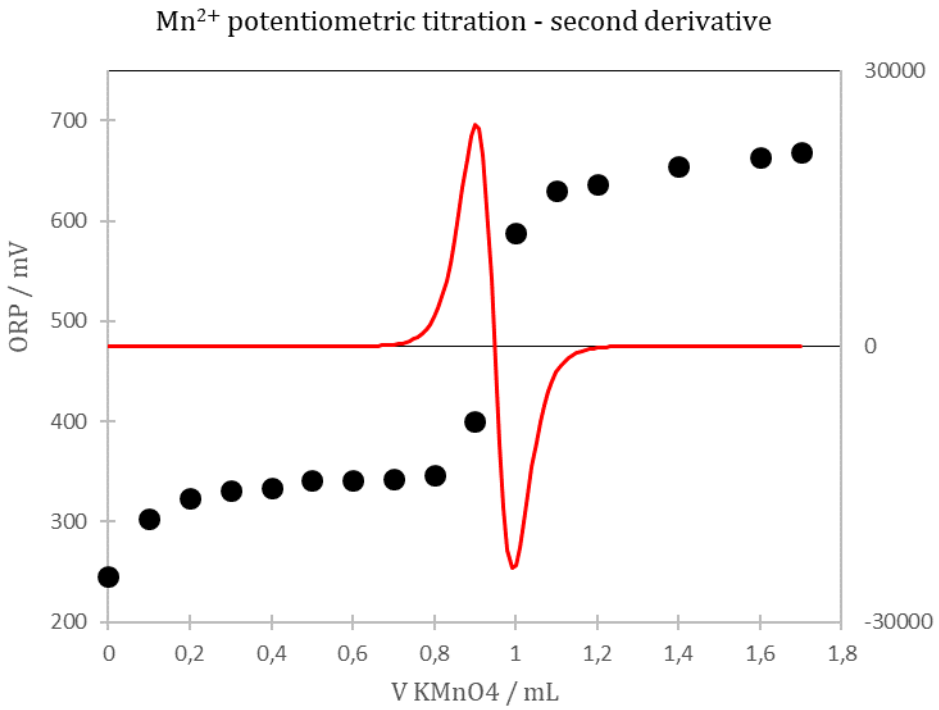

Figure 91: Second derivative of the sigmoidal function.

The obtained ORP values were plotted against pH for each different solution and temperature, Figure 92 - Figure 93 - Figure 94, and linear correlations between ORP versus pH were extrapolated; all data are summarized in Table 5.

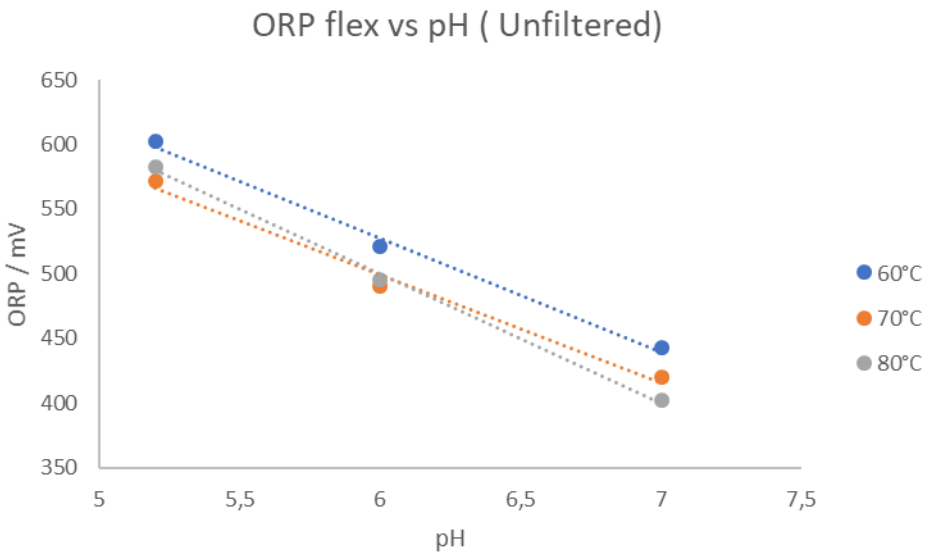

Figure 92: ORP flex vs pH at different temperature, unfiltered solution.

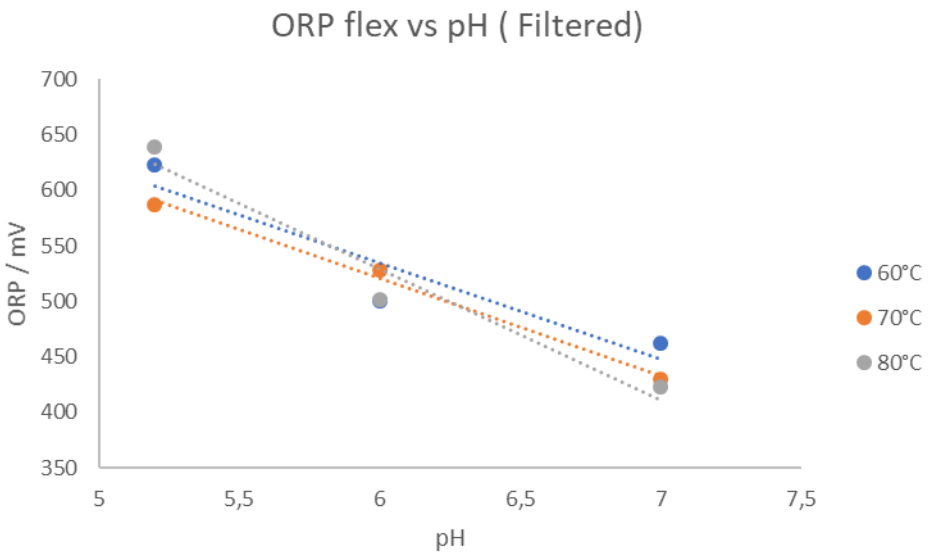

Figure 93: ORP flex vs pH at different temperature, filtered solution.

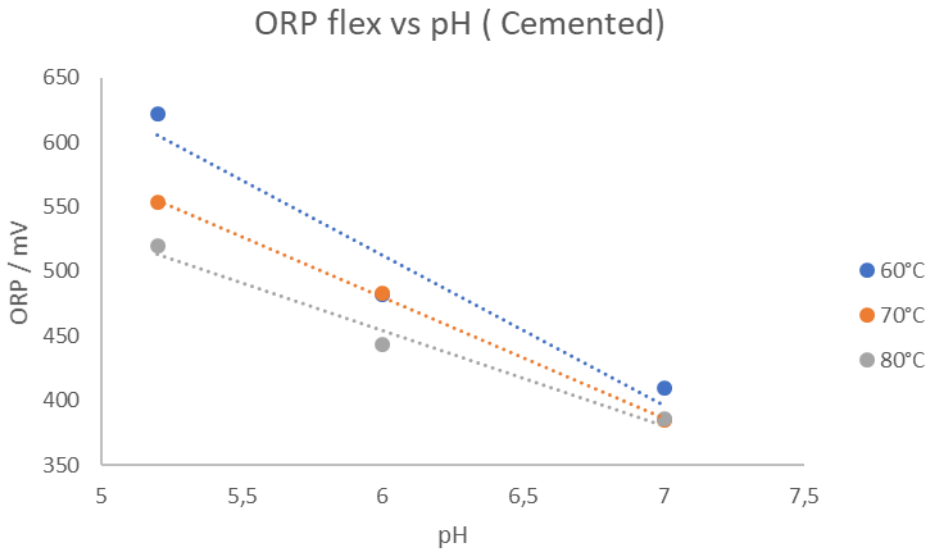

Figure 94: ORP flex vs pH at different temperature, cemented solution.

	T/°C	pH	$E_{flex/mV}$	Veq/ml	Slope	q
Unfiltered	60	5,2	602	1,05	-88,028	1056
	60	6	521	0,94		
	60	7	443	0,99		
	70	5,2	572	1,03	-83,654	1001,6
	70	6	491	0,95		
	70	7	420	1,04		
	80	5,2	583	1,13	-100,29	1101,9
	80	6	496	1,04		
	80	7	402	0,96		
Filtered	60	5,2	623	0,86	-87,116	1057,3
	60	6	500	0,80		
	60	7	463	0,93		
	70	5,2	587	0,88	-88,069	1049
	70	6	528	0,86		
	70	7	429	0,87		
	80	5,2	639	0,86	-118,69	1241
	80	6	501	0,86		
	80	7	423	0,97		
Cemented	60	5,2	622	0,93	-116,35	1210,5
	60	6	482	0,88		
	60	7	409	0,80		
	70	5,2	553	0,88	-93,826	1042,9
	70	6	483	0,87		
	70	7	385	0,90		
	80	5,2	520	0,97	-73,82	897,41
	80	6	443	0,87		
	80	7	386	0,98		

Table 5: Calculated ORP flex, Veq and slope (Eflex vs pH) obtained at different temperature for each different solution.

From the analysis of the results obtained, the influence of temperature appears minimal. It should be noted that experiments conducted at 80°C were problematic, the high temperature led to a rapid loss of ammonia resulting in a pH change that was not easy to control.

Excluding the experiments done at 80°C, the calculated slopes appear consistent. Considering the small variation between the experiments done on the three different solutions at 60 and 70°C, an average value of the slopes and intercepts can be used to derive a generic law that can establish the optimal ORP set point as a function of pH, Equation 7.

$$y = -92.84\,x + 1069.55$$

Equation 7: ORP set point/ pH correlation. Valid for pH range 5.2-7 and temperature 60-80°C. Note: the ORP electrode used referred to an Ag/AgCl electrode.

The correlation obtained is showed on the pourbaix diagram at the end of this report, it is in line with what was expected and deviates from what is reported on the pourbaix diagram because the matrix of the solution is different.

Permanganate consumption

Looking at the permanganate used to reach the equivalent volume during the titrations, Table 5, the demanganization of the leaching solutions containing EAFD required higher volumes than the others. it should be noted that the solutions all come from the same leaching, so the manganese content is assumed to be the same for all. there is no correlation between pH and consumption.

Averaging the data, the consumption of permanganate can be estimated at +11% if the demanganization is done in leaching.

Validation of the ORP/pH correlation

To validate experimentally derived correlation, 1L of EAFD leaching solution was prepared and filtered. Samples of 100 ml were heated to a certain temperature and the pH was adjusted to random values in the range 5.2-7. Given the pH, the ORP set point was calculated using the correlation reported in Equation 7.

A solution of potassium permanganate (0.02M), or sodium permanganate (0.029M), was added until the ORP value reached the calculated set point, the solution was then filtered and analyzed with AA. Results are reported in Table 6; in all tests, the final manganese content was less than 1 ppm.

	Test	pH	ORP set / mV	V $KMnO_4$ or $NaMnO_4$ / mL	T / °C	ppm Mn	Removal %
$KMnO_4$ 0,02M	1	6,2	494	2,6	60	0,07	99,75
	2	5,35	573	2,62	60	0,23	99,21
	3	6,77	441	2,6	60	0,08	99,75
	4	6,1	503	2,8	70	0,15	99,49
	5	5,47	562	2,8	70	0,45	98,49
	6	6,06	507	2,8	80	0,12	99,60
$NaMnO_4$ 0,029M	7	6,38	507	2	60	0,38	98,71
	8	5,9	522	1,9	60	0,44	98,5
	9	5,3	577	1,9	70	0,28	99,04

Table 6: Validation test, Removal percentage is calculated from Mn^{2+} initial concentration: 29,42 ppm (equal for each sample).

Filtered solids composition

EZINEX® *solutions*

The precipitates obtained after the addition of potassium permanganate to the filtered and cemented EZINEX® solutions were analyzed using the EDX technique; the results are shown in Table 7. The manganese-to-oxygen ratio is about 1:2 in both precipitates, leading to the assumption that the solid probably MnO_2. Both precipitates have a small amount of lead that cannot be classified as lead +2 or +4.

	EDX analysis			
	Filtered		Cemented	
	wt%.	at%.	wt%.	at%.
Manganese	49,82	28,14	53,81	29,14
Oxygen	29,19	56,62	34,21	63,62
Chlorine	15,33	13,42	5,07	4,25
Lead	3,08	0,46	1,26	0,18
Zinc	2,18	1,03	4,84	2,2
Calcium	0,42	0,32	0,81	0,6

Table 7: EDX analysis of solid precipitate formed after the addition of permanganate to a filtered and a cemented EZINEX® solution.

F.A.S.T. solution

The precipitate obtained after the addition of potassium permanganate to a sample of real F.A.S.T. solution was analyzed by the EDX technique, Table 8 shows the results obtained. Even in the presence of more than 5g/L of Pb^{2+}, no significant amount of lead was found in the precipitate.

EDX analysis

FAST

	wt%.	at%.
Manganese	51,81	26,48
Oxygen	39,29	68,95
Calcium	4,22	2,95
Lead	3,19	0,43
Chlorine	1,49	1,18

Table 8: EDX analysis of solid precipitate formed after the addition of permanganate to a real F.A.S.T. solution.

Observations

During experimentation, a significant variation in reaction rate was observed. The kinetics appeared to be faster at alkaline pH. This behavior is likely associated with the nature of the reaction producing acidity. A kinetic study could be of interest to establish process parameters such as reactor residence time and redox electrode position.

Conclusions

According to the Pourbaix diagram of manganese, even in ammonium chloride solutions, the equilibrium potential of Mn^{2+}/manganese oxides (MnO_2, Mn_2O_3, and Mn_3O_4) is pH dependent, with a negative slope. This means that using a fixed ORP set point to control permanganate addition is not an optimal choice; a variable ORP set point might be better.

By knowing the pH of the solution that is to be demanganized, it is possible to calculate the optimal ORP set point to use to ensure completion of the reaction and minimize permanganate waste.

The result obtained from the validation procedure, shows that manganese was reduced below 1 ppm in each random test condition (pH and T) with both potassium and sodium permanganate.

The consumption of permanganate was estimated at +11% if the demanganization is done in leaching.

Due to the many variables involved such as solution composition, residence time, agitation, and "dynamic" flow conditions, this correlation between ORP set point and pH needs to be validated under real process conditions.

EDX analysis on precipitates obtained after addition of permanganate to EZINEX® and F.A.S.T. solution showed a constant 1:2 manganese:oxygen ratio which means that its

composition could be MnO_2. In addition, the oxidation of lead from +2 to +4 by permanganate seems to be irrelevant; demanganization could also be used on lead-rich solutions avoiding the precipitation of lead compounds.

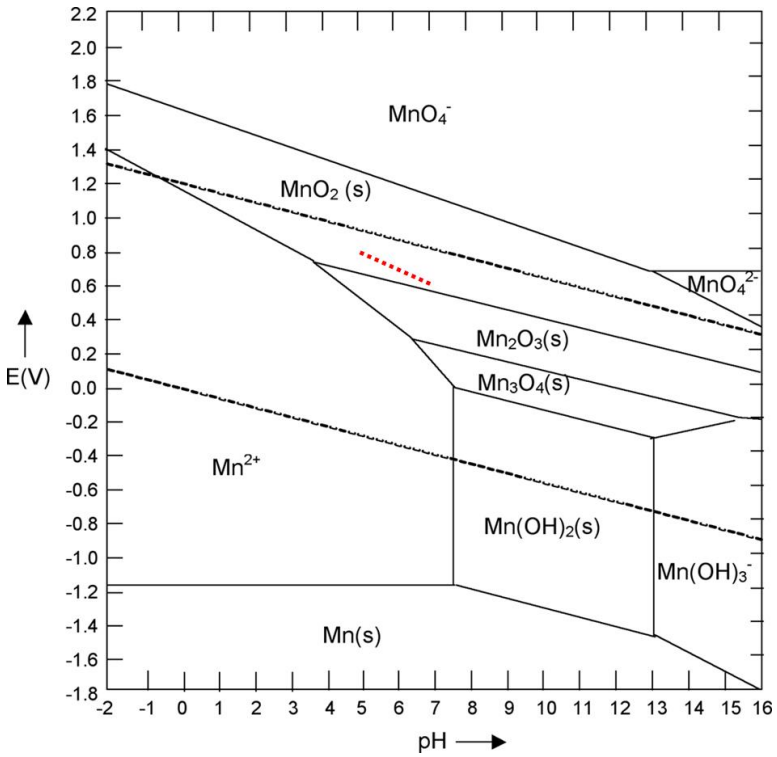

Figure 95: Manganese pourbaix - >> red dotted line << experimental equilibrium straight line in ammonium chloride. Note that the ORP electrode used referred to an Ag/AgCl electrode. In the pourbaix diagram, the E-pH correlation is reported vs hydrogen electrode.

Appendix 5 - Kinetic study of demanganization reaction

Manganese removal in the EZINEX® plant is done by the addition of permanganate, the solubilized manganese is oxidized to give insoluble manganese oxide which is removed through a filtration process. However, Mn^{2+} oxidation is not the only possible reaction, ammonium, iron (II) and organics in the EAFD can also be oxidized according to the following reactions.

$$2MnO_4^- + 2NH_4^+ \rightarrow 2MnO_2 + 4H_2O + N_2$$

$$MnO_4^- + 3Fe^{2+} \rightarrow MnO_2 + 3Fe^{3+}$$

More than 30% of the costs related to chemicals required by the EZINEX® process are comes from permanganate consumption and the mentioned reactions represent a possible waste of this reagent; a better understanding of the kinetics of these reactions under different conditions could lead to the optimization of permanganate consumption.

This study was carried out to estimate the speed at which all possible reactions take place at different temperature and pH.

Reaction's kinetics were determined using two different techniques: UV-Vis spectroscopy and oxidation reduction potential monitoring.

Experimental part

UV-Vis spectroscopy

The UV-Vis technique was used to study the kinetics of ammonia oxidation by permanganate anion by monitoring absorbance over time. A spectrophotometer equipped with a thermostatic chamber, a magnetic stirring device, and the ability to record spectra in ambient light was used for the measurements.

First, a spectrum of permanganate in water and ammonium chloride was recorded to check for interference in the permanganate absorbance region. A calibration curve of permanganate in water was then made to be able to correlate absorbance to concentration through determination of the molar extinction coefficient.

A 200 g/L NH_4Cl solution was used to determine reaction kinetics at three different temperatures (40-60-80 °C) and pH (5.3-6-7); pH was adjusted with HCl (37%) and NH_3 (30%).

A quartz cuvette was filled with the ammonium chloride solution and potassium permanganate was added; the cuvette was shaken, closed with a Teflon cap, inserted into

the thermostatically controlled cuvette holder, and kept under stirring. Spectra were recorded at regular intervals.

Absorbance @ 525nm was used to determine the residual permanganate concentration as a function of time and the kinetic constant was determined.

ORP monitoring

The oxidation of manganese by permanganate is an extremely fast reaction that requires rapid data sampling. The oxidation reduction potential of the solution can give an idea of the reaction rate under different conditions and can be sampled quickly.

Kinetic ORP measurements were made on several solutions:

- Synthetic solution (NH_4Cl 200 g /l + Mn^{2+} 100 ppm)
- Filtered Leaching solution (leaching of EAFD 50 g/L at 70°C for 1h in ammonium chloride)
- Unfiltered Leaching solution (leaching of EAFD 50 g/L at 70°C for 1h in ammonium chloride)
- Water with suspended dust (EAFD 50 g/L)

A platinum wire was attached to an Ag/AgCl reference electrode to make a combined ORP electrode, a potentiostat was used to record the potential difference between the two.

A small beaker was filled with 35 ml of the solution in question, the ORP electrode was inserted, and potassium permanganate was added under stirring. The collected data, ORP and time, were used to determine the reaction kinetics at different temperatures (40-60-80°C) and pH (5.3 - 6 - 7).

Results

UV-Vis spectroscopy results

The spectra of permanganate in water and in ammonium chloride solution were compared to assess possible electrolytic interferences; Figure 96 shows that the characteristic peaks of permanganate are still visible in the presence of ammonium chloride.

Absorbance of permanganate was then assumed unchanged in water and ammonium chloride solution, so a calibration curve was made using distilled water to avoid possible

concentration errors due to the reaction between permanganate and ammonia.

Calibration curve is shown in Figure 97, the calculated molar extinction coefficient was $2.4x10^3$ $M^{-1}cm^{-1}$@ 525nm.

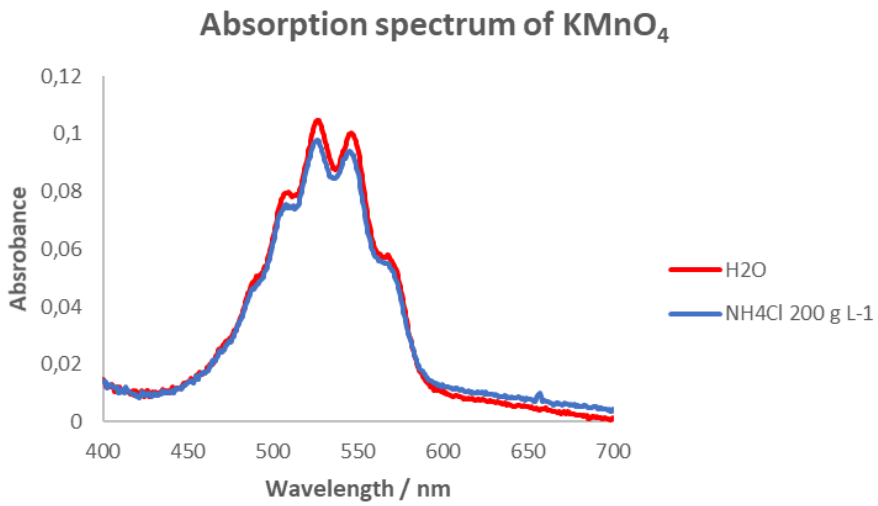

Figure 96: Spectra of permanganate in water and ammonium chloride solution.

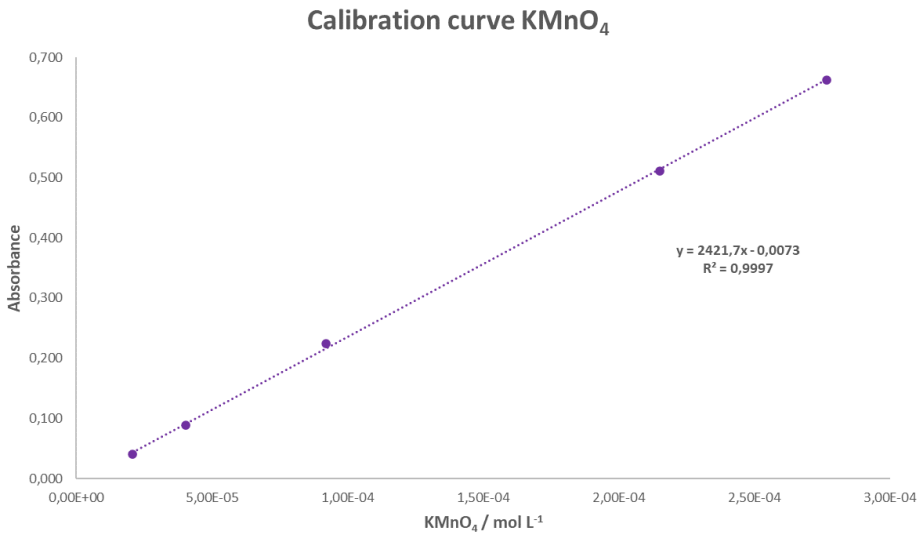

Figure 97: UV-Vis calibration curve of Potassium permanganate in H_2O.

A typical set of spectra obtained from the solution of ammonium chloride with permanganate is shown in Figure 98, the absorbance decreases with increasing time, signifying permanganate consumption.

Logarithm of absorbance shows a linear dependence on time; this indicates a first-order reaction with permanganate. The reaction rate constant, k, can be extrapolated using Equation 8 and Equation 9 while the reaction half-life, which is a measure of the time required to decrease to half the initial concentration of the reactant, can be calculated using Equation 10.

The kinetic laws obtained for pH 5.3, 6 and 7 at 40, 60 and 80°C are shown in Figure 99, Figure 100 and Figure 101 while Figure 102 shows the reaction half-life at different pHs and temperatures.

From the results obtained experimentally, the oxidation of ammonia by permanganate proceeds faster as pH and temperature increases.

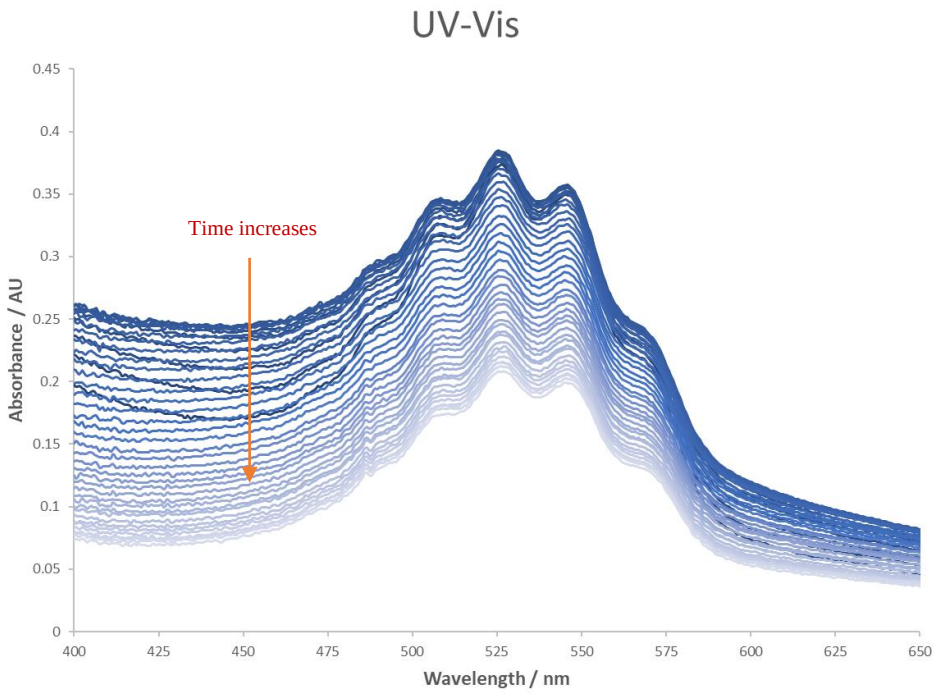

Figure 98: Series of UV-Vis spectra of permanganate in ammonium chloride solution at different times.

$$Rate = -\frac{\mathrm{d}[\mathrm{A}]}{dt} = k[A]$$

Equation 8: Differential rate law.

$$\frac{\ln [A]}{\ln [A_0]} = -kt$$

Equation 9: Integrated rate law.

$$t_{1/2} = \frac{\ln (2)}{k}$$

Equation 10: Half-life.

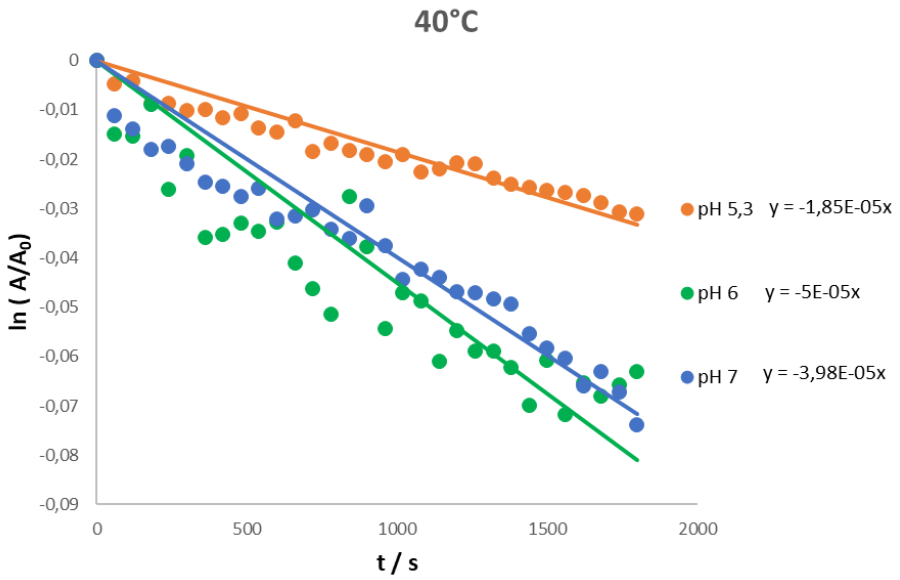

Figure 99: Kinetics of permanganate in NH4Cl 200 g L-1 @ 40°C.

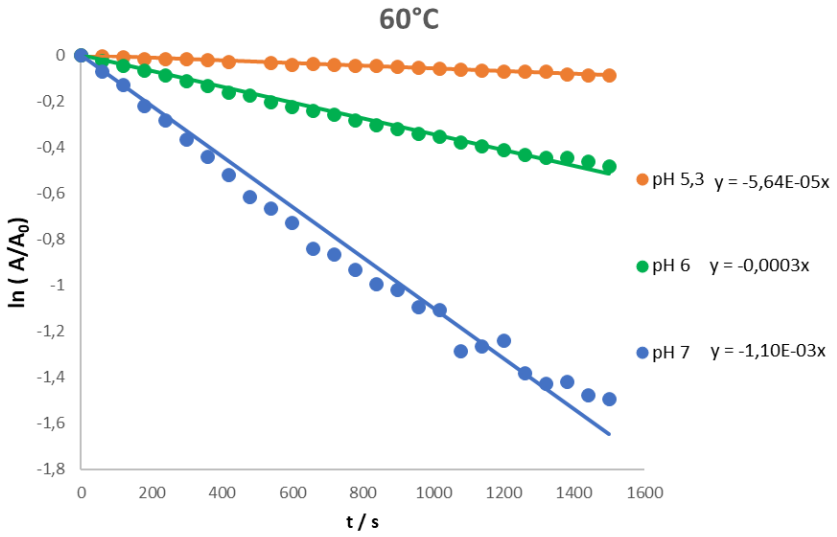

Figure 100: Kinetics of permanganate in NH4Cl 200 g L-1 @ 60°C.

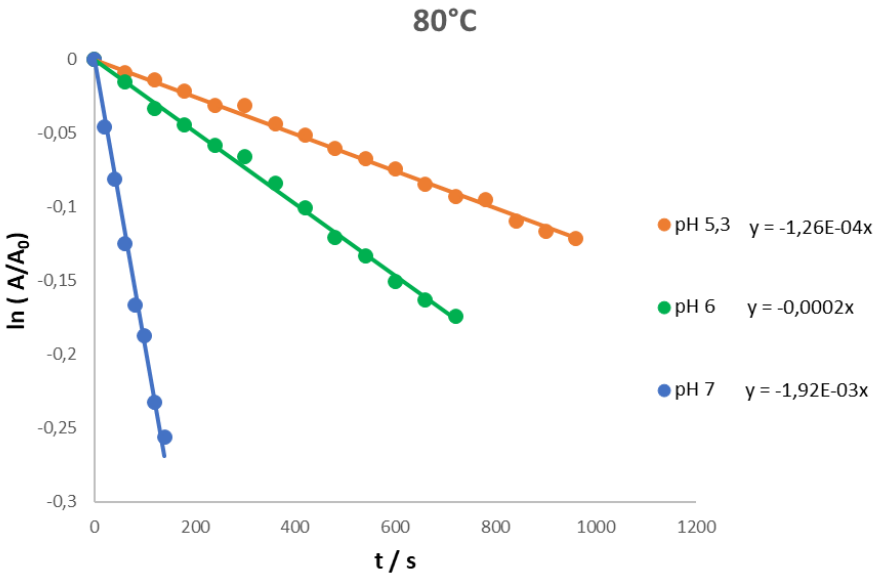

Figure 101: Kinetics of permanganate in NH4Cl 200 g L-1 @ 80°C.

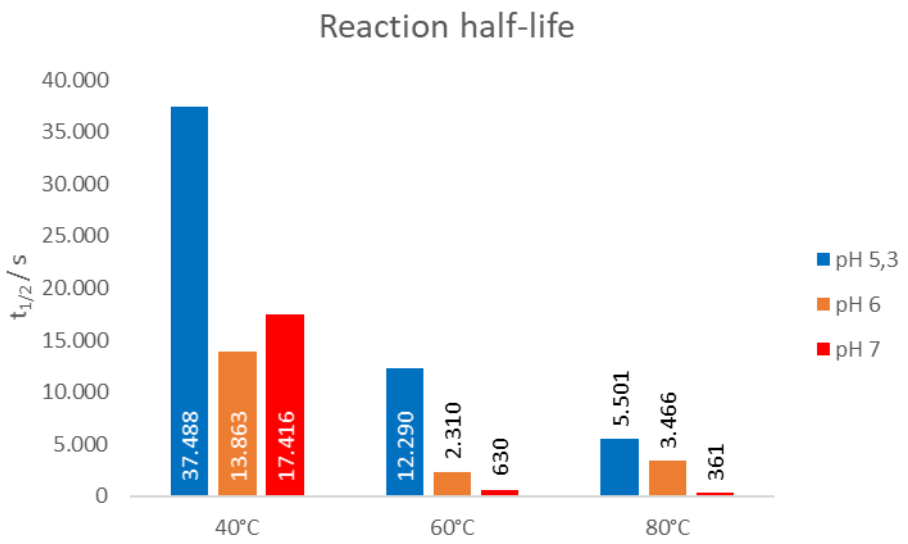

Figure 102: Reaction half-lives in function of pH and temperature.

ORP monitoring

The oxidation of manganese (II) by permanganate is a very fast reaction that proceeds on a time scale of seconds. As shown in Figure 103, the addition of permanganate to the solution rapidly increases the ORP, which subsequently decreases as permanganate is consumed. Since the ORP is concentration dependent, the differential of the ORP over time gives the reaction rate (Equation 11Equation 12), while the half-life of the reaction can be calculated using Equation 10.

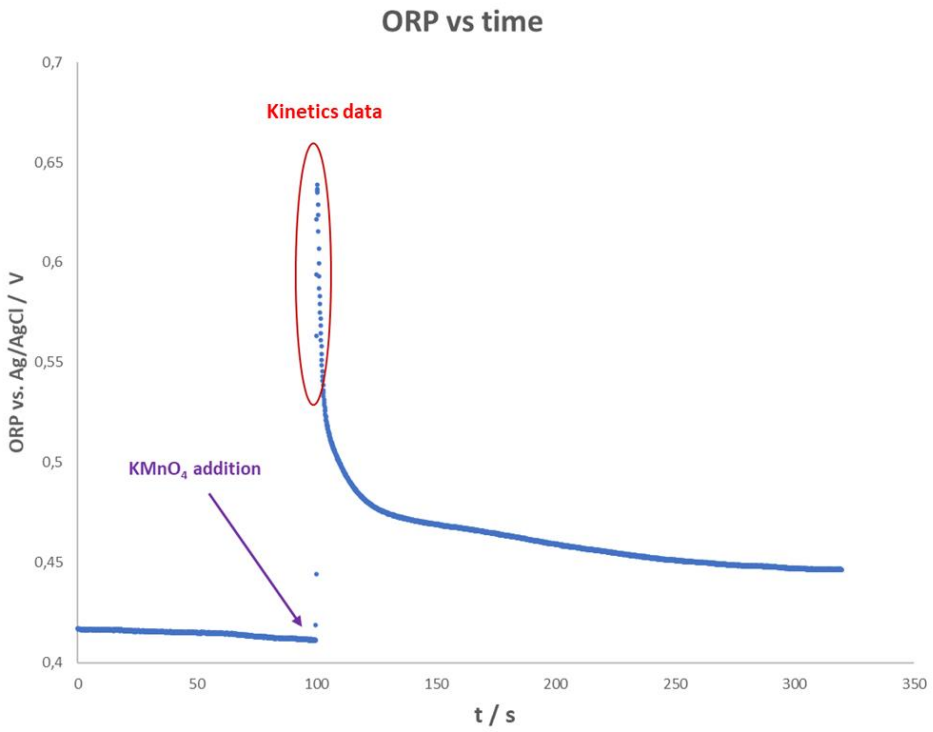

Figure 103: ORP behavior after permanganate addition.

$$Rate = -\frac{\mathrm{d\ ORP}}{dt} = k\ ORP$$

Equation 11: differential rate law.

$$\frac{\ln\ \mathrm{ORP}}{\ln\ \mathrm{ORP_0}} = -kt$$

Equation 12: integrated rate law.

Although the potential of a solution can be related to the concentration of a chemical species through the Nernst equation, going from ORP to molar concentration could produce a large error.

Looking at the two semi-reactions below, that make up reaction the manganese oxidation reaction, protons, pH, are involved and should be considered when calculating the concentration of MnO_4^-. In addition, ORP measurements are subject to an error that has a

significant impact on the determination of concentration via the Nernst equation. Therefore, it was chosen to express the reaction rate and kinetics in terms of ORP instead of molar concentration.

$$2MnO_4^- + 8H^+ + 6e^- \rightarrow 2MnO_2 + H_2O$$

$$3Mn^{2+} + 6H_2O \rightarrow 3MnO_2 + 12H^+ + 6e^-$$

$$2MnO_4^- + 3Mn^{2+} + 2H_2O \rightarrow 5MnO_2 + 4H^+$$

Extrapolated kinetic laws for synthetic and leaching solutions are reported in Figure 104 and Figure 105 respectively. Both solutions show a faster kinetic as temperature and pH increases. Reaction half-life, reported in Figure 106, clearly shows such trend. Table 9 reports all the experimentally obtained kinetic laws and reaction half-life; results obtained on leaching solution + EAFD and water + EAFD evidence an additional consumption of permanganate by EAFD.

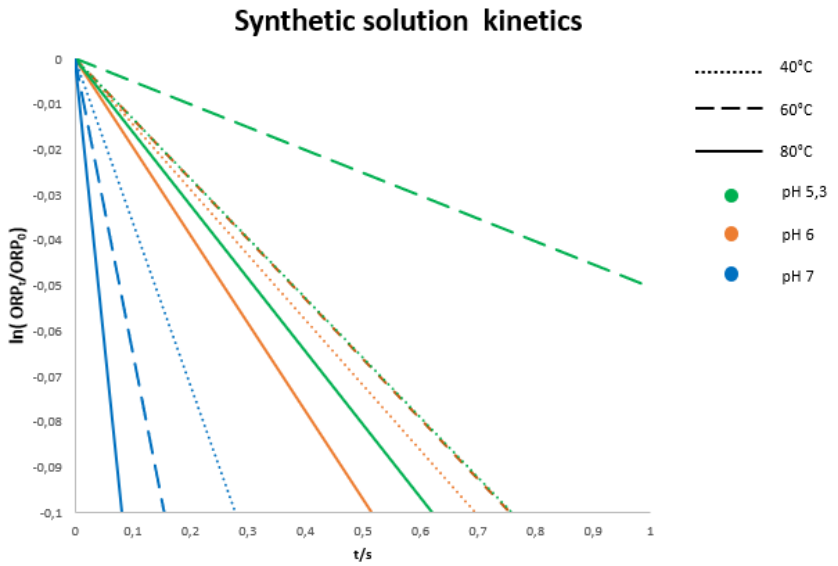

Figure 104: kinetics of permanganate in synthetic leaching solutions.

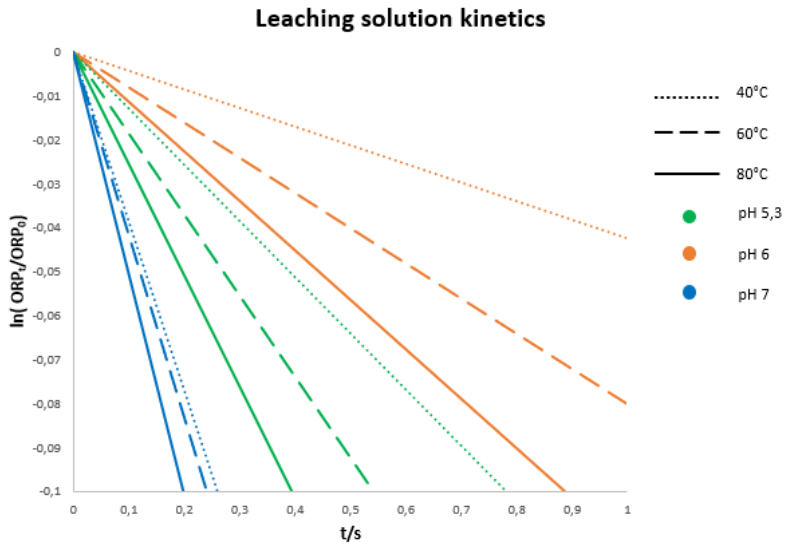

Figure 105: kinetics of permanganate in leaching solutions.

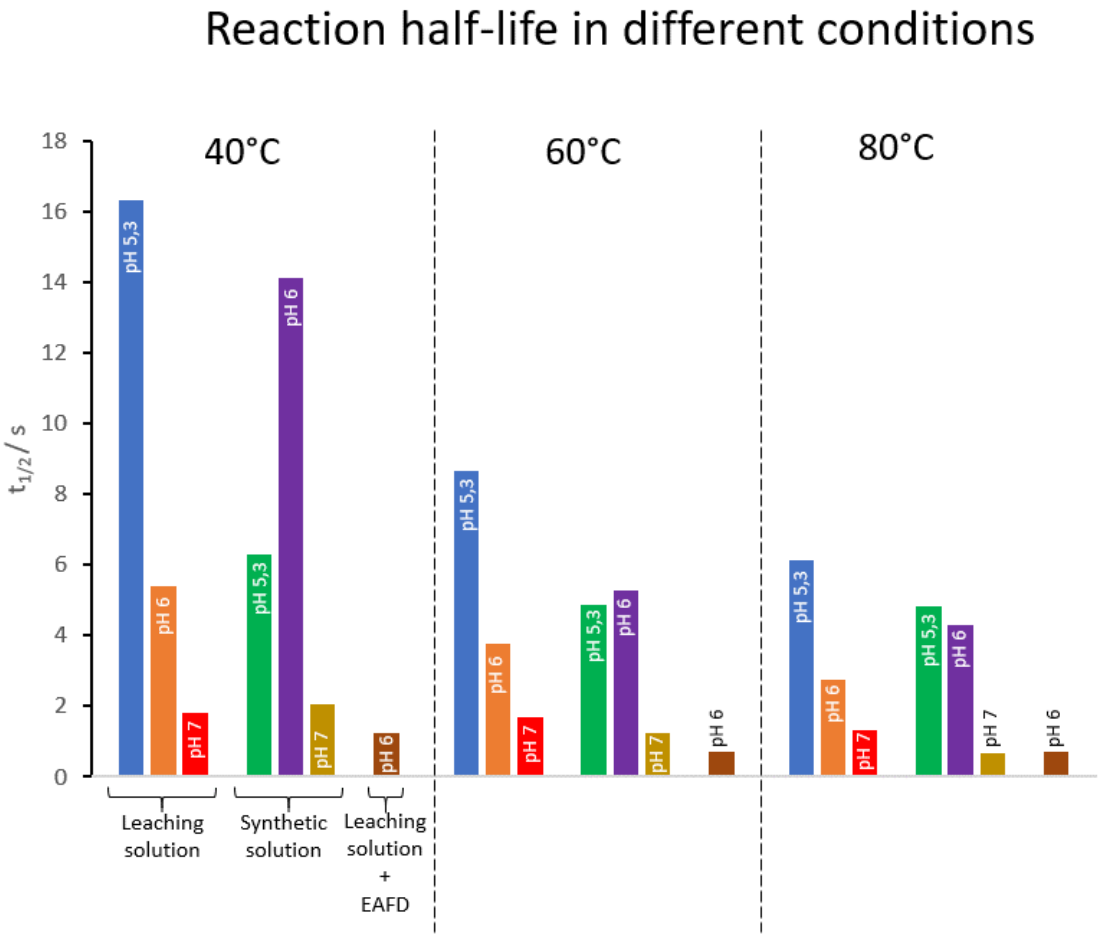

Figure 106: permanganate reaction half-life in different conditions.

	pH	T / °C	k / s^{-1}	$t_{1/2}$ / s
Leaching solution	5,3	40	0,04	16,35
		60	0,08	8,65
		80	0,11	6,16
	6	40	0,13	5,42
		60	0,18	3,76
		80	0,25	2,73
	7	40	0,38	1,81
		60	0,41	1,67
		80	0,52	1,33
Synthetic solution	5,3	40	0,11	6,28
		60	0,14	4,87
		80	0,14	4,82
	6	40	0,05	14,15
		60	0,13	5,29
		80	0,16	4,31
	7	40	0,34	2,06
		60	0,55	1,26
		80	1,04	0,66
Leaching solution + EAFD	6	40	0,55	1,25
		60	0,96	0,72
		80	0,97	0,71
Water +EAFD	6	40	0,007	105,02
		60	0,011	63,01
		80	0,029	23,98

Table 9: Permanganate reaction: kinetic constants and reaction half-life in different conditions.

Conclusions

The reaction of permanganate under different conditions, such as temperature, pH, and different nature of solution, was studied from a kinetic point of view. From what was obtained experimentally, the oxidation of ammonia by permanganate is a slow reaction compared to the comproportionation reaction of Mn^{2+} and permanganate.

The kinetics of both reactions were found to be faster with increasing pH and temperature. In addition, an increase in reaction kinetics was observed in the presence of unleached EAFD indicating a reaction between the powder and the oxidant resulting in increased permanganate consumption.

According to the data collected, the oxidation of ammonia by permanganate is too slow to be a problem from a consumption standpoint for the demanganization reaction. However, if wash water, which contains ammonia, is used to prepare the concentrated permanganate solution, a waste of permanganate is inevitable and should be considered.

While the above reaction can be considered irrelevant during the demanganization reaction, the presence of unleached EAFD should not. Therefore, from a chemical consumption point of view, the demanganization reaction should be done in a separate reactor after filtration of the leached EAFD.

Also, due to the fast kinetics, the demanganization reaction could be done directly in a solution stream avoiding the need for a dedicated reactor.

Appendix 6 – Manganese oxide particle size distribution

Secondary sources of zinc contain manganese that, in ammonium chloride solutions, is leached out and can be found in concentrations ranging from a few ppm up to 50 ppm.
Manganese, in the form of Mn^{2+}, is a problem for the electrolysis process and should be removed. The demanganization method relies on the comproportionation reaction that occurs between permanganate, Mn^{7+}, and Mn^{2+} to produce a precipitate that can be removed by liquid-solid separation techniques.
The experimentation reported here is intended to evaluate the particle size distribution of the precipitated manganese oxide obtained under different conditions.
Such data could be useful in selecting the most appropriate liquid-solid separation method.

Experimental part

The particle size distribution was evaluated using the static light scattering technique, Figure 107, the apparatus used was equipped with a centrifugal pump to keep the dispersed solid in suspension. The pump rpm was kept constant throughout the experiment (2000 rpm).

Two different solutions were analyzed:

Synthetic solution: 250 g/L NH_4Cl + 50 ppm Mn from $MnCl_2$

Filtered Leaching solution: 250 g/L NH_4Cl + 50 g/L EAFD, leaching time 1 hour.

For each measurement, 300 ml of the prepared solution was heated to the desired temperature and the pH was adjusted with NH_4OH or HCL. When the desired temperature and pH conditions were reached, 1 ml of 0.02 M $KMnO_4$ was added under stirring, and the resulting heterogeneous mixture was analyzed using the SLS technique.

Both synthetic and leach solutions were demanganized at 60/70/80 °C and pH 5.3/6/7.

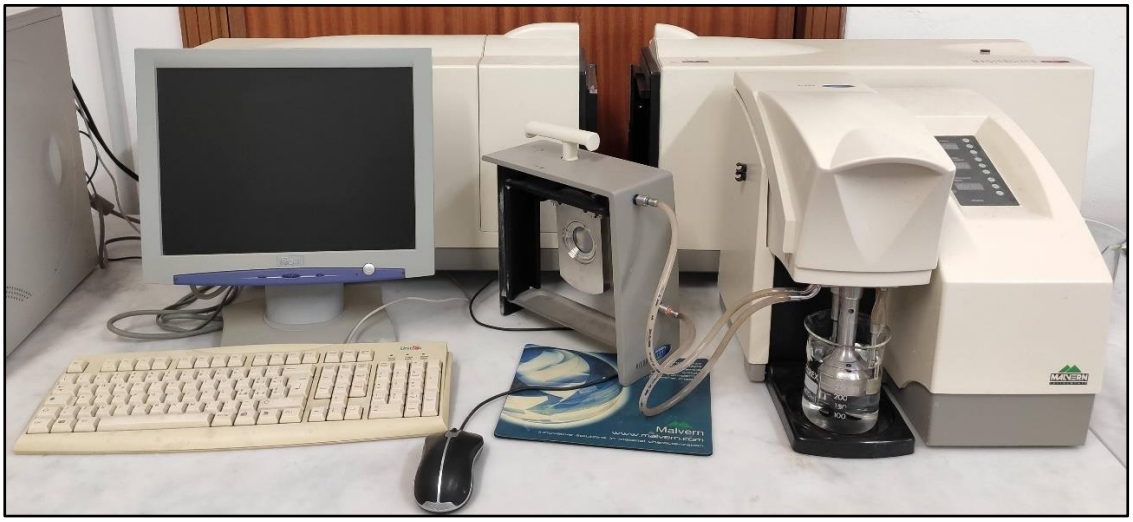

Figure 107: Static light scattering apparatus.

Results

Synthetic solution

Particle size distributions obtained from SLS analysis on synthetic solutions are shown below. At 60°C, the influence of pH is evident; as it decreases, the average particle size decreases from 25 µm at pH 7 to 2.5 µm at pH 5.3. This effect tends to be less pronounced as temperature increases; at 80°C, the average particle size distribution varies from 8 to 20 µm.

Synthetic solution 60°C

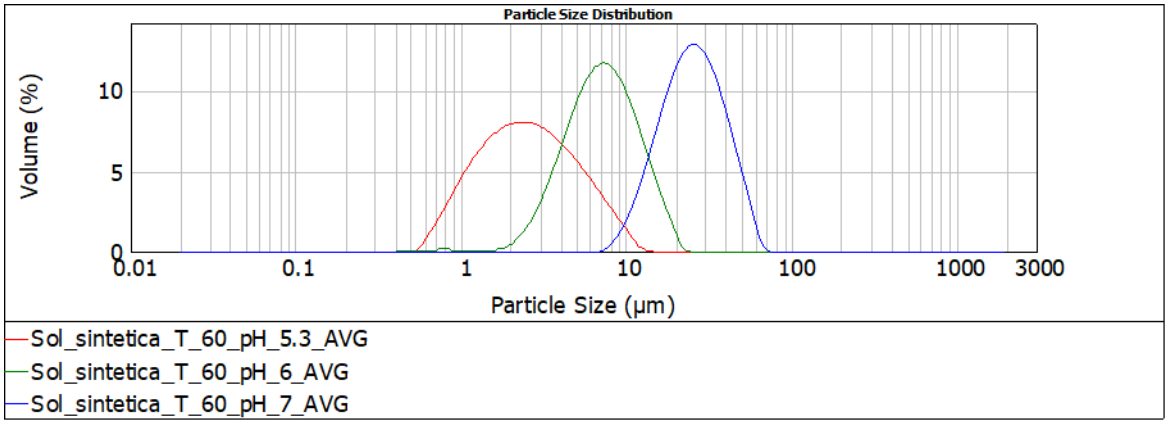

Synthetic solution 70°C

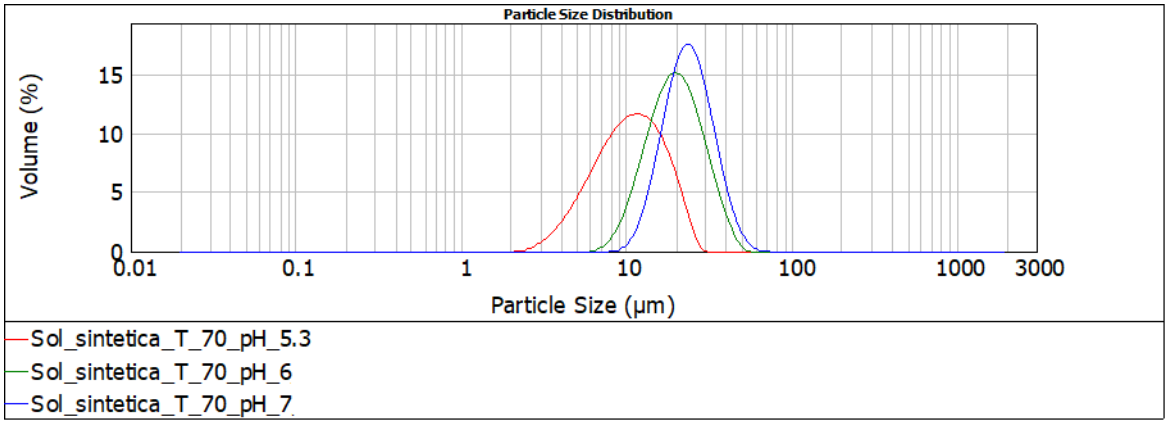

Synthetic solution 80°C

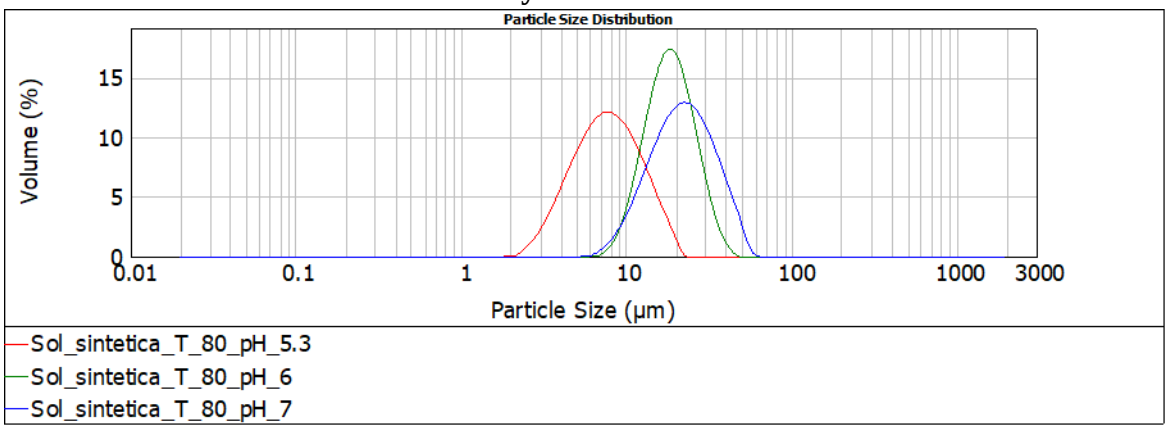

Leaching solution

The particle size distributions obtained from the SLS analysis on the leaching solutions are shown below. Compared to what was observed on the synthetic solutions, the peaks of the particle size distribution are narrower, this means that the particle sizes are more homogeneous. In addition, the influence of pH is less pronounced and as the temperature increases, the peaks tend to overlap. At the lowest pH and temperature, 5.3 and 60°C, an average particle size distribution of 6 µm was observed, while at all other conditions it increased to 15 µm.

Leaching solution 60°C

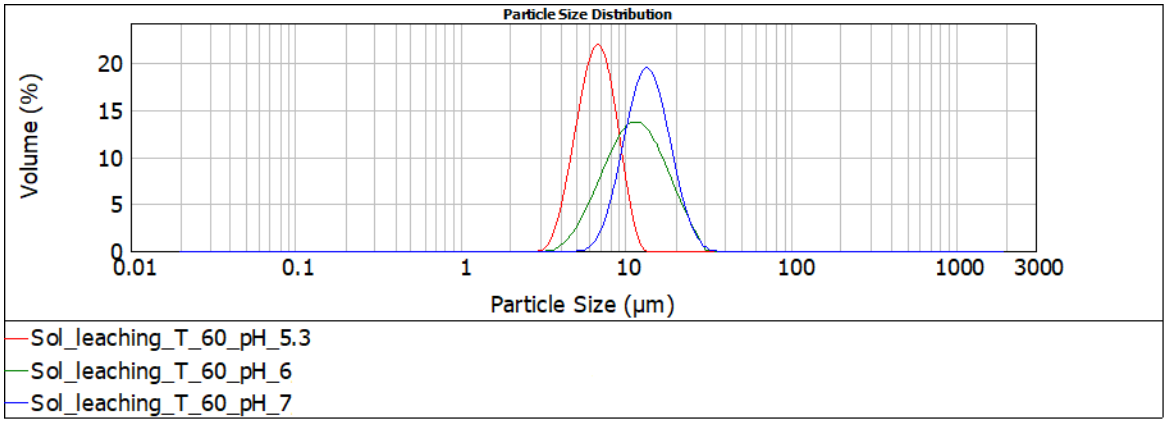

Leaching solution 70°C

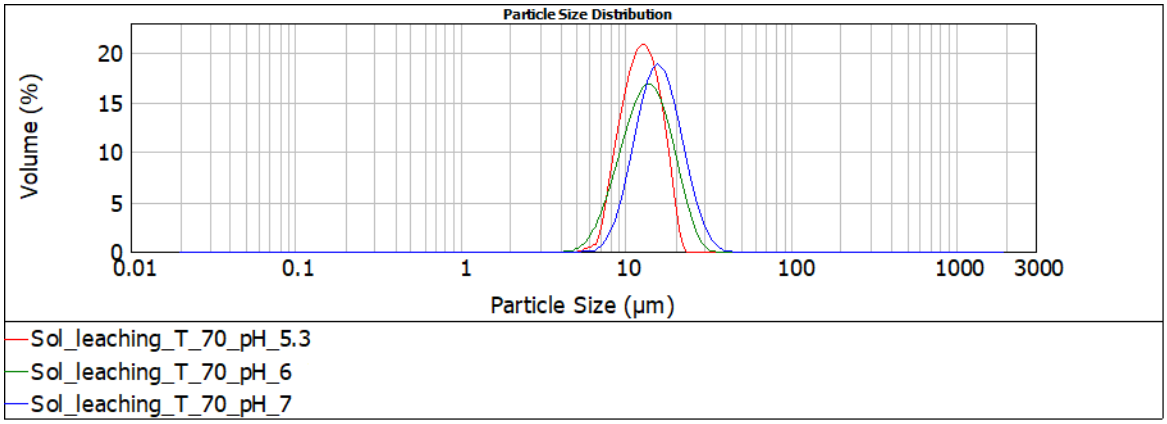

Leaching solution 80°C

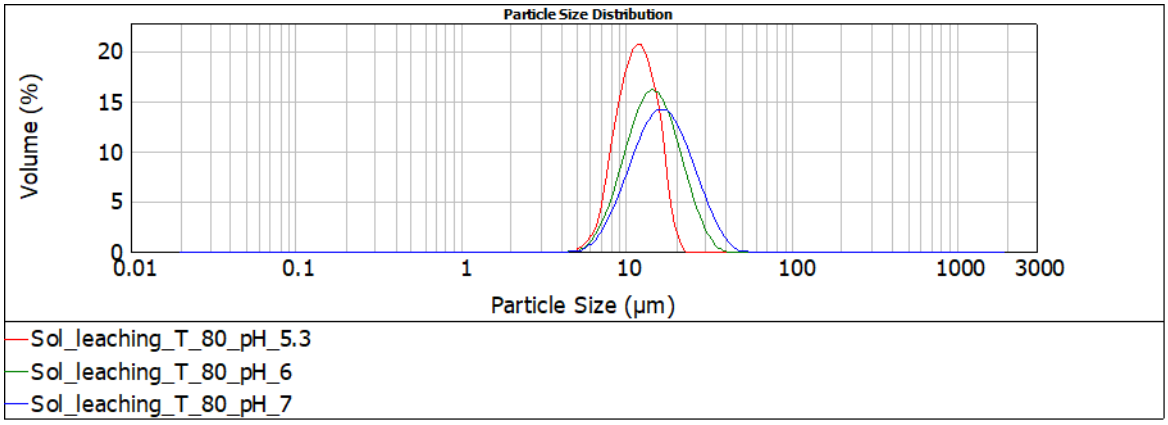

Influence of temperature – synthetic solution

To highlight the influence of temperature, the obtained particle size distributions were grouped as a function of pH. Looking at the graphs below, the differences on the particle size distribution tend to disappear with increasing pH, leading to an overlap of the distribution curves at pH 7 with an average particle size of 25 µm.

Synthetic solution pH 5.3

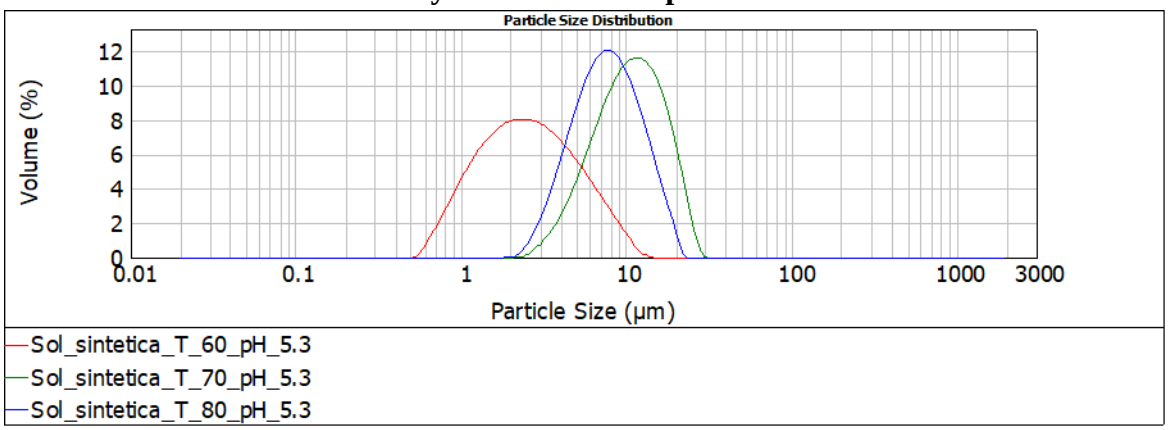

Synthetic solution pH 6

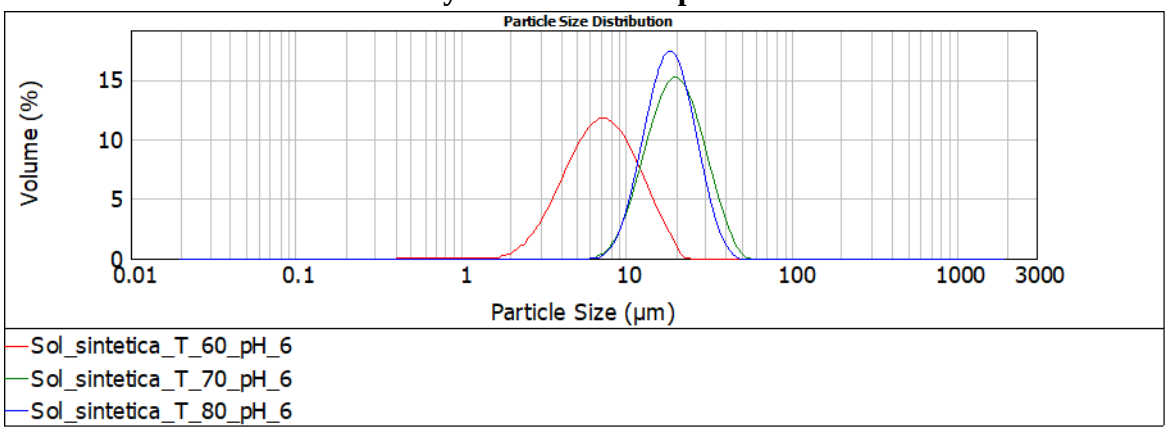

Synthetic solution pH 7

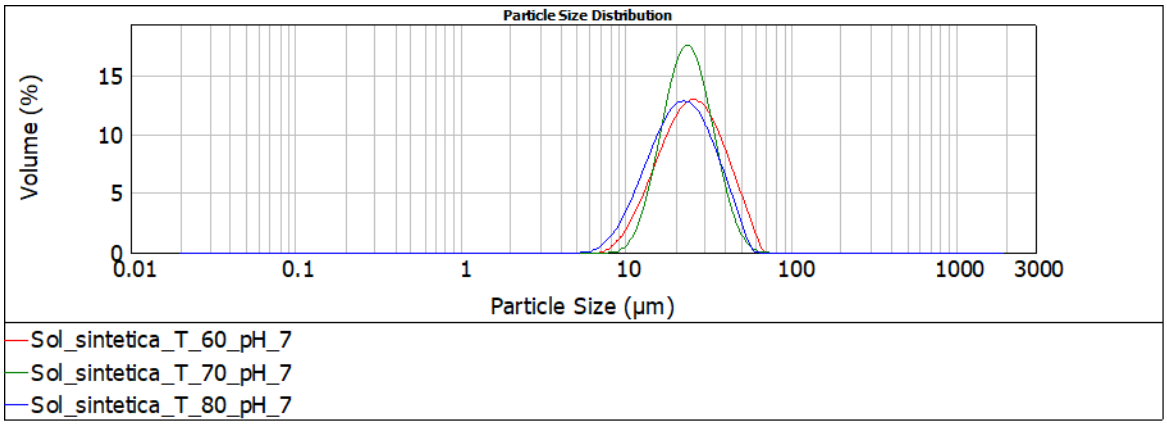

Influence of temperature – leaching solution

The data obtained on the demanganized leach solution were grouped as a function of pH to highlight the influence of temperature. The graphs below show closely overlapping distribution peaks except for the one obtained at lower pH and temperature. On average, the particle size was found to be 15 µm.

Leaching solutions pH 5.3

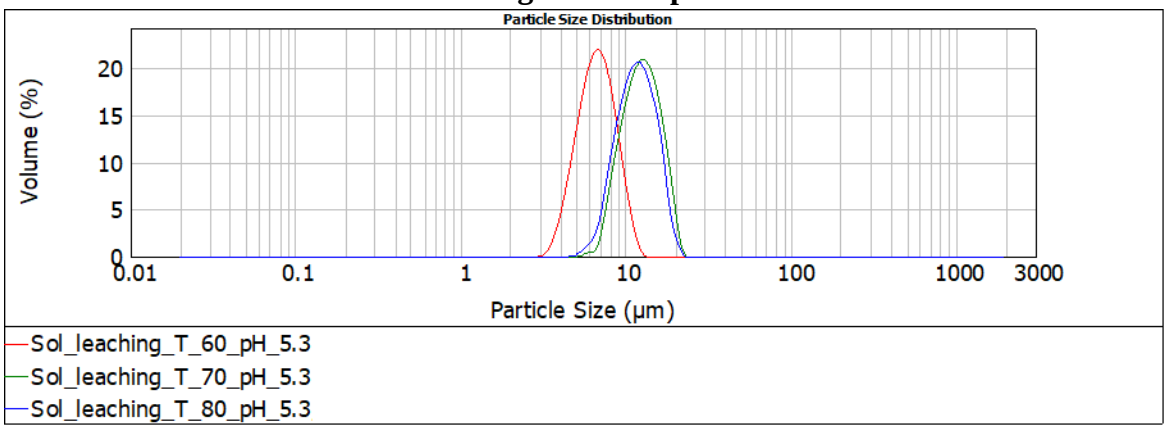

Leaching solutions pH 6

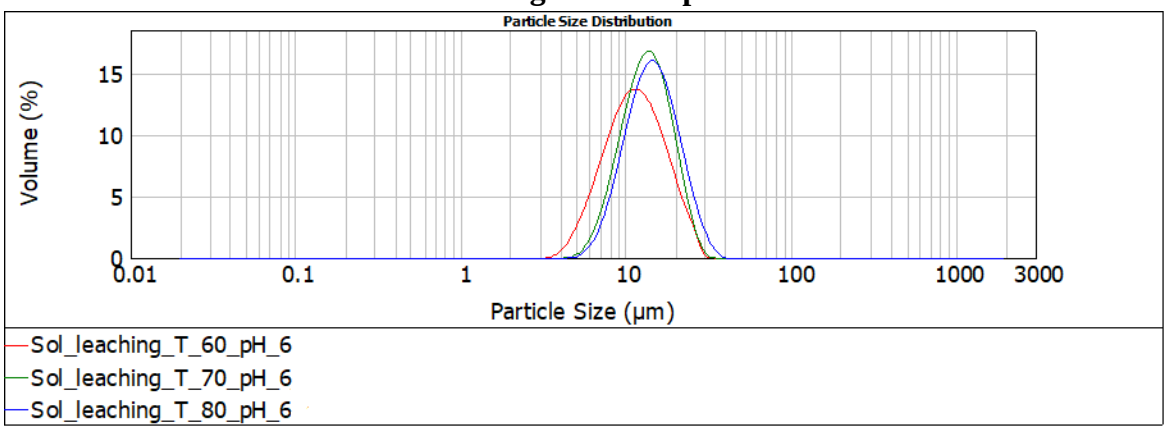

Leaching solutions pH 7

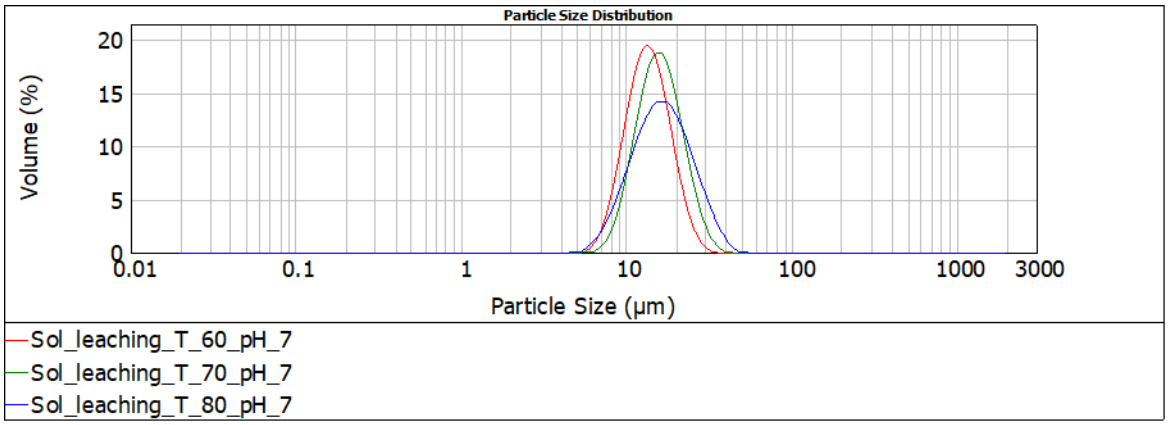

Observations

It should be noted that the SLS apparatus was equipped with a centrifugal pump, which may have broken up the aggregate particles.

Conclusions

Particle size distribution analysis was done on synthetic and leaching demanganized solutions using static light scattering technique. The influence of temperature and pH was evaluated in the intervals 60-80°C and 5.3-7 pH values. The results obtained show little difference between the two solutions. Regarding leaching solution, when the demanganization reaction is conducted at 60°C, pH seems to influence the particle size distribution by producing particles that increase in size as pH increases, from 6 µm to 13 µm. When this process is conducted at a higher temperature, the influence of pH is no longer evident, and the average precipitate size produced is 15 µm. The experimentally obtained data can be used as a starting point for choosing the most suitable solid-liquid separation system.

Appendix 7 – Manganese oxide formula determination

The secondary source of zinc treated with EZINEX® technology usually contains manganese that is solubilized as Mn^{2+} in the process solution during the leaching step.

Manganese removal in the EZINEX® system is accomplished by the addition of permanganate, the solubilized manganese is oxidized by permanganate to give manganese oxide which is removed by a filtration process. It is known that permanganate and manganese cations undergo a disproportionation reaction but, in the complex matrix of the EZINEX® solution, the precipitate formula is unknown.

Experimental part

The manganese precipitate, the unknown oxide, was obtained by addition of potassium permanganate to two different solutions containing Mn (II). One was a synthetic ammonium chloride solution 250 g/L with 100 ppm Mn (II), while the other was a real filtered EAFD leaching solution (NH_4Cl 250 g/L and 50 g/L EAFD, leaching time 1h). The reaction was done at 70 C° in both cases, the demanganization end point was determined using the E_{redox}-pH equation and a redox electrode. The obtained manganese oxide was then filtered, washed with hot distilled water, and dried at room temperature.

The two different samples were analyzed by EDX and XPS techniques.

For XPS analysis, the two samples were prepared by drop casting technique using titanium as substrate and acetone as dispersion medium.

Titrations were conducted on both the leach and synthetic solutions, at 60°C and pH 5.5, with a 0.02 M $KMnO_4$ standard solution until the specific redox set point was reached.

In addition, samples of the leaching and synthetic solutions were titrated with KMnO4 to determine the $KMnO^4/Mn^{2+}$ molar ratio.

Results

X-Ray diffraction analysis (XRD)

Manganese oxide obtained from synthetic and leaching solutions was analyzed by X-ray diffraction technique. Figure 108 shows the obtained XRD pattern. Both oxides were amorphous, and the resulting spectra have poor resolution. According to the available database, the most likely manganese oxide is $HMnO_2$.

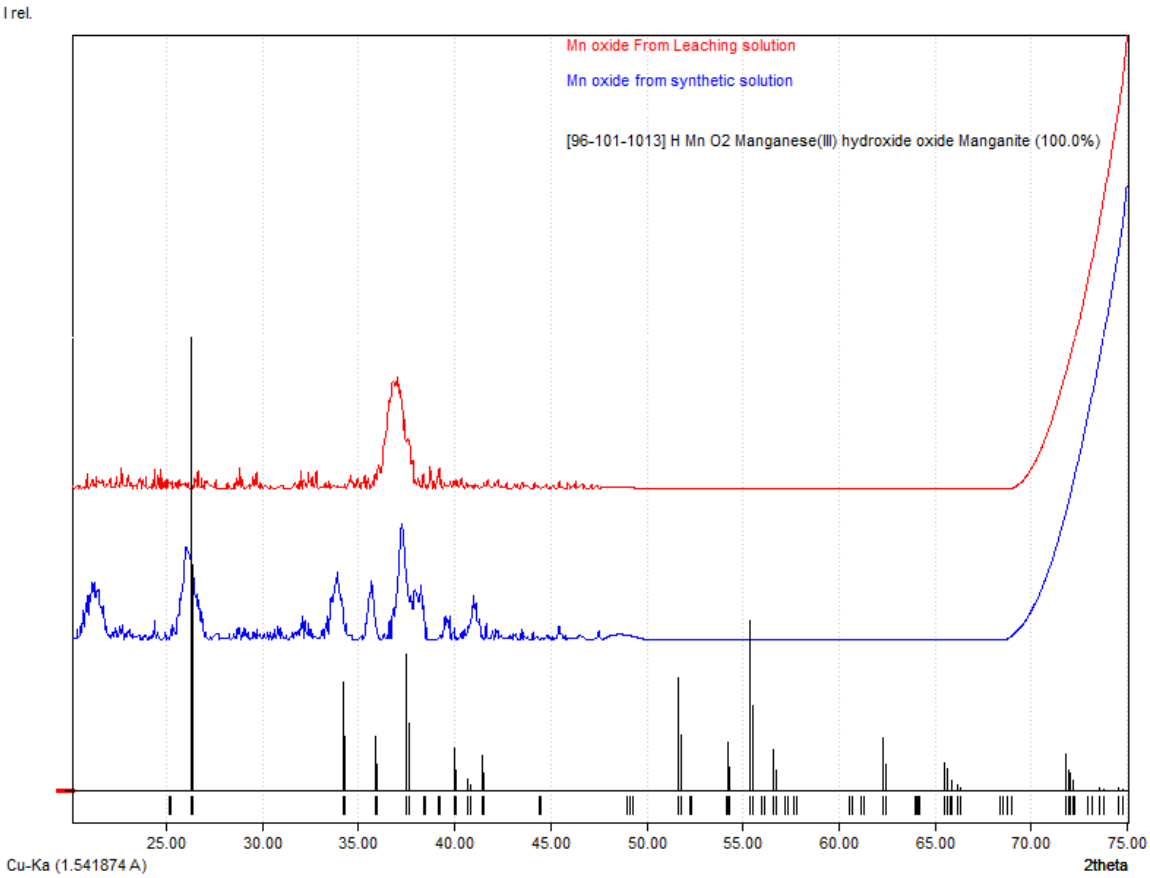

Figure 108: XRD pattern of manganese oxide obtained from synthetic and leaching solutions.

X-Ray photoelectron spectroscopy (XPS)

The XPS survey spectra are shown in Figure 109. Oxygen and manganese signals were detected in both spectra; zinc-related signals are present in the sample obtained from the leaching solution. The oxidation state of manganese can be distinguished using the Mn 3s peak; the splitted Mn 3s peak is caused by the coupling of the non-ionized 3s electron with the 3d valence band electrons. The width of the split is diagnostic of the oxidation state of Mn[39,40]

Figure 110 shows high resolution spectra of the Mn 3s peak, the difference between the

two splitted peaks is in both cases close to the value of 5.4 eV, this is diagnostic of the Mn (III) species. The sample obtained from the leaching solution shows a central peak superimposed on a system of two peaks, this is attributed to the presence of zinc which interferes with the identification of manganese.

The peak O 1s can be decomposed into three components 529, 530 and 531 eV, these are related respectively to the bonds Mn-O-Mn, Mn-OH and H-O-H; the change in the relative intensity of the Mn-O-Mn and Mn-OH signals indicates the change in the oxidation state of manganese[41]. The formula is given by Equation 13**.** The average oxidation state of Mn results in 3.02 for the synthetic sample and 3.01 for the leaching sample.

$$Oxidation\ state = \frac{[(4 * (MnOMn - MnOH)) + (3 * MnOH)]}{MnOMn}$$

Equation 13: Manganese average oxidation state, MnOMn and MnOH are expressed in terms of kcps.

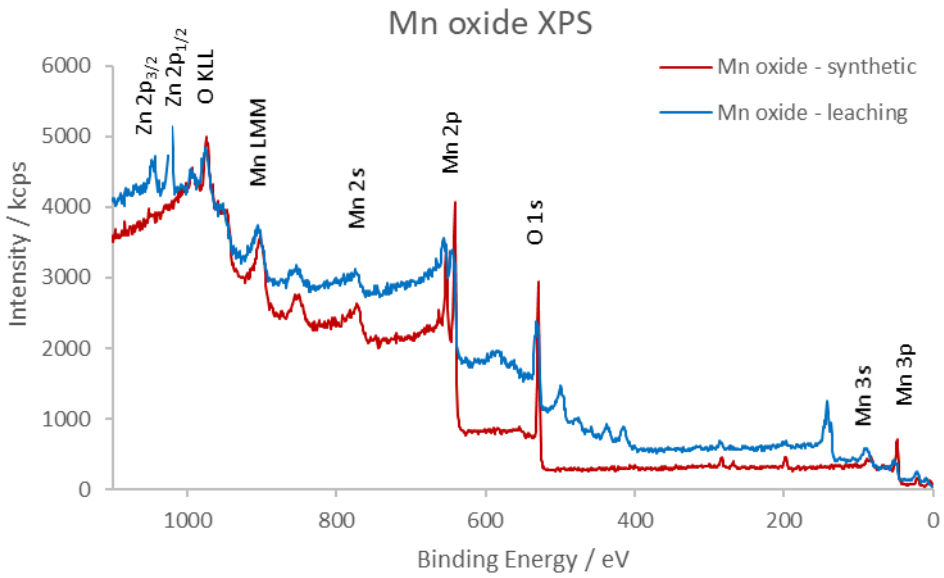

Figure 109: XPS survey spectra of Mn oxide obtained from synthetic and leaching solutions.

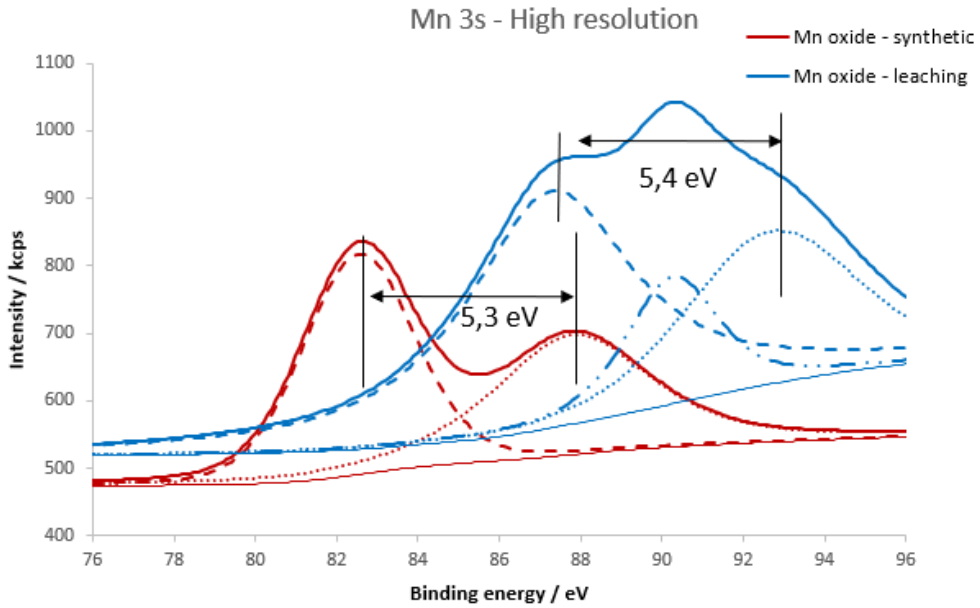

Figure 110: High resolution of Mn 3s peaks.

	At%	
	Mn oxide - synthetic	Mn oxide - leaching
C 1s	7,07	10,85
O 1s	61,98	59,52
Cl 2p	3,45	-
Mn $2p_{3/2}$	27,49	17,91
N 1s	-	1,53
Zn $2p_{3/2}$	-	10,19

Table 10: Elements Atomic percentage obtained from XPS analysis.

Potentiometric titrations

Samples of the two solutions were titrated with $KMnO_4$ until a specific redox value was reached. The results obtained are reported in Table 11. These suggest a 1:1 $KMnO_4/Mn^{2+}$ reaction and show an increase in permanganate consumption when demanganizing the leaching solution. This suggests that other species react with permanganate besides ammonia and Mn^{2+}, and these species come from EAFD leaching. Equation 14 can be used to determine the number of electrons gained by Mn^{7+} or loss by Mn^{2+}, this turns out to be, on average, 2.43; final oxidation state of manganese found to be about 4.5. These results are not in agreement with the stoichiometry of the hypnotized reaction; the final manganese oxide could be a mixture of several Mn compounds with various oxidation states. However, given the inconsistency of the results and the presence of secondary reactions, data obtained through XPS analysis are considered more reliable.

	Titration	Mn^{7+} / mol	Mn^{2+} / mol *	Mn^{7+}/ Mn^{2+} molar ratio	Exchanged electrons
Synthetic solution	1	2,00E-04	2,33E-04	0,86	2,31
	2	2,04E-04	2,33E-04	0,88	2,34
	3	2,08E-04	2,33E-04	0,89	2,36
Leaching solution	1'	2,00E-04	1,96E-04	1,02	2,52
	2'	1,96E-04	1,96E-04	1,00	2,50
	3'	1,98E-04	1,96E-04	1,01	2,51

Table 11: Potentiometric titrations: permanganate/manganese (II) molar ration and exchanged electrons.

$$x\left[\frac{mol\ e^-}{mol}\right] Mn^{2+}\,[mol] = (5-x)\left[\frac{mol\ e^-}{mol}\right] {MnO_4}^{2-}[mol]$$

Equation 14: number of electrons exchanged: lost/acquired by manganese (II)/(VII).

Conclusions

The products of the demanganization reaction obtained from two different solutions were analyzed by XRD and XPS technique. The results obtained from XRD analysis are of poor quality due to the amorphous characteristics of the samples, the most probable compound found is $HMnO_2$. The XPS analysis was able to discriminate the different oxidation states of manganese, the ΔeV of splitted Mn 3s reveals the presence of Mn (III). The average oxidation state of manganese, calculated with intensities relative to Mn-O bonds, is 3.

Potentiometric titration shows increased permanganate consumption when the demanganization reaction takes place in an EAFD leaching solution, suggesting the presence of side reactions, in addition to ammonia oxidation that is negligible considering the time scale in which the titration was done.

Considering the above, the manganese oxide produced by demanganization is a mixture of different species, the most likely compounds being Mn_2O_3 and $HMnO_2$.

Appendix 8 – Kinetics of cementation reactions

The following study aims to evaluate the influence of temperature on the cementation kinetics of the main interfering metal cations present in EZINEX® solutions.

Experimental setup

Cementation tests were conducted using the experimental apparatus shown in Figure 111. Zinc metal pellets were placed on a perforated polypropylene support, stirring by means of a magnetic stirrer (4 cm) was kept constants for all the tests performed (700 rpm). The solutions were thermostated at different temperatures (40, 60 and 80°C) by means of a heating plate equipped with a temperature probe.

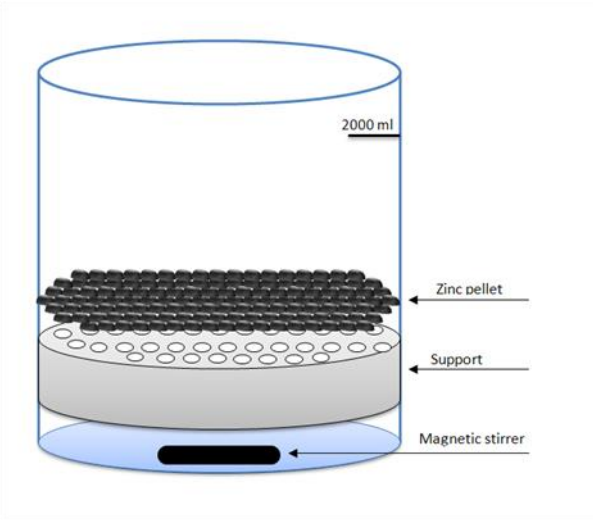

Figure 111: Cementation reactor.

The same amount of metallic zinc (0.15 kg) was used for all tests. At the end of each test, the zinc pellets were washed with water to remove the cements formed.

Typical EZINEX® solutions having the following average composition were used:

NH_4Cl	250 g/L
Zn^{2+}	15 g/L
Ag^{+}	1-2 ppm
Cu^{2+}	20-25 ppm
Pb^{2+}	400-500 ppm

The pH was adjusted in the range of 6.5-7 by addition of a 50% NaOH aqueous solution.

Samples (10 ml) were taken at different reaction times and the concentrations of interfering metal cations were analyzed by atomic absorption spectroscopy.

The redox potential of the solution was also monitored during the tests using an ORP electrode (Ag/AgCl ref).

Results

Tests were conducted at three different temperatures: 40, 60 and 80°C.The three cementation reactions are found to obey first-order kinetics according to the following equations:

$$[M^{x+}] = [M^{x+}]_0 \cdot e^{-kt} \qquad ln[M^{x+}] = -kt + ln[M^{x+}]_0$$

k indicates the kinetic constant expressed in s^{-1}.

Figure 112 shows the results obtained and the extrapolated kinetic constants.

Figure 113 shows the Arrhenius plot constructed using the kinetic constants obtained (averaged) and the value of the activation energies of the three cementation reactions. The activation energy was derived from the slopes obtained via the Arrhenius plot according to the equation below:

$$\ln k = -\frac{E_a}{RT} + \ln A$$

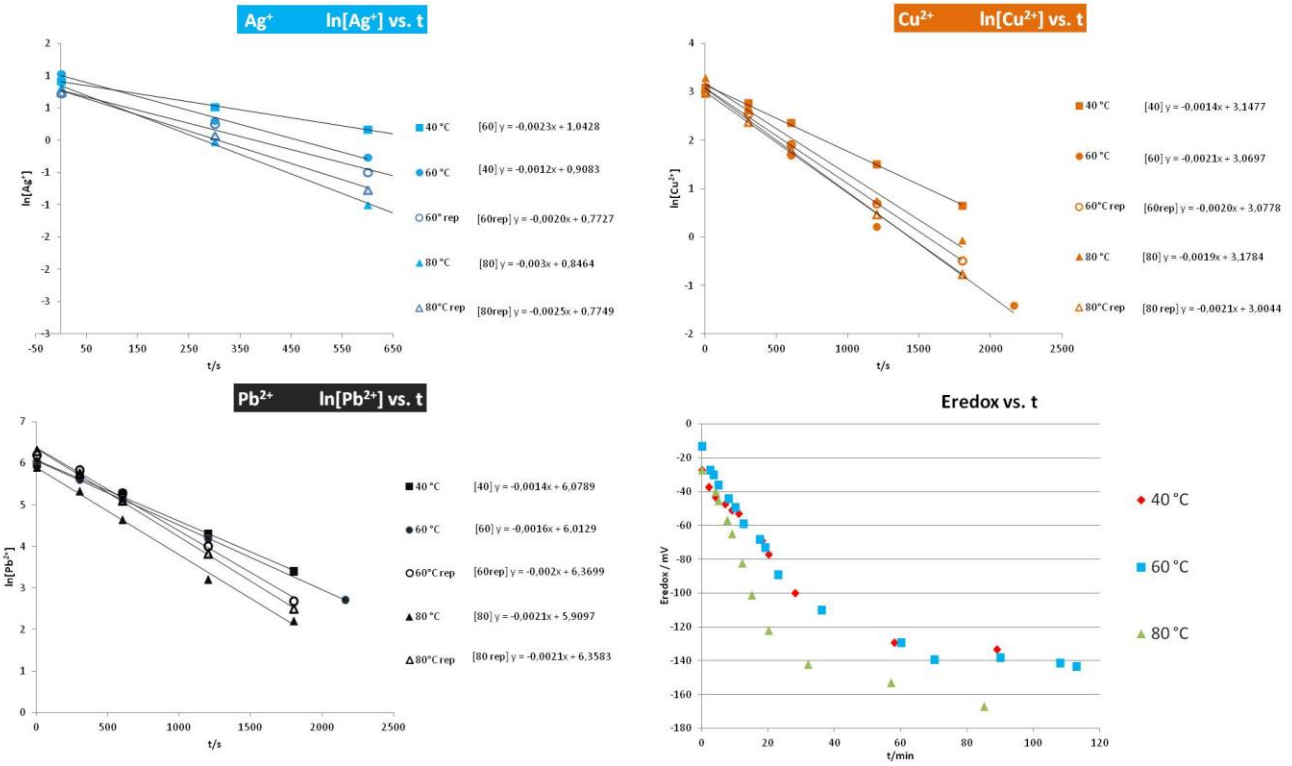

Figure 112: Trend of the concentration of different metal cations as a function of reaction time at different temperatures. Development of redox potential at different temperatures.

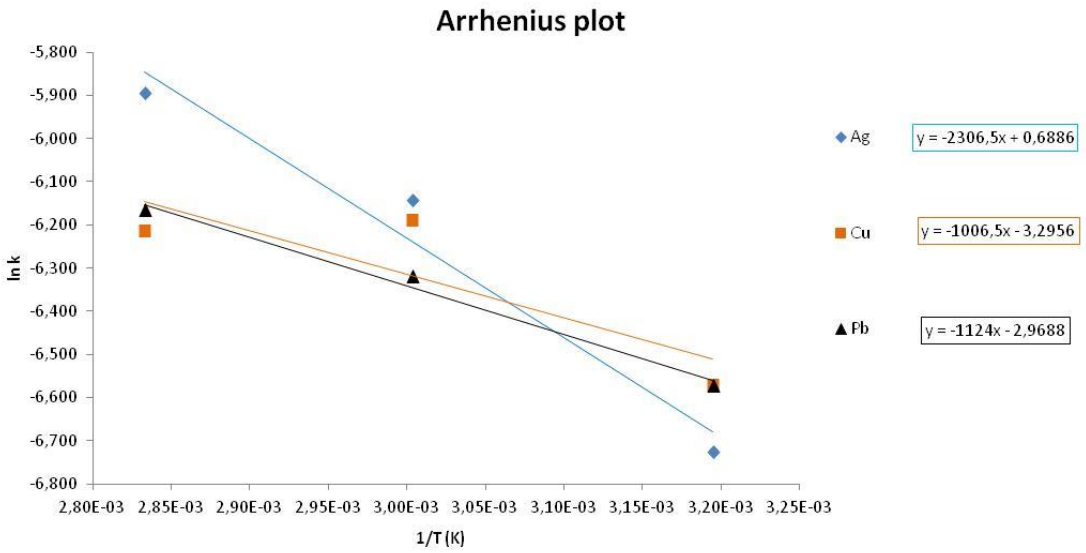

	$Ag^{+}+e^{-}\rightarrow Ag^{0}$	$Cu^{2+}+2e^{-}\rightarrow Cu^{0}$	$Pb^{2+}+2e^{-}\rightarrow Pb^{0}$
Ea (kj/mol)	19.17	8.36	9.34

Figure 113: Arrhenius plot and activation energies.

According to peters[35], activation energies lower than 10 kJ/mol, for cementation reactions, are to be attributed to processes under diffusive control while Ea > 40 kJ/mol are typical of reactions under chemical/electrochemical control.

To reduce the limiting factor, diffusion, and more appropriately evaluate the influence of temperature on the process under investigation, further cementation tests were performed by stirring the solution with a paddle shaker and placing the zinc pellets on the bottom. An additional element, cadmium, was also added to get a more complete view of the cementation kinetics of EZINEX® solutions.

Figure 114 shows the results obtained and the extrapolated kinetic constants. Figure 115 shows the Arrhenius graph and the activation energies obtained

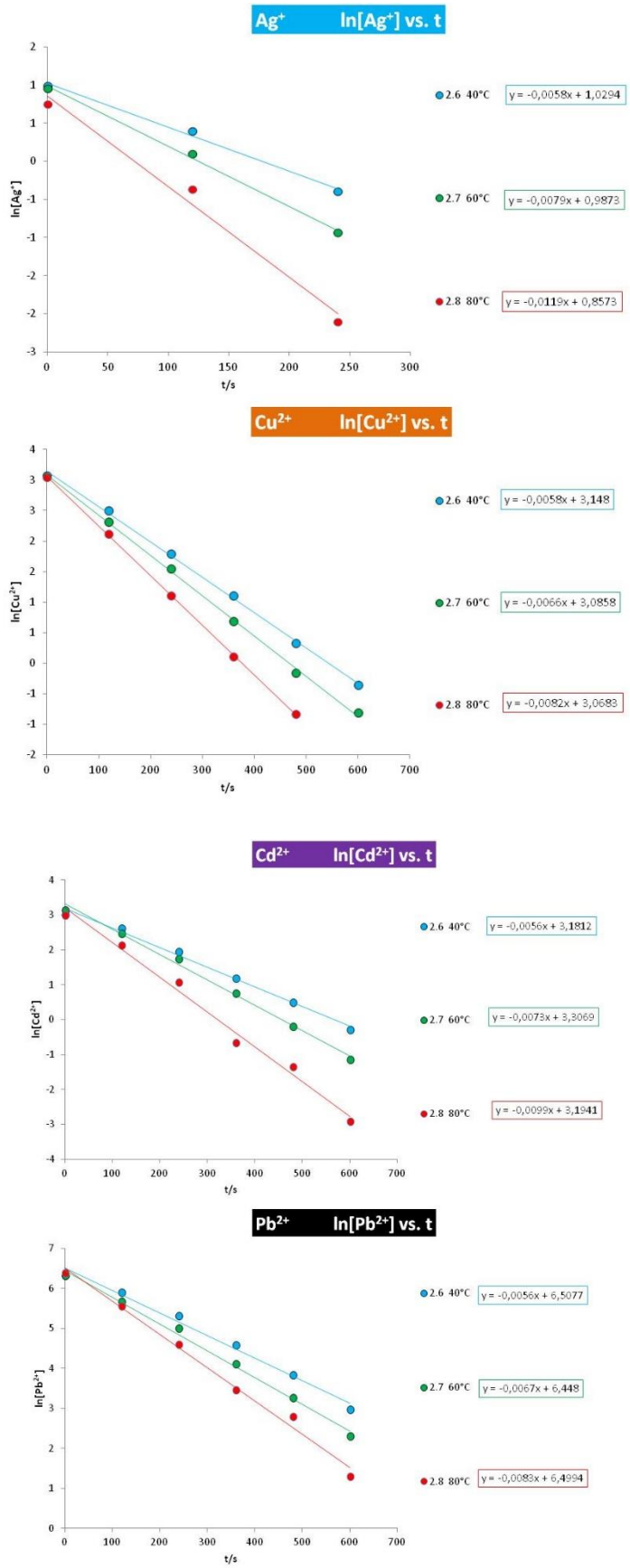

Figure 114: Trend of the metal cations concentration as a function of reaction time at different temperatures.

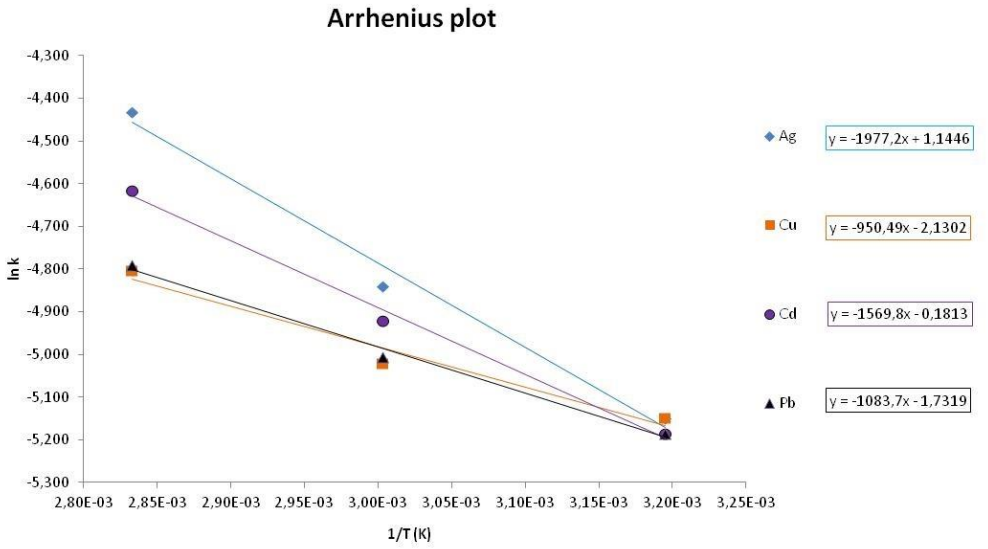

	$Ag^{+}+e^{-}\rightarrow Ag^{0}$	$Cu^{2+}+2e^{-}\rightarrow Cu^{0}$	$Cd^{2+}+2e^{-}\rightarrow Cd^{0}$	$Pb^{2+}+2e^{-}\rightarrow Pb^{0}$
Ea (kj/mol)	16.44	6.78	13.04	9.004

Figure 115: Arrhenius plot and activation energies.

Despite the improved hydrodynamics of the system, the activation energies obtained indicate that, except for silver reduction, the reactions under investigation are still under diffusive control.

Conclusions

From the analysis of the data obtained, the kinetic constant related to the reduction reaction of silver, copper, lead, and cadmium appears to be proportional to temperature. From the activation energies obtained from the first test, the cementation reactions appear to be under diffusive control. Even under vigorous stirring, the second testing methodology, the activation energies indicate that the processes remain under diffusive control, except for the silver reduction. Thus, it can be concluded that the cementation reactions under study proceed very rapidly, and that diffusion plays a determining role.

The rate of purification of EZINEX® solutions from silver, copper, lead, and cadmium is therefore temperature dependent and strongly influenced by the hydrodynamics of the system.

Appendix 9 – Cementation through rotary reactor

This study was performed with the purpose of verifying the feasibility of the cementation of the EZINEX® solution using a rotating cylindrical reactor filled with zinc metal pellets.

From a previou study, it was found that the kinetics of cementation is limited by the diffusion of interfering species, the method in question aims to minimize the diffusive component to increase the efficiency of the cementation step. The cements formed on the surface of the zinc pellets inhibit the progress of the reaction, the rotary motion should allow the rubbing of the pellets renewing the surface. Very fine cements are expected to remain in suspension so that the flow of the solution can carry them out of the cylinder.

The experimental apparatus was tested under different conditions of flow rate, rpm, temperature, amount of zinc inside and the influence of these variables on the efficiency of cementation was evaluated.

Experimental part

The experimental apparatus used is shown in Figure 116; it was made of polypropylene with an internal grid placed between the small end cylinder and the body of the vessel. Inside the cylinder, two baffles were installed to ensure dragging and mixing of the zinc pellets.

The reactor was placed in a thermostated chamber to prevent salts precipitations due to cooling of the solution.

The rotation speed was measured with a digital tachometer while the flow rate was controlled with a peristaltic pump. The inlet solution temperature was set to 60°C.

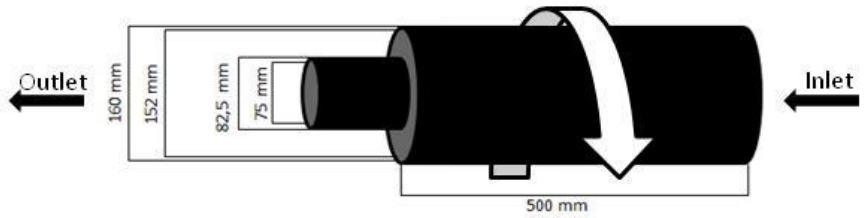

NH_4Cl	250 g/L
Zn^{2+}	15 g/L
Ag^{+}	1-2 ppm
Cu^{2+}	20-25 ppm
Pb^{2+}	400-500 ppm

Figure 116: Rotary cementation reactor and inlet solution composition.

All tests were performed using a solution volume of 5 L, the pH was adjusted in the range of 6.5-7 with the addition of 28% NH3 in aqueous solution. Solution composition is reported in the table above. The data reported in the results refer to analyses performed on the reactor output solutions; the metal cation content was analyzed by atomic absorption spectroscopy.

Results

Influence of rotary speed

Three different rotation speeds were tested: 30, 60 and 90 rpm. For all three tests, the solution flow rate and static load were kept constant (1.38 L/h and 2kg). Rsults are reported in Table 12 and Figure 117. Time zero refers to the instant when the solution begins to come out of the cylinder.

	sampling time (min)	inlet	0	2	5	10	20	30	60	90	120
30 rpm	Ag^{+} / ppm	1,59	0,00	0,00	0,00	0,00	0,00	0,00	0,00	0,00	0,00
	Cu^{2+}/ ppm	20,52	0,63	0,53	0,48	0,49	0,48	0,49	0,52	0,47	0,51
	Pb^{2+}/ ppm	461,40	9,73	7,90	7,14	7,01	7,31	7,43	7,26	6,95	6,81
60 rpm	sampling time (min)	inlet	0	2	5	10	20	30	60	90	120
	Ag^{+} / ppm	1,47	0,00	0,00	0,00	0,00	0,00	0,00	0,00	0,00	0,00
	Cu^{2+}/ ppm	20,20	0,39	0,36	0,36	0,35	0,37	0,31	0,30	0,30	0,30
	Pb^{2+}/ ppm	410,90	5,12	5,54	5,02	4,90	5,65	4,18	4,46	4,30	4,31
90 rpm	sampling time (min)	inlet	0	2	5	10	20	30	60	90	120
	Ag^{+} / ppm	1,54	0,00	0,00	0,00	0,00	0,00	0,00	0,00	0,00	0,00
	Cu^{2+}/ ppm	20,33	2,30	0,36	0,39	0,34	0,34	0,37	0,33	0,31	0,30
	Pb^{2+}/ ppm	393,60	24,30	5,34	5,05	4,68	4,74	4,87	4,39	4,21	3,90

Table 12: Influence of rotary speed: solution composition at different times.

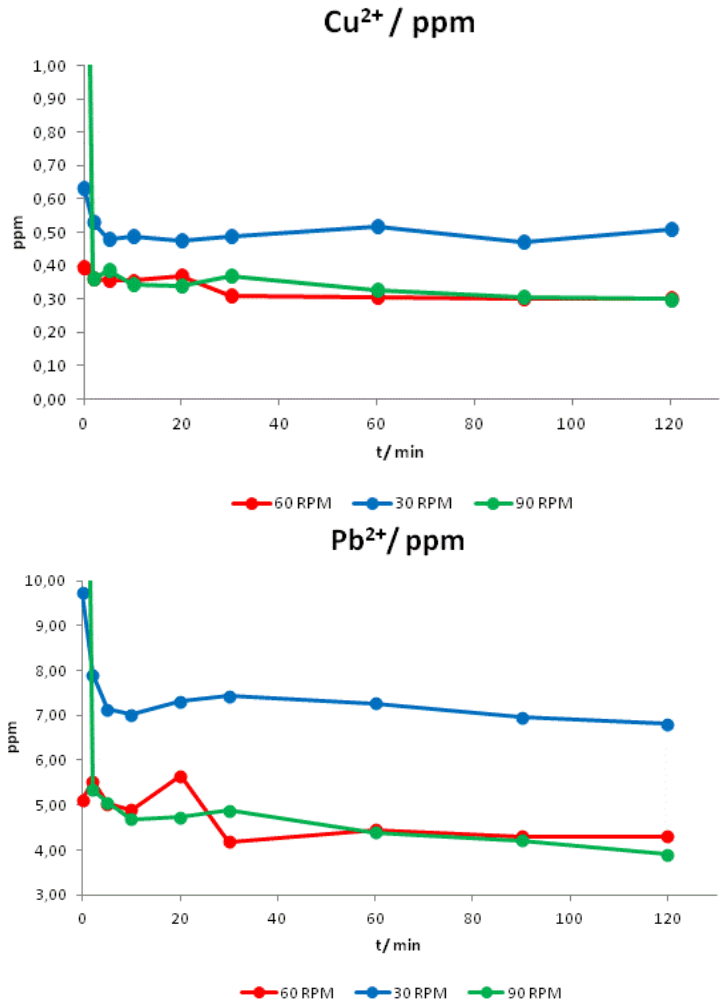

Figure 117: Influence of rotary speed: solution composition at different times.

Influence of flow rate

Two different solution flow rates were tested: 1.38 L/h and 5 L/h. For both tests, the rotational speed (30 rpm) and the static load of zinc (2 kg) were kept constant.

Table 13 and Figure 118 show the obtained results.

	sampling time (min)	inlet	0	2	5	10	20	30	40
5 L/h	Ag^{+} / ppm	0,00	0,00	0,00	0,00	0,00	0,00	0,00	0,00
	Cu^{2+}/ / ppm	18,51	0,70	0,60	0,59	0,54	0,46	0,45	0,45
	Pb^{2+} / ppm	364,00	11,27	10,69	9,93	8,51	7,72	6,59	6,52

	sampling time (min)	inlet	0	2	5	10	20	30	60	90	120
1,38 L/h	Ag^{+}/ ppm	1,59	0,00	0,00	0,00	0,00	0,00	0,00	0,00	0,00	0,00
	Cu^{2+}/ / ppm	20,52	0,63	0,53	0,48	0,49	0,48	0,49	0,52	0,47	0,51
	Pb^{2+}/ / ppm	461,40	9,73	7,90	7,14	7,01	7,31	7,43	7,26	6,95	6,81

Table 13: Influence of flow rate: solution composition at different times

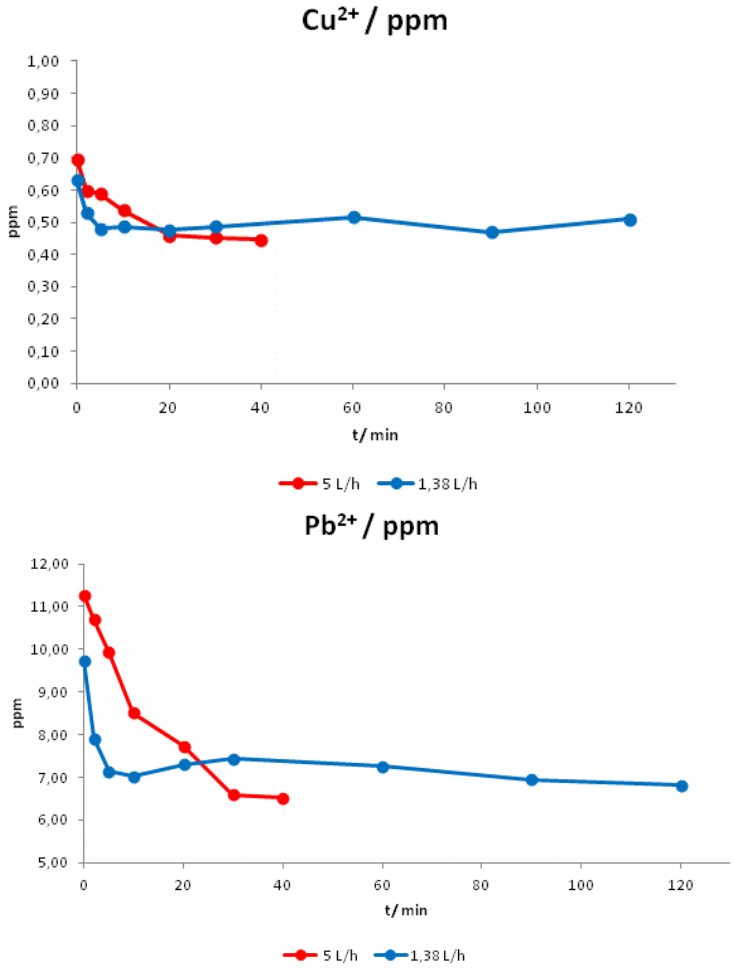

Figure 118: Influence of flow rate: solution composition at different times

Influence of the zinc static load

Three different static loads were tested: 2, 3 and 4 kg. For both tests, the rotational speed (30 RPM) and flow rate (1.38 L/h) were kept constant. Results in Figure 119 and Table 14.

2 kg (Zn)	sampling time (min)	inlet	0	2	5	10	20	30	60	90	120
	Ag^{+}/ ppm	1,54	0,00	0,00	0,00	0,00	0,00	0,00	0,00	0,00	0,00
	Cu^{2+}/ ppm	20,33	2,30	0,36	0,39	0,34	0,34	0,37	0,33	0,31	0,30
	Pb^{2+}/ ppm	393,60	24,30	5,34	5,05	4,68	4,74	4,87	4,39	4,21	3,90

3 kg (Zn)	sampling time (min)	inlet	0	2	5	10	20	30	60	90	120
	Ag^{+}/ ppm	1,39	0,00	0,00	0,00	0,00	0,00	0,00	0,00	0,00	0,00
	Cu^{2+} / ppm	17,62	0,39	0,29	0,32	0,28	0,28	0,27	0,27	0,27	0,28
	Pb^{2+}/ ppm	392,40	4,26	3,41	3,17	3,49	3,02	2,87	2,87	2,64	2,69

4 kg (Zn)	sampling time (min)	inlet	0	2	5	10	20	30	60	90	120
	Ag^{+}/ ppm	1,63	0,00	0,00	0,00	0,00	0,00	0,00	0,00	0,00	0,00
	Cu^{2+}/ ppm	22,39	0,37	0,31	0,30	0,29	0,25	0,24	0,21	0,25	0,23
	Pb^{2+}/ ppm	413,50	3,63	3,51	3,13	3,09	2,60	2,61	2,04	2,12	2,08

Table 14: Influence of the zinc static load: solution composition at different times

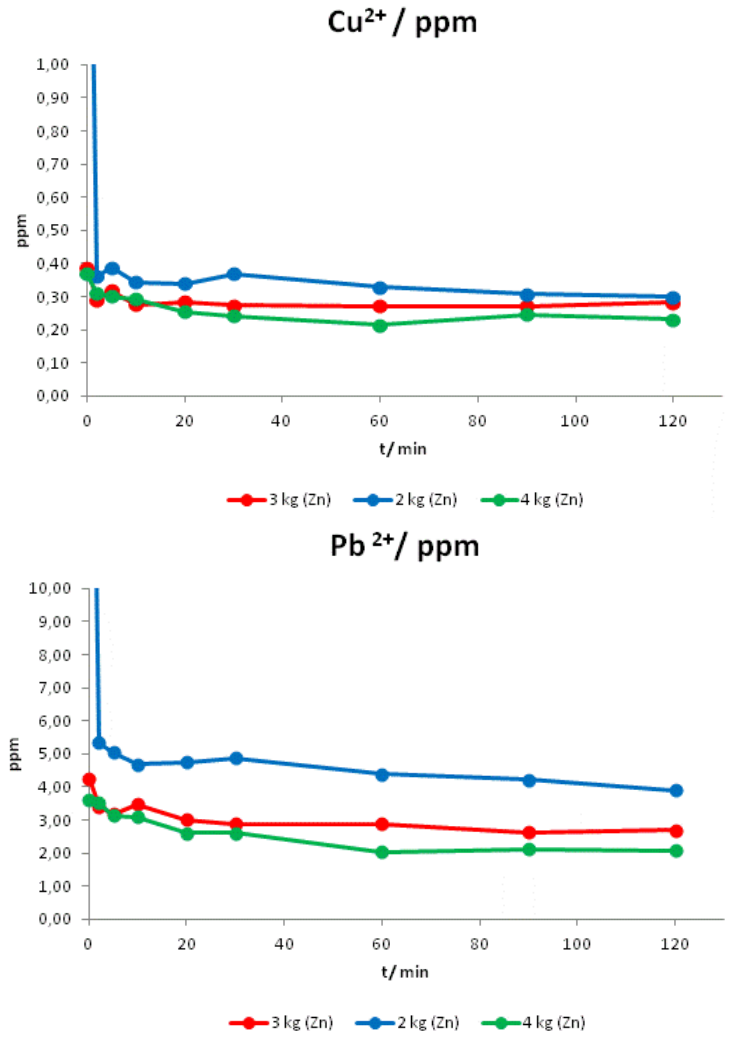

Figure 119: Influence of the zinc static load: solution composition at different times

Note

Additional tests were performed in the presence of cadmium, 25 ppm. These confirmed the results obtained previously and showed a Cd concentration of less than 1 ppm in the output solution.

Conclusions

In all tests performed, a rapid removal of interferents was observed within the first few minutes of testing. After this initial phase, concentrations reached stable values. This indicates that the reactor was able to maintain a stable condition throughout the duration of the test, however, the volumes available did not allow the realization of longer tests.

By analyzing the results and the influence of the variables, it can be concluded that although each of them has its influence, what still plays the key role is diffusion.

Increasing rotational speed, static load, and residence time lead to output solutions with fewer interferents. Removal of cements through the outlet solution could not be verified because of the small volume of treatable solution.

Appendix 10 – Manganese effect on activated titanium anodes

Activated titanium anodes are a viable substitute for graphite that is currently used in the EZINEX® process; they have the advantage of lowering the overpotential of the anodic reaction, occurring in the electrolysis cell, reducing energy consumption. However, such electrode material may suffer from the presence of manganese which, if present in solution, can be oxidized at the anode forming a solid manganese oxide. Due to the morphology of the catalytic coating (a mud-like structure), the formation of solid species can mechanically erode this layer, leading to deactivation of the electrode.

The experimentation in this report tries to evaluate the influence of manganese on the service life of activated titanium.

Typically, the service life of activated titanium electrodes (ATE) is evaluated by applying different current densities, usually higher than the designed operating current, and monitoring their potential over time. The electrode is considered deactivated when its potential begins to rise rapidly. The data collected, applied current density and lifetime, are used to extrapolate the service lifetime of the electrode at the designed operating current density.

This is a time-consuming experiment (several months) and should be evaluated by the anode manufacturer. As a preliminary indication, the experimentation reported here seeks to evaluate whether activated titanium anodes suffer from the presence of manganese during electrolysis.

Experimental part

Electrode preparation

From a sheet of ATE supplied by Chemical Newtech S.p.a., Ruthenium-based CNT 10A coating, small pieces were cut and welded onto a titanium bar. The catalytic coating was mechanically removed from one face of the electrode and Teflon tape was used to leave an active surface area of 1 cm2, Figure 120.

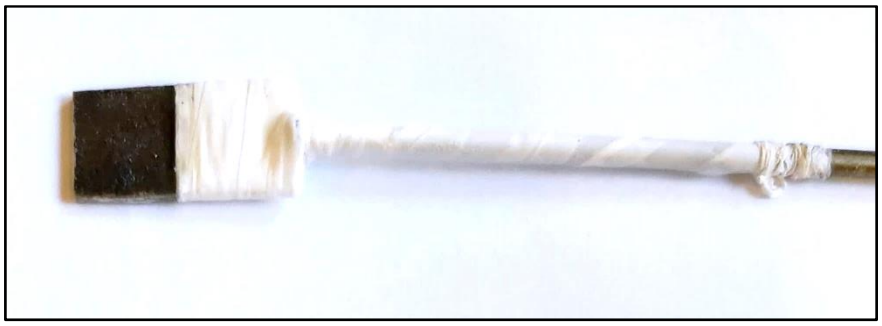

Figure 120: Activated titanium electrode prepared for tests

Experimental setup and analysis

Figure 121 shows the experimental setup; four electrochemical cells (1 L volume) were connected in series to a DC supplier, each cell was equipped with a magnetic stirrer and heated with a hot plate. Grade 1 titanium was used as the cathode and cells were covered with a PP cap with holes for electrode insertion to maintain a constant cell geometry. Two cells were filled with ammonium chloride 200 g/L while the other two were filled with ammonium chloride 200 g/L and 100 ppm of Mn^{2+}, from $MnCl_2$. To begin the experimentation, a current density of 1 kA/m^2 was applied. During electrolysis, the temperature was maintained at 60°C while the pH was kept in the range 5.3 - 6 with the addition of a 33% ammonia solution. Cell potentials were measured during the experiment until they increased rapidly, sign of electrode breakdown.

A 0-50 V, 0-1A DC power supply was used to apply the desired current density.

Since the pH had to be constantly monitored and adjusted, it was not possible to continue testing for more than 8 consecutive hours. The electrolysis was therefore stopped and restarted several times. For each stop and start, the current was increased, or decreased, gently to avoid false breaks due to sudden changes in current density.

SEM-EDX and XPS analyses were done to check electrode morphology and ruthenium content in order to collect as much information as possible.

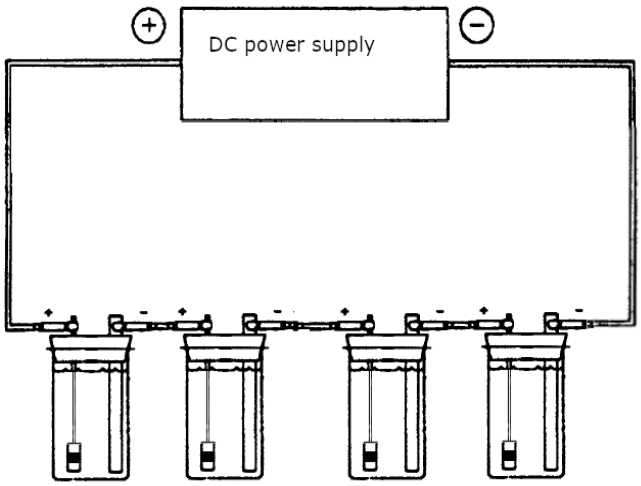

Figure 121: Galvanostatic test experimental setup

Results

Ammonium chloride solution containing manganese was initially transparent and turned brownish as electrolysis proceeded due to oxidation of Mn^{2+}, Figure 122. During the first few minutes of electrolysis, the formation of a fine brown powder was observed in the immediate vicinity of the anode electrode, Figure 123.

It is unclear if the powder was formed on the electrode surface and then mechanically detached due to the production of anodic gas or if it is a mediated reaction that occurs in solution after the production of oxidizing species at the anode.

Figure 124 shows the appearance of the solutions after 1 hour of electrolysis; in the absence of manganese the solutions remain transparent, turbidity is given by the presence of anodic gas, indicating that the brownish color is due to the presence of oxidized manganese.

Figure 125 reports cell potentials as a function of time: after 23 hours of electrolysis at $1kA/m^2$, the potential of cells with manganese begins to increase while the potential of cells without manganese remains constant. As the catalytic coating deactivates, sustaining the applied current density becomes more difficult for the electrode and the potential increases.

After 25 hours of electrolysis, the potential of one electrode began to increase, so the electrodes were removed from solution and visually inspected Figure 126. The NH_4Cl + Mn^{2+} electrode (A) appeared corroded at the edges, Figure 127, while the other electrodes, with a stable potential, were not visually altered.

Electrolysis was then continued in the Mn-containing cells until a potential 10 times higher than the initial potential was reached. At the end of the test, the solutions of the eroded electrodes were cloudy, probably due to the presence of TiO_2 dissolved from the anodes.

Activated titanium usually loses its catalytic activity due to the loss of the coating, but its substrate remains unaffected, in the form of passivated titanium. However, under the conditions tested, the electrodes lost their metal substrate, Figure 127 .

The results suggest that the activated titanium used for this experiment has a shorter lifetime in the presence of the amount of manganese used. However, such a short lifetime was not expected and another pair of samples was tested under the same manganese and pH conditions to confirm the results. This time, the non-activated titanium parts of the samples were covered with a lacquer coating, Figure 128.

Figure 129 shows the potential of the cells of the replicate test, the potential starts to increase after 20 hours of electrolysis confirming the results obtained with the previous experimentation. The lacquer coating used to protect the non-activated titanium was found to be unable to resist the oxidant species produced at the anode.

Figure 122: Ammonium chloride solution with manganese before electrolysis, A, and after 5, 15, 60 min, B, C, D.

Figure 123: Detail of titanium activated electrode during the first minutes of electrolysis in presence of manganese.

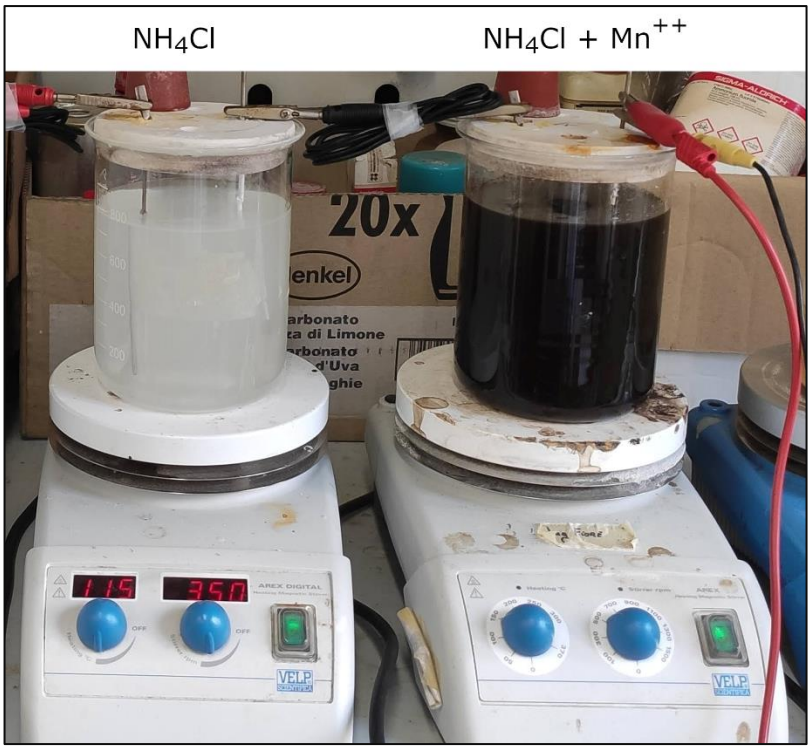

Figure 124: Solution appearance after 1 hour of electrolysis.

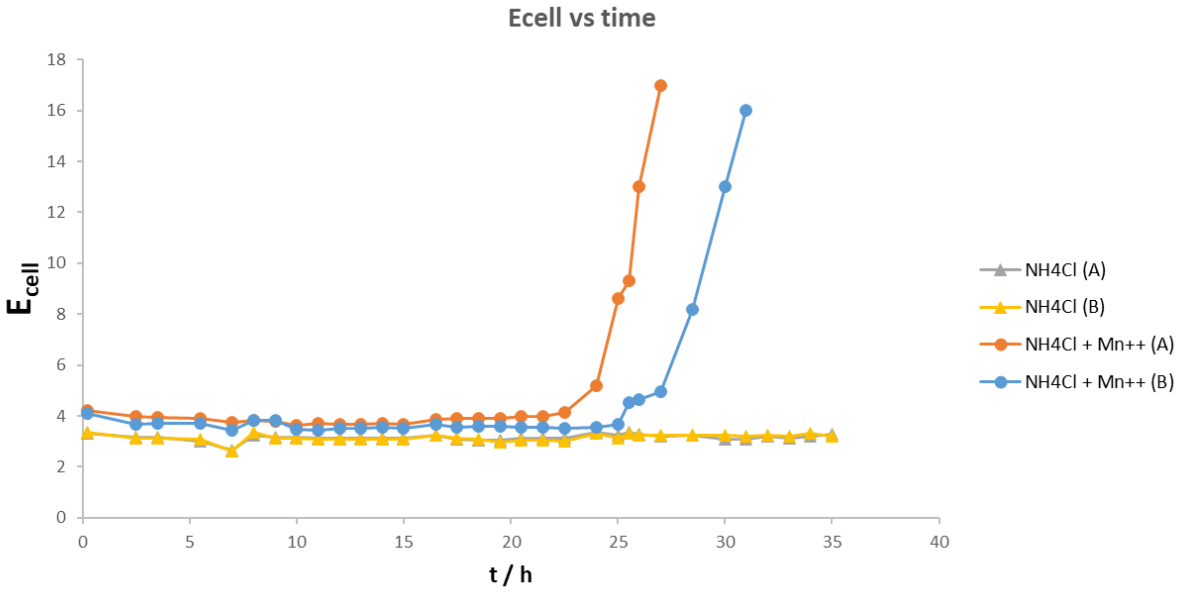

Figure 125: Cell potential vs time.

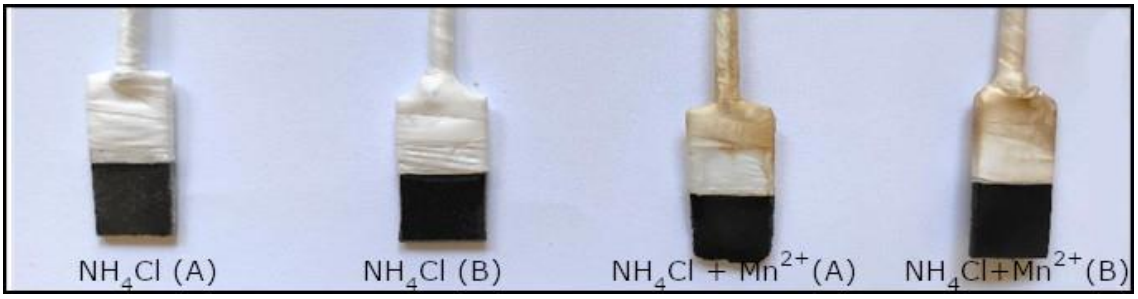

Figure 126: Electrodes after 25 hours of electrolysis.

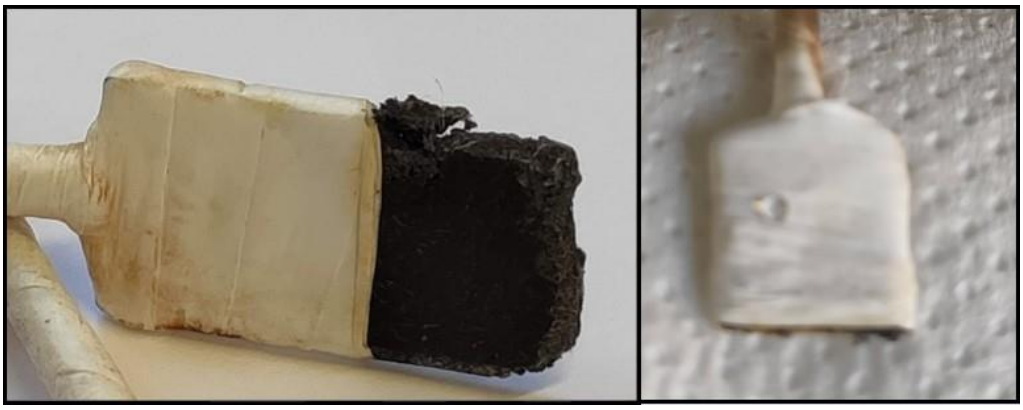

Figure 127: Detail of activated titanium electrode after 25 (left) and 27 hours of electrolysis (right).

Lacquer coating before electrolysis **Lacquer coating After electrolysis**

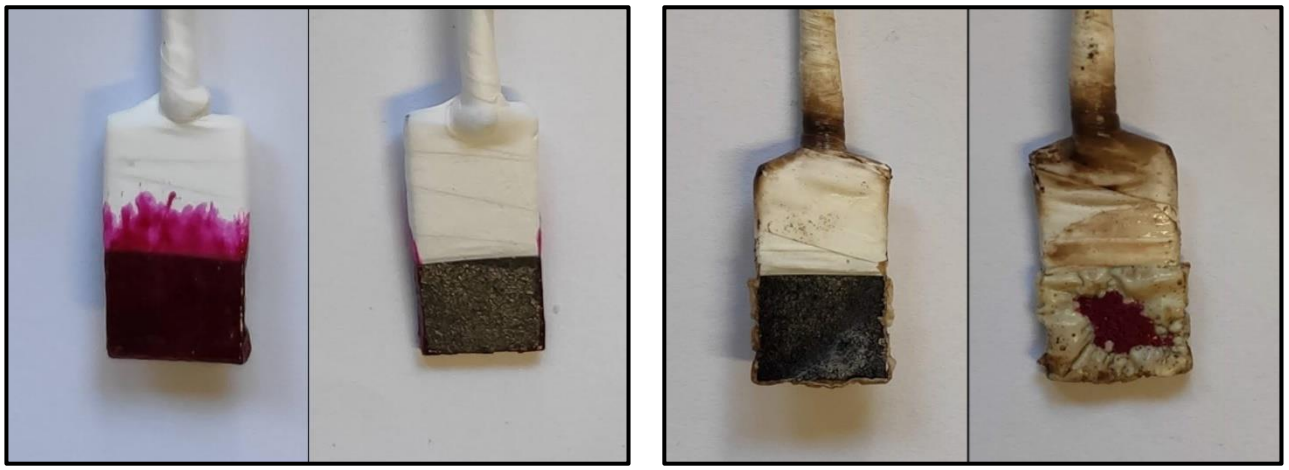

Figure 128: Electrodes shielded with lacquer coating before (Left) and after (right) electrolysis.

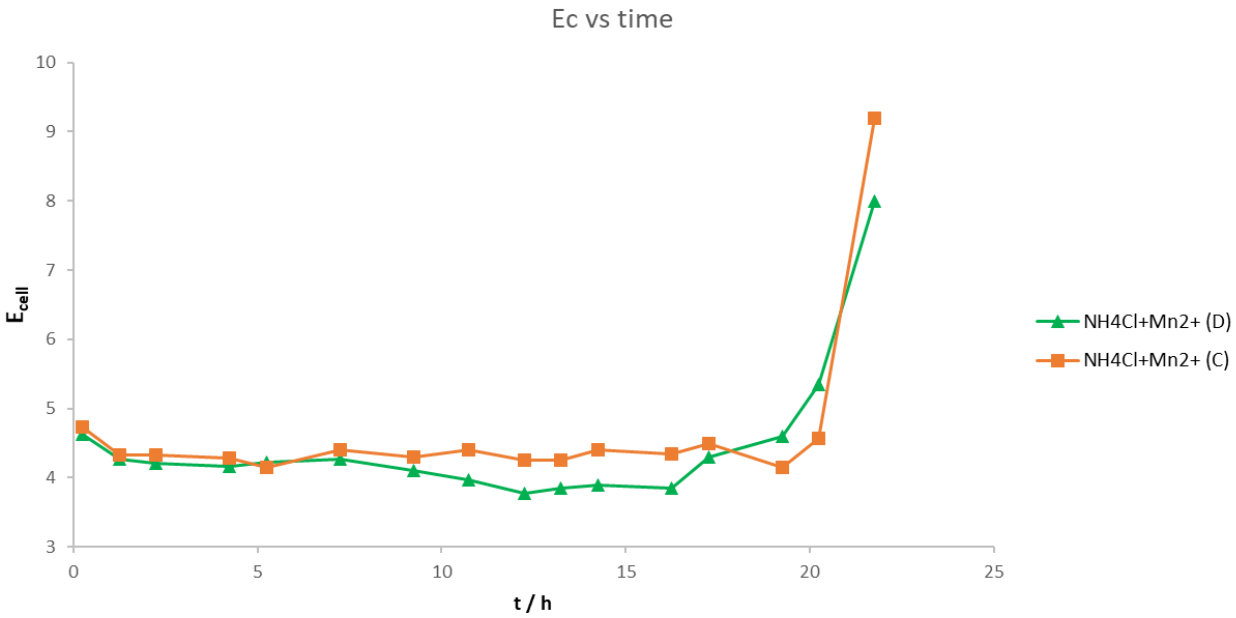

Figure 129: Cell potential vs time.

SEM-EDX analysis

Electrodes were analyzed by SEM-EDX technique after electrolysis in both tested solutions. Figure 130 shows the differences between the surface of an activated titanium electrode without and with the presence of manganese in the electrolysis solution. On the latter, which was close to its exhaustion, the analysis was done on a whitish spot that was visibly corroded. The surface morphology between the two is completely different: in the presence of manganese the typical mud-like coating structure tends to have deeper and larger cracks. This could be due to the formation of manganese oxide, which is solid, stressing the coating causing it to detach and thus a loss of ruthenium. EDX Analysis, Figure 131 ,shows a depletion of ruthenium content on the surface of the electrode that worked in the presence of manganese.

This anode was then embedded in resin and polished for cross section analysis. A compact titanium and a corroded zone are clearly distinguishable, Figure 132, the latter appears as a porous mass in which small "cracked bubbles" are embedded. From EDX analysis in the corroded zone, Figure 133, oxygen is present in a 2:1 ratio to titanium indicating that the material is mainly TiO_2. Nitrogen and chloride were detected, likely due to electrolyte residues, while carbon is attributable to resin particles deposited in the porous corroded titanium during polishing.

On the surface of the cathode that worked in the presence of manganese, ruthenium was unexpectedly found, Figure 134 . The detection of Ru suggests that it was previously

dissolved from the anode and then deposited on the cathode surface. The ruthenium peaks can be confused with the main chlorine peak, 2.558 keV for Ru and 2.61 keV for Cl. However, ruthenium has a second peak, at 19.233 keV, which confirms its presence.

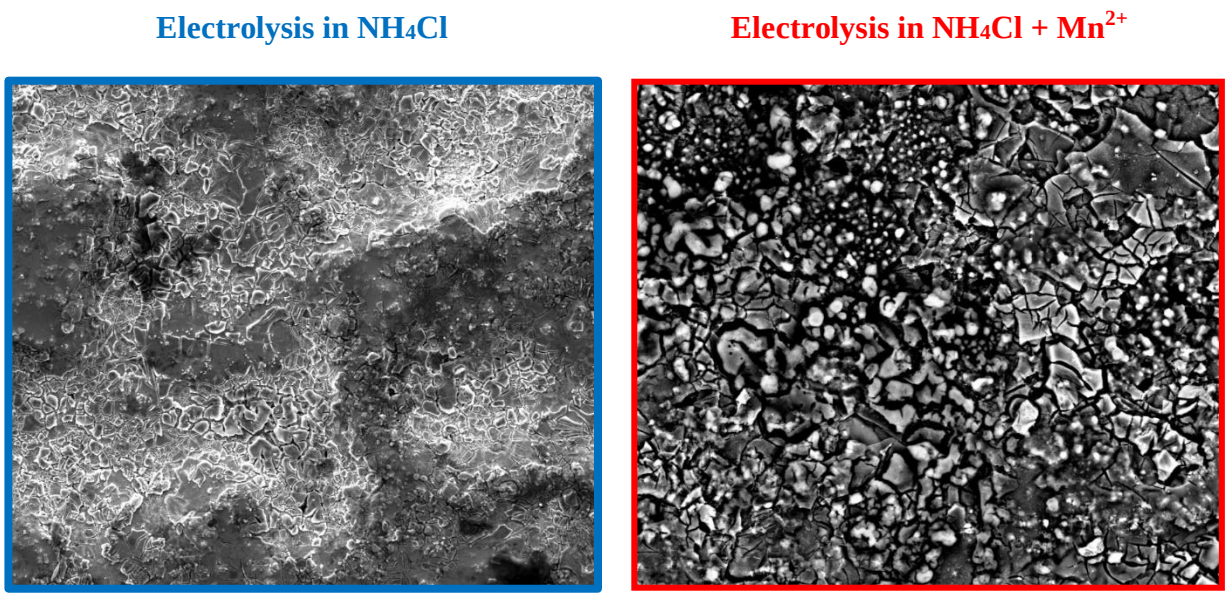

Figure 130: Surface morphology of activated titanium after electrolysis; 500X magnification.

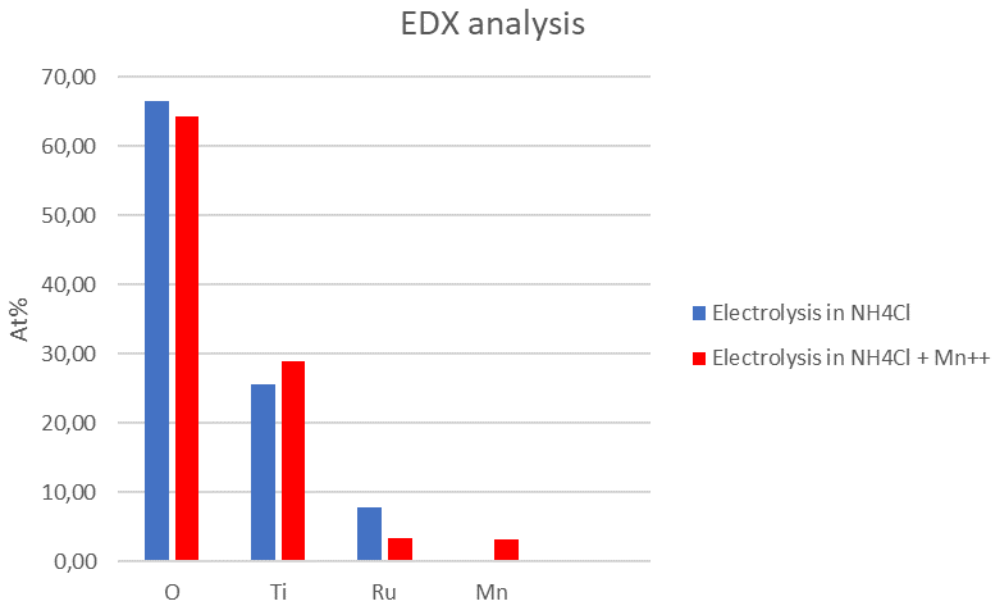

Figure 131: EDX analysis on titanium activated electrodes.

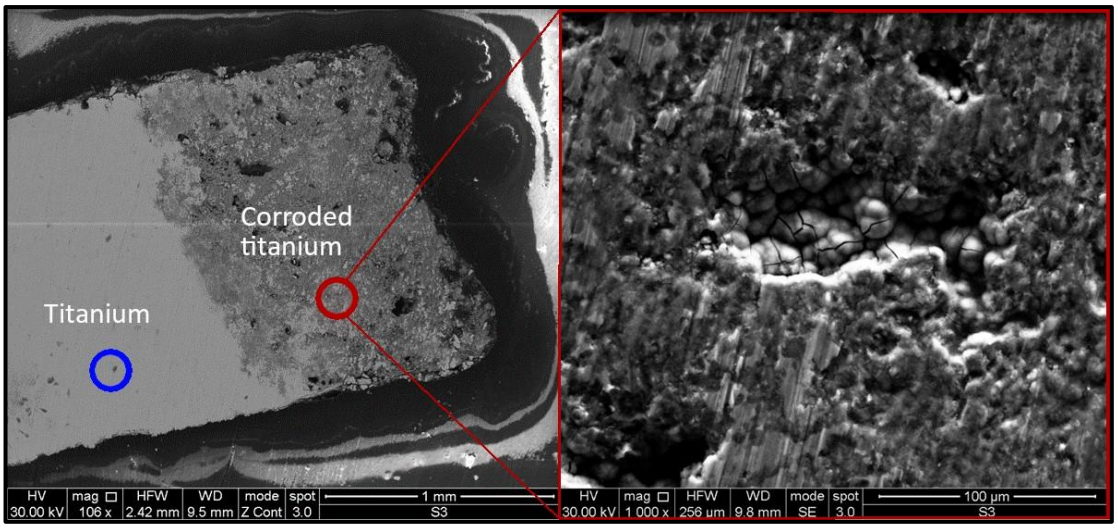

Figure 132: Corroded titanium anode cross section and magnification of the corroded structure.

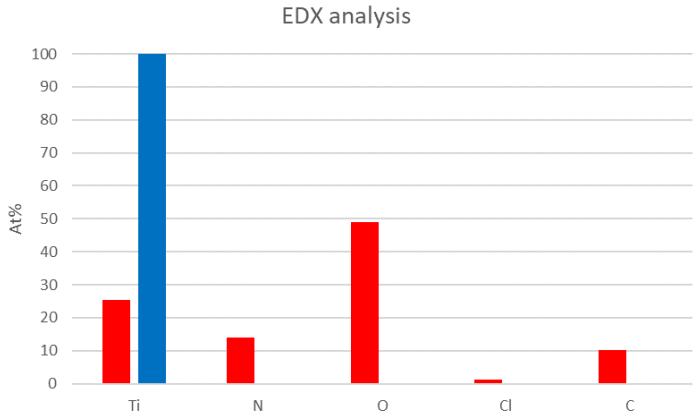

Figure 133: EDX analysis on blue and red spot of Figure 132.

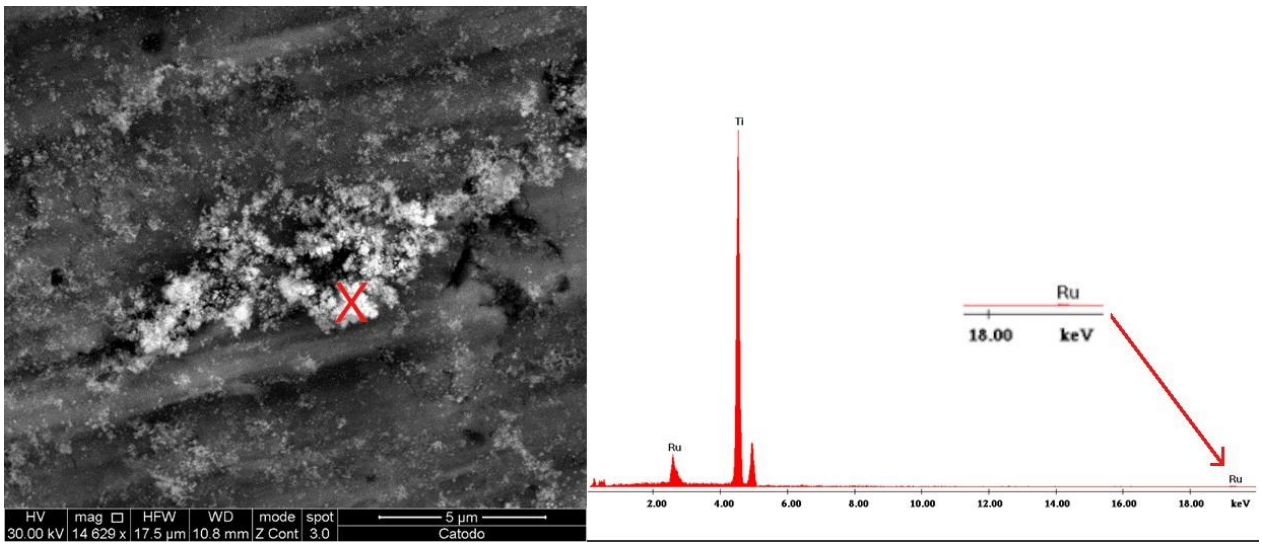

Figure 134: Ruthenium on titanium cathode.

XPS analysis

XPS analyses were done on new and nearly depleted electrodes, Figure 135. The results reveal that on a depleted electrode, just prior to the sharp increase in potential, ruthenium depletion begins in a certain area and spreads throughout the coating.

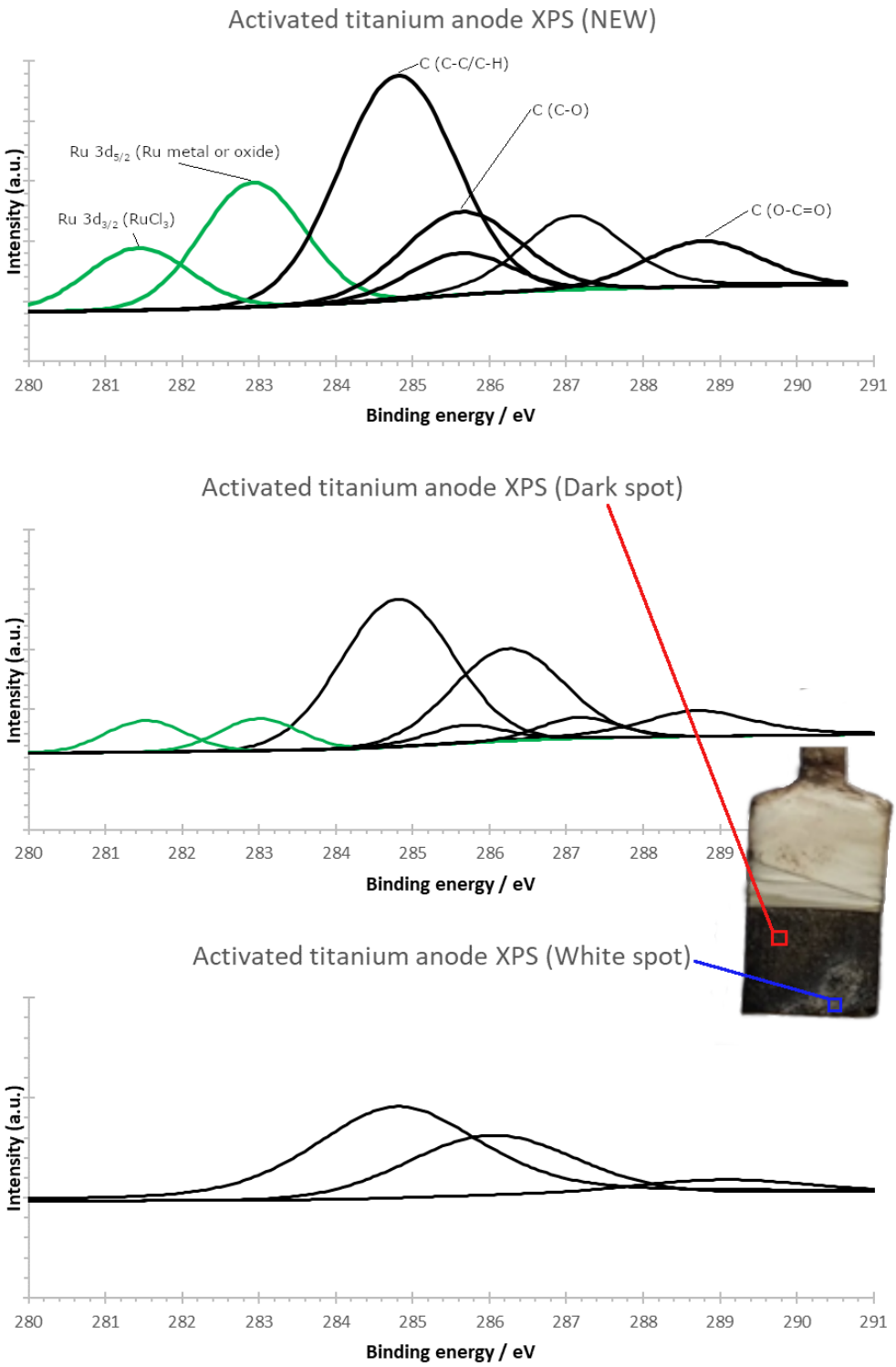

Figure 135: XPS of activated titanium, both new and semi exhausted.

Conclusions

This experimentation was performed to preliminarily evaluate the effect of manganese. A specific type of activated titanium (CNT 10A) was tested during electrolysis in ammonium chloride with 100 ppm Mn^{2+}.

The results obtained suggest that the lifetime of these electrodes is reduced when manganese is present. In addition, an unexpected complete dissolution of the anode was observed, which is not usual for this type of material, the mechanism behind the deactivation is unclear.

The oxidation pathway of manganese remains unknown; it is unclear whether oxidation occurs directly on the electrode surface, mechanically peeling off the catalytic coating, or whether the reaction occurs as a reaction mediated by the action of oxidizing species generated at the anode.

Ruthenium was found on cathodes working in the presence of manganese; this and other evidence suggests that mechanical and chemical factors are both involved in the deactivation of the anodic catalytic layer.

Appendix 11 – Electrodeposition additives for the EZINEX® process

This study was conducted to perform a basic screening of the effect of some additives on the electrodeposition of zinc in ammonium chloride electrolyte. Additives used in metal electrodeposition induce changes in the morphology of the deposit through adsorption on the active growth sites. At the same time, structural changes occur in the deposit, affecting structure, internal stresses, dislocations, etc.

Additives can significantly alter the nucleation and growth processes by changing the type of nucleation (e.g., instantaneous with progressive), changing the competition between nucleation and growth, or between different types of growth mechanisms (e.g., vertical growth and lateral growth) of the electrodeposited layers. The growth process by nucleation depends not only on the nature of the additive, but also on the nature of the substrate and experimental conditions such as additive/metal ion concentration ratio, applied overpotential, temperature, electrolyte, pH, etc.

The literature lacks experimental data regarding the electrodeposition of zinc in ammonium chloride solutions, the characteristic electrolyte of the EZINEX® process. Therefore, several classes of additives were considered and tested using a Hull cell. As a first screening, parameters such as zinc concentration, temperature, and ammonium chloride concentration were kept unchanged; only the additive was changed. Cell potential, adhesion, fracture type, surface morphology, and cross-sectional appearance were the parameters considered for additive evaluation. Theoretically, the best additive is one that does not increase cell potential, produces an adherent, smooth and compact deposit, free of pores and dendrites, with good adhesion to the cathode during electrodeposition and easy stripping. A deposit with these characteristics will be suitable for melting in a molten zinc bath for hot dip galvanizing or for casting pure zinc ingots with low slag formation.

This experimentation was divided into three parts; initially the additives were tested individually, then the best were tested in pairs, and finally the most promising were tested in mixtures of three.

Experimental part

Experimental testing apparatus

Additives were tested using the Hull cell, a testing device with specific geometrical parameters widely used in metals deposition research to test simultaneously the effect of different current densities within a single experiment (Figure 136).

Figure 137 shows the current distribution occurring in the cell, it varies with the distance between anode and cathode.

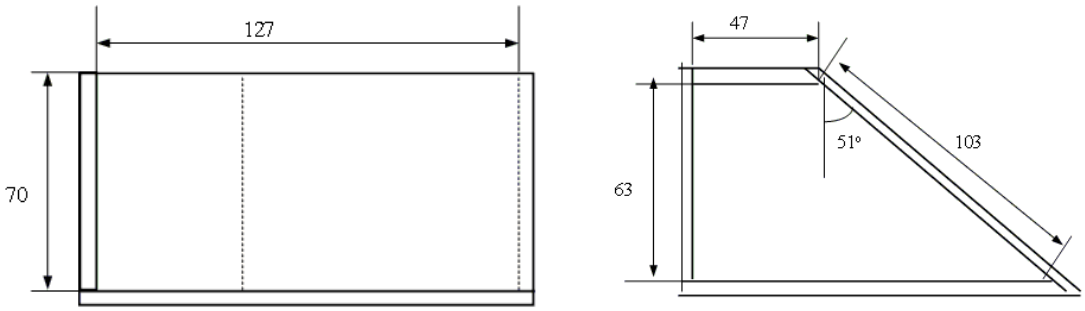

Figure 136: Hull cell dimensions (mm), side (left) and top view (right).

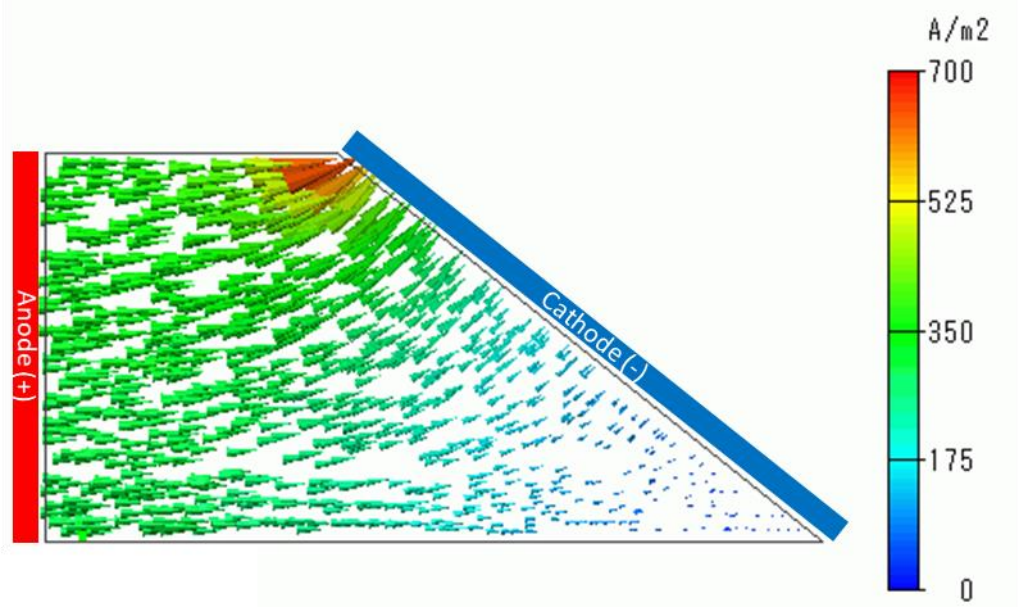

Figure 137: Simulated current distribution in a typical Hull cell (1A), top view. (www.muratasoftware.com)

As it is, the Hull cell is designed for short experiments, 5-10 min, however, such a short time was not sufficient to produce a zinc deposit thick enough to be evaluated from a morphological standpoint. To produce a thicker deposit, the cell was adapted to be able to work for 5 hr without significant depletion of the zinc concentration in the electrolyte solution, starting from 10 g/L to ~7.7 g/L of Zn at the end of the experiment. An overview of the experimental apparatus is shown in Figure 138.

A 4-liter recirculation tank was used to store the electrolyte that was continuously injected into the cell through a peristaltic pump. A cathode holder was specially designed to hold a rigid tube with equally spaced holes through which the solution was injected into the cell to prevent zinc depletion on the cathode surface.

The liquid level within the cell was kept constant by the addition of an overflow by which excess electrolyte was sent directly back to the recirculation vessel.

Air sparging was provided by a series of small holes below the cathode. A flow meter was used to regulate and maintain constant flow.

Electrodeposition experiments were performed at constant temperature (60°C) by heating the recirculation tank with a temperature-controlled heating plate. The recirculation tank was kept under agitation using a magnetic stir bar.

Figure 138: Experimental setup. 1-pH electrode, 2-Hull cell, 3-Potential logger, 4-Recirculating tank, 5-Potentiostat, 6-Heating plate, 7-Peristaltic pump.

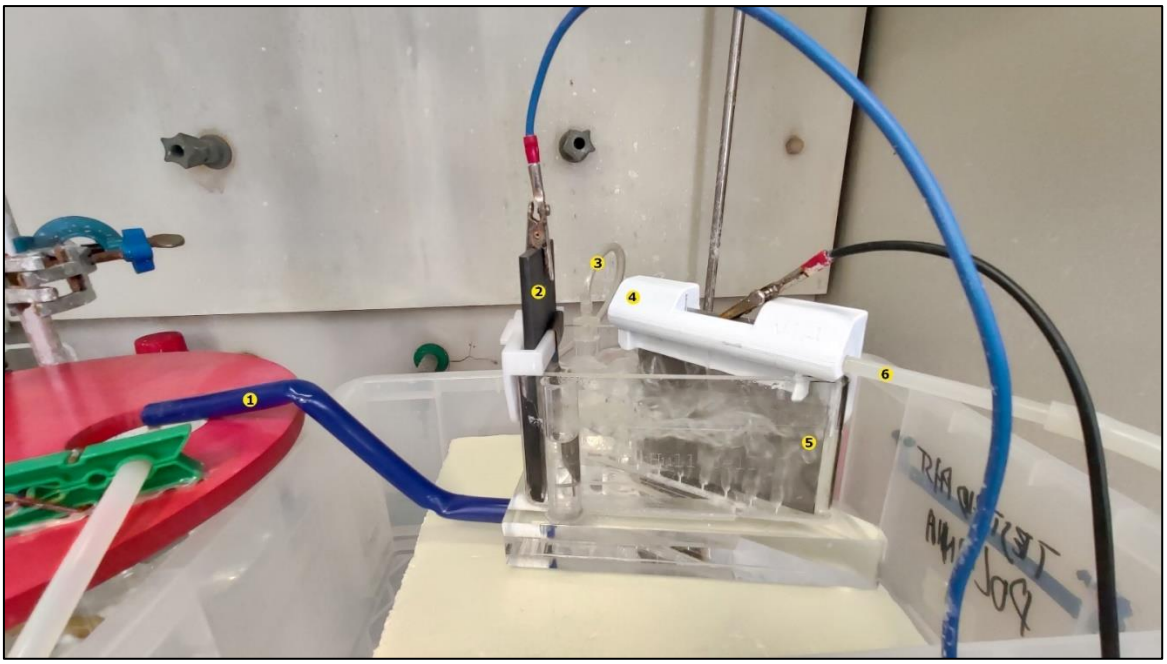

Figure 139: Hull cell detail. 1-Overflow, 2- Anode (graphite), 3-Air inlet for air sparging, 4-Cathode holder, 5-Cathode (titanium Gr1), 6-Solution inlet from peristaltic pump.

Materials and method

Anodic and cathodic materials were graphite and titanium grade 1, respectively. Cathodes were polished with sandpaper, 180-500-1200 grit, and cleaned with ethanol before each test. Two types of solution were tested: a real EZINEX® leaching solution and a synthetic one prepared as follows:

Real EZINEX® leaching solution:	Synthetic solution:
NH_4Cl 300 g/L	NH_4Cl 300 g/L
EAFD 30 g/L	Zn^{2+} 10 g/L (from ZnO)

Real EZINEX® solutions were prepared following a common leaching route; EAFD was added to an ammonium chloride solution and allowed to react for 1 h at 70 °C under vigorous stirring. The suspension was then filtered and cemented with zinc metal powder to remove impurities such as lead, copper, silver, and cadmium; a portion was demanganized following the procedure given in Appendix 4. In order to keep the variables as controllable as possible, the concentration of zinc in this solution was first determined by titration with EDTA and then adjusted to 10 g/L by addition of ZnO.

For each experiment, the pH of the solution was initially adjusted to 5.3 by the addition of

37% HCl and constantly monitored and increased with a 32% NH3 solution, when necessary, since the anodic reaction tends to consume ammonium and decrease the pH. For this reason, it was not possible to maintain an accurate pH value throughout the test. Therefore, it was chosen to maintain the pH within the range of 5.2-5.4.

The literature is full of hypotheses about the action mechanism of additives, however, it is still a topic of debate. The effectiveness of additives is practically based on experimental evidence. Since ammonium chloride is an atypical electrolyte that has not been considered until now, the widest possible range of additives has been selected. The following scheme lists them divided by class.

Class	Additive
Quaternary ammonium salts:	➢ **Cetyltrimethylammonium bromide** ➢ **Tetraethylammonium chloride**
Glues and gelatins:	➢ **Agar** ➢ **Gum arabic** ➢ **Bone glue**
Pyridine carboxylic acid:	➢ **Nicotinic acid** ➢ **Isonicotinic acid** ➢ **Piconicotinic acid**
Saponins:	➢ **Aesculus hippocastanum extract** ➢ **Liquorice**
Polyether:	➢ **PEG 300** ➢ **PEG 4000**
Others:	➢ **Thiourea** ➢ **Vanillin** ➢ **Calcium Ligninsulfonate**

Deposits analysis

After 5 hours of constant current electrolysis (1.5 A), cathodes were removed, rinsed in distilled water, air dried, and photographed next to a current density ruler. The zinc deposits were then peeled off and cut horizontally in half; the top was used for surface analysis, while the bottom was cut into six parts and mounted in thermosetting resin for cross-section analysis (Figure 140). Cross-section embedded specimens were mirror polished prior to analysis (180-500-1200 grit in that order). SEM images were taken at 300-200-100 A/m^2 zones while deposit adhesion and its fracture behavior, brittle or ductile, were evaluated on a 1-5 scale (arbitrary scale: 1 low adhesion/fragile fracture, 5 high adhesion/ductile fracture).

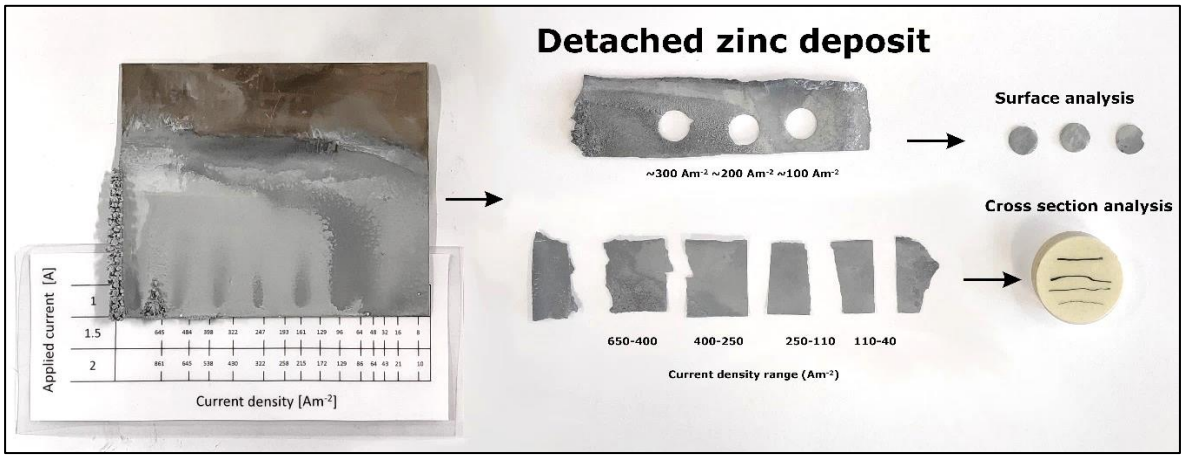

Figure 140: Sample preparation. From left: obtained zinc deposit, horizontally cut deposit, samples ready for SEM analysis.

Electrodeposition additives for the EZINEX® process

Part I

[T27] No additive – No air sparging

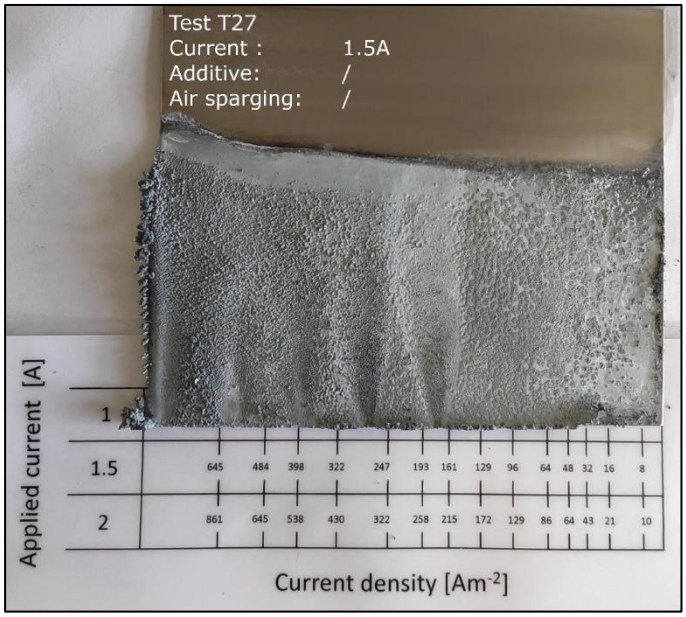

	Low	High
Adhesion	★★★☆☆	
	Brittle	Ductile
Fracture	★★★★☆	

Figure 141: Test T27, Deposit appearance.

The T27 test was performed using synthetic solution; without additives and air sparging; the resulting deposit, Figure 141, shows a uniformly distributed rough surface filled with small dendrites at all current densities, even at the lowest. The top shows a tendency to peel off but the overall adhesion was good while the fracture was quite ductile. Surface analysis, Figure 143 , shows a porous, dendritic structure that tends to disappear at the lowest current density. At 100 A/m^2 a small overlapping grain structure can be identified.

Cross section analysis, Figure 144, shows that the dendritic structure is present only on the "outer" part, the one in contact with the electrolyte, while the "inner" part, the one attached to the titanium cathode, is more compact. At the lowest current density, the cross section appears compact with a smooth outer part. The small black dots turn out to be grains of silicon dioxide,Figure 142 , which were incorporated into the soft zinc during the polishing process.

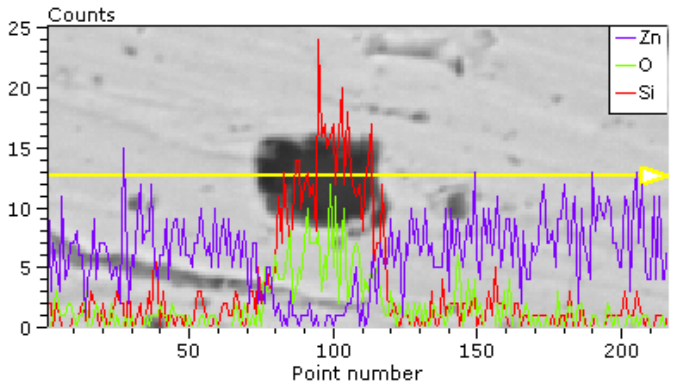

Figure 142: black dots EDX.

Surface

300 A m^{-2}	200 A m^{-2}	100 A m^{-2}

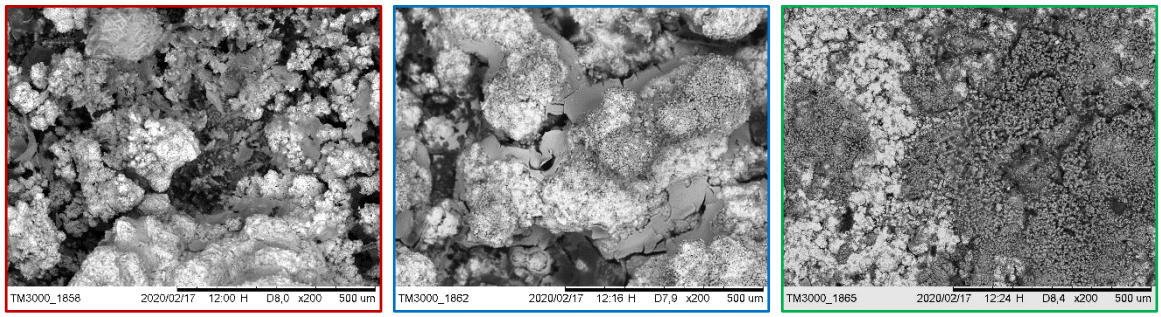

X200

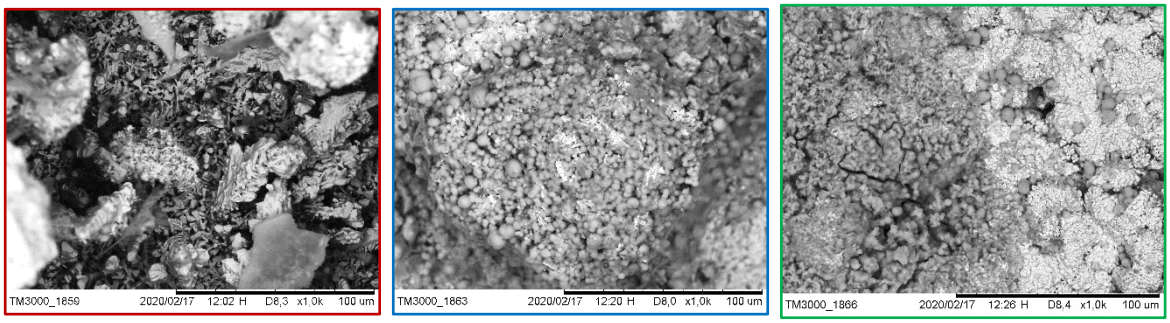

X1000

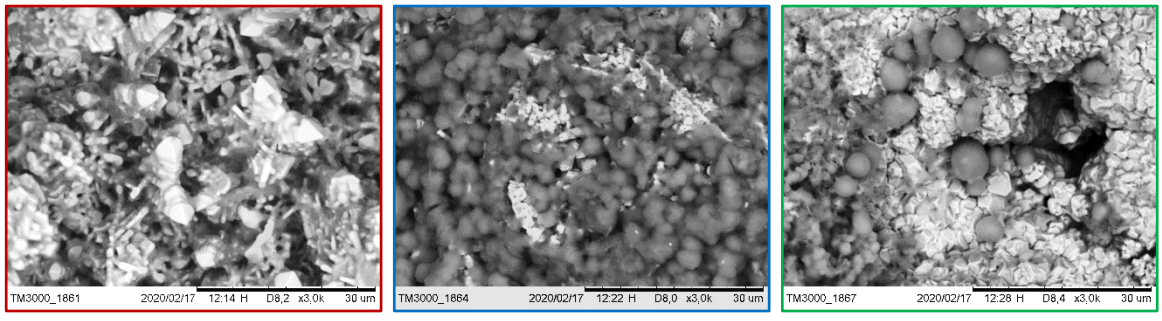

X3000

Figure 143: Test T27, Deposit surface at different current densities and magnification.

Cross section

300 A m^{-2}	200 A m^{-2}	100 A m^{-2}

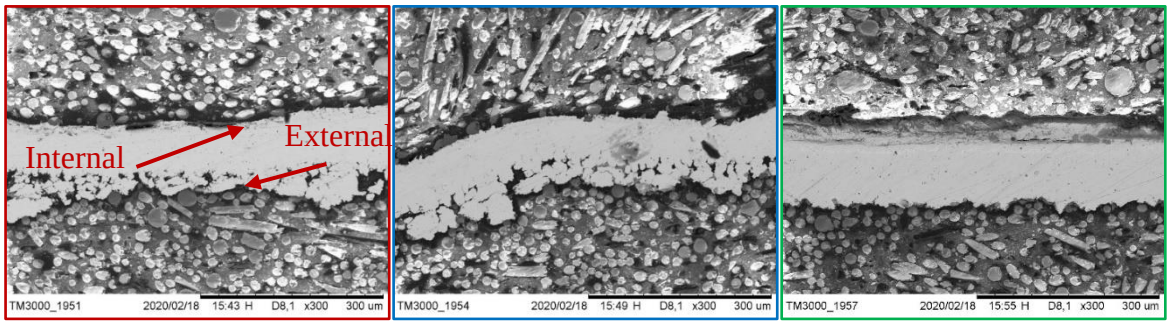

X300

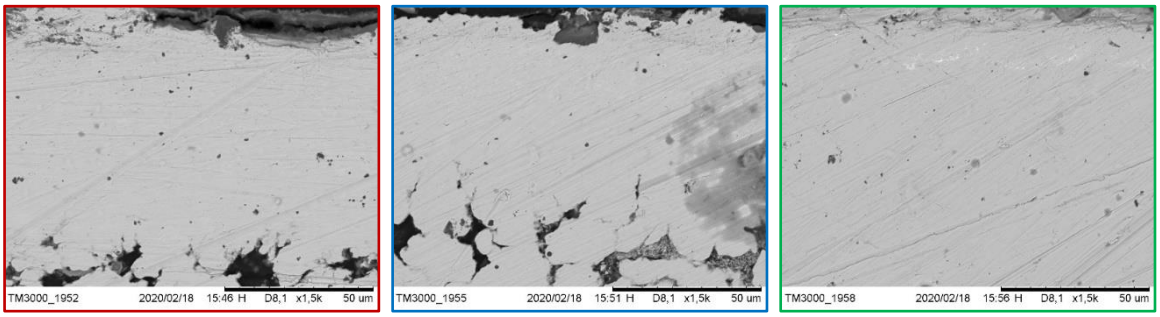

X1500

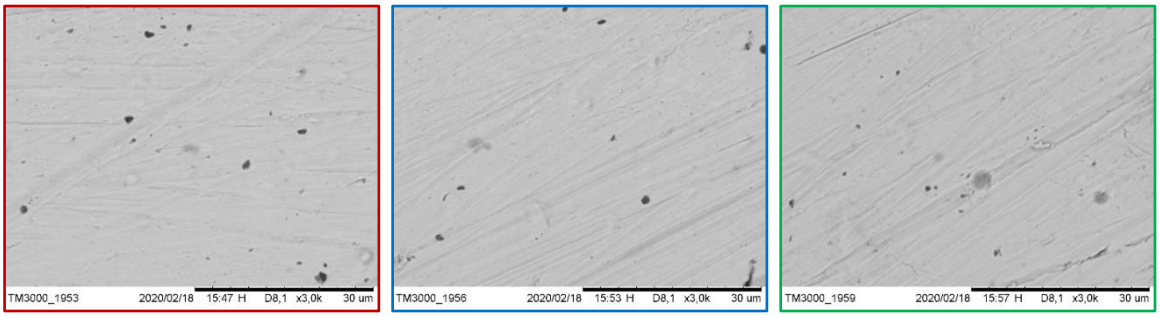

X3000

Figure 144: Test T27, Deposit cross section at different current densities and magnification.

[T28] No additive – Air sparging 4 l/min

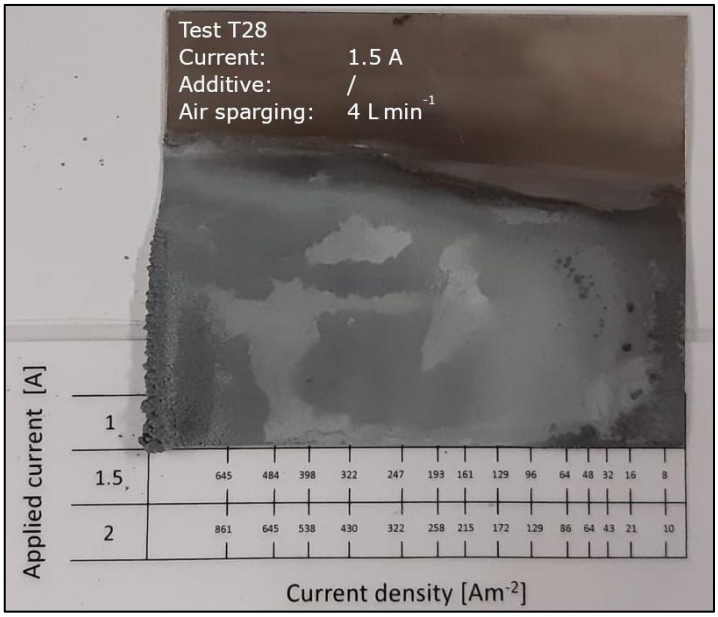

	Low	High
Adhesion	★★☆☆☆	

	Brittle	Ductile
Fracture	★★★★☆	

Figure 145: Test T28, Deposit appearance.

Test T28 was performed with the same condition as the previous test except for the presence of air sparging which was fixed at 4 l/min. The appearance of the deposit ,Figure 145, is clearly improved, dendrites are present only at the extreme left edge of the zinc sheet while the surface appears smooth overall. Adhesion was a somewhat lower in presence of air sparging while the fracture remains quite ductile.

Magnification of the surface, Figure 146, shows a vertical lamellar structure, 300-200 A/m^2, which disappears at the lowest current density where it tends to maintain vertical growth with a grain stack structure. Porosity is quite high throughout the deposit. Cross-section analysis, Figure 147, shows a compact deposit free of pores and dendrites on the outside; it should be mentioned that the soft nature of zinc and the polishing process could help to hide and homogenize the appearance of the cross-section by closing small pores and cracks. From this test, the effect of air spraying is clear; dendrite formation was drastically reduced while the surface morphology appears more homogeneous.

Surface

300 A m^{-2}	200 A m^{-2}	100 A m^{-2}

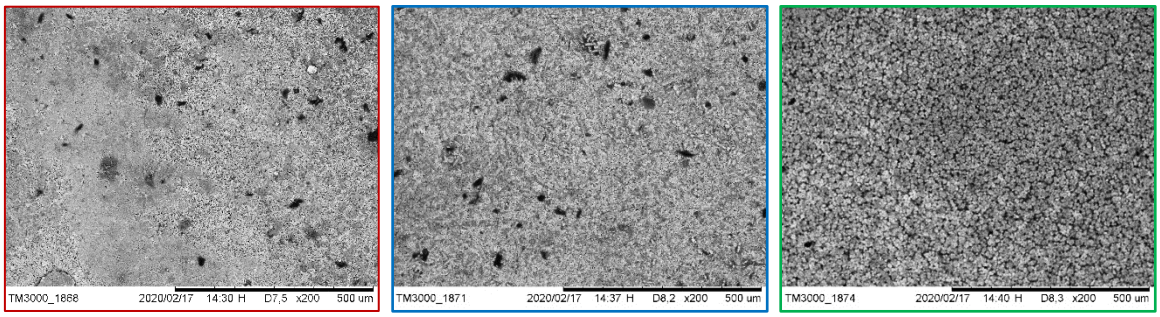

X200

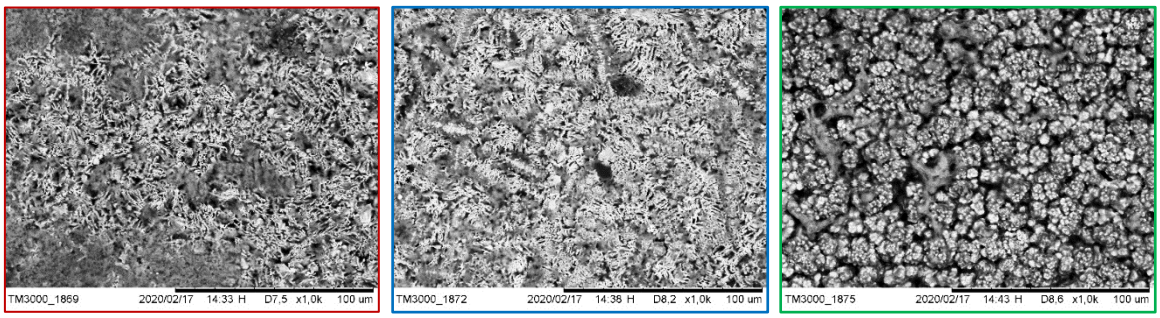

X1000

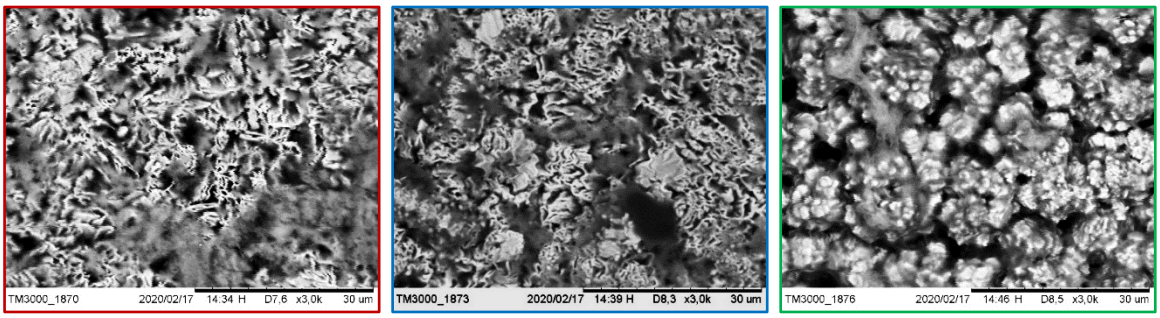

X3000

Figure 146: Test T28, Deposit surface at different current densities and magnification.

Cross section

300 A m^{-2}	200 A m^{-2}	100 A m^{-2}

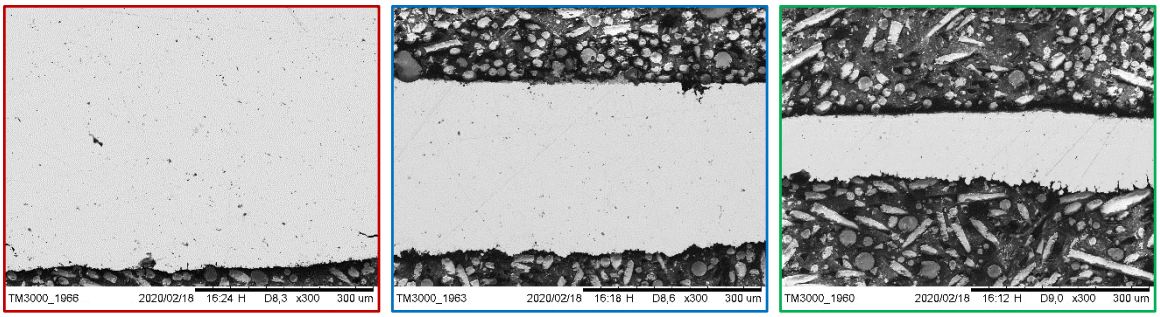

X300

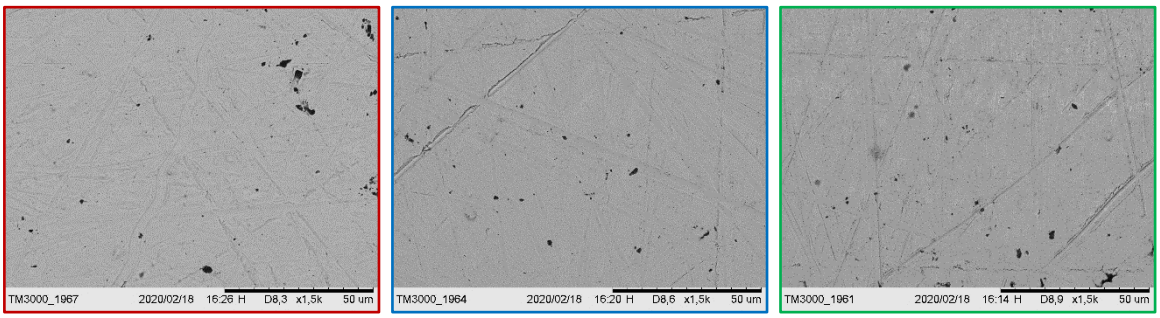

X1500

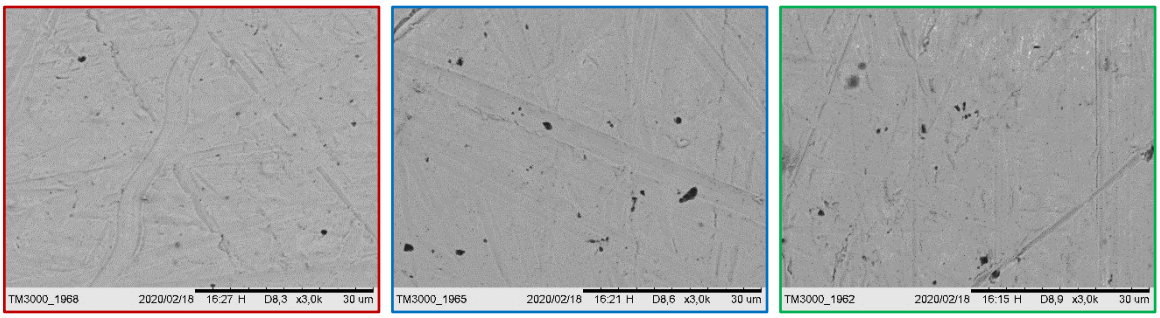

X3000

Figure 147: Test T28, Deposit cross section at different current densities and magnification.

[T29] No additive – Air sparging 7 l/min

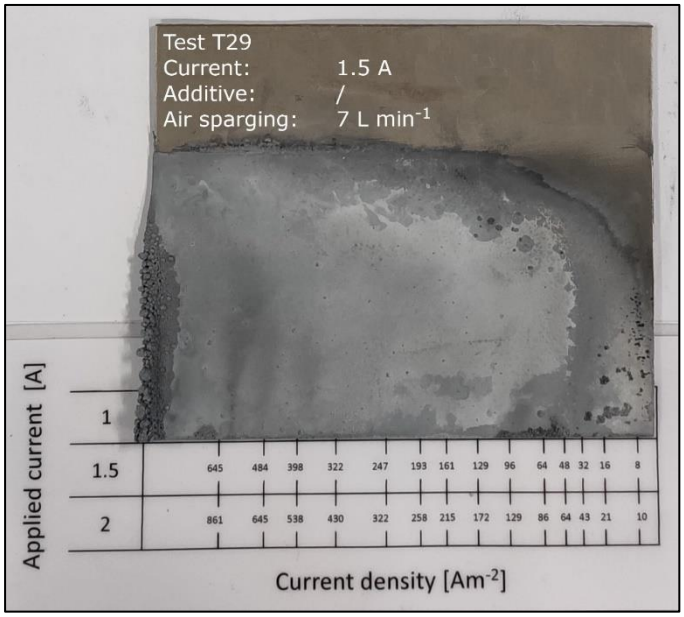

	Low	High
Adhesion	★★★☆☆	

	Brittle	Ductile
Fracture	★★★★★	

Figure 148: Test T29, Deposit appearance.

The purpose of the T29 test is to evaluate whether the air sparging rate contributes significantly to the deposit morphology; in this test, air sparging was set at 7 l/min. The appearance of the deposit, Figure 148, is very similar to that obtained with the lower air sparging rate; the adhesion and fracture type are also almost the same. The surface structure, Figure 149, exhibits the same characteristics observed in the T28 test. Cross-section analysis, Figure 150, shows the presence of discontinuities and cracks at the highest current density. Observing the results obtained from the T28-T29-T30 tests, it was chosen to continue the experimentation with air sparging set at 4 l/min; a higher flow rate does not increase the quality of the deposit while the absence of this variable leads to the formation of dendrites all over the zinc foil.

Surface

300 A m^{-2}	200 A m^{-2}	100 A m^{-2}

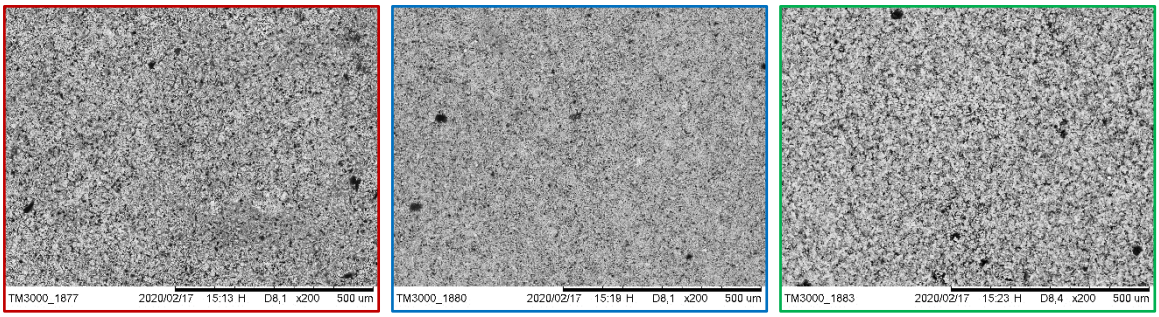

X200

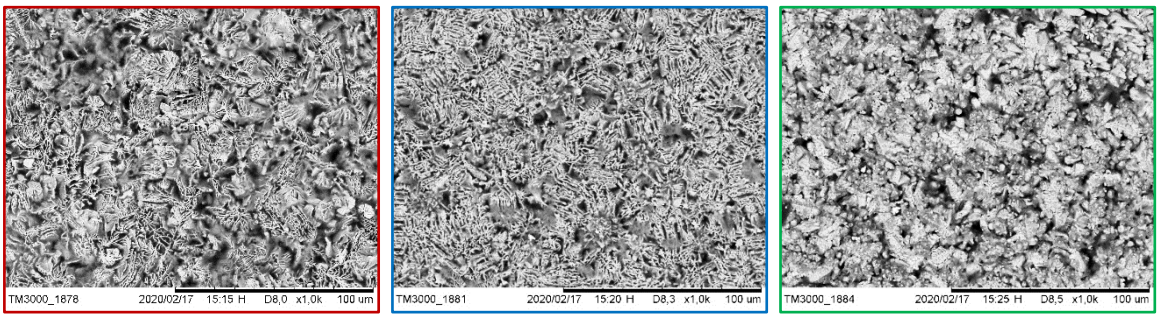

X1000

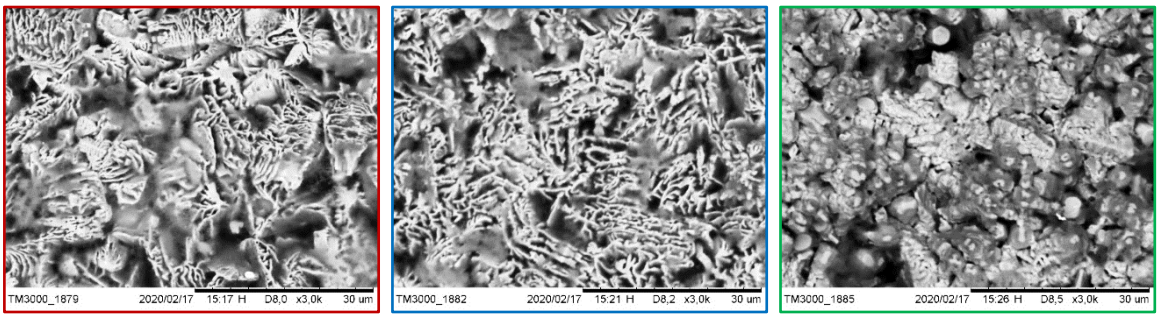

X3000

Figure 149: Test T29, Deposit surface at different current densities and magnification.

Cross section

300 A m^{-2}	200 A m^{-2}	100 A m^{-2}

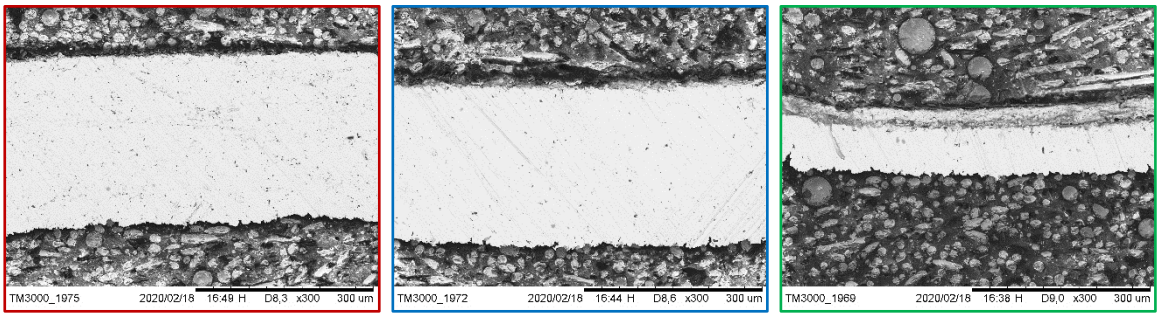

X300

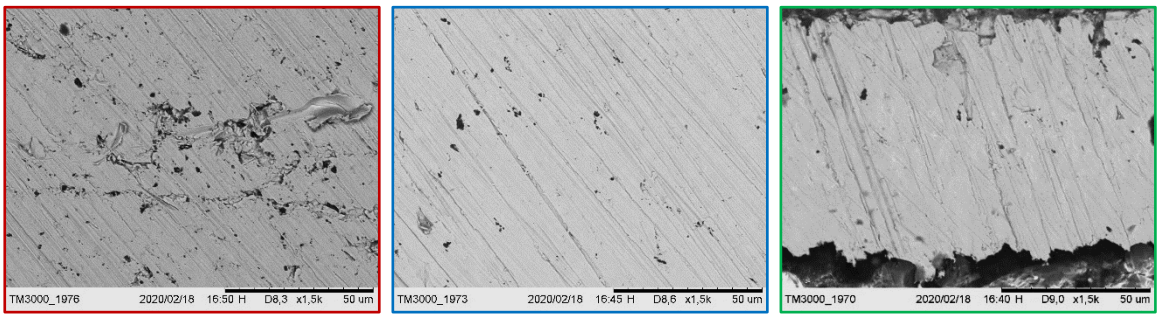

X1500

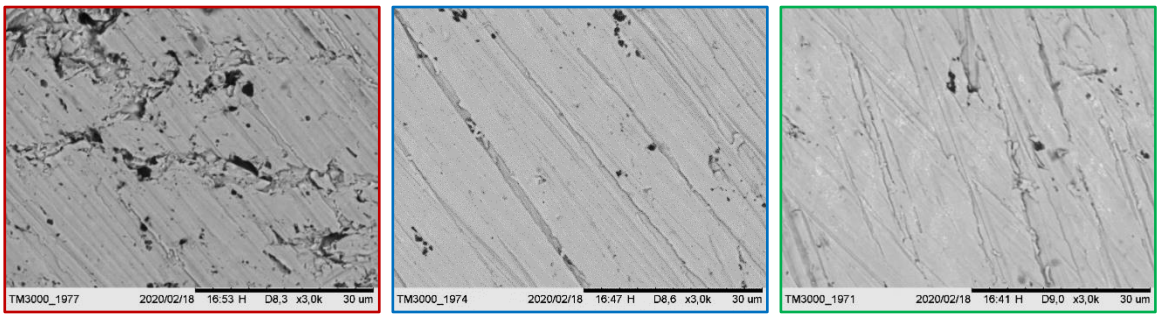

X3000

Figure 150: Test T29, Deposit cross section at different current densities and magnification.

[T30] Real EZINEX® solution - Cemented

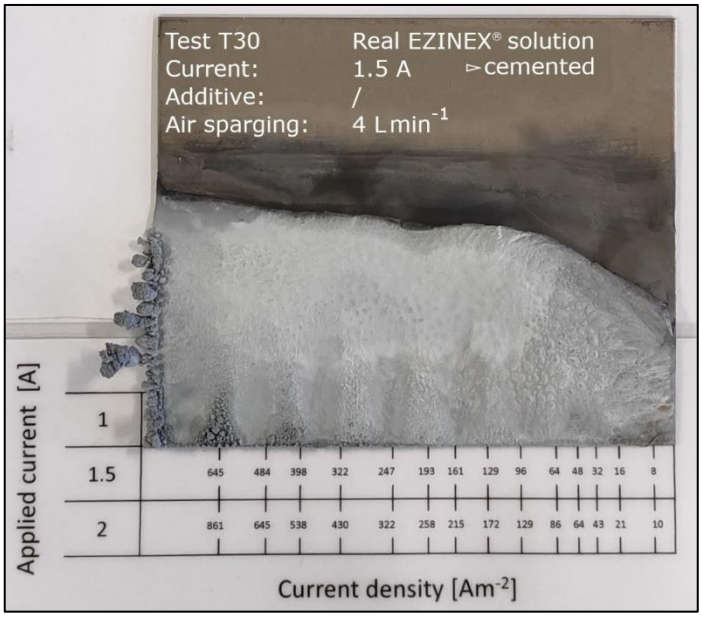

	Low	High
Adhesion	★☆☆☆☆	

	Brittle	Ductile
Fracture	★★★★★	

Figure 151: Test T30, Deposit appearance.

The T30 test was performed using a real EZINEX® solution that was cemented to remove metallic impurities; manganese was not removed. The lead content, after the cementation process, was less than 2 ppm while cadmium, copper and silver were below their LOD for the atomic absorption analysis. After a few minutes of electrolysis the solution turned slightly brown then brown after 1 hour, this was caused by the presence of manganese which is oxidized from an Mn^{+2} to an Mn^{+4} oxidation state at the anode forming a solid particulate. Figure 151 shows a smooth deposit with the presence of dendrites at extremely high current densities; the top was completely detached from the titanium cathode. Below the detached top there was a black powdery deposit that was found to contain lead after an EDX analysis. Adhesion was very poor, while the fracture type was very ductile. The surface, Figure 152, is characterized by a grain structure that tends to grow vertically creating a porous surface that is somewhat more compact at the lower current density. The cross sections, Figure 153, show the presence of small holes whose density tends to increase at low current densities. It should be noted that the EAFD used to produce the real EZINEX® solution, in addition to mainly zinc, iron and lead compounds, may contain organic compounds, found in recycled scrap metal, which are distilled during the melting operation in electric arc furnaces. These compounds may act as a kind of additive that may or may not be beneficial to zinc electrodeposition.

Surface

300 A m^{-2}	200 A m^{-2}	100 A m^{-2}

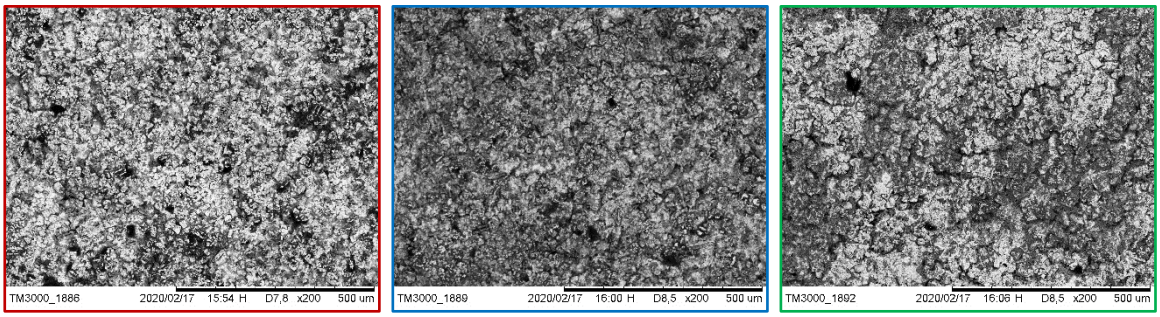

X200

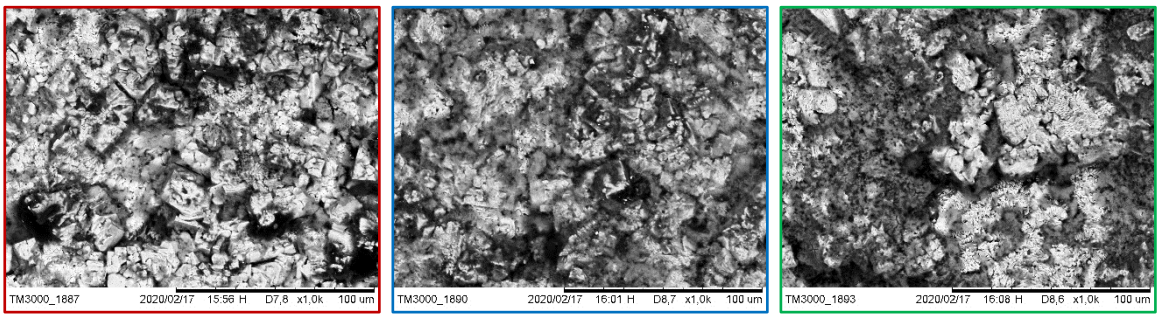

X1000

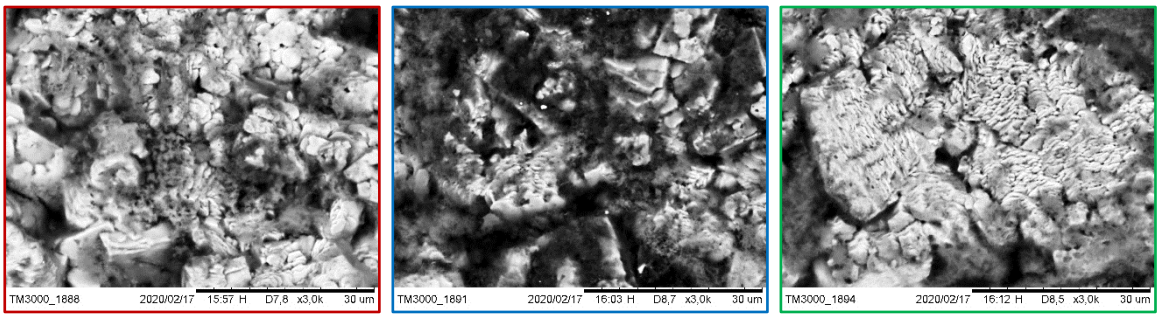

X3000

Figure 152: Test T30, Deposit surface at different current densities and magnification.

Cross section

300 A m^{-2}	200 A m^{-2}	100 A m^{-2}

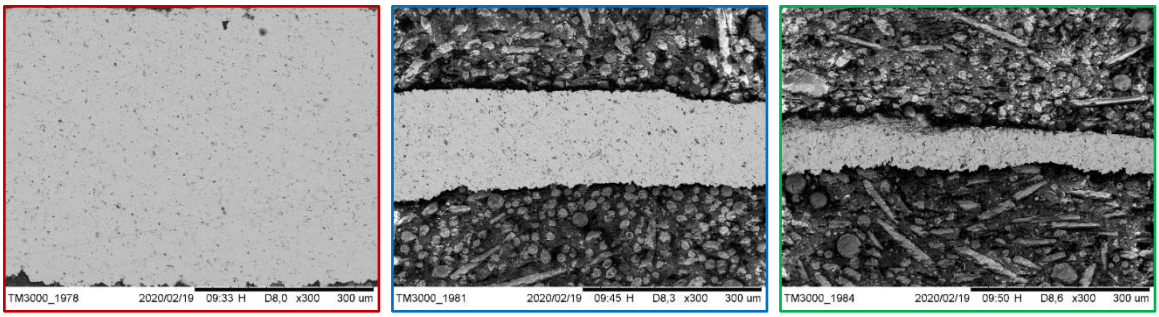

X300

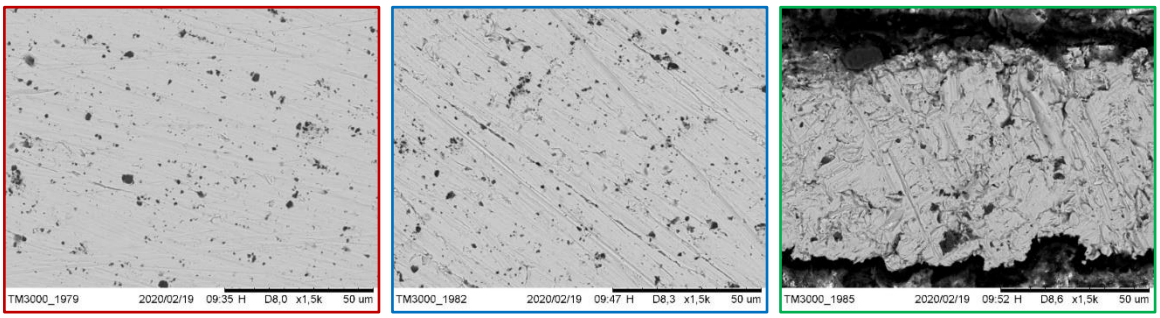

X1500

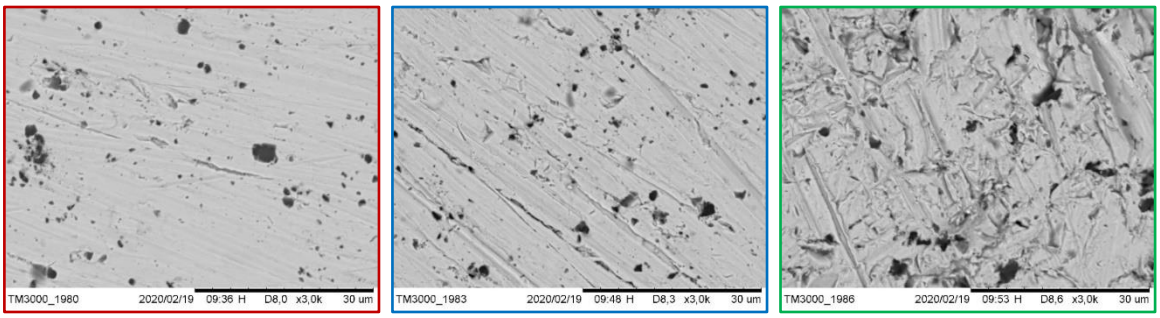

X3000

Figure 153: Test T30, Deposit cross section at different current densities and magnification.

[T31] Real EZINEX® solution – Cemented and demanganized

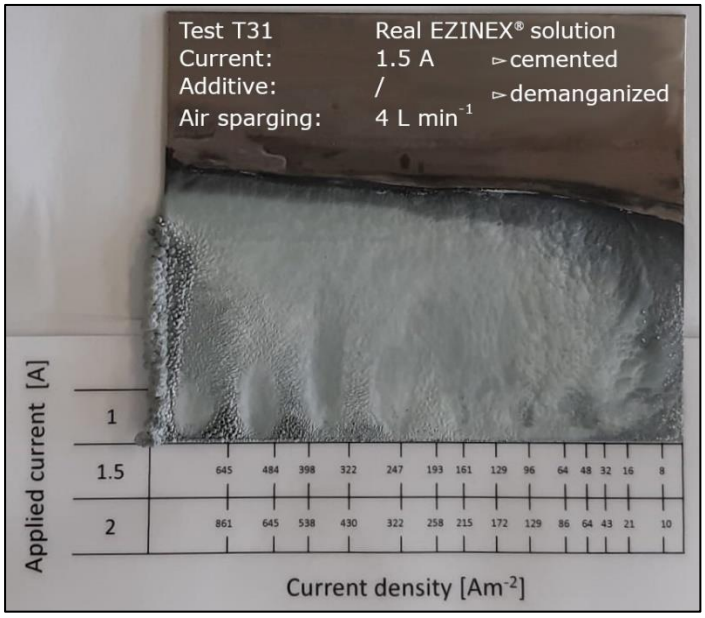

	Low	High
Adhesion	★★☆☆☆	

	Brittle	Ductile
Fracture	★★★★★	

Figure 154: Test T31, Deposit appearance.

The T31 test was performed to evaluate the influence of manganese on the morphology of the zinc deposit. The real EZINEX® solution was cemented and demanganized; the resulting manganese content was less than 1 ppm, AA analysis. Figure 154 shows a completely different deposit than that obtained in the presence of manganese; the top did not detach from the substrate, but removal of the entire deposit was easy while the fracture type remains ductile.

Surface analysis, Figure 155, shows a microporous deposit at the highest current density, but the structure changes completely at 200 and 100 A/m^2; a structure of compact, mainly planar growing grains can be recognized. The grains tend to be smaller as the current density decreases however, in both cases, the deposit appears to be very compact and free of pores or holes. The cross sections, Figure 155, show compact deposits with small defects.

The presence of manganese in the electrolyte solution seems to have a very important effect, it seems to reduce the tendency of zinc to grow into a grain structure and reduce the adhesion of the deposit.

Surface

300 A m^{-2}	200 A m^{-2}	100 A m^{-2}

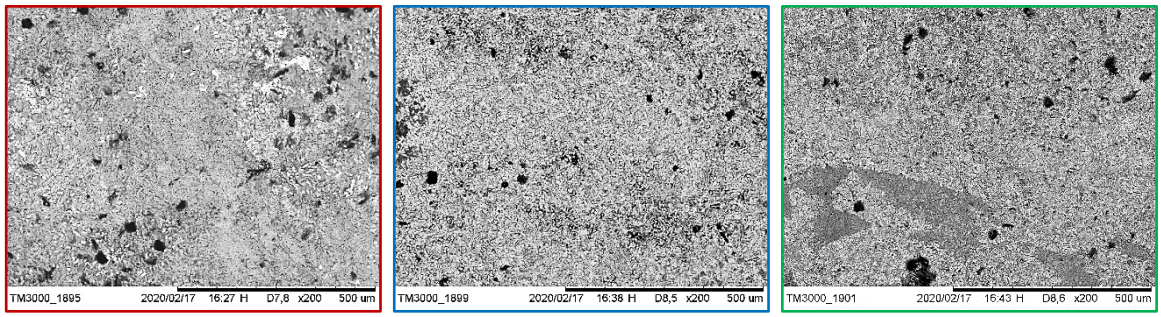

X200

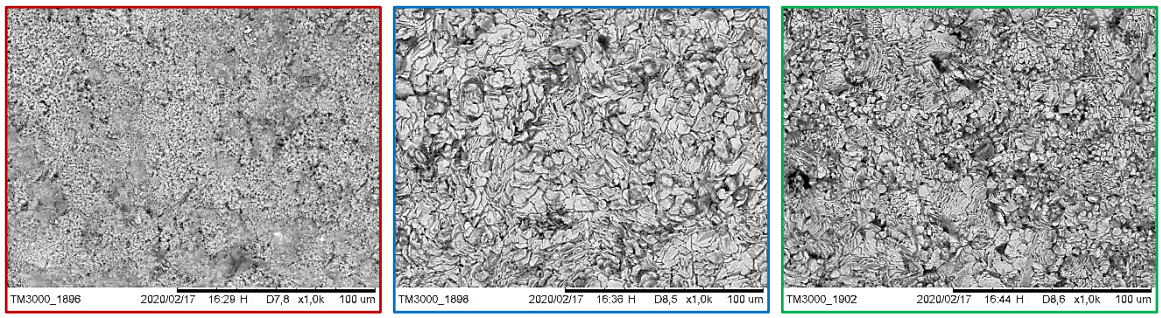

X1000

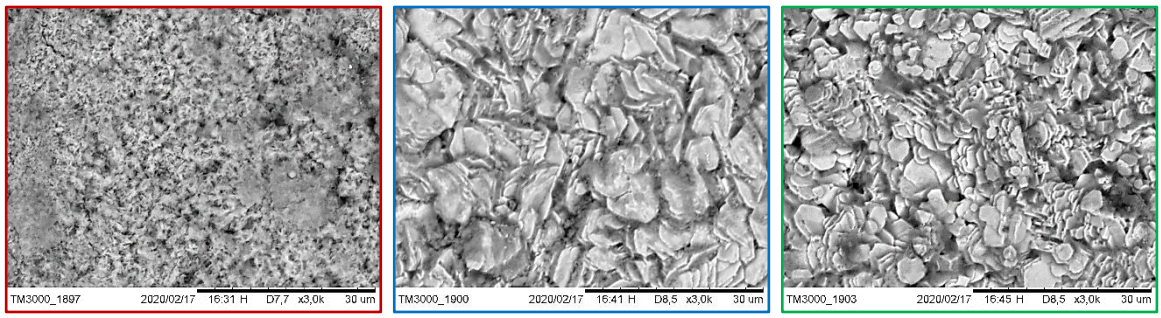

X3000

Figure 155: Test T31, Deposit surface at different current densities and magnification.

Cross section

300 A m^{-2}	200 A m^{-2}	100 A m^{-2}

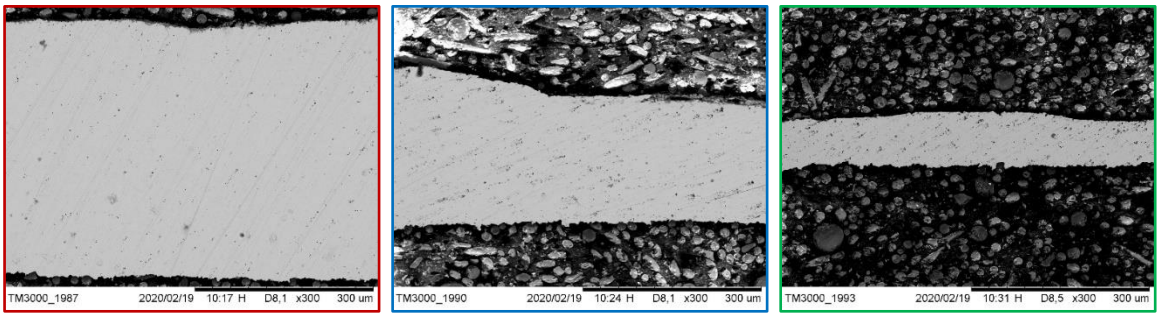

X300

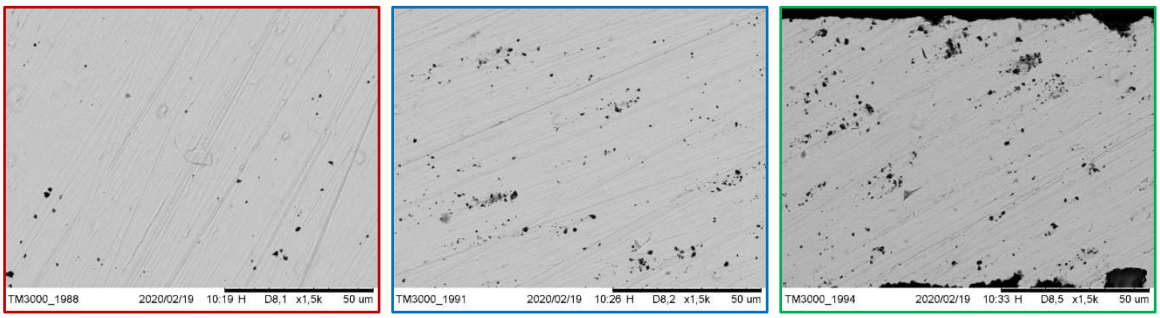

X1500

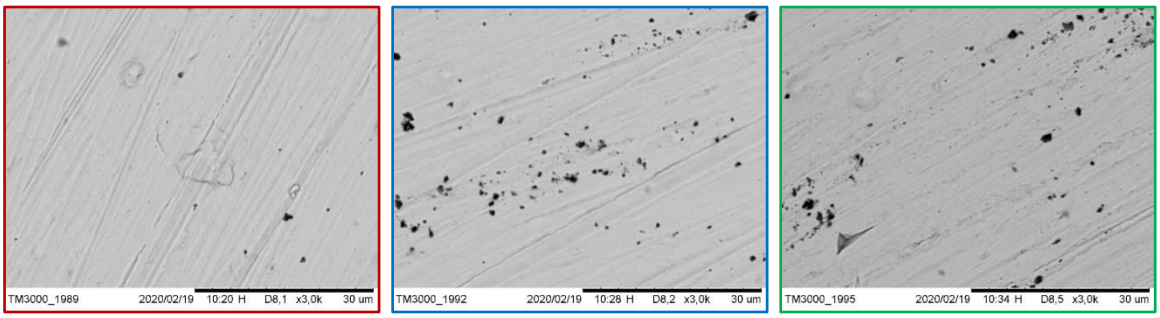

X3000

Figure 156: Test T31, Deposit cross section at different current densities and magnification.

[T32] Real EZINEX® solution - Cemented

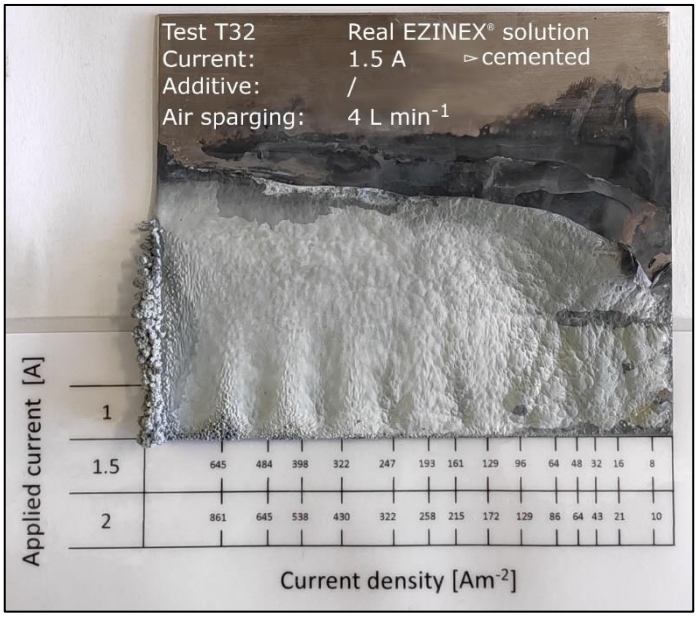

	Low	High
Adhesion	★☆☆☆☆	

	Brittle	Ductile
Fracture	★★★★★	

Figure 157: Test T32, Deposit appearance.

The T32 test was a replica of the T30 test, the purpose was to confirm the role of manganese on zinc electrodeposition. The appearance of the deposit, Figure 157, is very similar to that previously observed in the T30 test, the detachment of the top of the zinc deposit and a general low adhesion are confirmed and can be attributed to the presence of manganese. The surface and cross sections, Figure 158 and Figure 159 respectively, are also very similar; magnification of the surface shows a tendency for the deposit to form a grain structure that appears to prefer vertical rather than planar growth.

These results confirm the beneficial effect of manganese removal on the morphology of the zinc deposit.

Surface

300 A m^{-2}	200 A m^{-2}	100 A m^{-2}

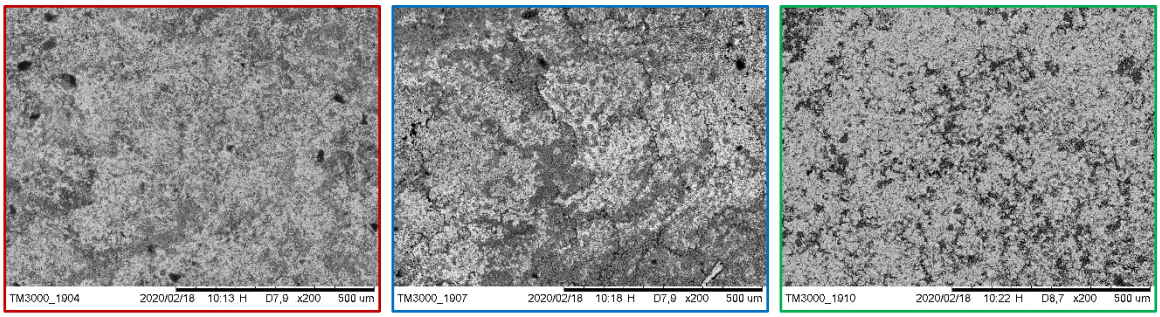

X200

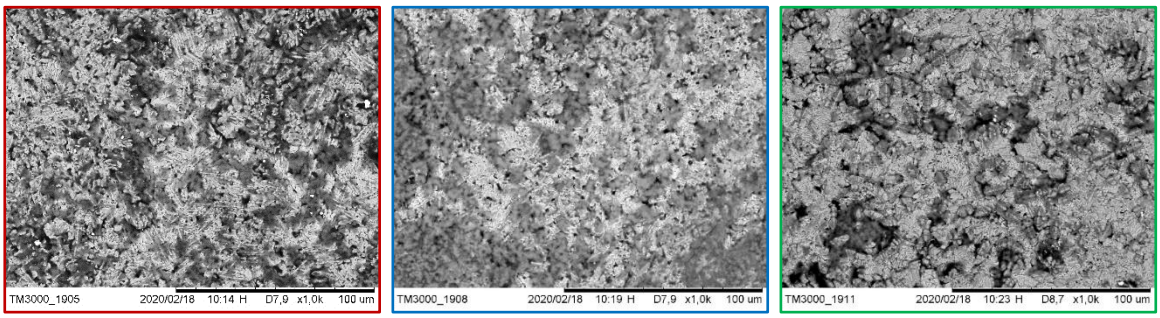

X1000

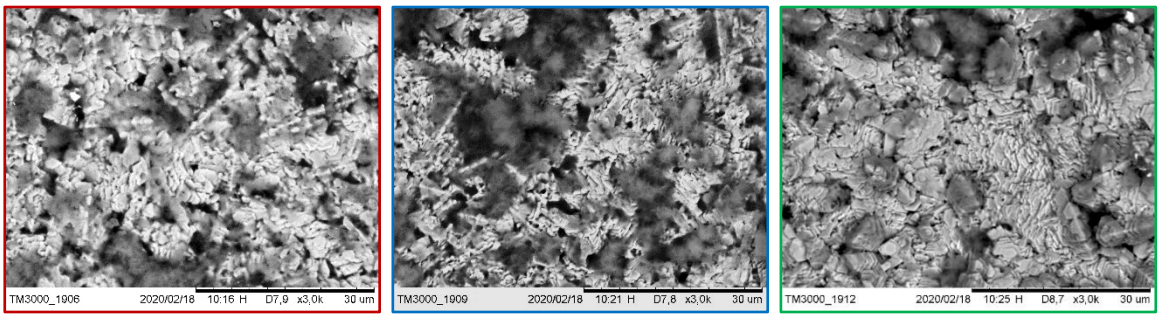

X3000

Figure 158: Test T32, Deposit surface at different current densities and magnification.

Cross section

300 A m^{-2}	200 A m^{-2}	100 A m^{-2}

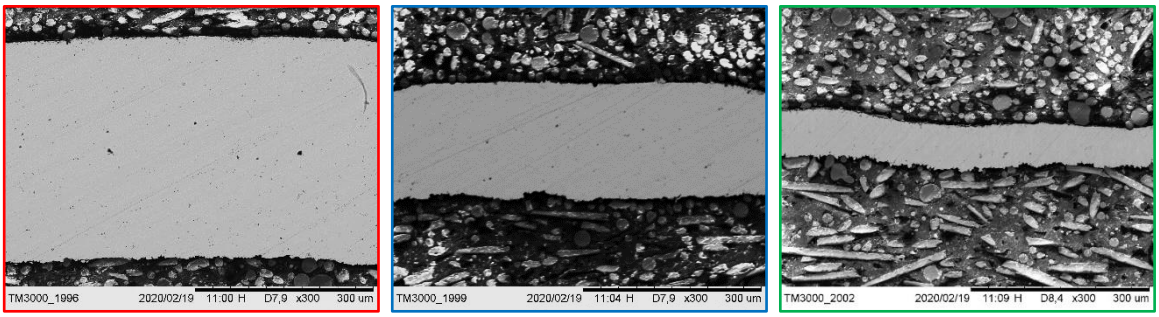

X300

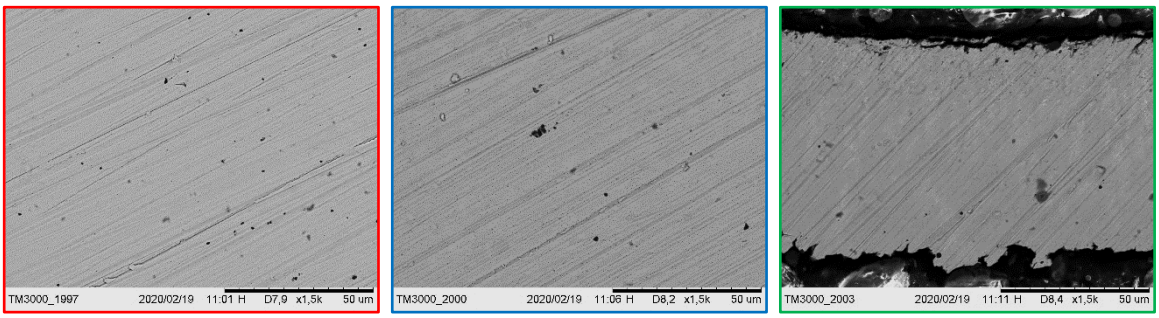

X1500

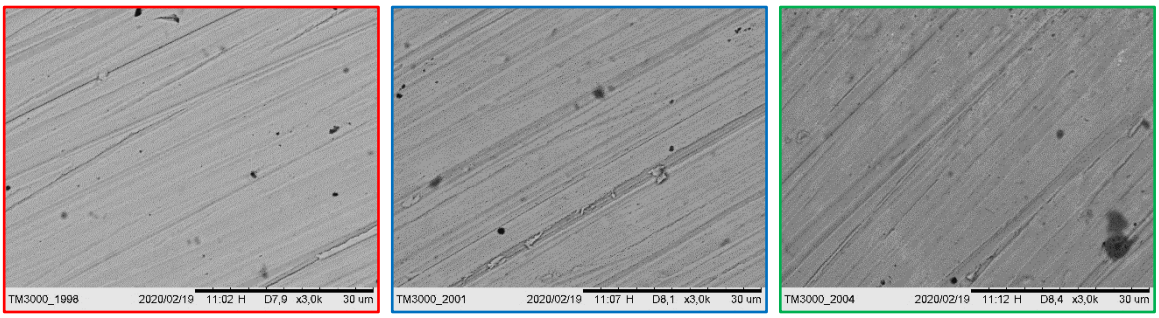

X3000

Figure 159: Test T32, Deposit cross section at different current densities and magnification.

[T33] Cetyltrimethylammonium bromide

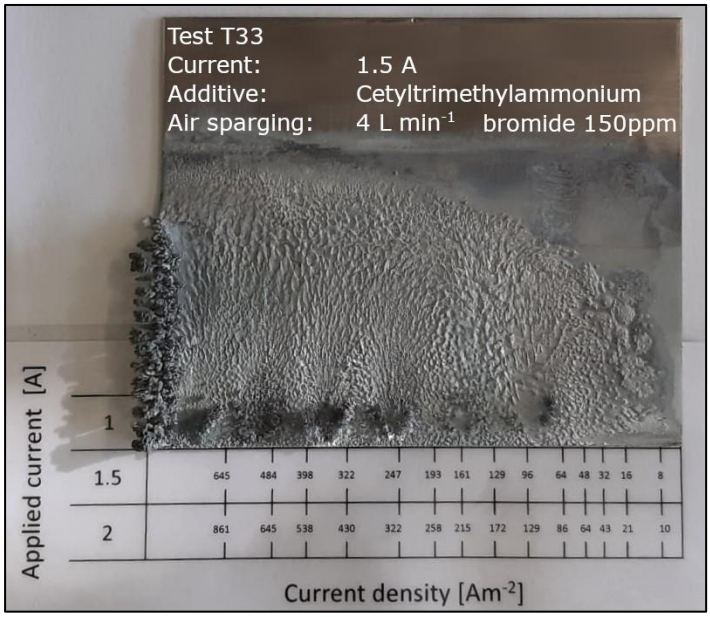

	Low	High
Adhesion	★★★★★	

	Brittle	Ductile
Fracture	★★☆☆☆	

Figure 160: Test T33, Deposit appearance.

Previous tests showed the beneficial effect of air sparging, so it was decided to set its flow rate at 4 l/min for the additive testing experiments. Starting with the T33 test, synthetic solutions were prepared as previously described with the addition of 150 ppm of the additive under test. The T33 test shows the effect of a quaternary ammonium salt; the zinc deposit, Figure 160, appears rough with a significant amount of dendrites on the left and bottom edges. Adhesion was extremely high, removal of the deposit was very difficult while the fracture type was quite brittle. The surface of the deposit, Figure 161, is generally characterized by large overlapping spots, at 300 A/m^2 an embedded lamellar structure can be recognized. At lower current densities, this structure gradually disappears giving way to a more compact structure. The cross sections, Figure 162, show some defects at the highest current density, while in general some cracks can be seen; this could be related to the hot assembly process and the brittle nature of the deposit.

Surface

300 A m^{-2}	200 A m^{-2}	100 A m^{-2}

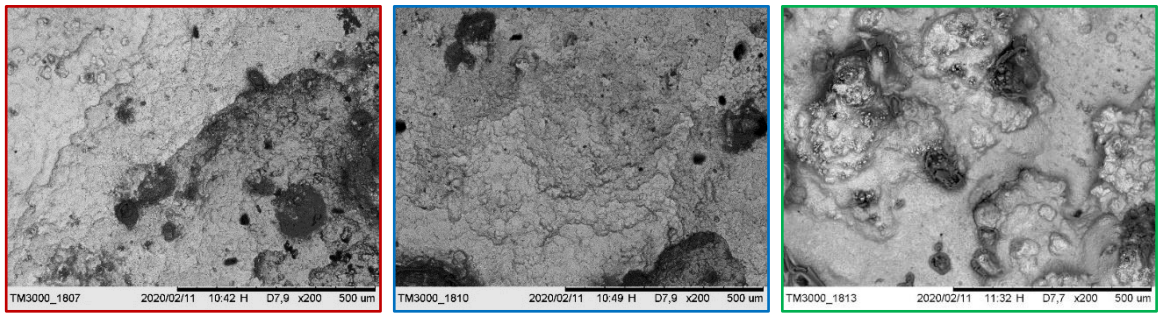

X200

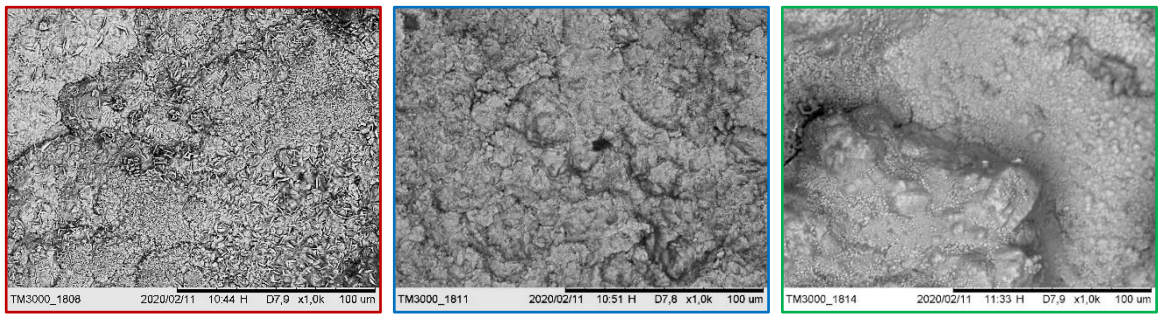

X1000

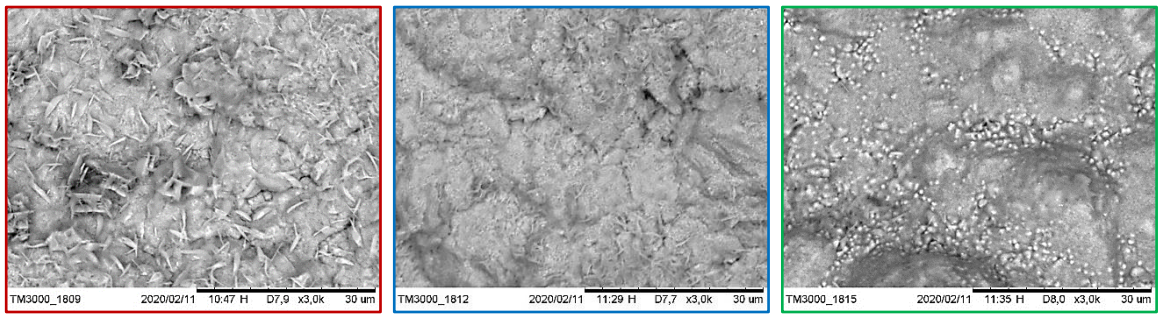

X3000

Figure 161: Test T33, Deposit surface at different current densities and magnification.

Cross section

300 A m^{-2}	200 A m^{-2}	100 A m^{-2}

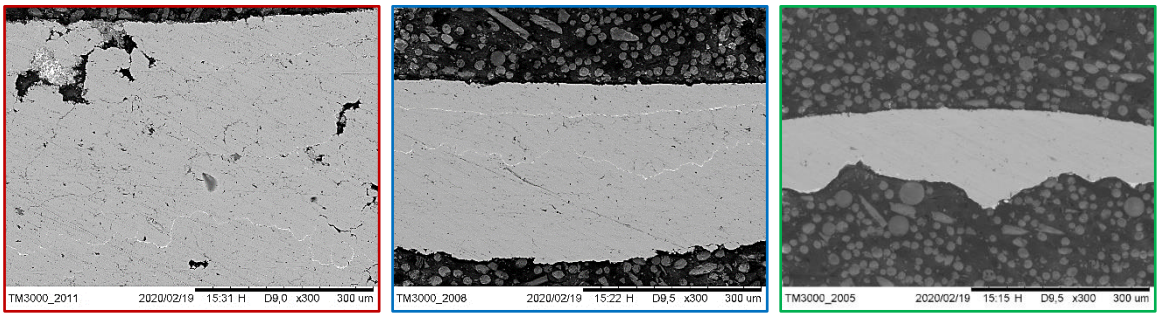

X300

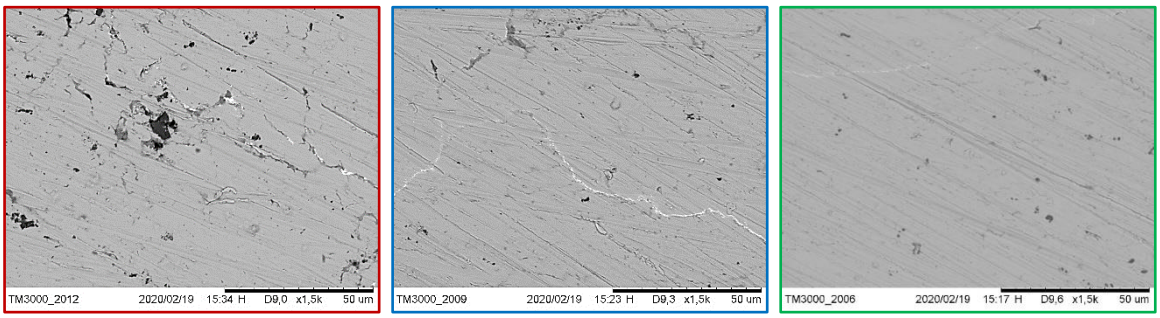

X1500

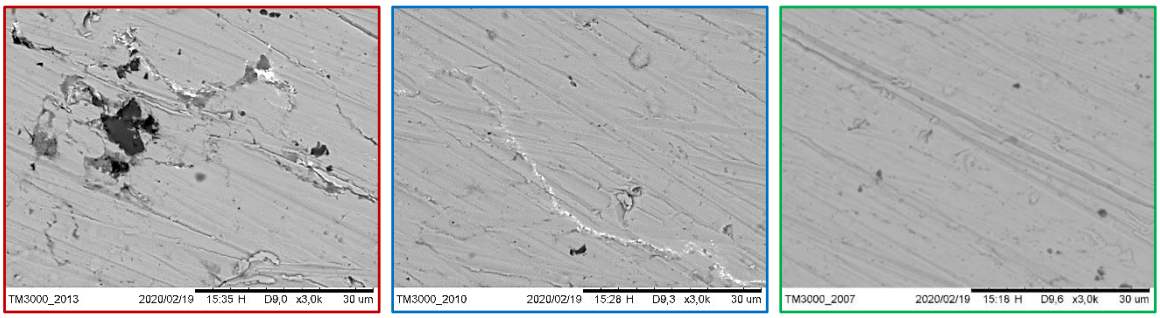

X3000

Figure 162: Test T33, Deposit cross section at different current densities and magnification.

[T34] Thiourea

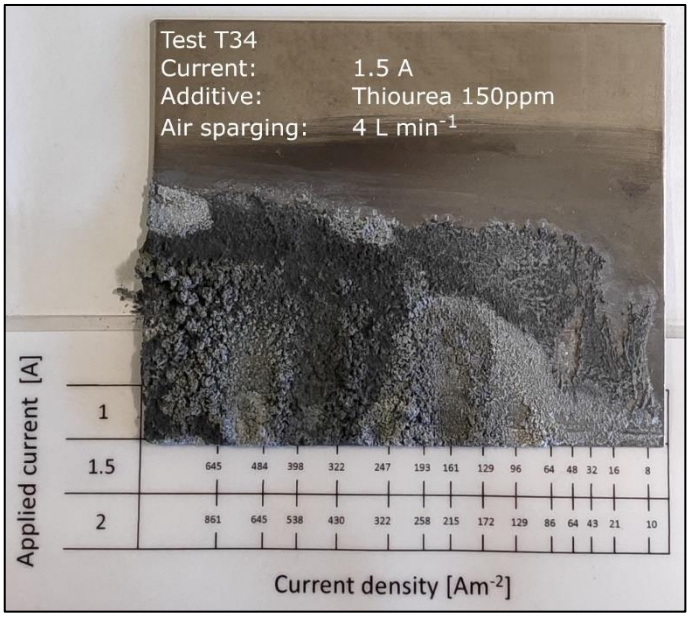

	Low	High
Adhesion	★☆☆☆☆	

	Brittle	Ductile
Fracture	★☆☆☆☆	

Figure 163: Test T34, Deposit appearance.

The T34 test shows the effect of thiourea on the zinc deposit. As can be seen in Figure 163, the deposit was floury and clearly with an undesirable structure; surface and cross-sectional analysis were not done

[T35] Tetraethylammonium chloride

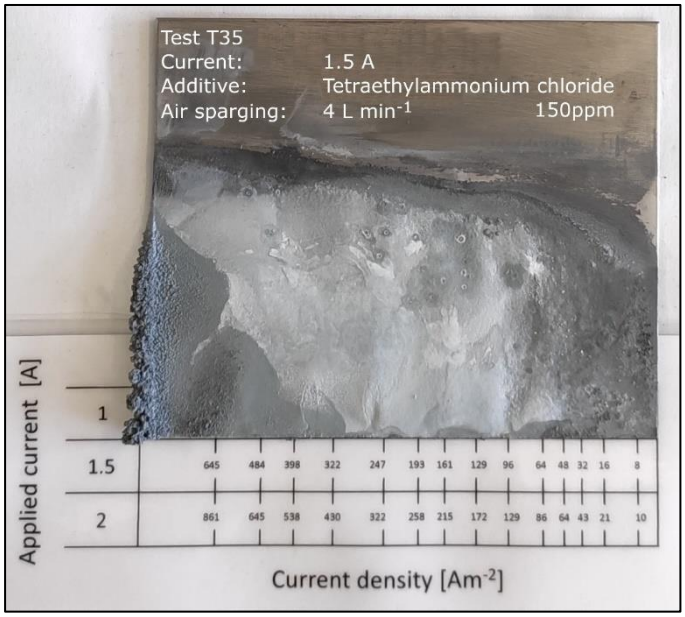

	Low	High
Adhesion	★★★★☆	

	Brittle	Ductile
Fracture	★★★☆☆	

Figure 164: Test T35, Deposit appearance.

Tetraethylammonium chloride, another quaternary ammonium salt, was tested in the T35 test. The resulting deposit, Figure 164, was smooth with the presence of a compact dendritic structure on the left edge. Adhesion was good, the detachment process was difficult only for the edges of the deposit while the central part was already detached. The fracture type was halfway between brittle and ductile. Surface analysis, Figure 165, shows large flat islands embedded in a porous sea at the highest current density, these flat islands tend to become larger at 200 A/m^2 but disappear at the lowest current density giving way to a highly porous structure. The cross sections, Figure 166, appear compact with some defects.

Surface

300 A m^{-2}	200 A m^{-2}	100 A m^{-2}

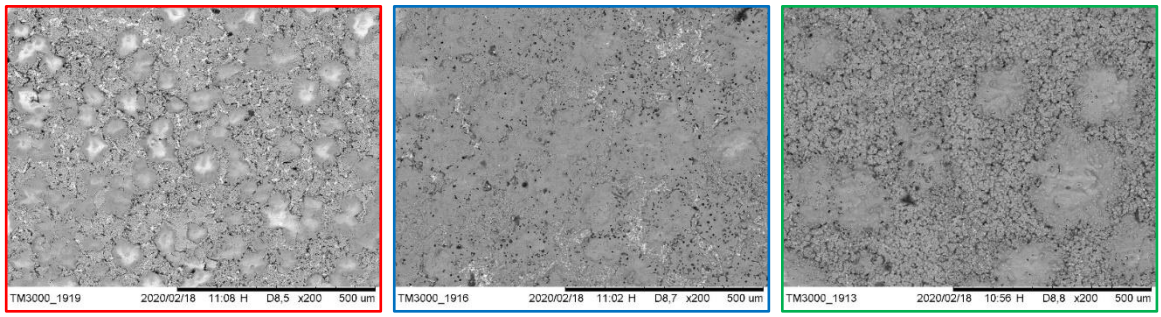

X200

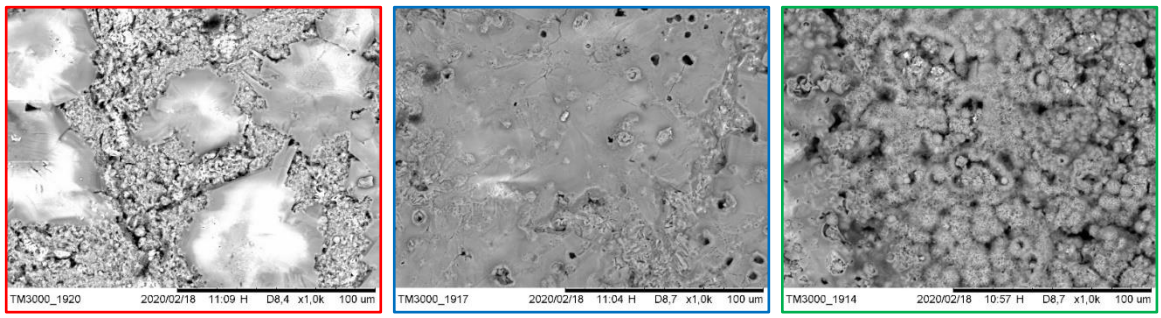

X1000

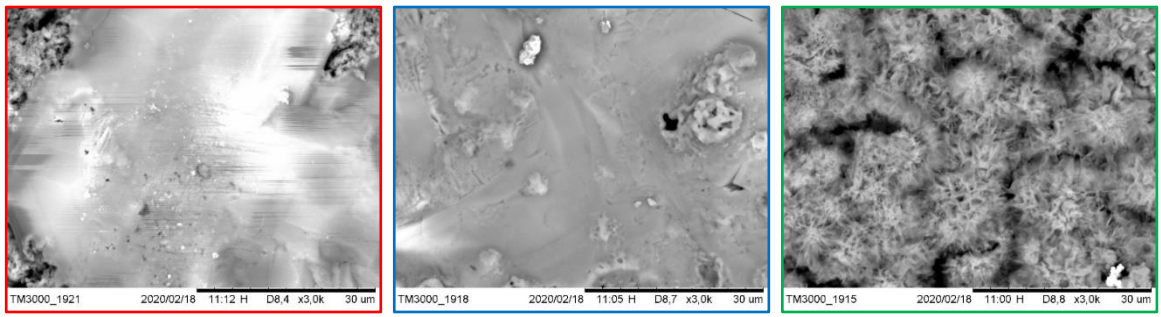

X3000

Figure 165: Test T35, Deposit surface at different current densities and magnification.

Cross section

300 A m^{-2}	200 A m^{-2}	100 A m^{-2}

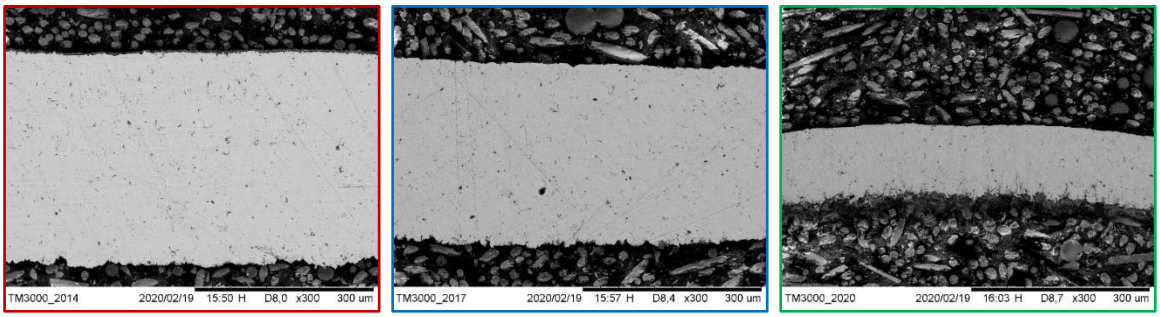

X200

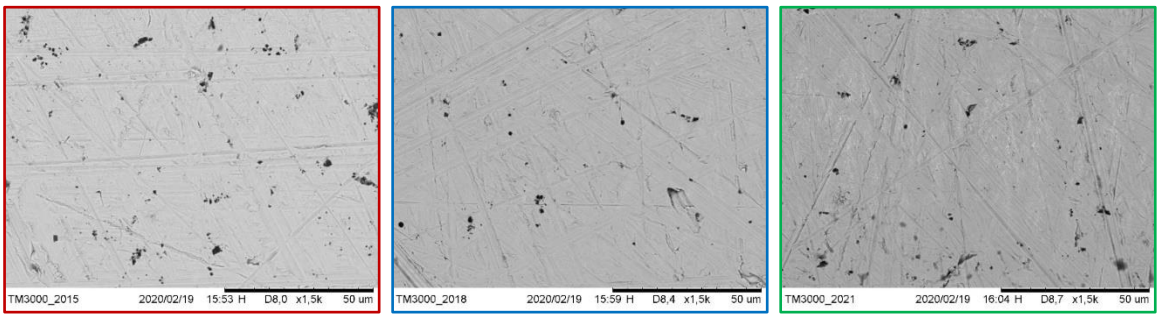

X1500

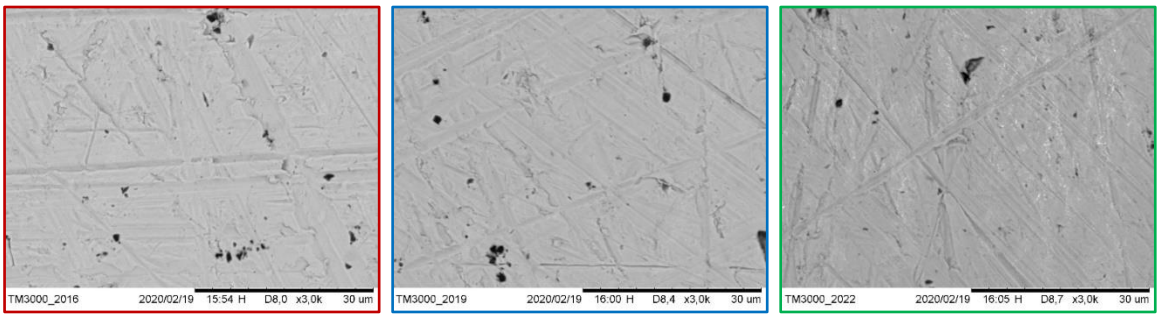

X3000

Figure 166: Test T35, Deposit cross section at different current densities and magnification.

[T36] PEG 4000

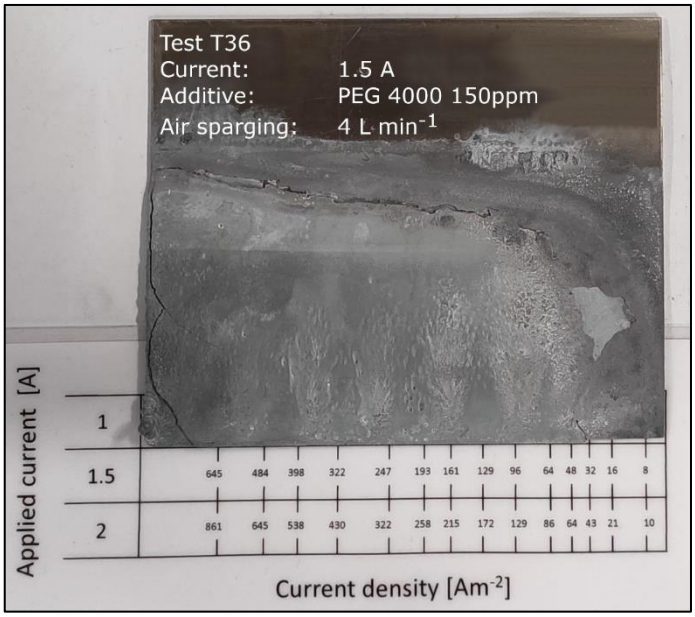

Low High

Adhesion ★★★★★

Brittle Ductile

Fracture ★☆☆☆☆

Figure 167: Test T36, Deposit appearance.

PEG 4000 stands for polyethylene glycol with an average molecular weight of 4000, the T36 test shows its effect on zinc electrodeposition. The deposit obtained, Figure 167, was extremely smooth, dendrites were absent even at the highest current density. Adhesion was very high while the fracture type was brittle. Starting with surface analysis at 300 A/m^2, Figure 168, two different zones can be distinguished; one is represented by a compact deposit while the other shows an acicular-lamellar structure embedded in a compact matrix. At the intermediate current density, the aciculo-lamellar structure is predominant and organized into patches with well-defined edges. The lower current density produced a deposit characterized by patches of aciculo-lamellar structure and grain agglomeration. Looking at the cross-section analysis, Figure 169, the deposit obtained at the highest current density appears compact with some defects, lower current densities show instead a mix of compact and porous zones. While at 100 A/m^2 such zones are distributed along the entire cross section, at 200 A/m^2 the highly porous zones are localized on the outer part of the deposit where an acicular-lamellar structure is clearly distinguishable.

Surface

300 A m^{-2}	200 A m^{-2}	100 A m^{-2}

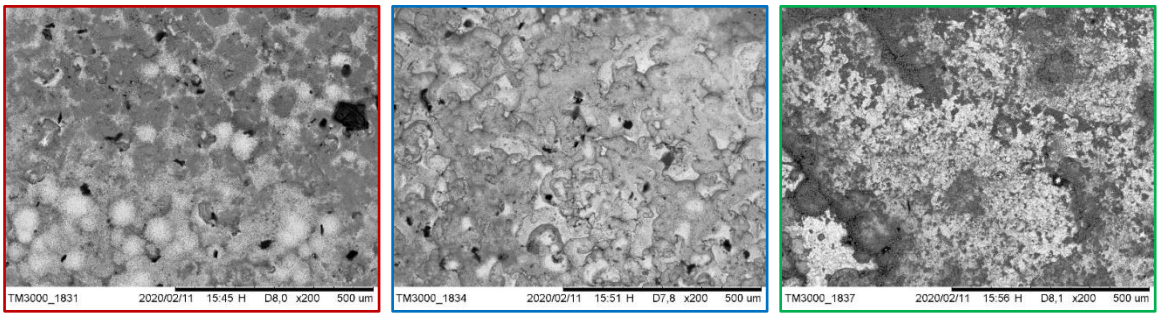

X200

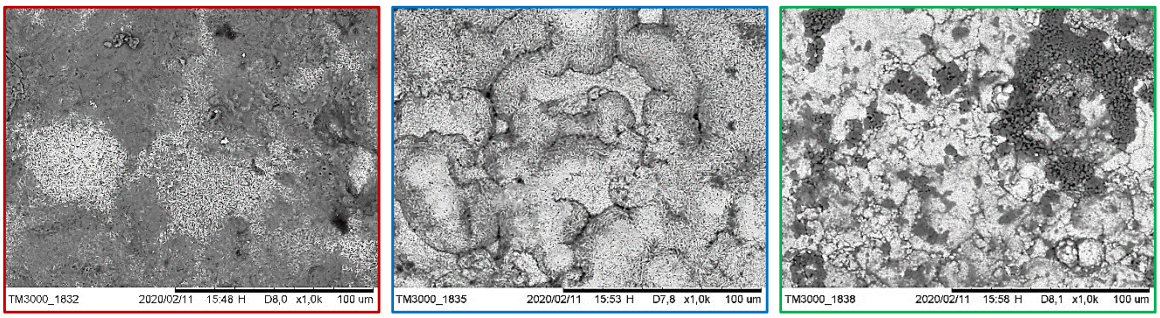

X1000

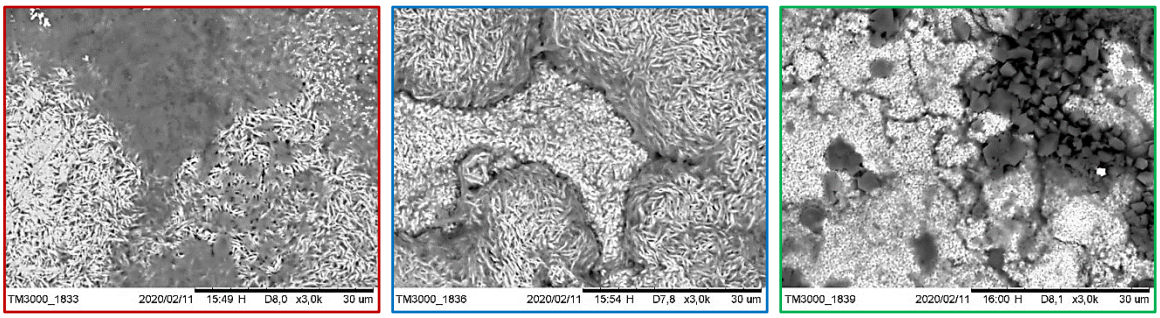

X3000

Figure 168: Test T36, Deposit surface at different current densities and magnification.

Cross section

300 A m^{-2}	200 A m^{-2}	100 A m^{-2}

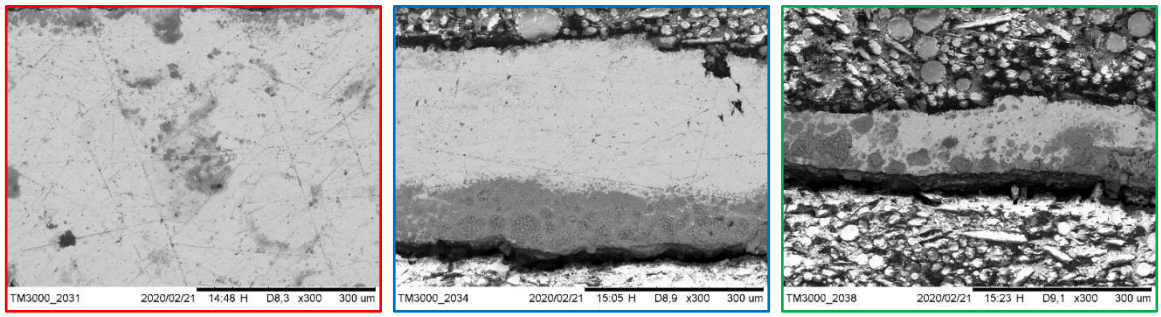

X300

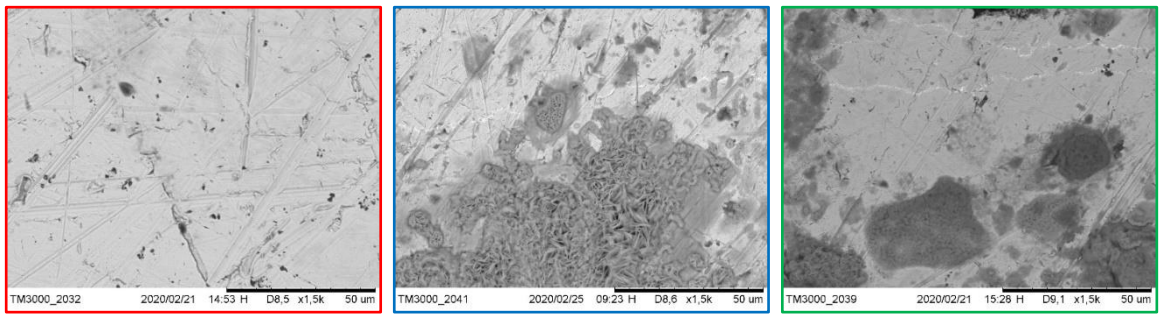

X1500

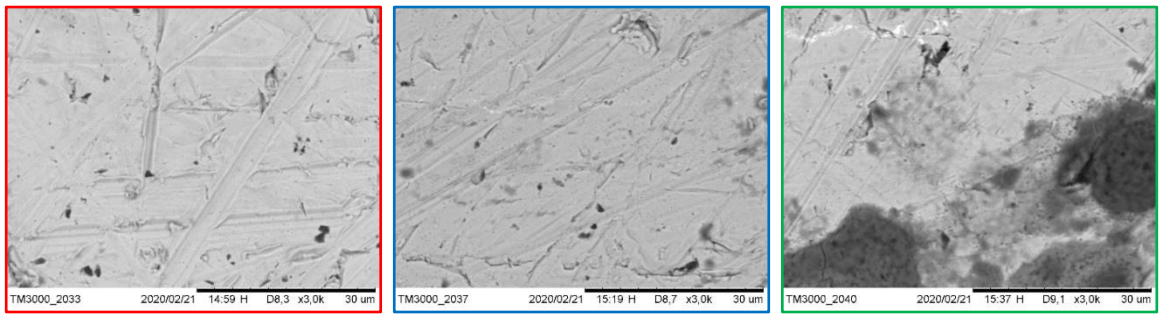

X3000

Figure 169: Test T36, Deposit cross section at different current densities and magnification.

[T37] Agar

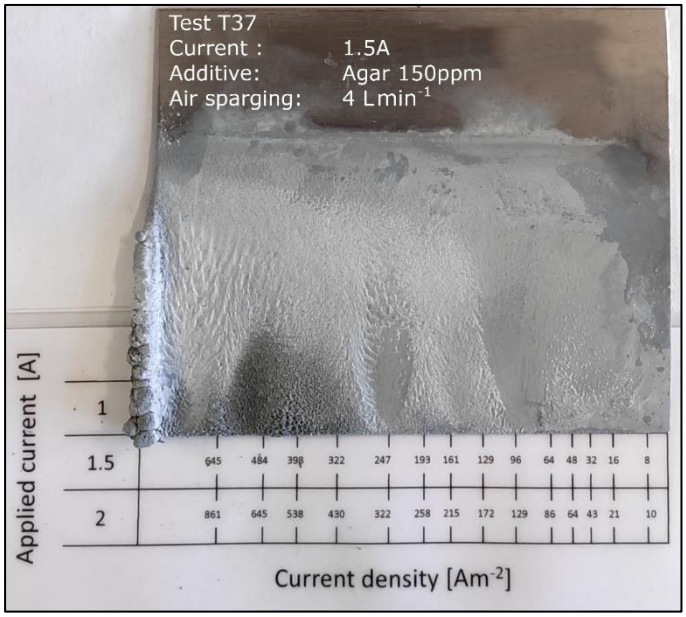

Low High

Adhesion ★★★☆☆

Brittle Ductile

Fracture ★☆☆☆☆

Figure 170: Test T37, Deposit appearance.

Agar is a plant gelatin extracted from an alga; its effect was tested in the T37 test. The deposit appeared a bit rough, the left edge showed dendritic growth that was smoothed by the effect of the additive. Adhesion was good while the fracture type was very brittle. At 300 A/m^2 the surface structure, Figure 171, can be described as blob like islands in which a not fully defined grain structure is present. As the current density is lowered, the grain structure tends to disappear giving way to a more porous morphology that prevails at 100 A/m^2. The cross section, Figure 172, shows a very compact structure with no substantial differences between the three current densities tested; a few small random holes are present.

Surface

300 A m^{-2}	200 A m^{-2}	100 A m^{-2}

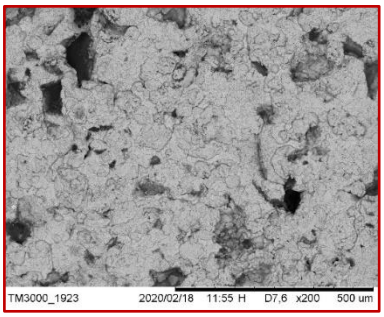

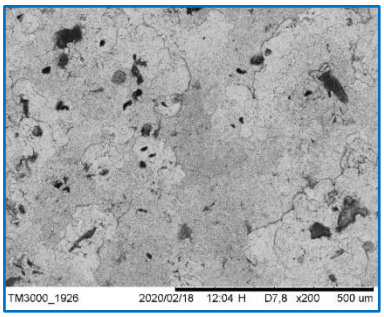

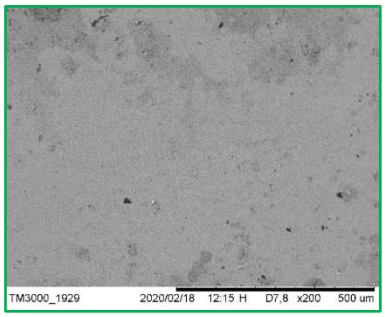

X200

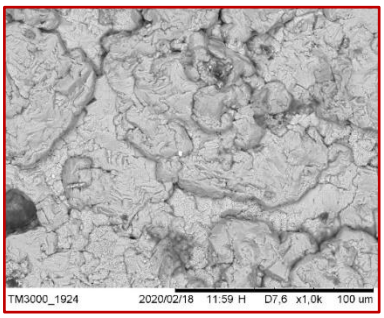

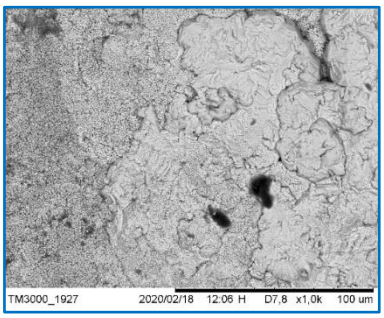

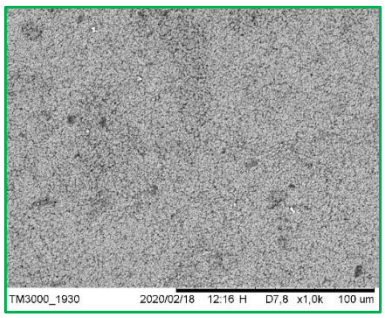

X1000

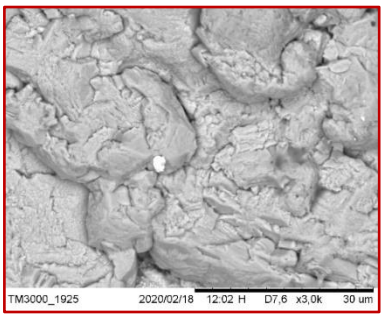

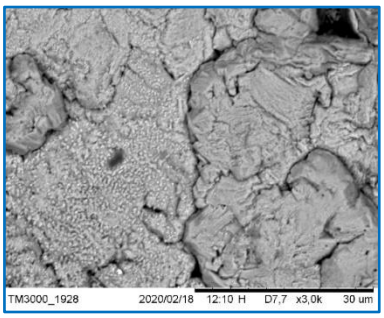

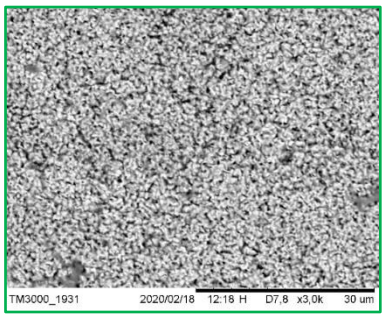

X3000

Figure 171: Test T37, Deposit surface at different current densities and magnification.

Cross section

300 A m^{-2}	200 A m^{-2}	100 A m^{-2}

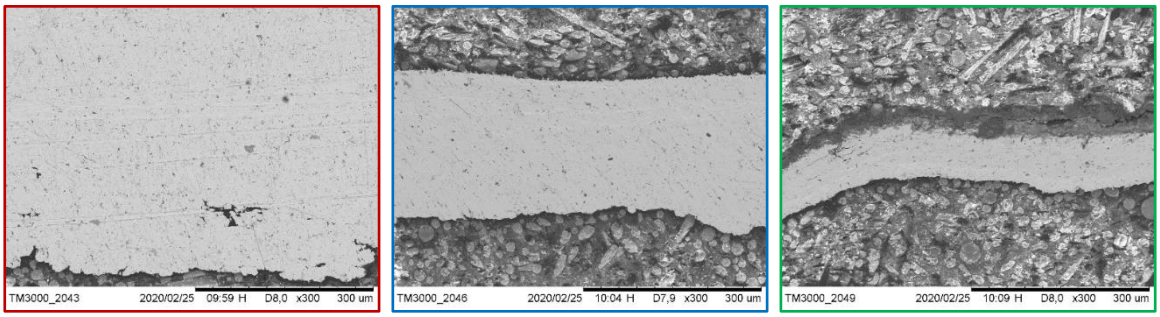

X300

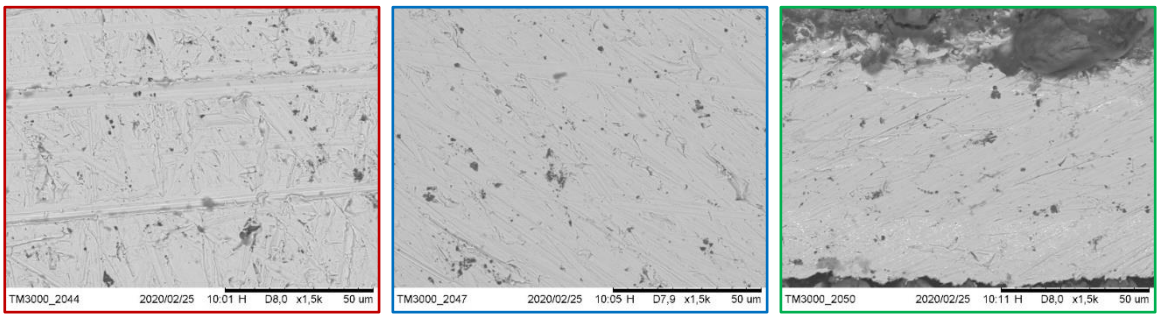

X1500

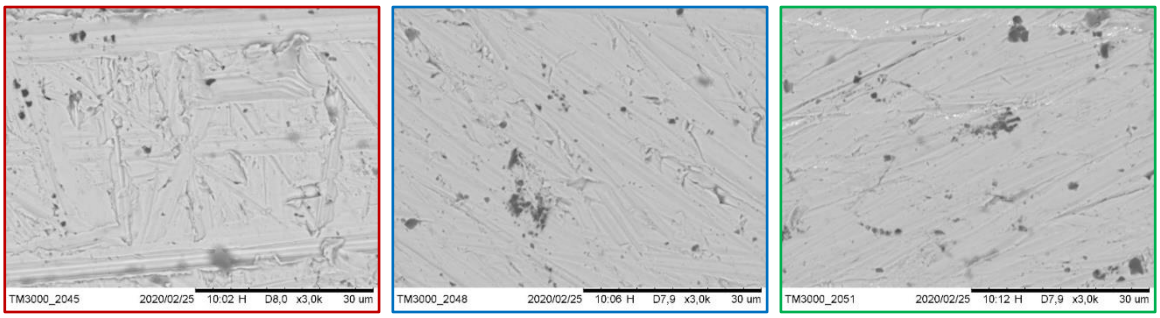

X3000

Figure 172: Test T37, Deposit cross section at different current densities and magnification.

[T38] PEG 300

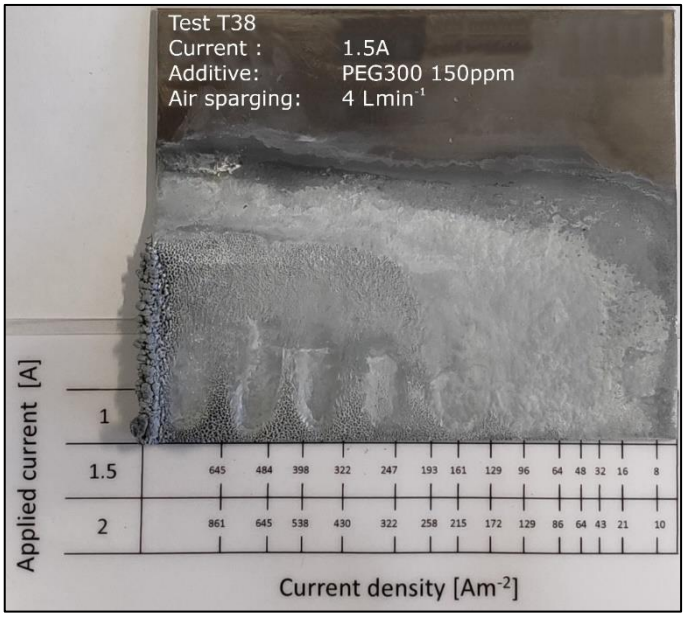

Low High

Adhesion ★★★★☆

Brittle Ductile

Fracture ★★☆☆☆

Figure 173: Test T38, Deposit appearance.

Test T38 shows the effect of PEG 300, polyethylene glycol with an average molecular weight of 300. The appearance of the deposit, Figure 173, differs from that obtained in the T36 test where a PEG with a higher average molecular weight was used; in this test it appears more porous at higher current densities and dendrite formation at the left edge is more abundant. Compared with the T36 test, the adhesion is somewhat lower while the fracture type is somewhat more ductile. The surface morphology, Figure 174, appears completely different; at 300 A/m^2 it is highly porous with an undefined shape, however, by lowering the current density, the deposit tends to take on a snowflake structure even though it remains porous. The cross sections, Figure 174, appear compact in general, some defect is present at low current densities which disappears at 300A/m^2.

Surface

300 A m^{-2}	200 A m^{-2}	100 A m^{-2}

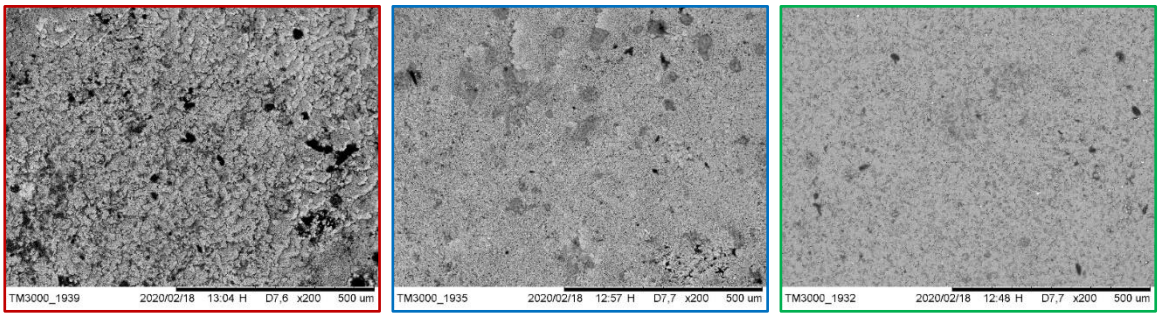

X200

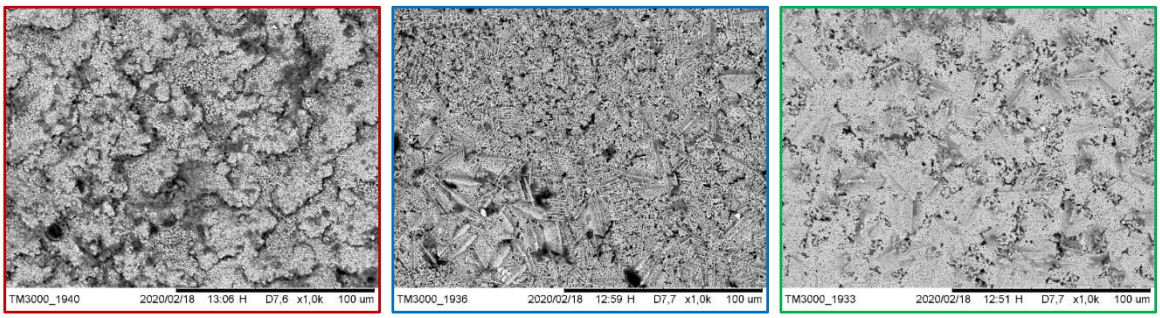

X1000

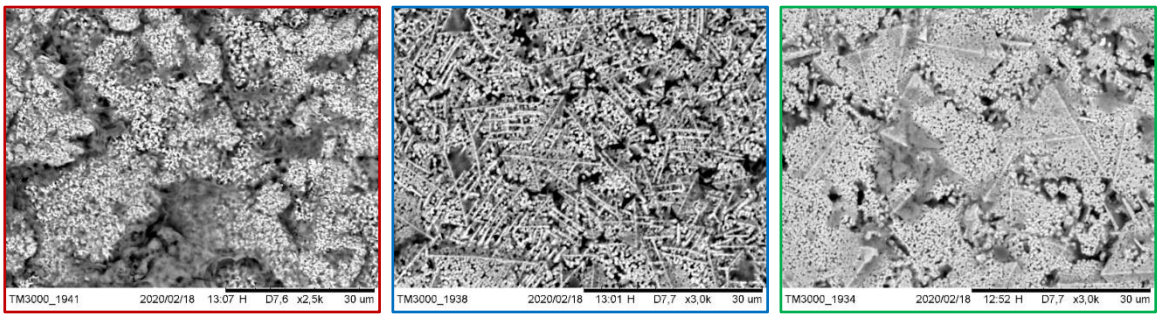

X3000

Figure 174: Test T38, Deposit surface at different current densities and magnification.

Cross section

300 A m^{-2}	200 A m^{-2}	100 A m^{-2}

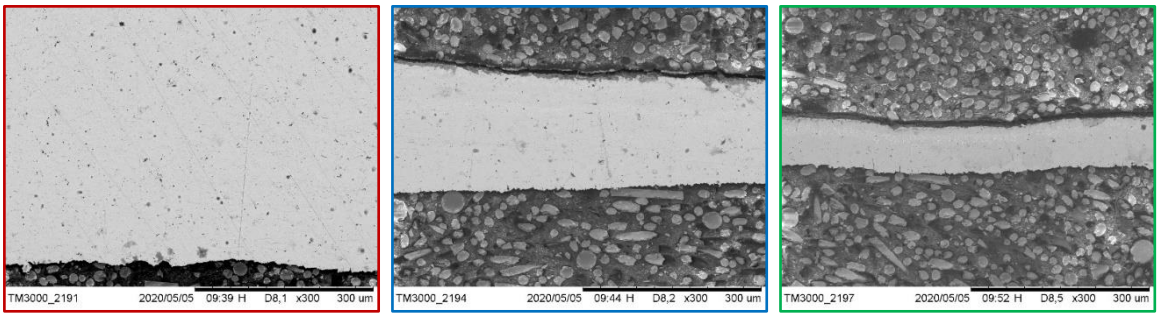

X300

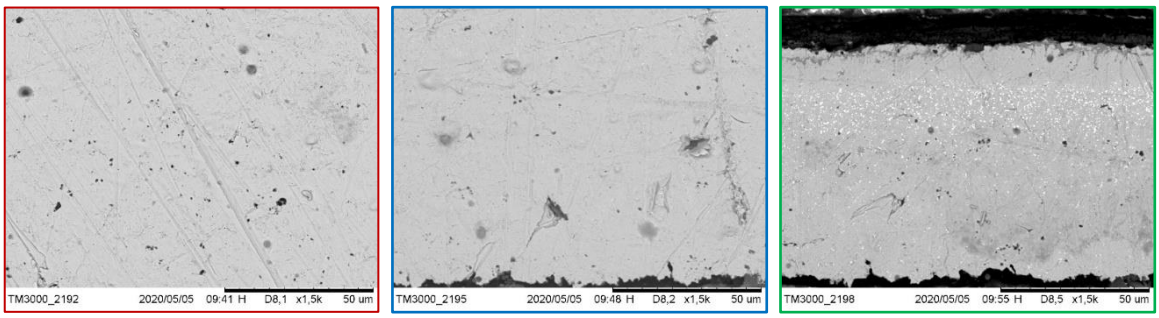

X1500

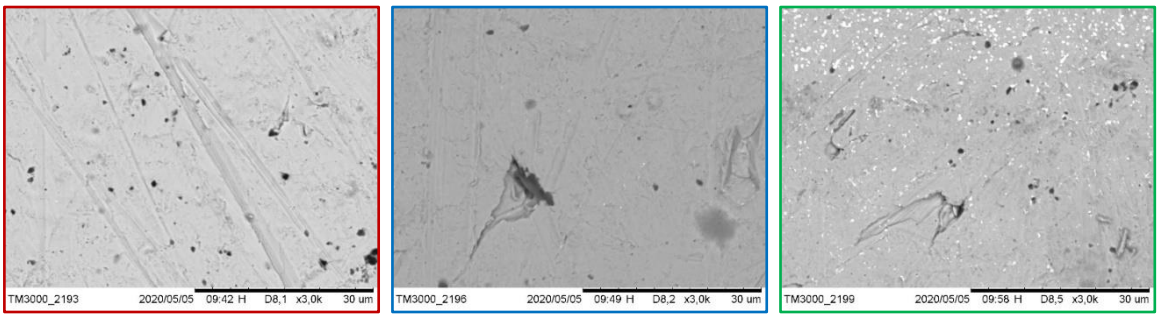

X3000

Figure 175: Test T38, Deposit cross section at different current densities and magnification.

[T39] Nicotinic acid

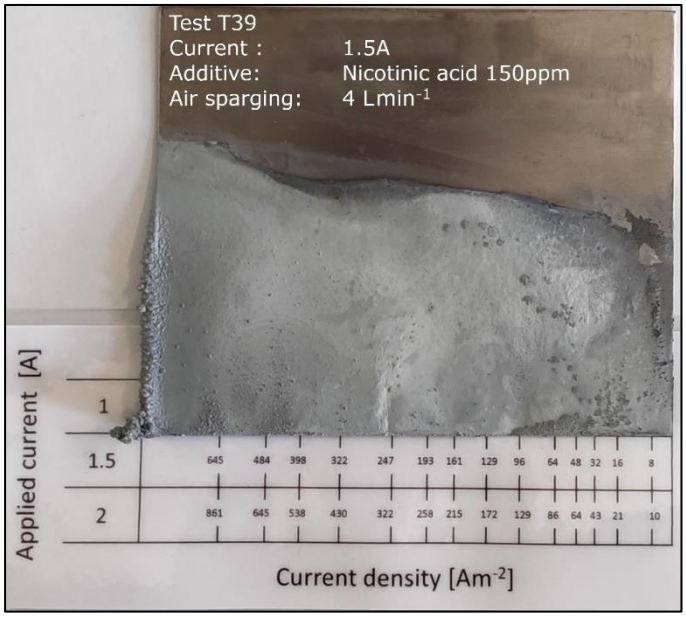

	Low	High
Adhesion	★★☆☆☆	

	Brittle	Ductile
Fracture	★★★☆☆	

Figure 176: Test T39, Deposit appearance.

The effect of nicotinic acid is shown in the T39 test, the deposit appears quite smooth, Figure 176, with a few small dendrites scattered across the surface. The left edge shows dendritic growth that appears to be partially inhibited by the additive, adhesion was quite low while the fracture type was somewhere between brittle and ductile. At the highest current density, the surface structure appears to be composed of a lamellar-type deposit embedded in a highly microporous matrix, Figure 177. As the current density is lowered, the deposit takes on a fine grain structure that appears to grow vertically and become denser at 100 A/m^2. Again, cross-sectional analysis shows an overall compact structure with random defects at all current densities, Figure 178.

Surface

300 A m^{-2}	200 A m^{-2}	100 A m^{-2}

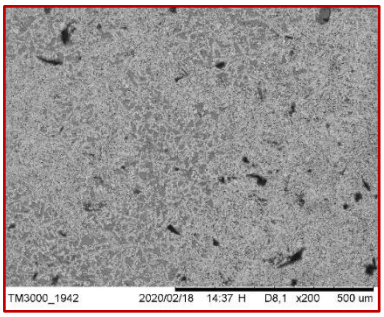

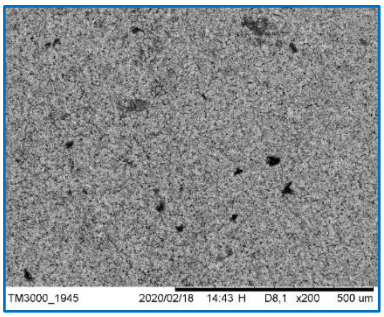

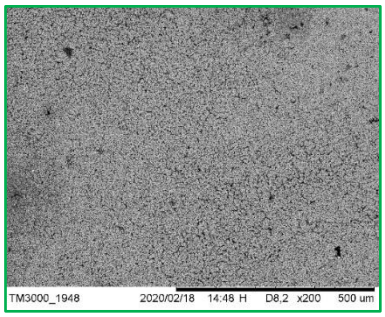

X200

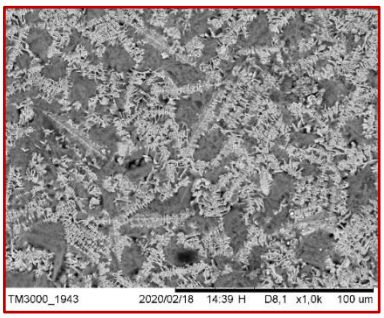

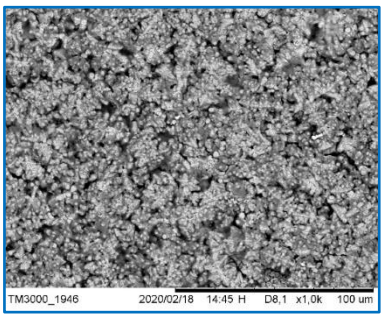

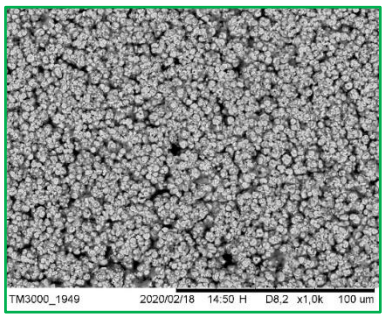

X1000

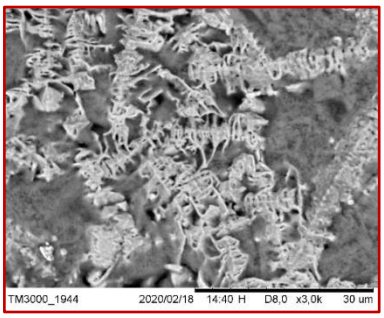

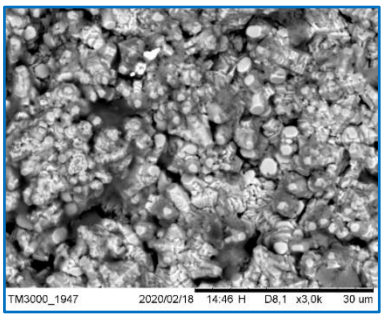

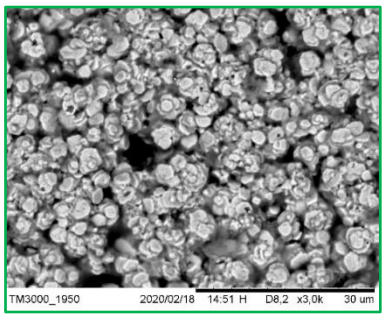

X3000

Figure 177: Test T39, Deposit surface at different current densities and magnification.

Cross section

300 A m^{-2}	200 A m^{-2}	100 A m^{-2}

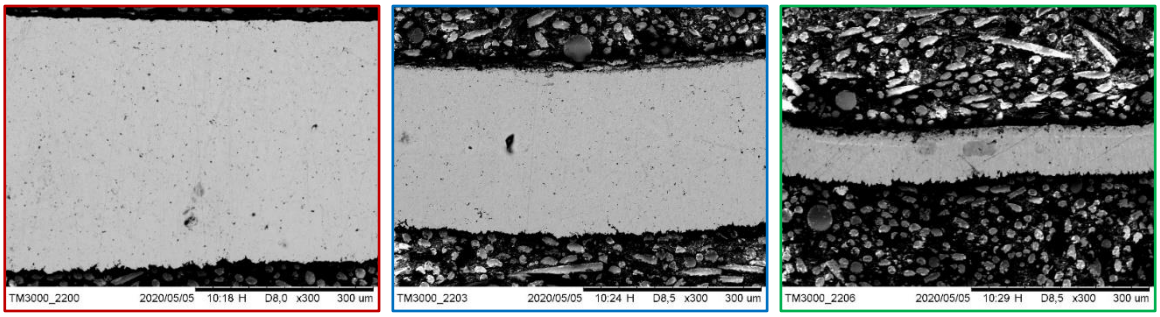

X300

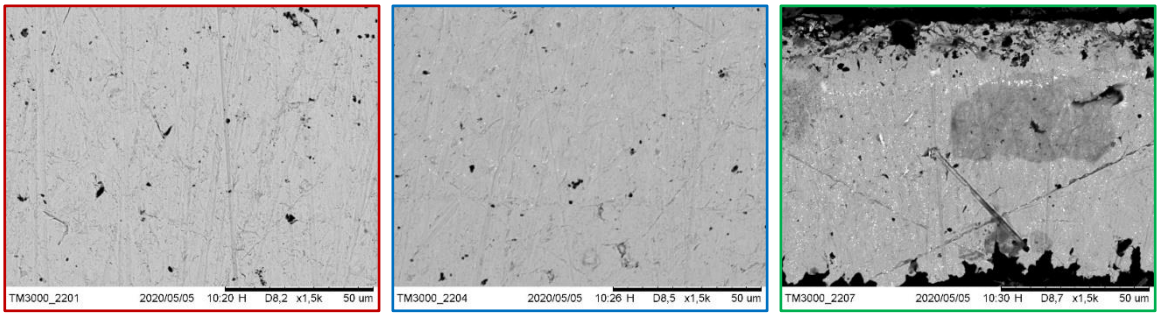

X1500

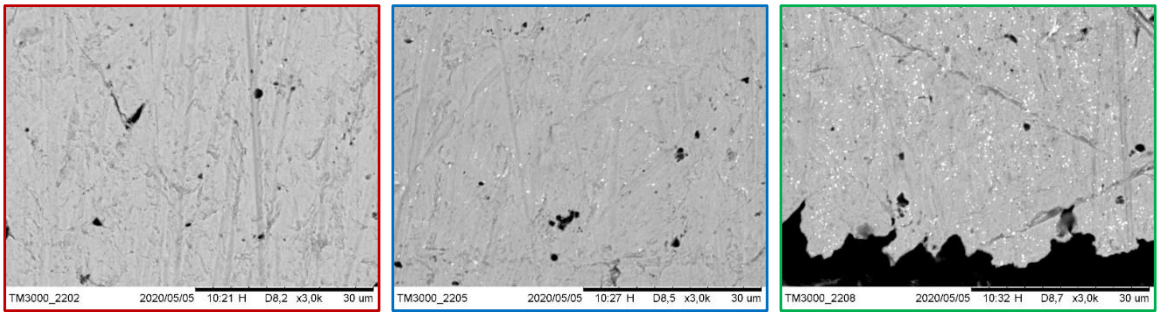

X3000

Figure 178: Test T39, Deposit cross section at different current densities and magnification.

[T40] Isonicotinic acid

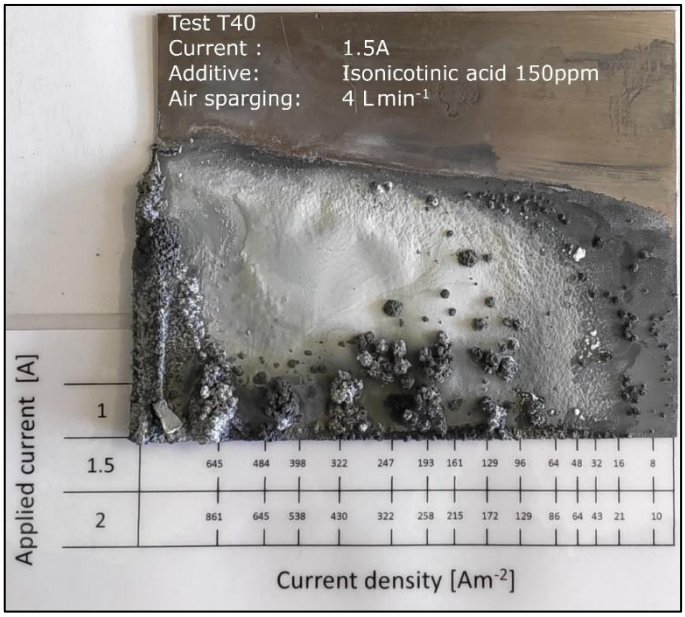

Low High

Adhesion ★★★★☆

Brittle Ductile

Fracture ★☆☆☆☆

Figure 179: Test T40, Deposit appearance.

The T40 test shows the effect of isonicotinic acid; the deposit appears smooth in the central part, Figure 179, but has clusters of dendrites that are spread over the entire current density range. Adhesion was quite high while the fracture type was very brittle. Looking at the surface analysis, Figure 180, the overall structure resembles a desert rose shape in which flattened crystals are randomly arranged. The size of the crystals appears to decrease at low current density, except for the 200 A/m^2 case where the above shape is mixed with areas where the deposit appears more compact. Cross section analysis, Figure 181, shows a compact structure mixed with scattered porous zones.

Surface

300 A m^{-2}	200 A m^{-2}	100 A m^{-2}

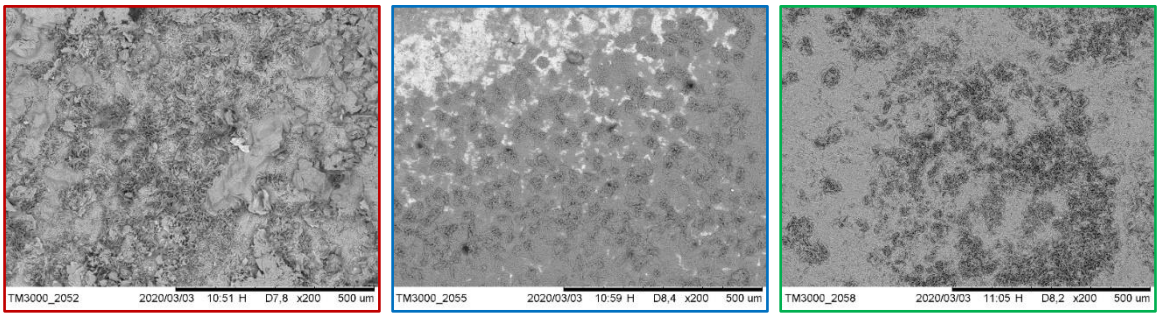

X200

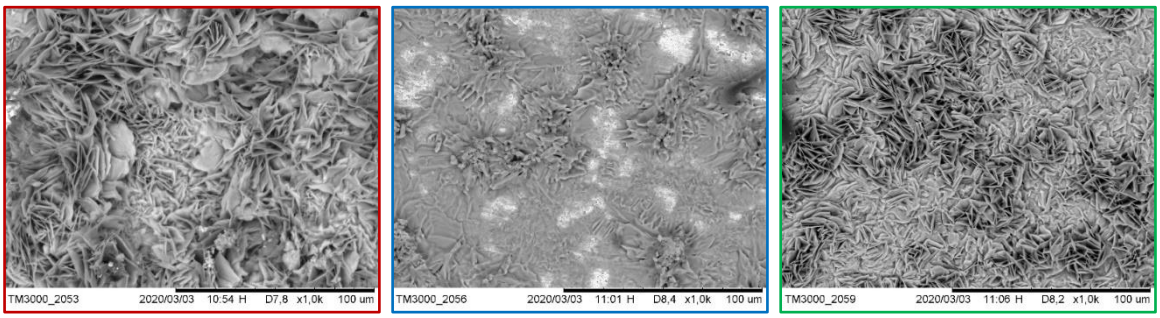

X1000

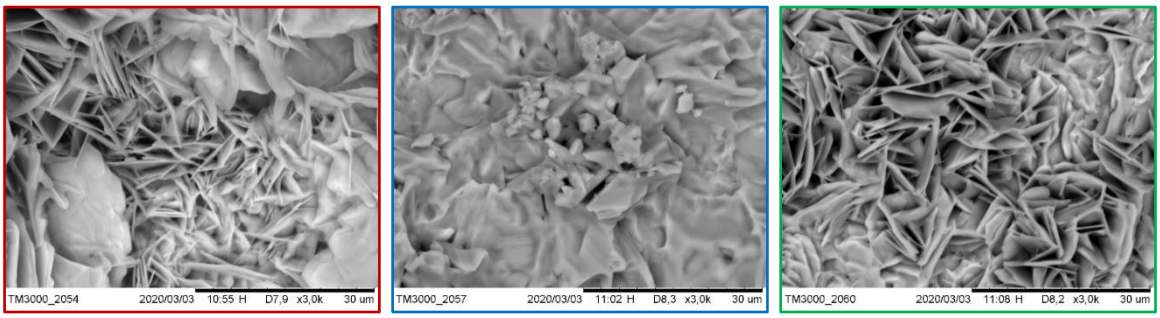

X3000

Figure 180 Test T40, Deposit surface at different current densities and magnification.

Cross section

300 A m^{-2}	200 A m^{-2}	100 A m^{-2}

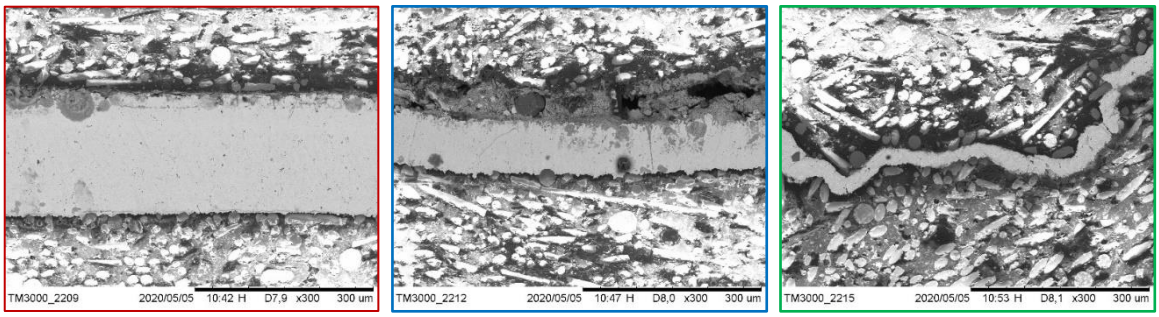

X300

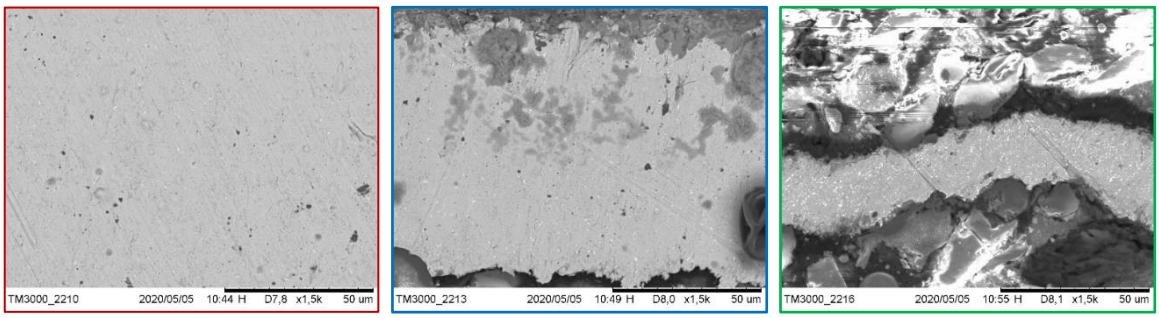

X1500

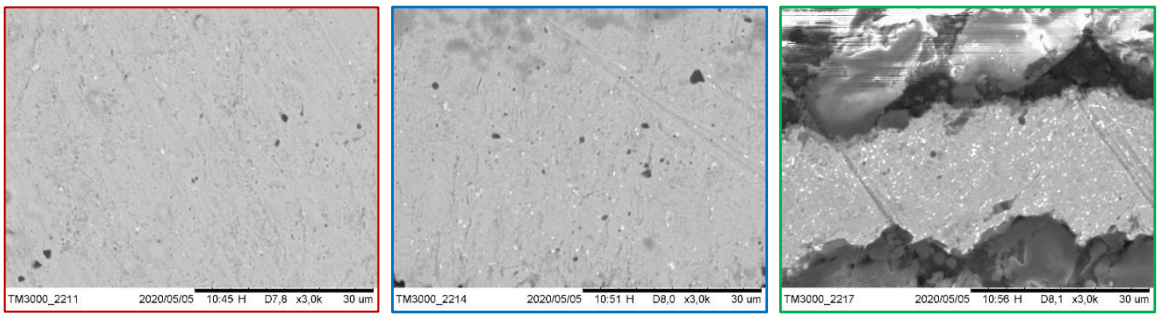

X3000

Figure 181: Test T40, Deposit cross section at different current densities and magnification.

[T41] Piconicotinic acid

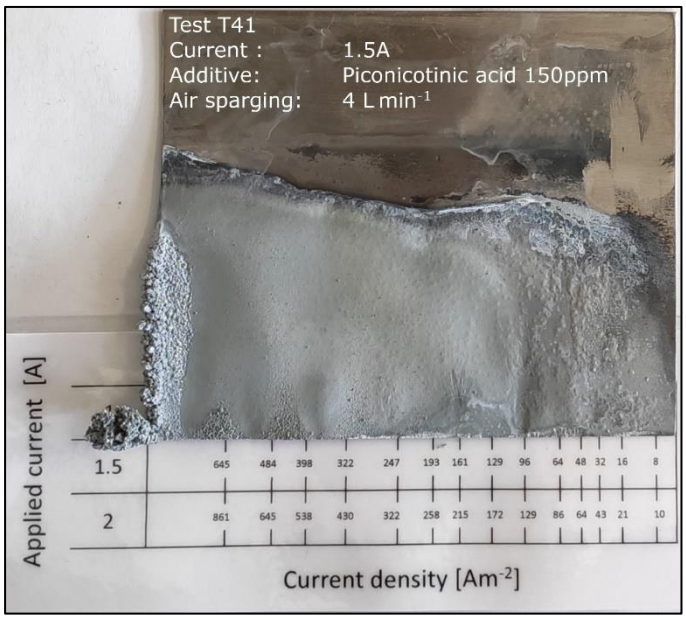

	Low	High
Adhesion	★★☆☆☆	

	Brittle	Ductile
Fracture	★★★☆☆	

Figure 182: Test T41, Deposit appearance.

The effect of piconicotinic acid is shown in the T41 test; the deposit appears quite smooth, Figure 182, with some dendrites on the left edge. The top of the deposits is detached from the titanium cathode, so adhesion was low; the type of fracture was in the middle between ductile and brittle behavior. Magnifications of the surface, Figure 183, show a structure composed of small grains clustered together at 100 A/m^2 while at higher current densities, the grains disappear giving way to a lamellar structure that tends to grow vertically. In both cases the deposit appears to be highly porous. Cross-sectional analysis, Figure 184, shows a compact structure with clusters of small holes that disappear at the lowest current density.

Surface

300 A m^{-2}	200 A m^{-2}	100 A m^{-2}

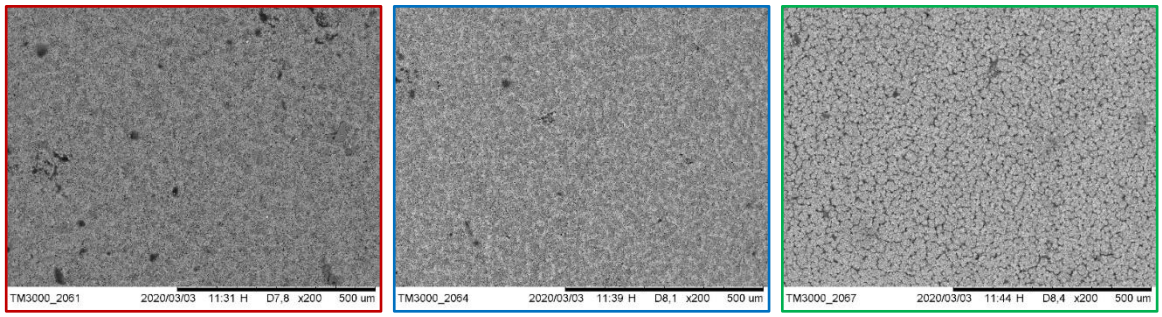

X200

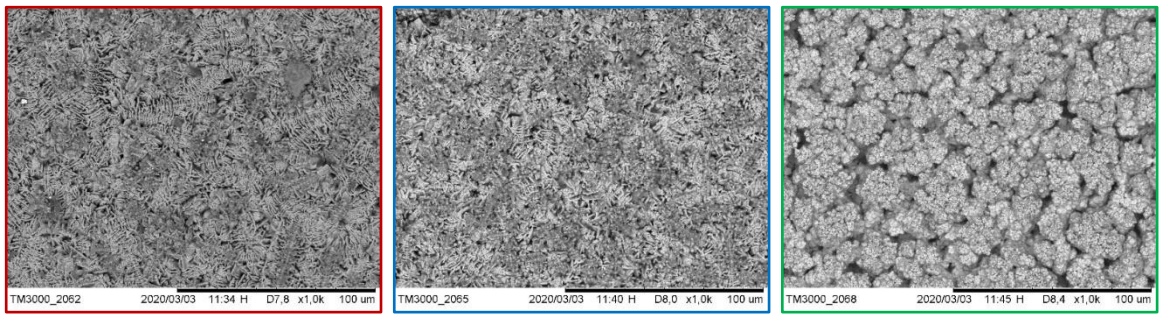

X1000

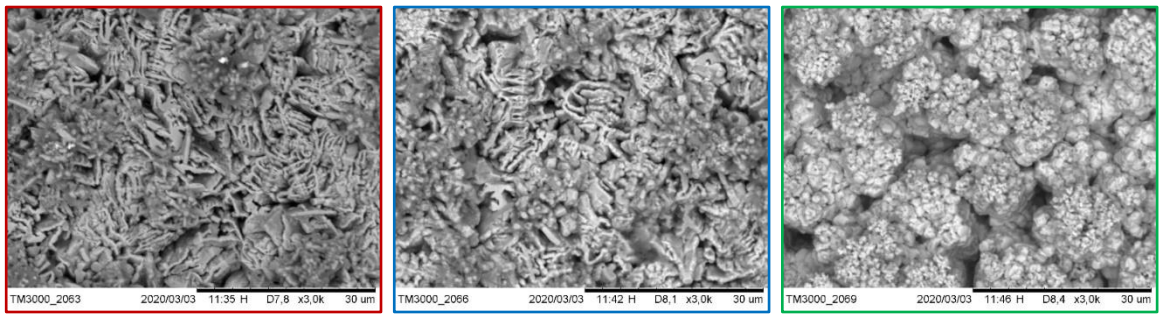

X3000

Figure 183: Test T41, Deposit surface at different current densities and magnification.

Cross section

300 A m^{-2}	200 A m^{-2}	100 A m^{-2}

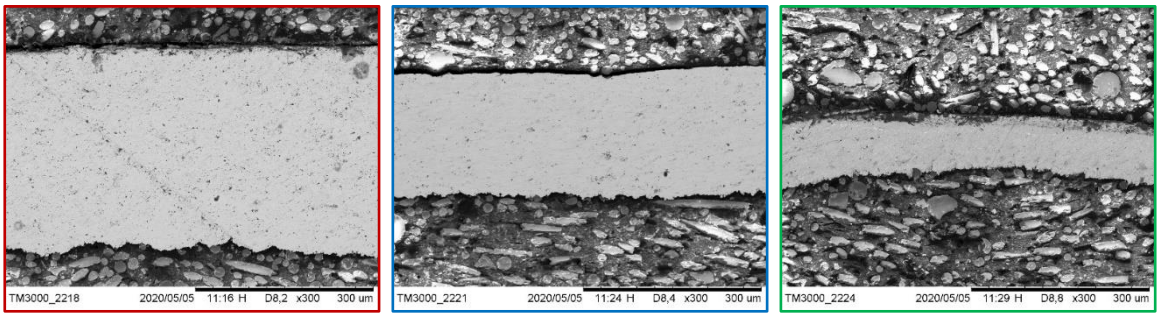

X300

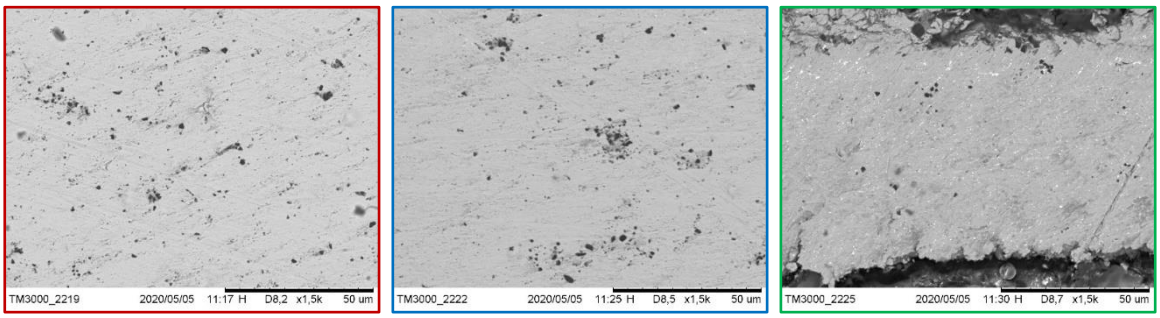

X1500

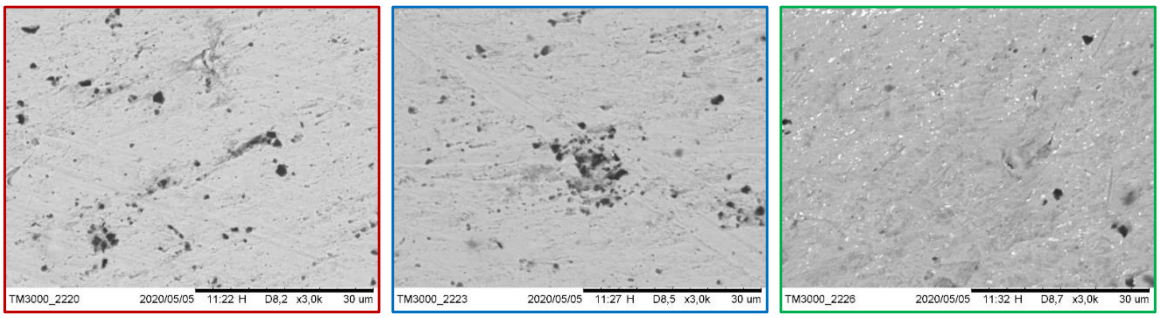

X3000

Figure 184: Test T42, Deposit cross section at different current densities and magnification.

[T42] Aesculus hippocastanum

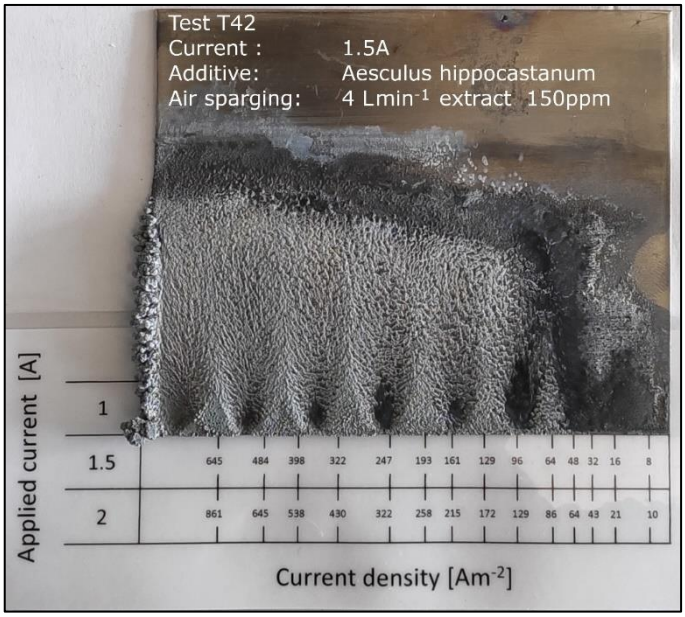

	Low	High
Adhesion	★★★☆☆	

	Brittle	Ductile
Fracture	★★☆☆☆	

Figure 185: Test T42, Deposit appearance.

Aesculus hippocastanum extract, as a source of escin, was tested in the T42 test. The surface of the deposit, Figure 185, appears knurled with a pine-like structure at the air sparging holes; some dendrites were present at the left edge. Adhesion was medium while the fracture type was quite brittle. Surface analysis, Figure 186, reveals a compact structure arranged in a terraced conformation; as the current density is lowered, this structure tends to become more porous. Cross section, Figure 187, reveals a structure that appears to be composed of the superposition of several layers of deposit; this is more pronounced at the highest current density. At 100 A/m^2, the deposit appears more porous especially in the outer part.

Surface

300 A m^{-2}	200 A m^{-2}	100 A m^{-2}

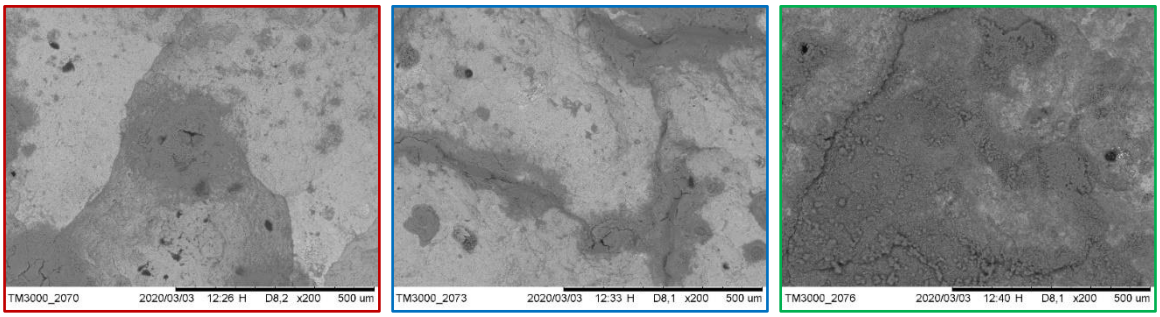

X200

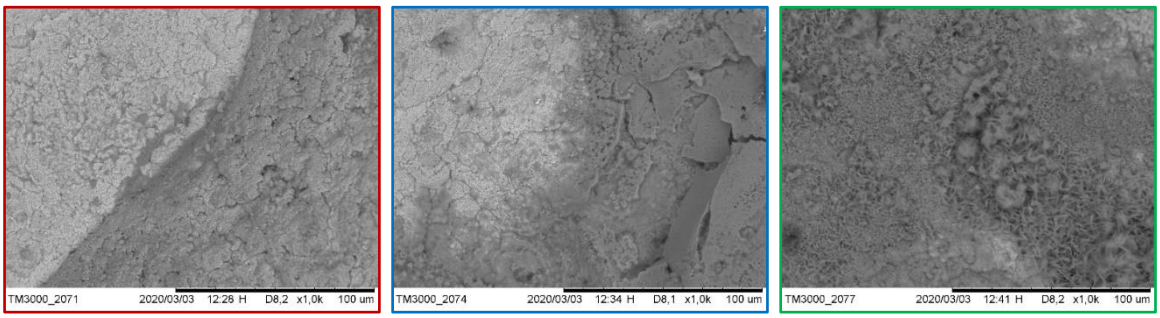

X1000

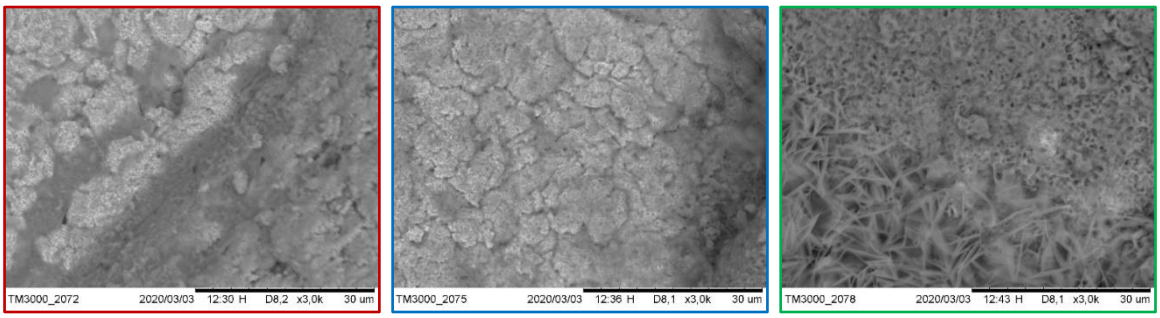

X3000

Figure 186: Test T42, Deposit surface at different current densities and magnification.

Cross section

300 A m^{-2}	200 A m^{-2}	100 A m^{-2}

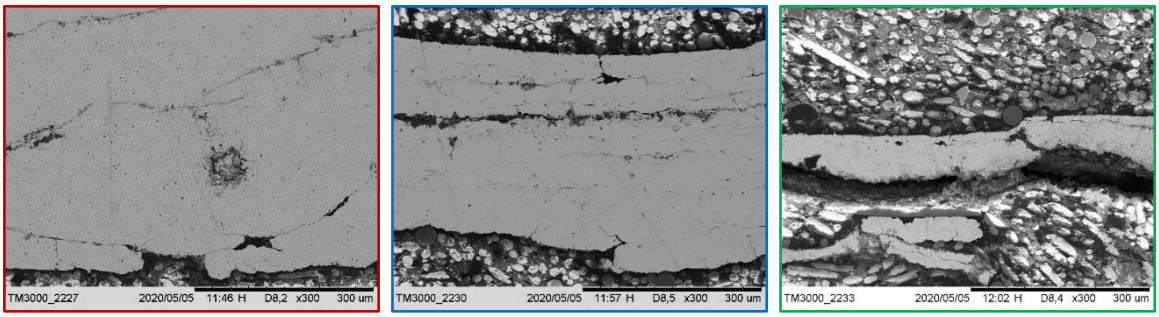

X300

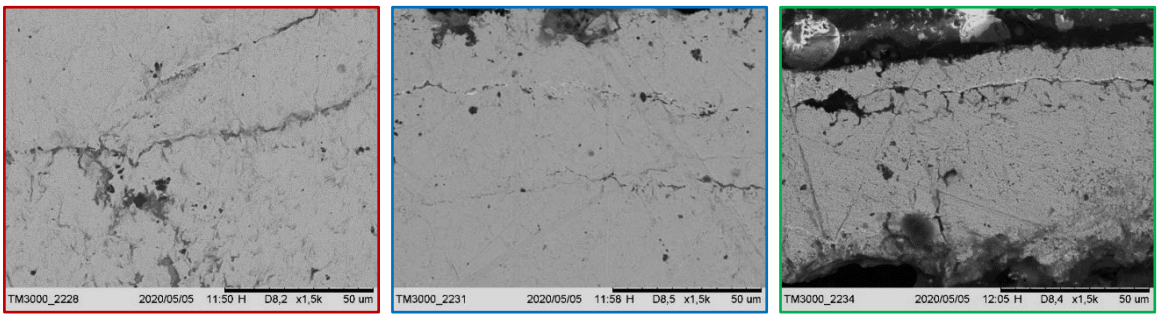

X1500

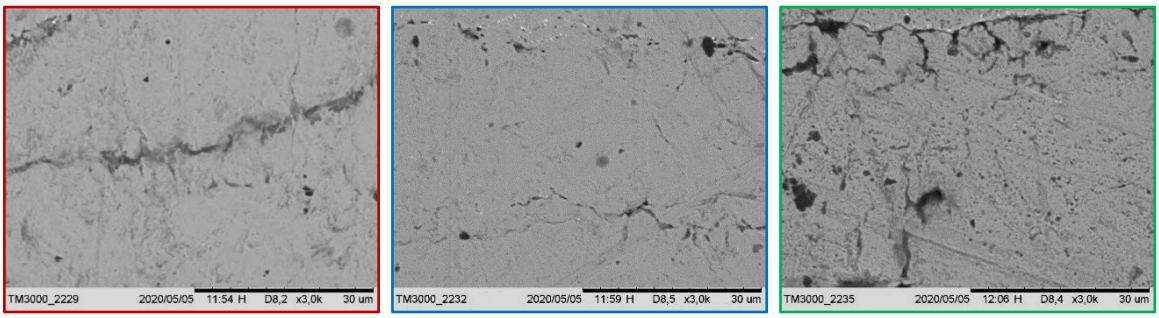

X3000

Figure 187: Test T42, Deposit cross section at different current densities and magnification.

[T43] Liquorice

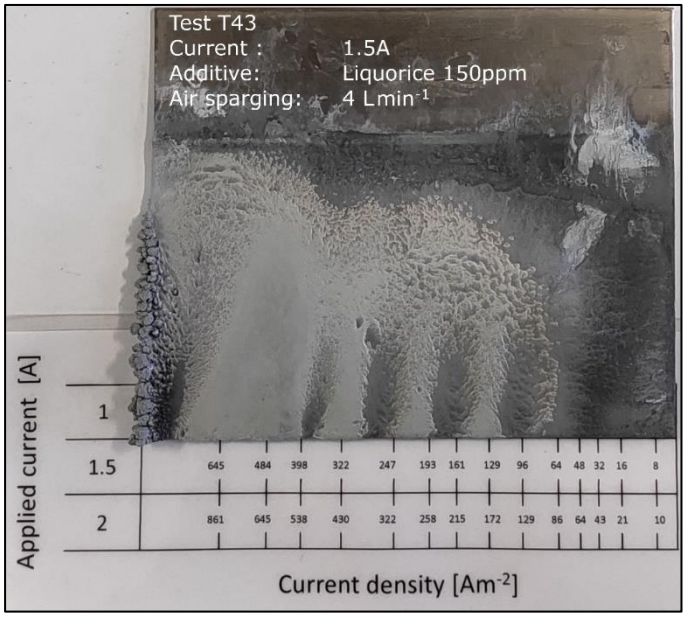

	Low	High
Adhesion	★★★★☆	

	Brittle	Ductile
Fracture	★★☆☆☆	

Figure 188: Test T43, Deposit appearance.

Another source of saponins is liquorice, tested in the T43 test. Some areas of the deposit appeared smooth while others resembled the texture of artificial leather. Adhesion was quite high while the fracture type was brittle. Even with this saponin, the surface structure, Figure 189, appears arranged in a terraced conformation. These are composed of large grains that tend to disappear as the current density is lowered, however, the deposit is generally very compact. Cross-sectional analysis, Figure 190, shows a compact deposit at the highest current density that tends to become more porous as the current density decreases.

Surface

300 A m^{-2}	200 A m^{-2}	100 A m^{-2}

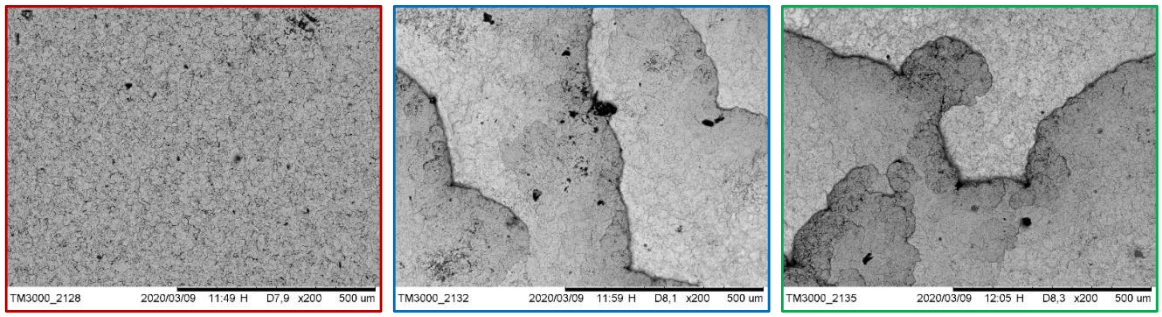

X200

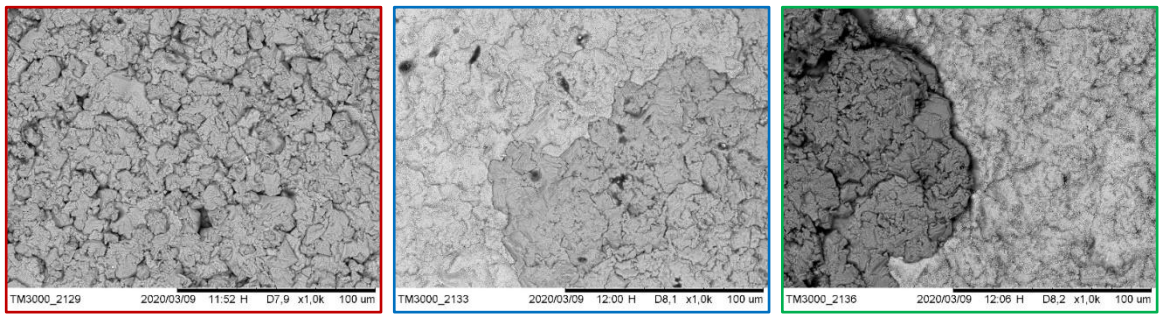

X1000

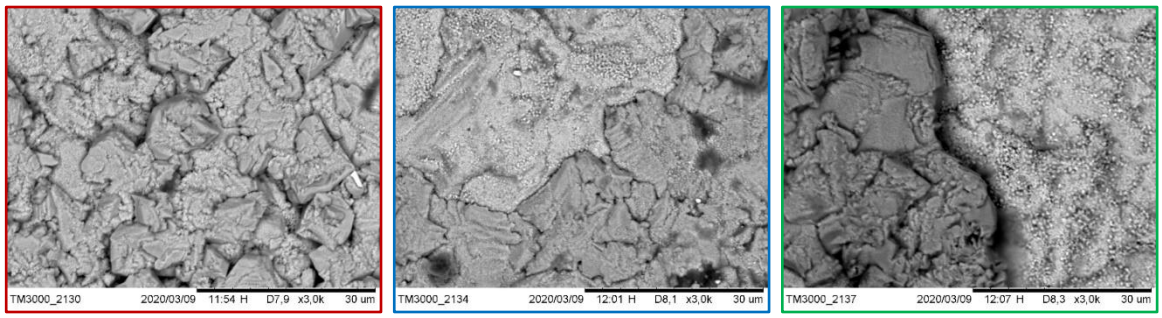

X3000

Figure 189: Test T43, Deposit surface at different current densities and magnification.

Cross section

300 A m^{-2}	200 A m^{-2}	100 A m^{-2}

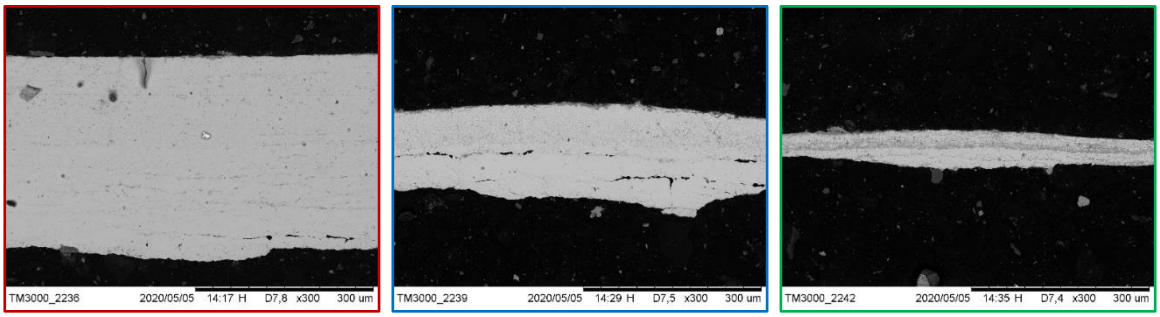

X300

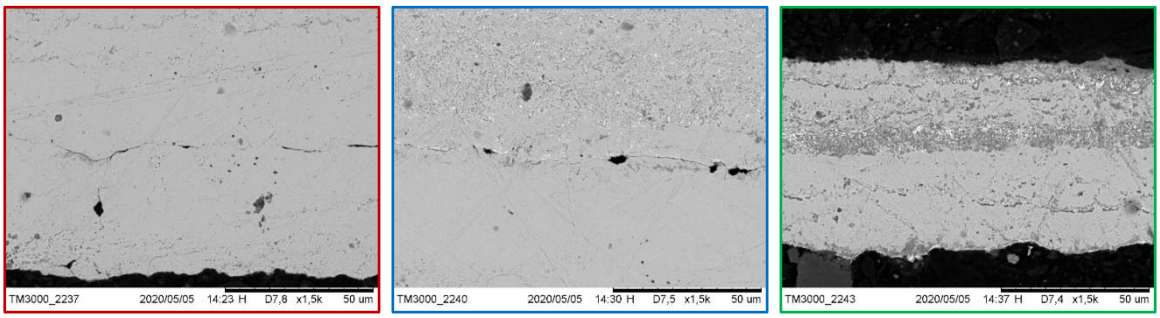

X1500

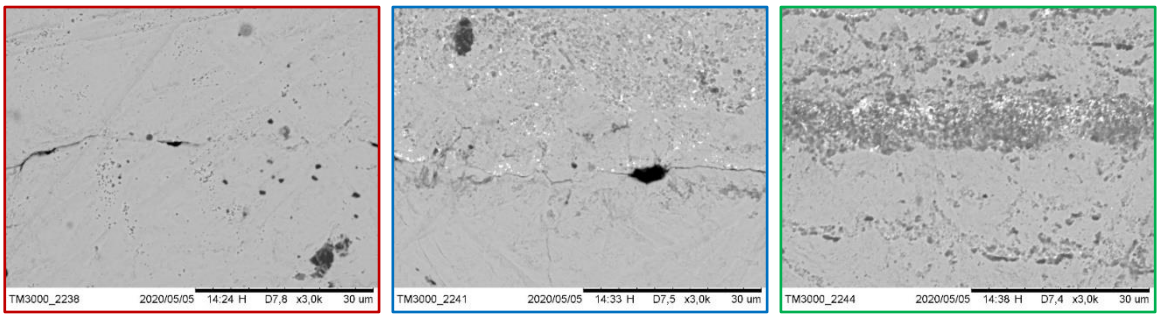

X3000

Figure 190: Test T43, Deposit cross section at different current densities and magnification.

[T44] Ligninsulfonate

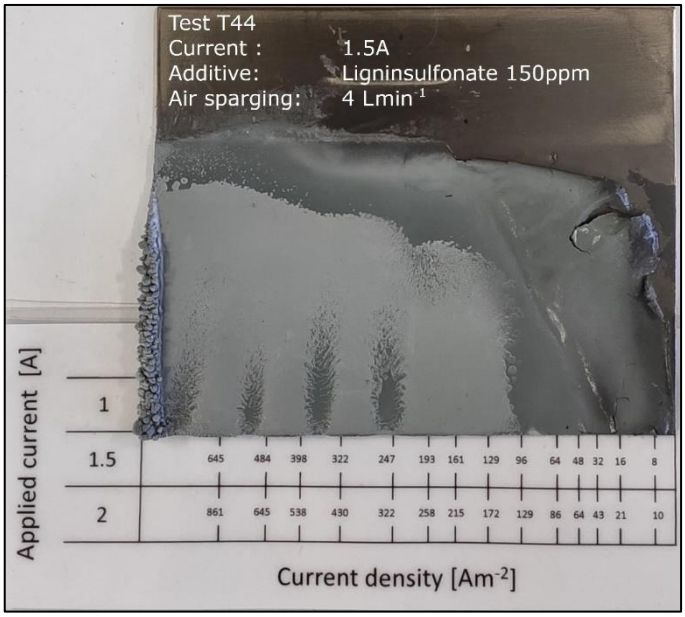

	Low	High
Adhesion	★★☆☆☆	

	Brittle	Ductile
Fracture	★☆☆☆☆	

Figure 191: Test T44, Deposit appearance.

The T44 test shows the effect of calcium ligninsulfotane. From the point of view of smoothness, this deposit, Figure 191, is one of the best obtained in this study. The left edge has some small dendrites, the right edge is detached from the cathode. Adhesion is quite low, while the fracture is brittle. Surface analysis, Figure 192, shows a small lamellar structure organized into a network-like morphology at the lowest current density. This structure tends to disappear as the current density is increased, giving way to a large grain structure that is more compact. The cross-section images, Figure 192, show a porous structure at the lowest current density that becomes more compact as the current density is increased. The cross-section images of 200 and 300 A/m^2 resemble a grain structure.

Surface

300 A m^{-2}	200 A m^{-2}	100 A m^{-2}

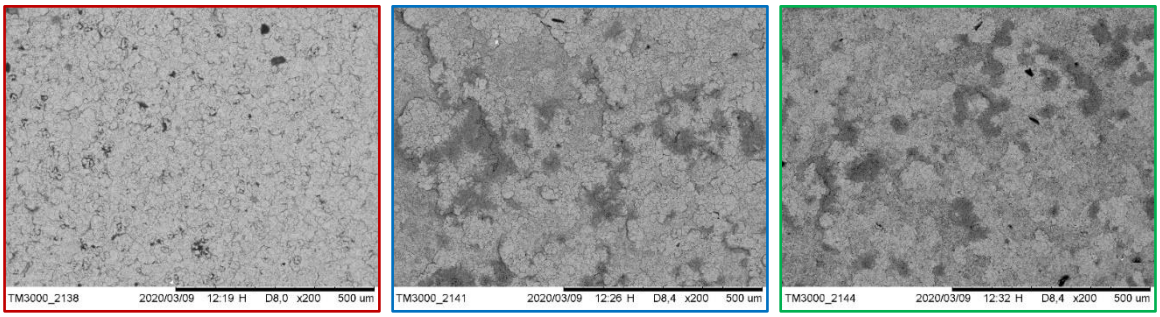

X200

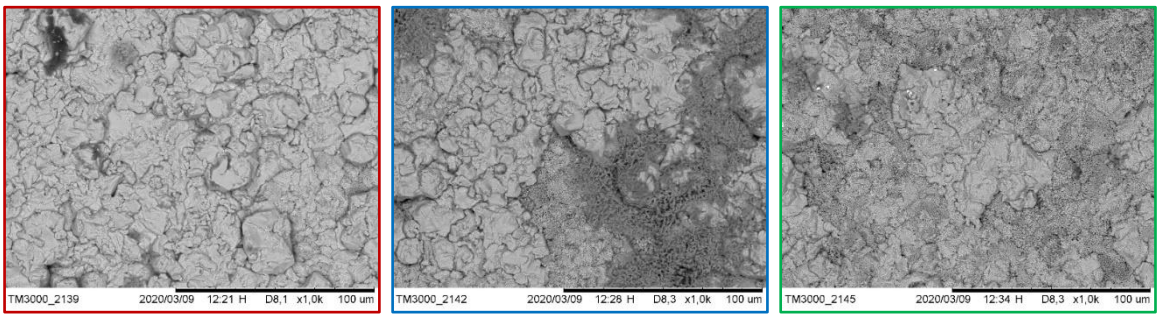

X1000

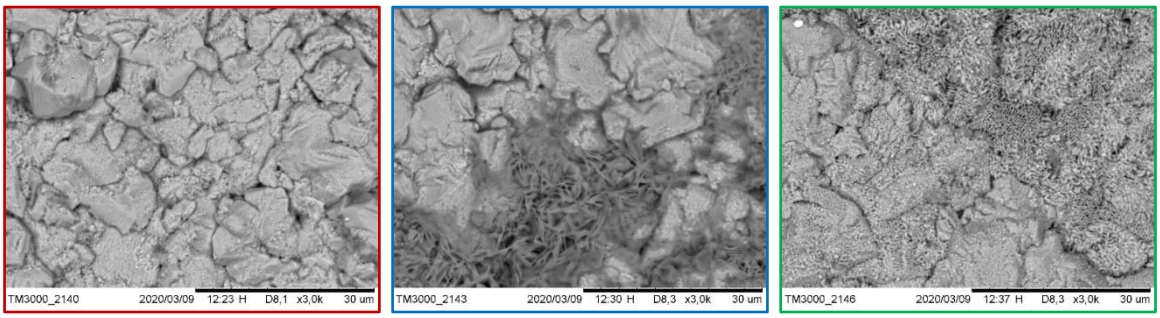

X3000

Figure 192: Test T44, Deposit surface at different current densities and magnification.

Cross section

300 A m^{-2}	200 A m^{-2}	100 A m^{-2}

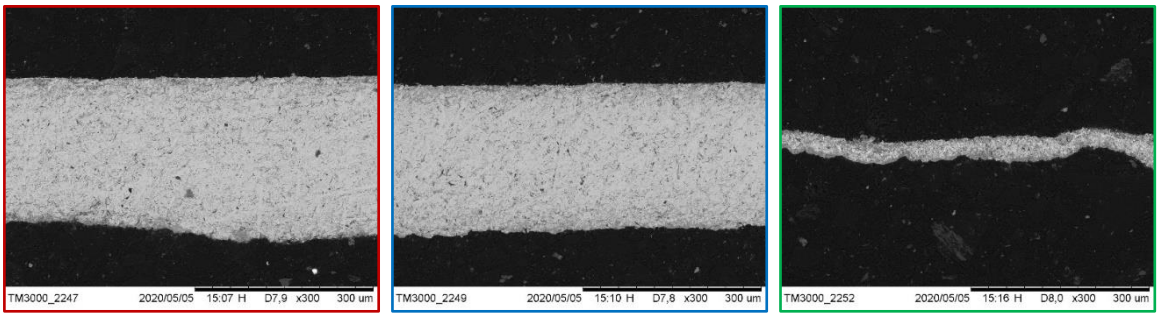

X300

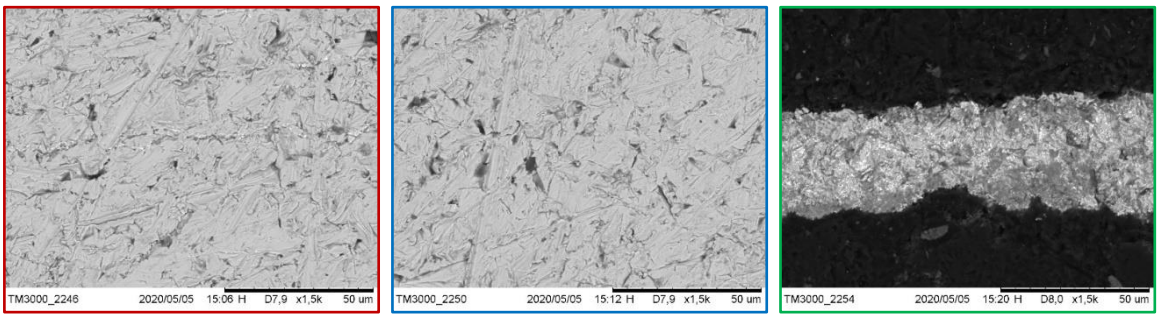

X1500

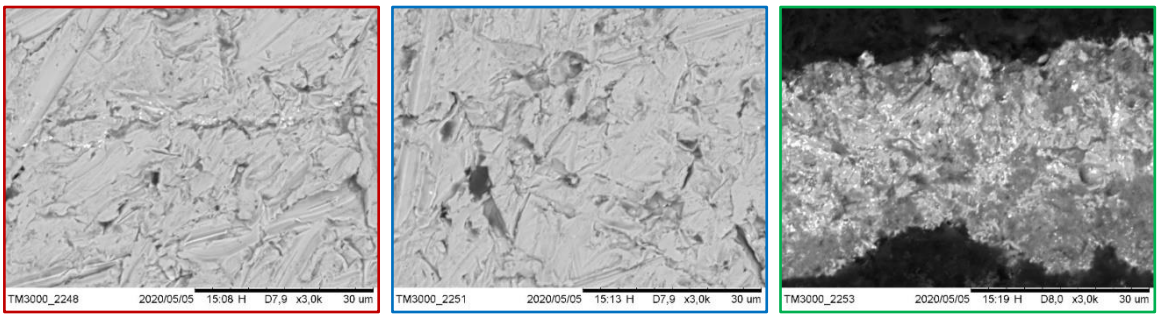

X3000

Figure 193: Test T44, Deposit cross section at different current densities and magnification.

[T45] Gum arabic

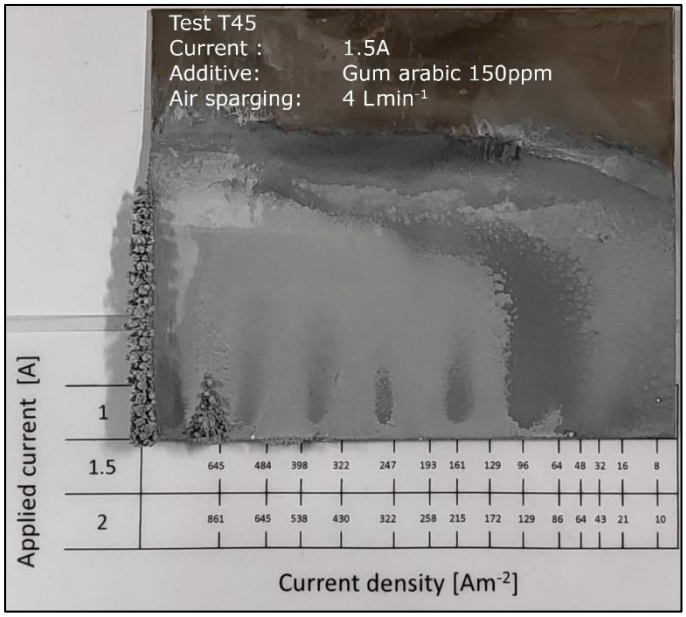

	Low	High
Adhesion	★★★★★	

	Brittle	Ductile
Fracture	★★☆☆☆	

Figure 194: Test T45, Deposit appearance.

The gum arabic was tested in the T45 test. The deposit, Figure 194, appears very smooth, like that obtained with ligninsulfonate but with some dendrites on the left edge. Adhesion was very high while the fracture type was quite brittle. At 100 A/m^2, the surface, Figure 195, is microporous and tends to become more compact as the current density increases. at 200 and 300 A/m^2, some grains can be recognized but the overall structure remains lamellar/acicular and microporous. Cross section analysis, Figure 196, shows a compact deposit that tends to become porous as current density increases.

Surface

300 A m^{-2}	200 A m^{-2}	100 A m^{-2}

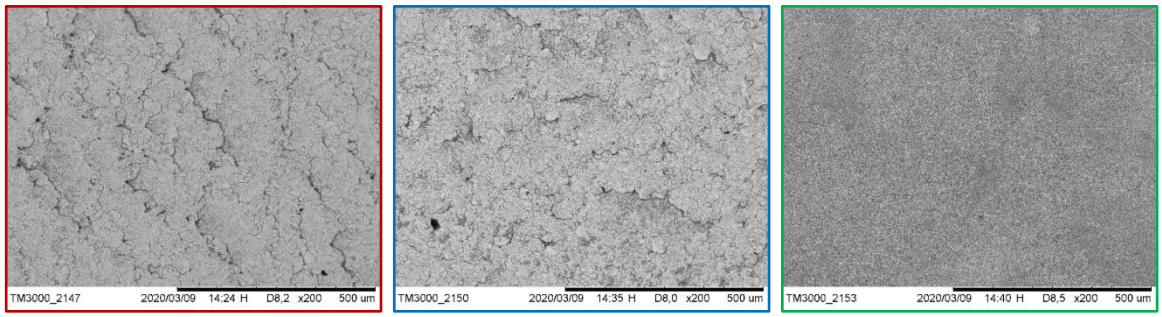

X200

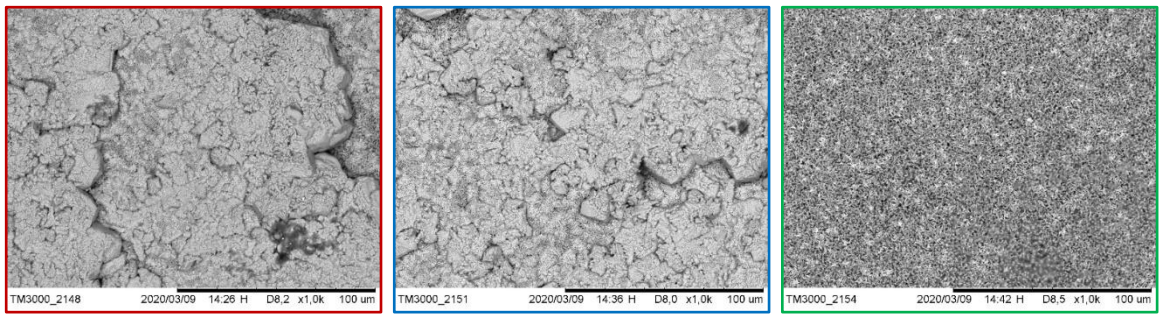

X1000

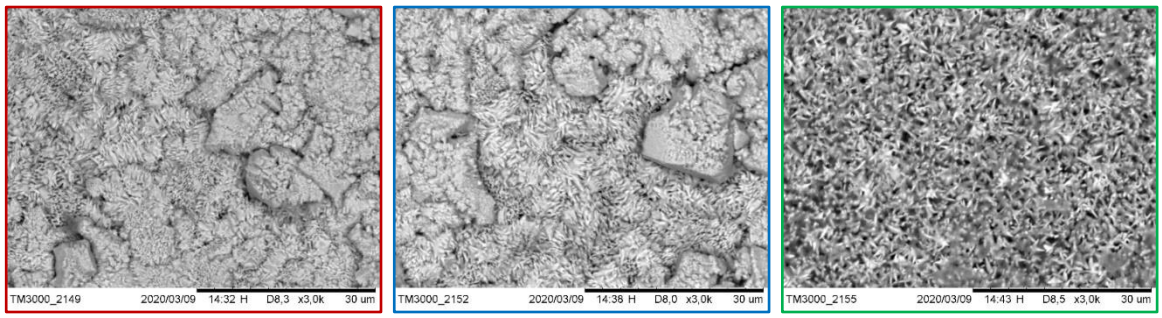

X3000

Figure 195: Test T45, Deposit surface at different current densities and magnification.

Cross section

300 A m^{-2}	200 A m^{-2}	100 A m^{-2}

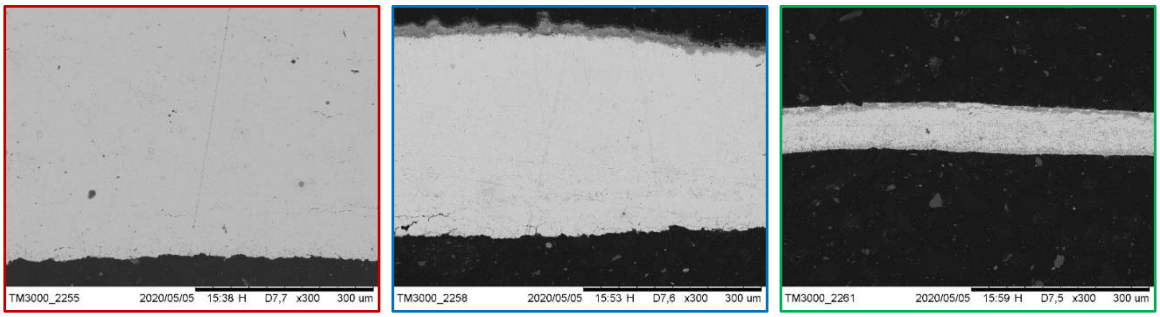

X300

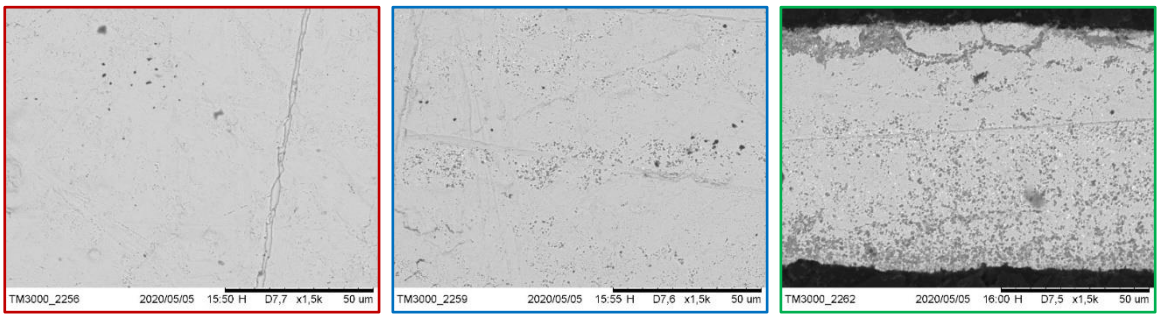

X1500

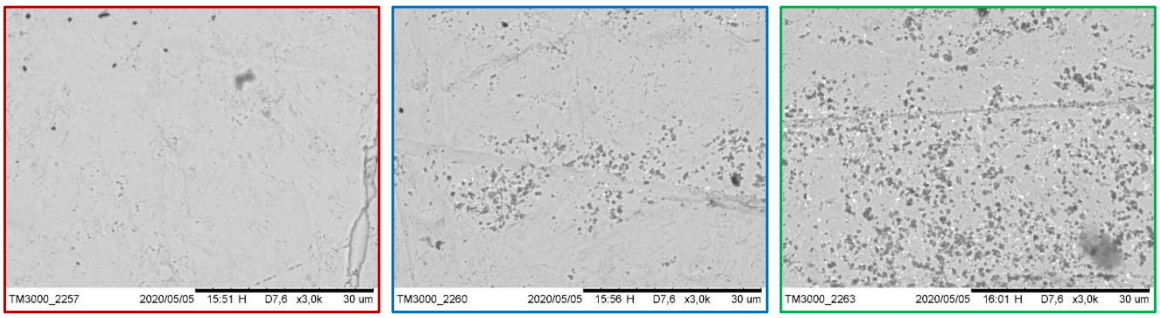

X3000

Figure 196: Test T45, Deposit cross section at different current densities and magnification.

[T46] Bone glue

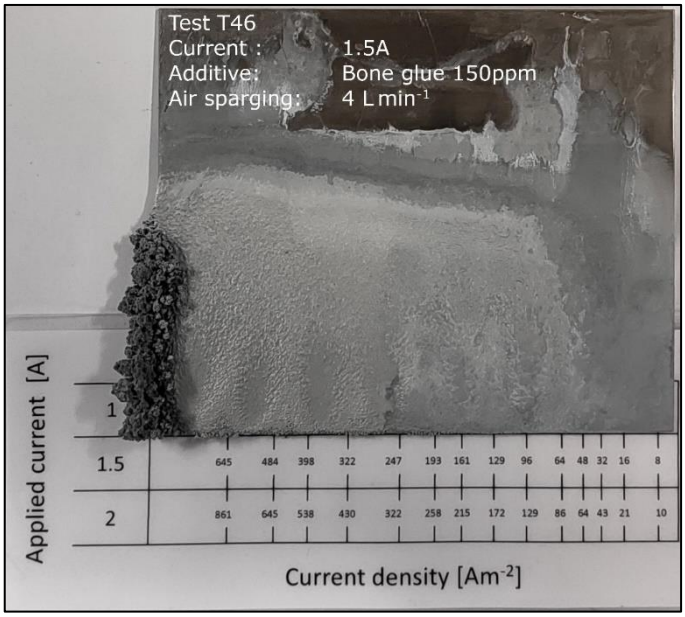

Low High

Adhesion ★★★★★

Brittle Ductile

Fracture ★☆☆☆☆

Figure 197: Test T46, Deposit appearance.

T46 test shows the effect of bone glue. The deposit, Figure 197, appears rough with many dendrites on the left edge. Adhesion was very high while the fracture type was brittle. From magnification of the surface, Figure 198, a morphology similar to a desert dune can be recognized, at the highest current density the deposit is organized into a lamellar structure embedded in a very compact matrix. As the current density is lowered this structure disappears leaving room for a dotted surface that still remains compact. Cross-sectional analysis shows a structure that appears to have grown through successive layer formation, however the deposit appears compact with some small defects, Figure 199.

Surface

300 A m^{-2}	200 A m^{-2}	100 A m^{-2}

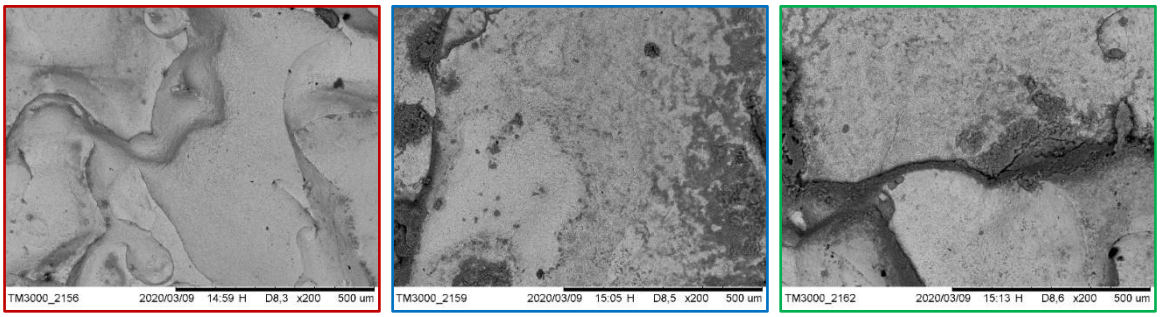

X200

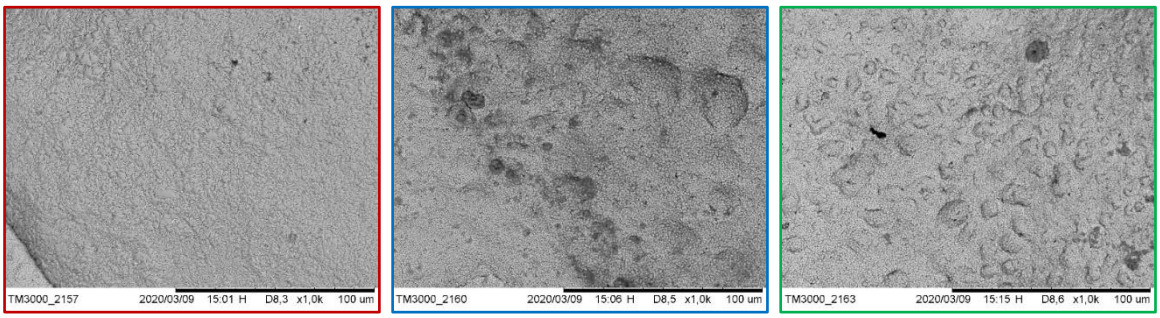

X1000

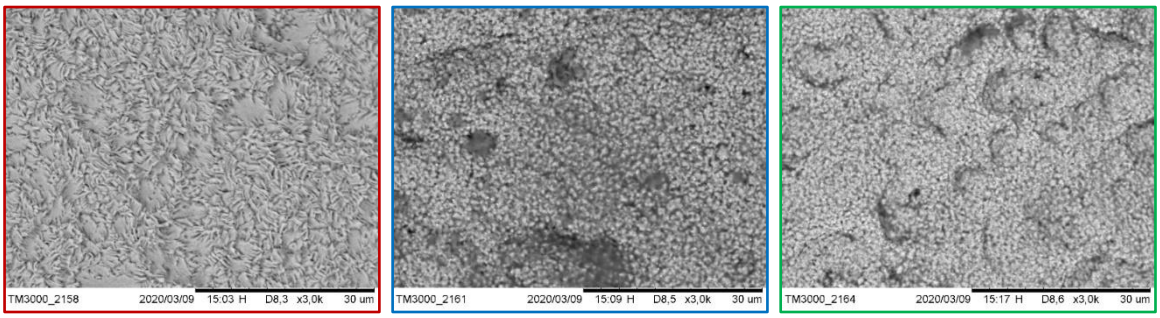

X3000

Figure 198: Test T46, Deposit surface at different current densities and magnification.

Cross section

300 Am^{-2}	200 A m^{-2}	100 Am^{-2}

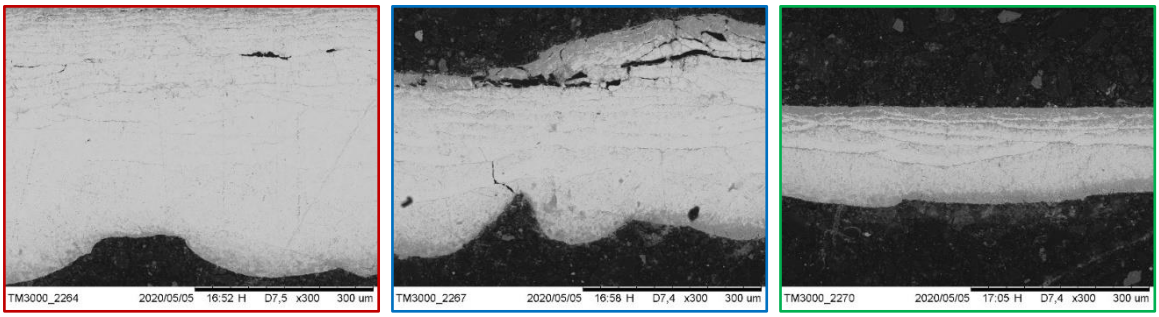

X300

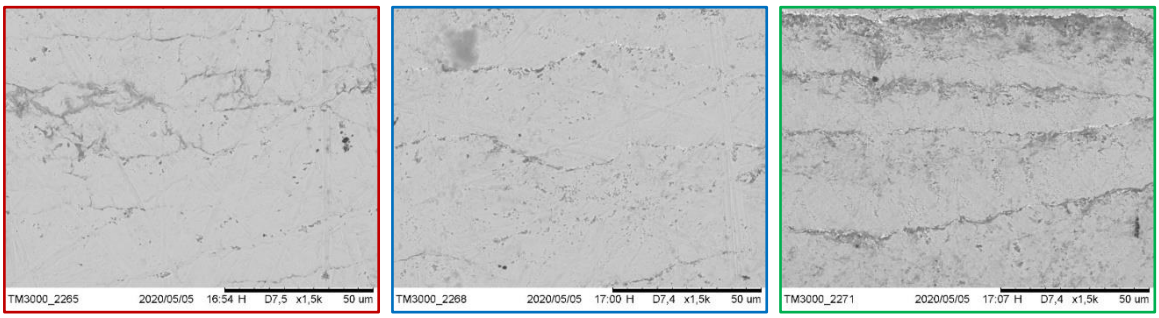

X1500

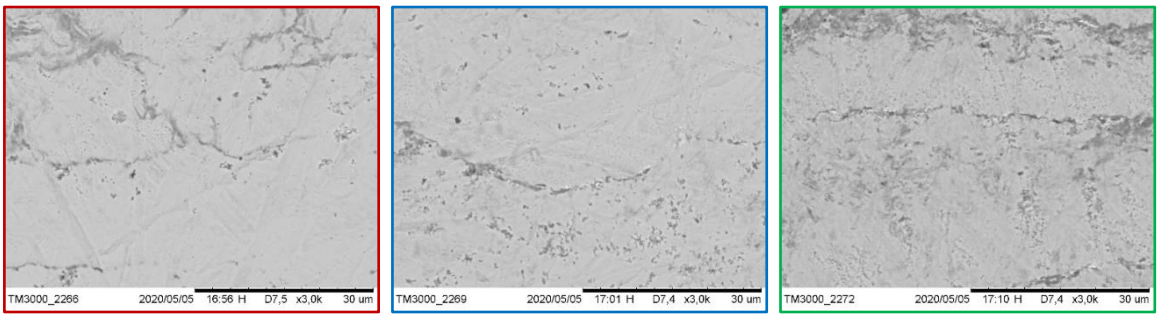

X3000

Figure 199: Test T46, Deposit cross section at different current densities and magnification.

[T47] Vanillin

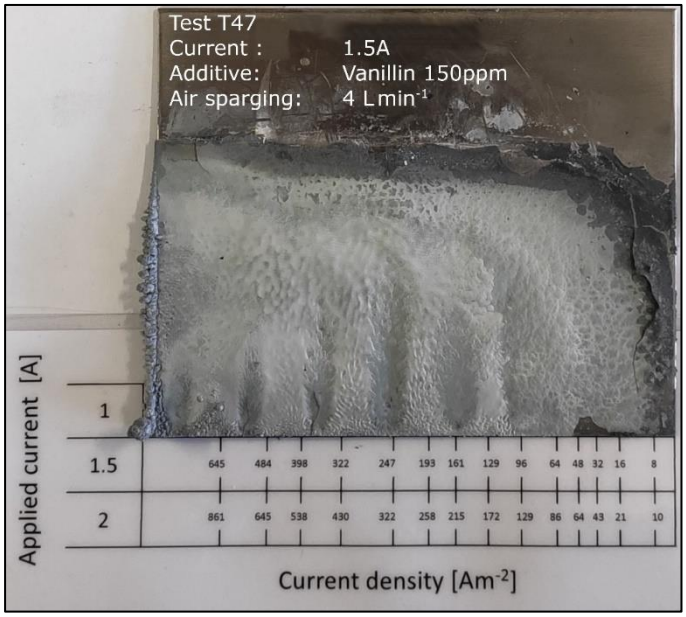

	Low	High
Adhesion	★★★★☆	

	Brittle	Ductile
Fracture	★★☆☆☆	

Figure 200: Test T47, Deposit appearance.

Test T47 shows the effect of vanillin. The deposit obtained, Figure 200, is quite smooth with some irregularities and low dendritic formation on the left edge. Adhesion was good while the fracture type was quite brittle. At the lowest current density, the surface appears microporous, Figure 201, while at higher current density more dense areas divided by highly porous edges can be recognized.

Surface

300 A m^{-2}	200 A m^{-2}	100 A m^{-2}

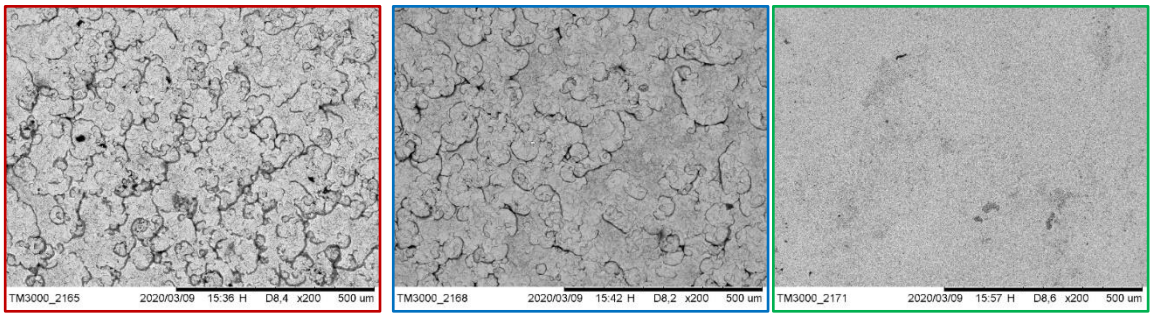

X200

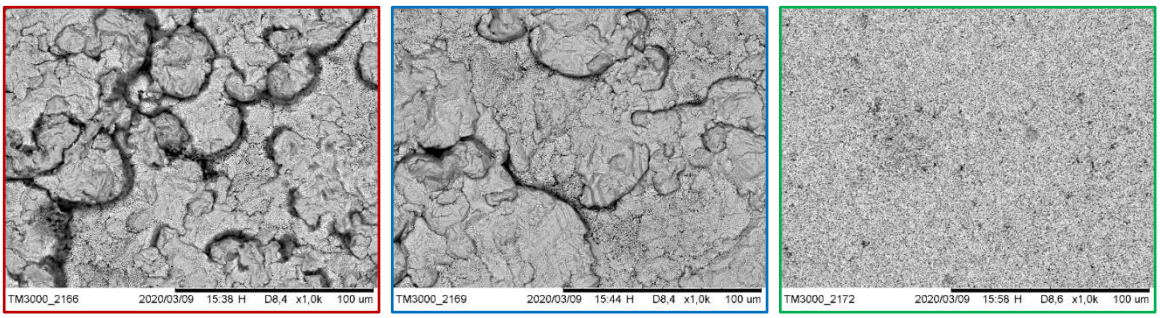

X1000

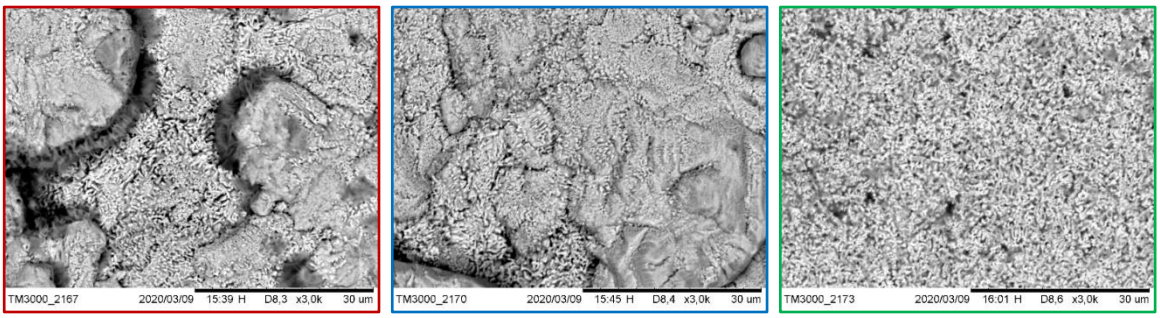

X3000

Figure 201: Test T47, Deposit surface at different current densities and magnification.

Cross section

300 A m^{-2}	200 A m^{-2}	100 A m^{-2}

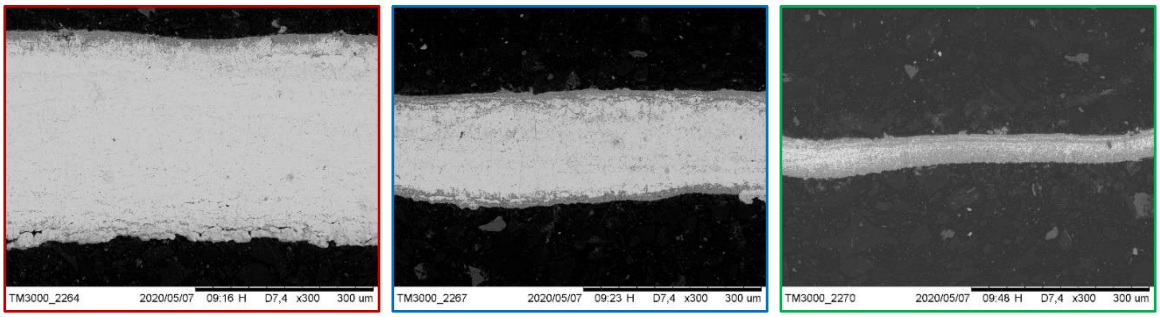

X300

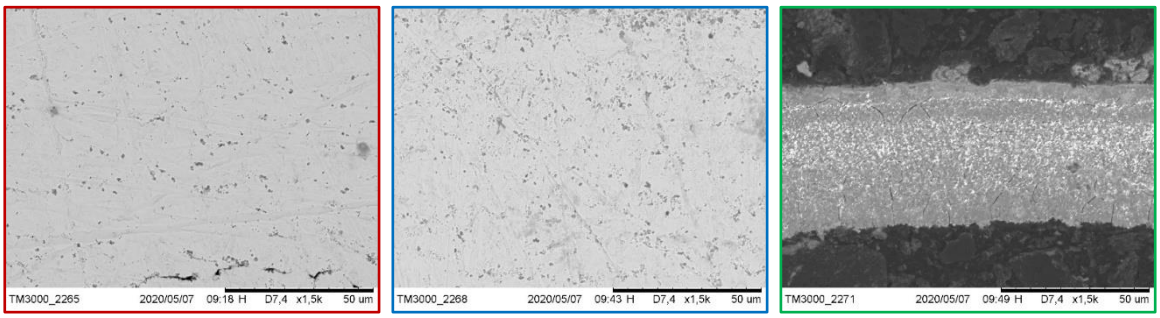

X1500

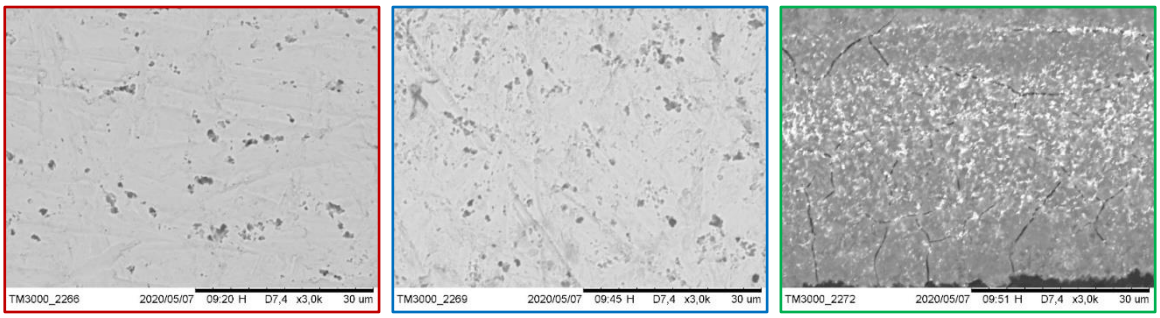

X3000

Figure 202: Test T47, Deposit cross section at different current densities and magnification.

Cell potential

Cell potential was recorded throughout each test, Figure 203, to assess the effect of additives on this parameter. For a clearer comparison, potentials were averaged and compared to a baseline. The baseline was taken as the average potential of the T28/T29 tests, synthetic solution with air sparging in the absence of additives. Figure 204 shows the difference between the calculated baseline and the average cell potential of each test. First, it highlights the potential drop that can only be achieved by air sparging, second, a quick comparison can be made between the additives. Some of them increase the cell potential by up to +200 mV while others decrease it by up to -150 mV.

The increase or decrease in cell potential could be attributed to the adsorption and/or inhibition effect of the additive on zinc deposition or its electrochemical consumption or degradation. The change in cell potential, with these data and the experimental setup used, cannot be attributed to the anodic or cathodic electrode.

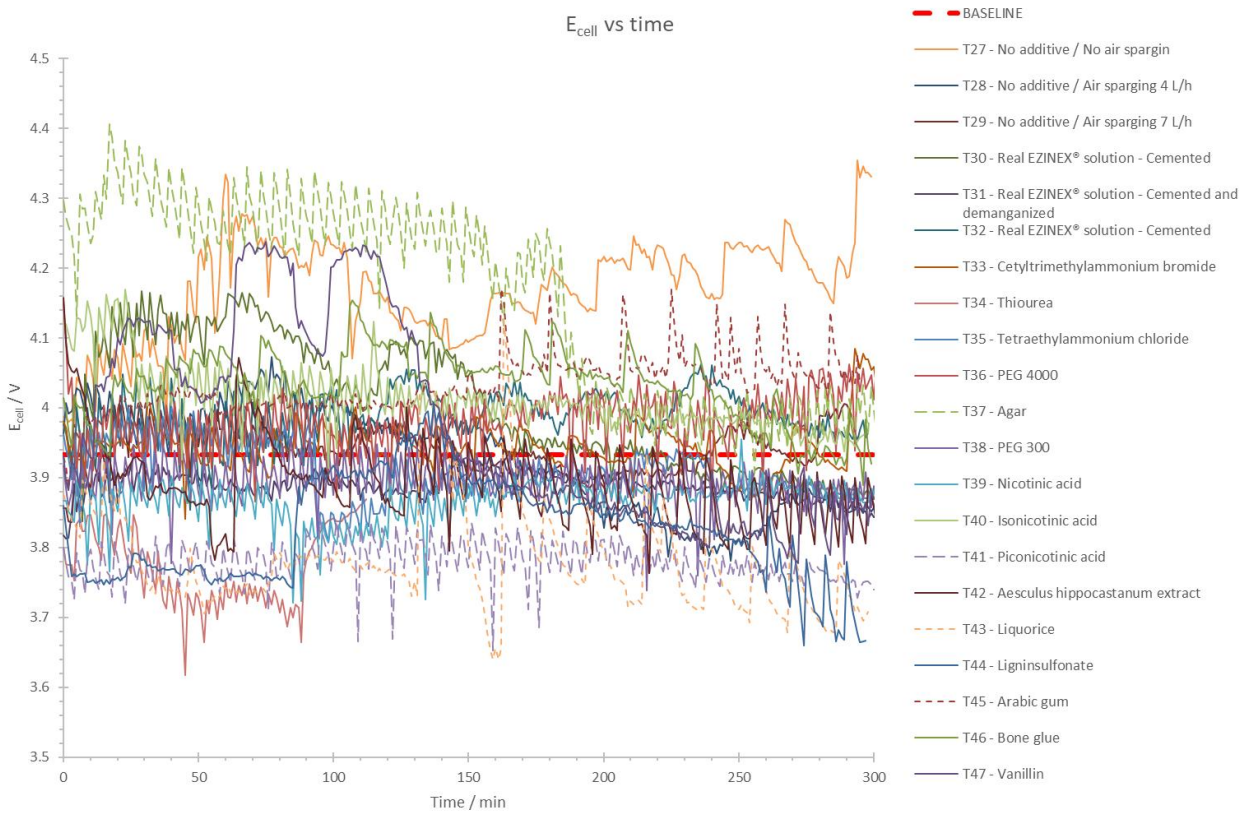

Figure 203: Cell potential vs time.

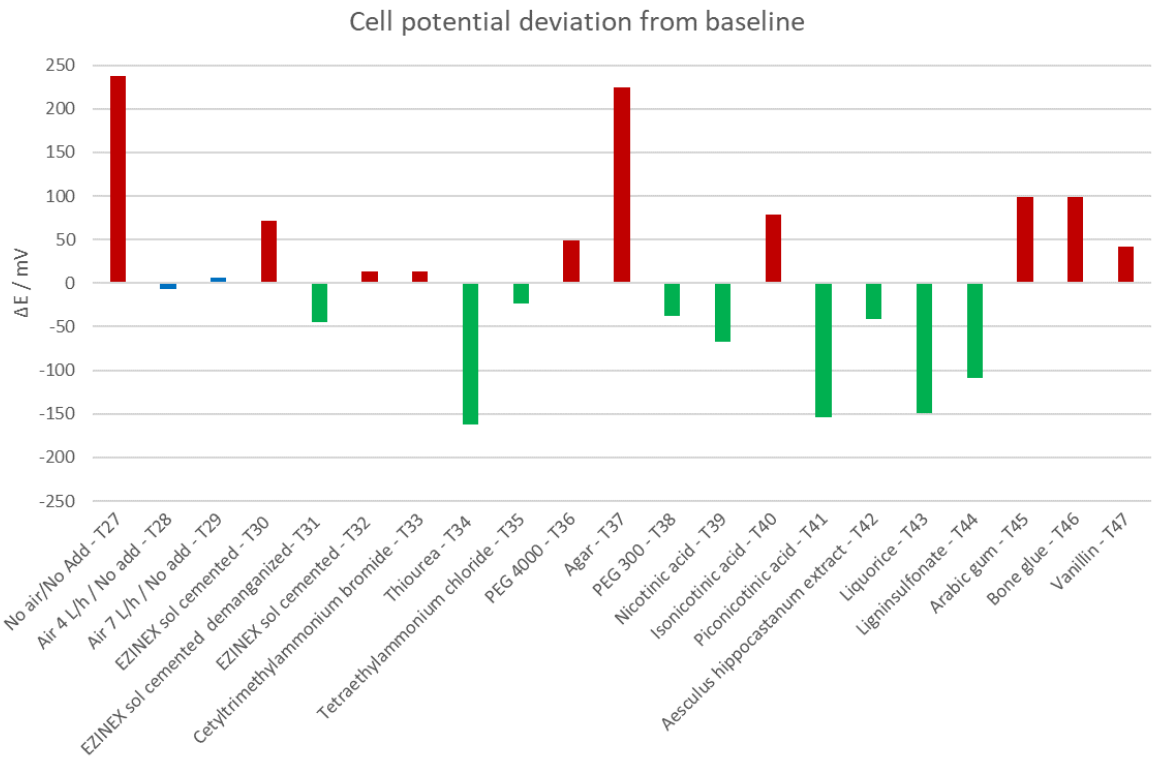

Figure 204: Cell potential difference from baseline.

Notes

It should be noted that some additives, saponins and lignin sulfonate, tend to produce a large amount of foam due to the presence of air sparging; control methods or defoaming chemicals should be considered for their use in an industrial plant.

Specific equipment for evaluating fracture type and adhesion was not available during this experiment; as mentioned above, an arbitrary scale was used and is subjective.

This report does not define whether or not an additive could be used in an industrial cell; further evaluations, such as degradation product accumulation, long-term effects, optimal concentration, etc., should be made.

Conclusions

In this study, the effect of air sparging, demanganization and 15 additives on the electrodeposition of zinc in ammonium chloride was tested. The presence of air sparging showed a beneficial effect on the appearance of the deposit: dendrite formations were localized on the left edge instead of covering the entire surface. The two air sparging flow rates that were tested, 4 and 7 l/min, produced a very similar deposit so one could conclude that even the lower flow rate is sufficient, however, this consideration should not work for large-scale electrodeposition because such behavior is related to cell geometry.

The deposit obtained using real EZINEX® solutions was completely different from that produced by a synthetic solution, this could be attributed to the presence of organic in the EAFD which acts as a kind of additive. The presence of manganese decreases adhesion and increases porosity, its absence promotes the growth of a compact grain structure.

Each additive showed its own effect on the structure and appearance of the deposits. It was noted that although the deposit appears smooth, its surface magnification can reveal a high porous structure, however, it could not be determined if this porous structure was characteristic of the surface or was present along the entire thickness of the deposit. Cross-section analysis rarely showed pores and defects, this could be attributed to the assembly and polishing process combined with the ductility of zinc; this resulted in compact cross-sections that were unable to reveal any particular structures.

The presence of additives generally reduced the ductility of the deposit by promoting a brittle fracture type, this was observed for all additives, only real EZINEX® solutions and synthetic solutions without additives produced a ductile deposit.

Each additive presented its own pros and cons, with the results obtained from this study, six additives have been selected as candidates for their use in blending.

Aesculus hippocastanum, PEG 4000, agar, bone glue, gum arabic, and ligninsulfonate were chosen to be tested in pairs in the second part of test.

Electrodeposition additives for the EZINEX® process

Part II

Introduction

Previously, several additives were tested for the electrodeposition of zinc from ammonium chloride solutions. Each additive showed a different effect on the zinc deposit; one exhibited leveling characteristics, one promoted a compact deposit, one inhibited dendrite growth, and so on. From the analysis of the obtained deposits, six additives were selected and tested in combinations of two to take advantage of the effect of both additives to achieve the most compact deposit possible without dendrites.

The experimental setup has remained unchanged compared to the tests conducted previously, it was decided not to evaluate the cross-section because no appreciable differences were noted in the previous experimentation.

To find a parameter, useful to quickly determine the additive concentration, at beginning and end of each test, solutions surface tension was measured using the stalagmometric method.

The tests were carried out according to the following matrix:

	Agar	Aesculus hipp. extract	Gum arabic	Bone glue	Lignin sulfonate
Peg 4000					
Agar					
Aesculus hipp. extract					
Gum arabic					
Bone glue					

Table 15: Additives combinations (50 ppm + 50 ppm).

.

Current density distribution

As described earlier, the Hull cell is designed to explore a wide range of current densities in a single experiment. At each point on the cathode, the current density can be described by the following equation:

$$i = I[5.1 - 5.24\ Log\ (L)]$$

Equation 15: Hull cell current distribution law.

Where i (A/dm^2) and I (A) are the current density and the applied current respectively while L is the distance (cm) from the right edge.

For long experiments this law should be verified, the formation of dendrites can change the current distribution by absorbing a significant portion of the total current. To verify the goodness of equation 9, a zinc plate was cut into small strips (5 mm) that were individually weighed, Figure 205. A current density vs right edge distance plot was constructed and the logarithmic equation was extrapolated.

This analysis was done on 4 different zinc plates that exhibited different degree of dendritic formations. Results are reported ath the endo of this report.

Figure 205 Zinc plate cut in 5 mm strips for current density distribution analysis.

TII 1 – Peg 4000 / Agar

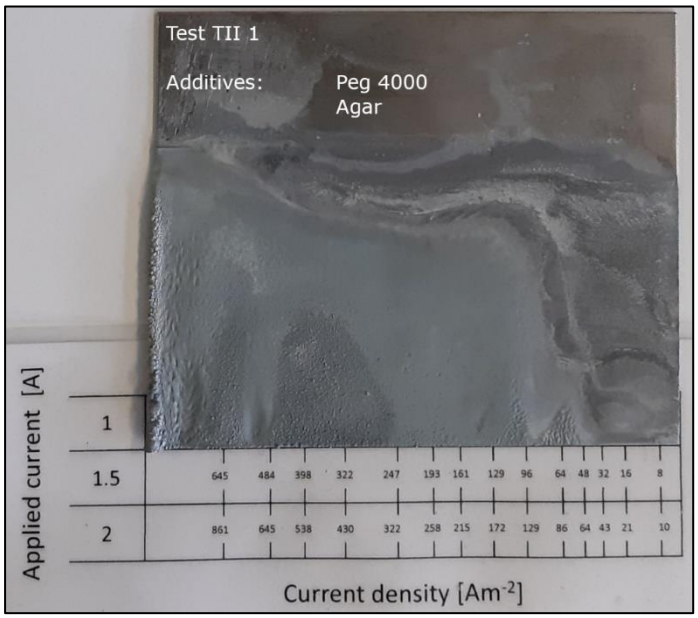

	Low	High
Adhesion	★★★★☆	

	Brittle	Ductile
Fracture	★★☆☆☆	

Figure 206: Test TII 1, Deposit appearance.

The TII 1 test was done using PEG 4000 and agar, 50 ppm each. Figure 206 shows the appearance of the deposit, the overall surface was smooth while dendrite formation appears to be inhibited. The zinc foil was very adherent to the titanium substrate and the fracture was quite brittle. Analysis of the surface, Figure 207, reveals an acicular structure that is compact at low current densities but tends to be porous at 300 A/m^2.

Surface

300 A m^{-2}	200 A m^{-2}	100 A m^{-2}

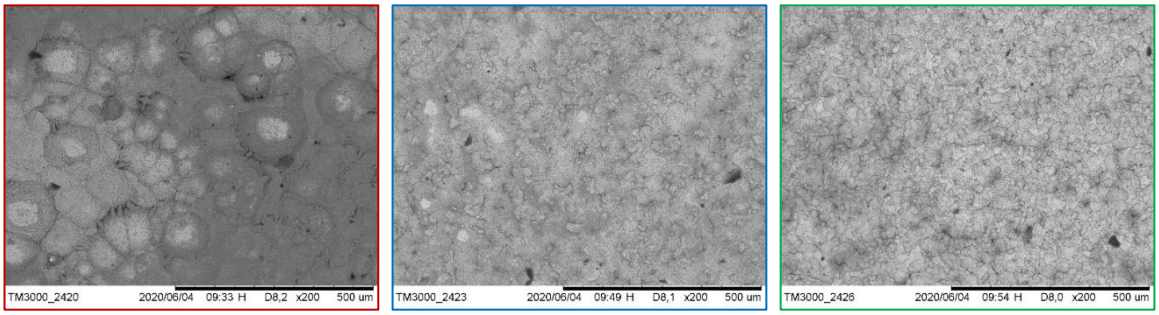

X200

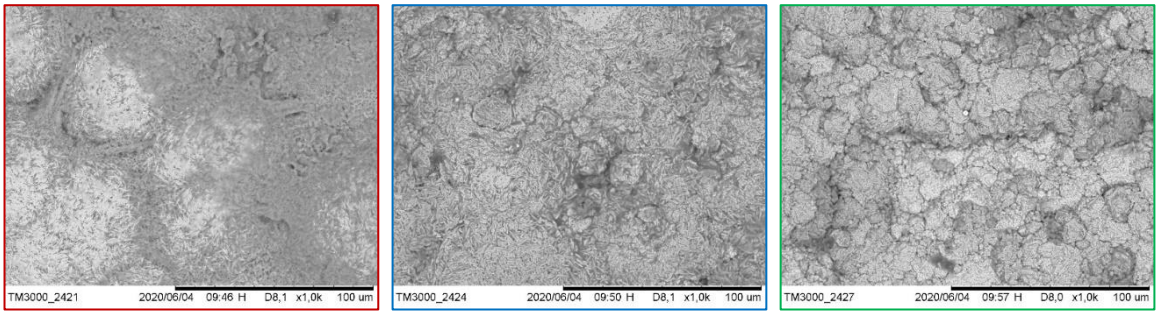

X1000

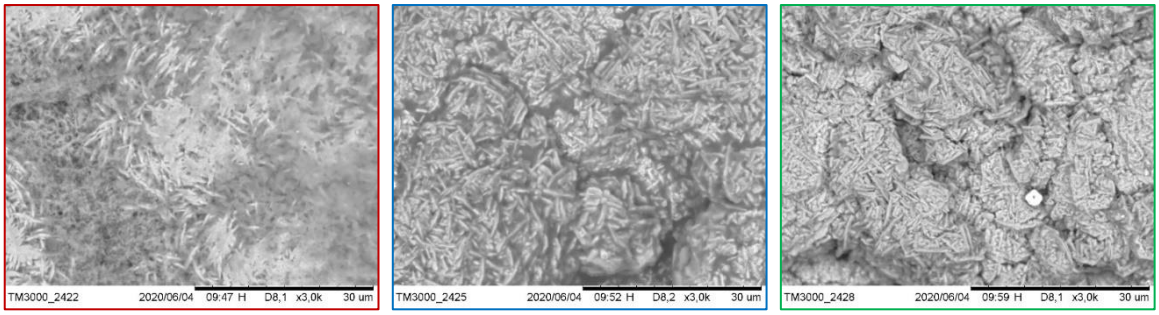

X3000

Figure 207: Test TII 1, Deposit surface at different current densities and magnifications.

TII 2 – Peg 4000 / Aesculus hippocastanum extract

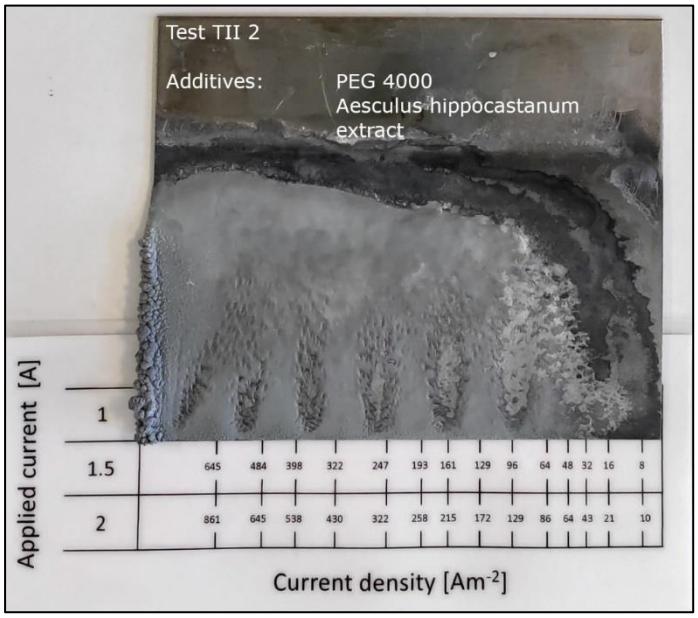

	Low	High
Adhesion	★★★☆☆	

	Brittle	Ductile
Fracture	★★☆☆☆	

Figure 208: Test TII 2, Deposit appearance.

The TII 2 test was done with PEG 4000 and aesculus hippocastanum extract. The deposit appears smooth, Figure 208, with an obvious mark due to air sparging. Smooth dendrites are visible on the edge at high current density. Adhesion was medium while the fracture type was quite brittle. Magnifications of the surface reveal a not so compact structure, Figure 209, the porosity increases with increasing current density.

Surface

300 A m^{-2}	200 A m^{-2}	100 A m^{-2}

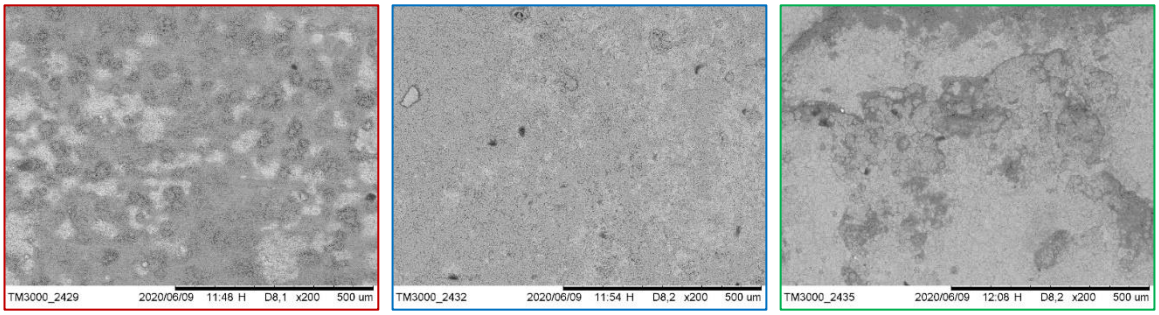

X200

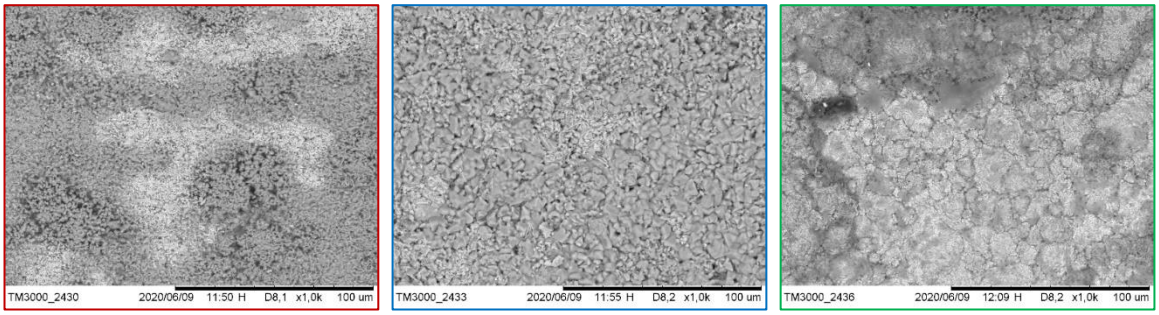

X1000

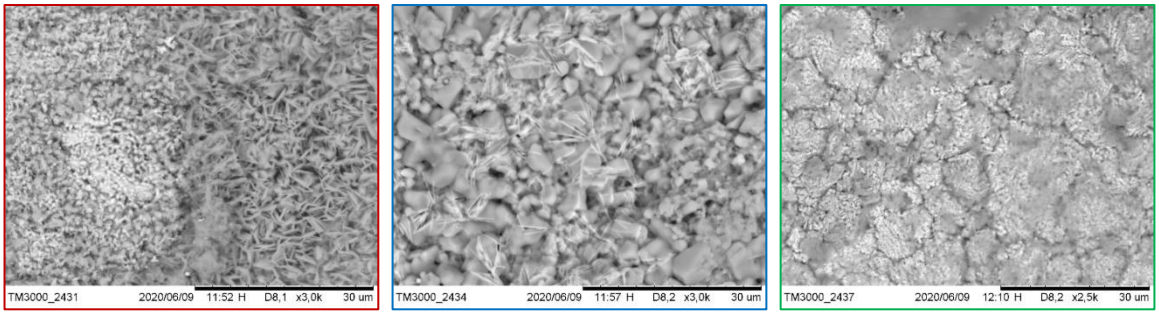

X3000

Figure 209: Test TII 2, Deposit surface at different current densities and magnifications.

TII 3 – Peg 4000 / Gum arabic

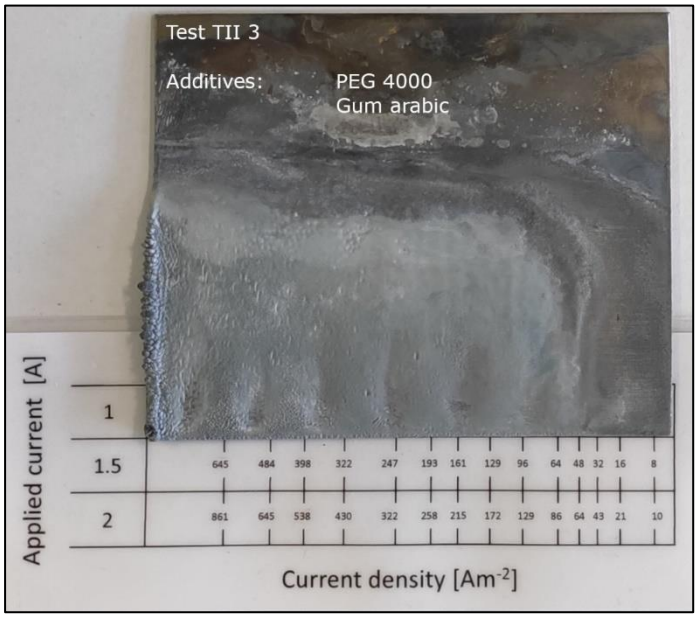

	Low	High
Adhesion	★★★☆☆	

	Brittle	Ductile
Fracture	★★☆☆☆	

Figure 210: Test TII 3, Deposit appearance.

Figure 210 shows the zinc deposit obtained from the TII 3 test in the presence of 50 ppm PEG 4000 and 50 ppm gum arabic. The deposit appears smooth with dendrites on the right edge; these are very rounded and protrude only a few millimeters. Adhesion was average while the fracture type was quite brittle. Surface analysis, Figure 211, shows an acicular structure organized into blob-like agglomerates, the porosity appears to remain the same.

Surface

300 A m^{-2}	200 A m^{-2}	100 A m^{-2}

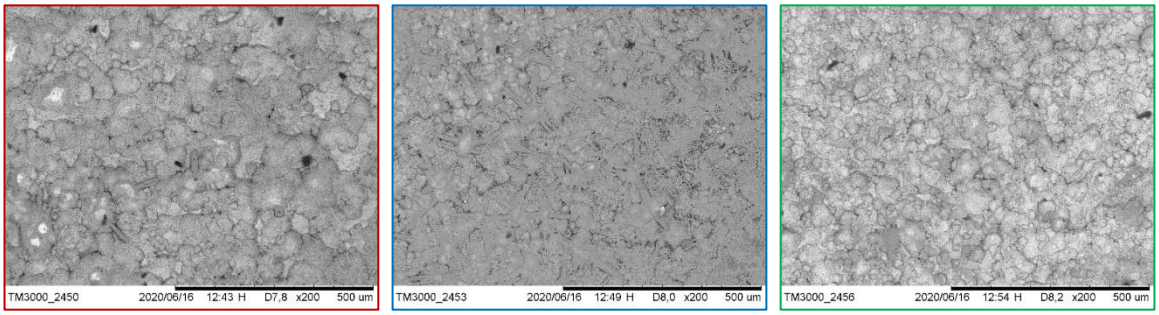

X200

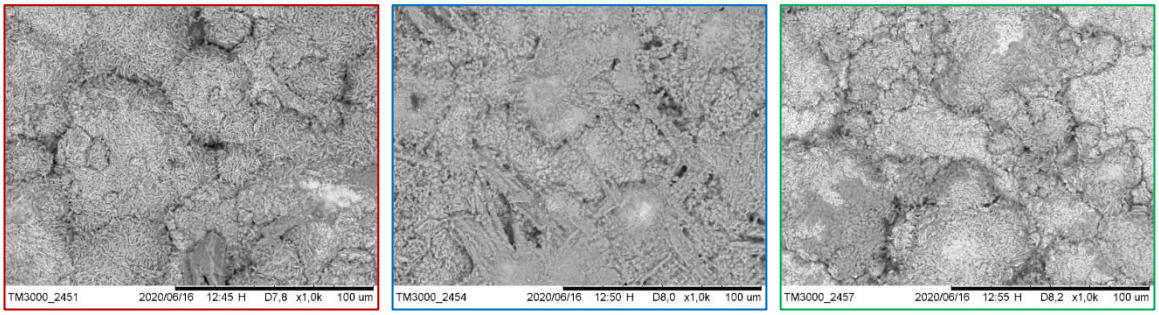

X1000

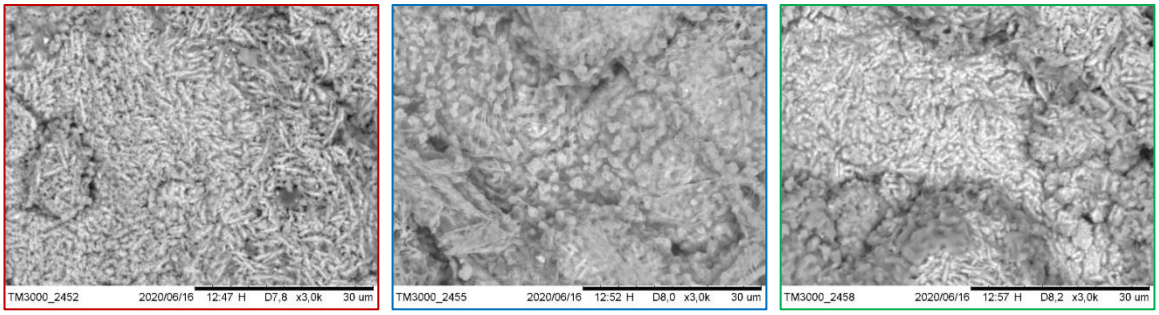

X3000

Figure 211: Test TII 3, Deposit surface at different current densities and magnifications.

TII 4 – Peg 4000 / Bone glue

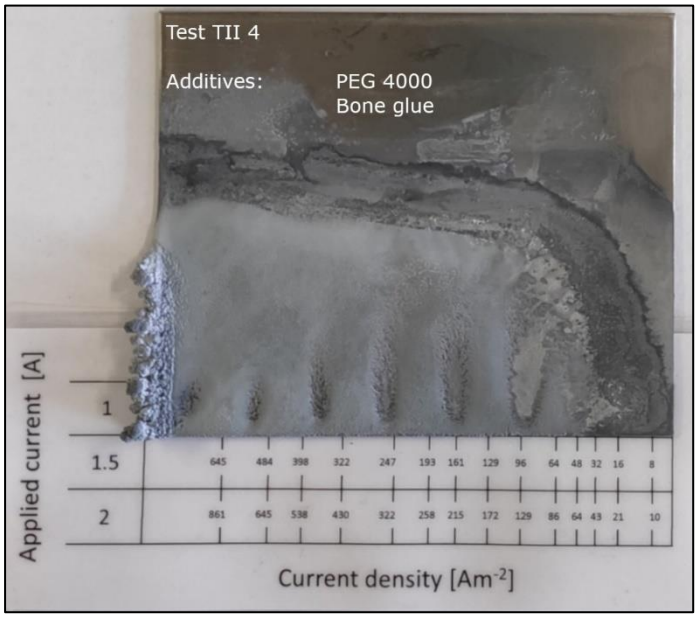

	Low	High
Adhesion	★★★★☆	

	Brittle	Ductile
Fracture	★★★☆☆	

Figure 212: Test TII 4, Deposit appearance.

The TII 4 test was done using PEG 4000 and bone glue. Dendrites are present in large quantity, Figure 212, and the deposit appears somewhat porous at first glance. Adhesion was quite high while the fracture type was halfway between brittle and ductile. Magnification of the surface shows a broccoli-like structure, Figure 213; porosity is quite high at each current density.

Surface

300 A m^{-2}	200 A m^{-2}	100 A m^{-2}

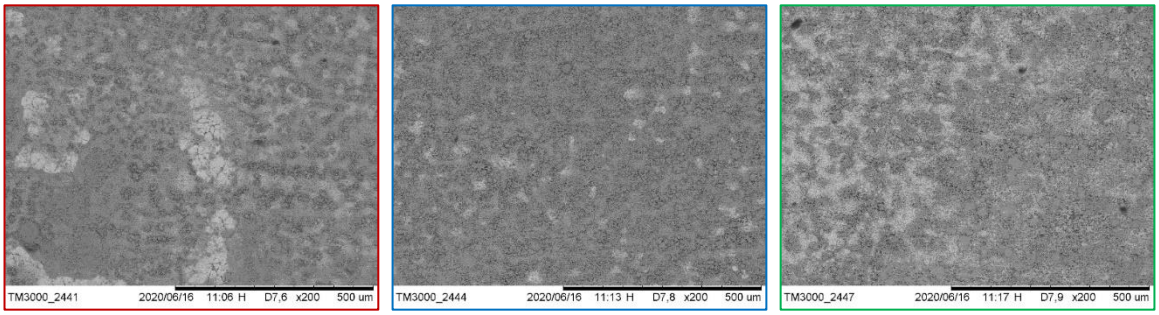

X200

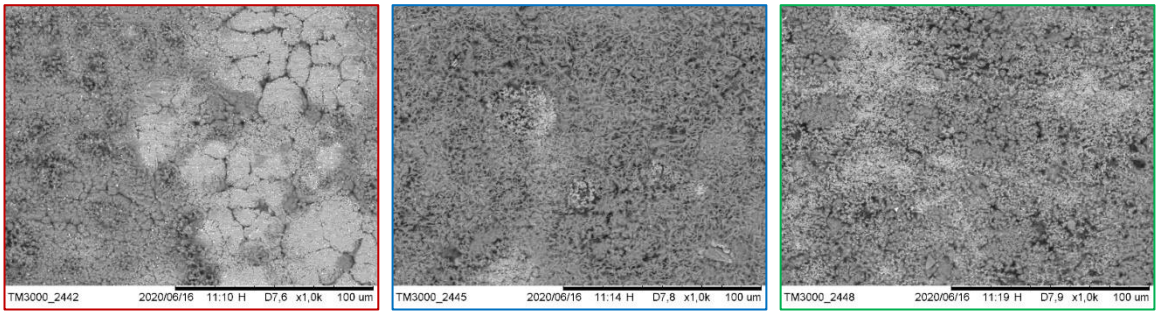

X1000

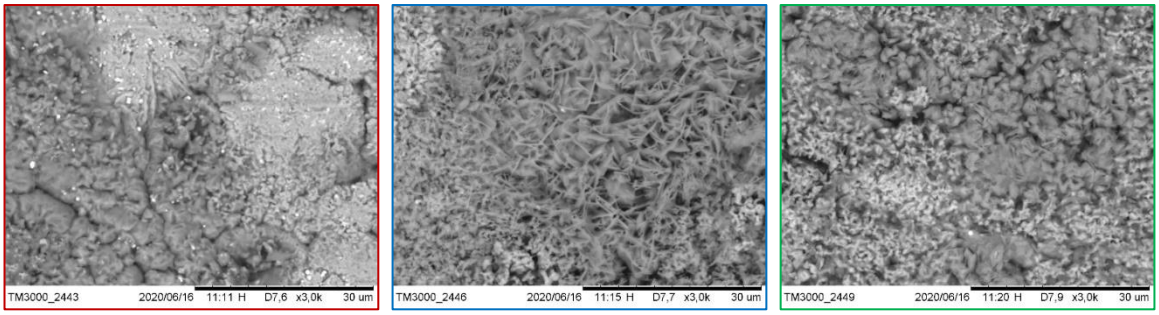

X3000

Figure 213: Test TII 4, Deposit surface at different current densities and magnifications.

TII 5 – Peg 4000 / Lignin sulfonate

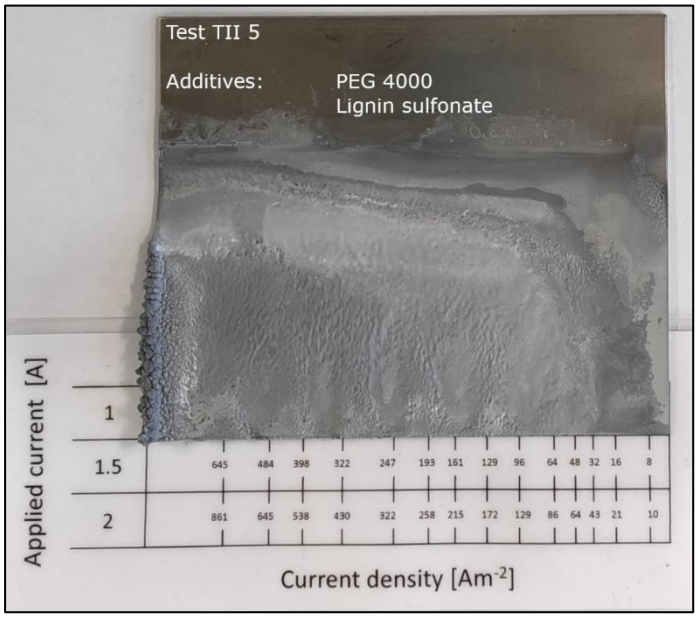

	Low	High
Adhesion	★★★☆☆	

	Brittle	Ductile
Fracture	★★☆☆☆	

Figure 214: Test TII 5, Deposit appearance.

TII5 test shows the effect of PEG 4000 and lignin sulfonate. The deposit appears somewhat wavy but smooth, Figure 214, dendrites are present on the left edge but are rounded. Adhesion was medium while the fracture type was quite brittle.

From magnifications of the surface, Figure 215, a compact acicular structure can be recognized at the lowest current density but as this increases, the structure tends to become more porous resembling a sponge like appearance.

Surface

300 A m^{-2}	200 A m^{-2}	100 A m^{-2}

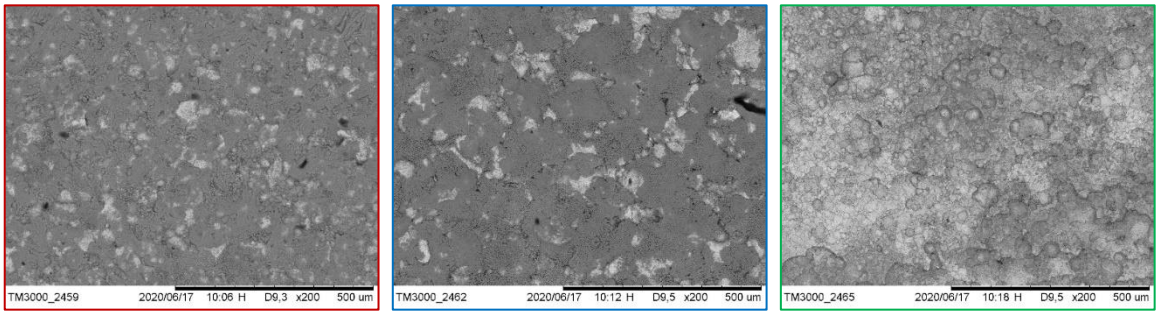

X200

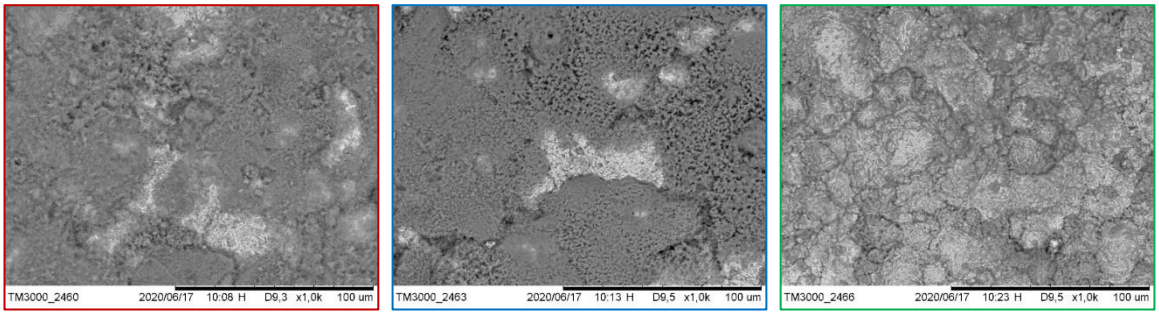

X1000

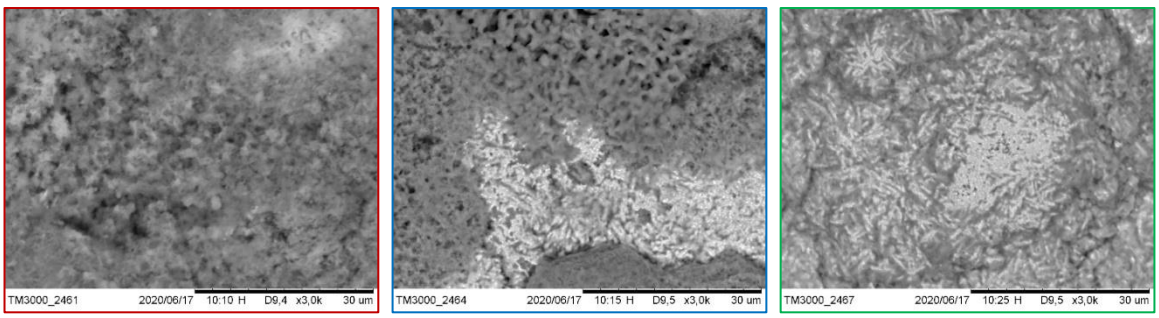

X3000

Figure 215: Test TII 5, Deposit surface at different current densities and magnifications.

TII 6 – Agar / Aesculus hippocastanum extract

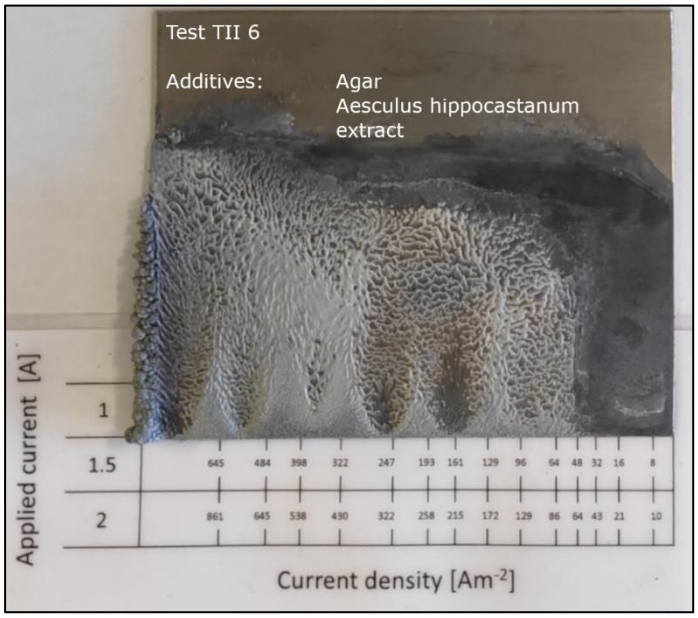

	Low	High
Adhesion	★★★★☆	

	Brittle	Ductile
Fracture	★★★☆☆	

Figure 216: Test TII 6, Deposit appearance.

TII6 test shows the effect of agar and aesculus hippocastanum extract. The appearance of the deposit, Figure 216, is very corrugated with air sparging marks; polished dendrites are present on the edge at higher current density. Adhesion was very high and the fracture type was between brittle and ductile. Analysis of the surface, Figure 217, shows a very compact structure at each current density. Looking at lower magnification, lighter and darker areas can be distinguished, but their structure appears very similar.

Surface

300 A m^{-2}	200 A m^{-2}	100 A m^{-2}

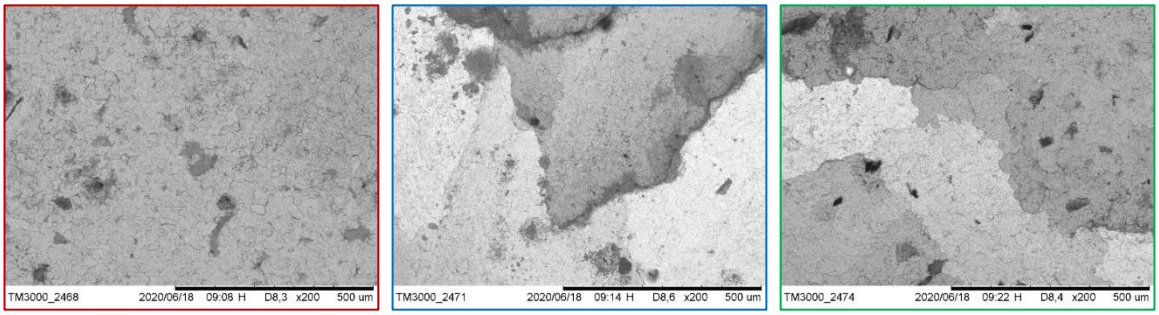

X200

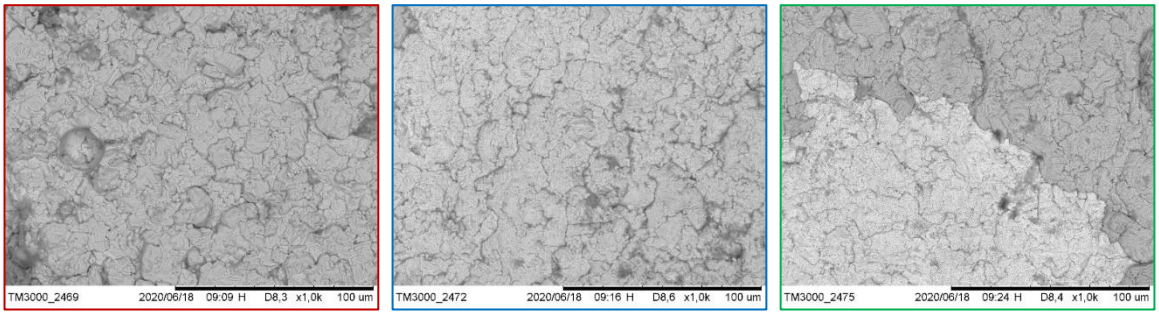

X1000

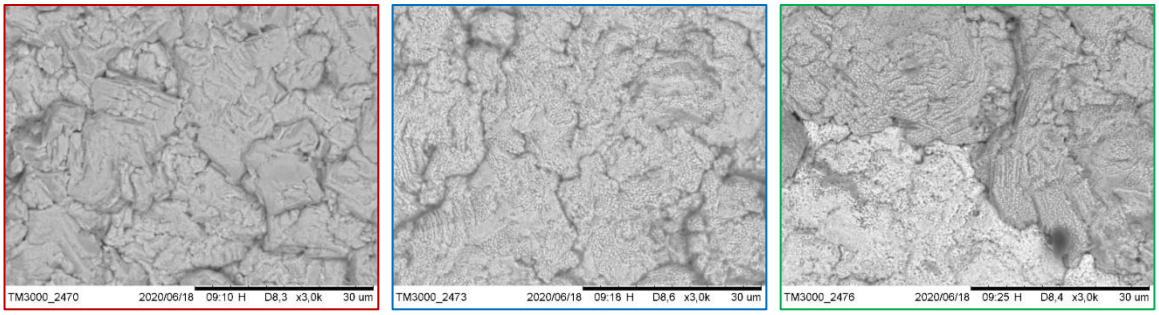

X3000

Figure 217: Test TII 6, Deposit surface at different current densities and magnifications.

TII 7 – Agar / Gum arabic

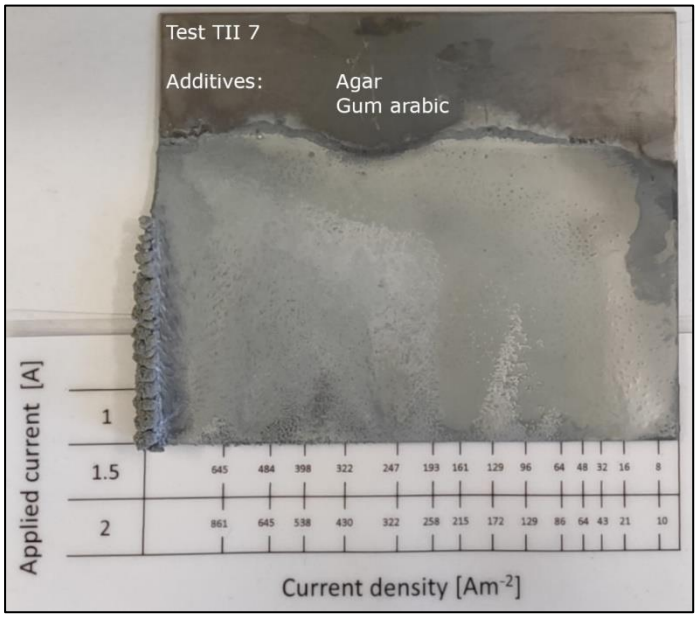

	Low	High
Adhesion	★★★☆☆	

	Brittle	Ductile
Fracture	★★☆☆☆	

Figure 218: Test TII 7, Deposit appearance.

TII7 test shows the effect of agar and gum arabic. The appearance of the deposit, Figure 218, shows a rough surface with some dendrites on the edge at high current density. Adhesion was quite high while the fracture type was brittle. Surface magnification, Figure 218, reveals a porous structure at lower current density that tends to become more compact as the latter increases.

Surface

300 A m^{-2}	200 A m^{-2}	100 A m^{-2}

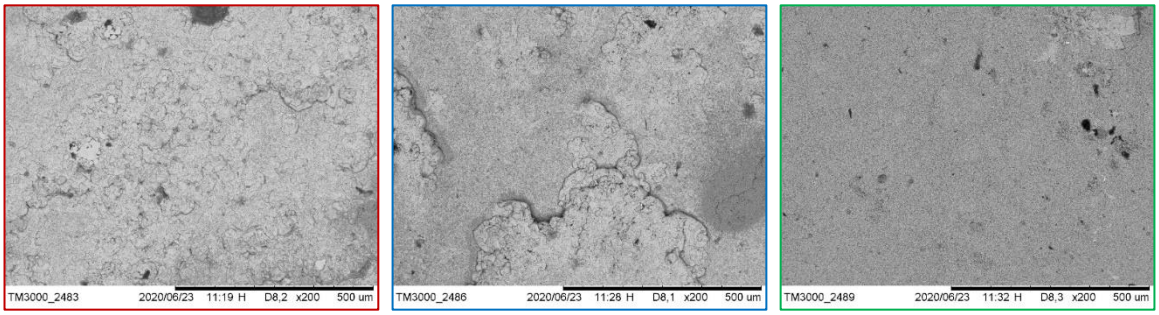

X200

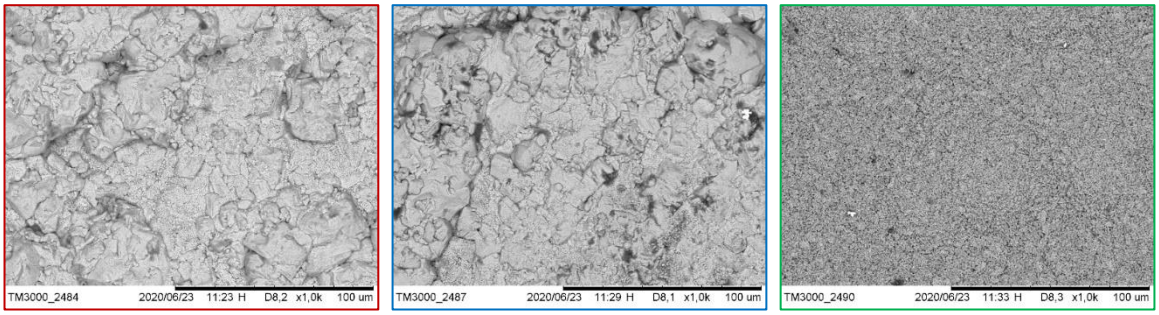

X1000

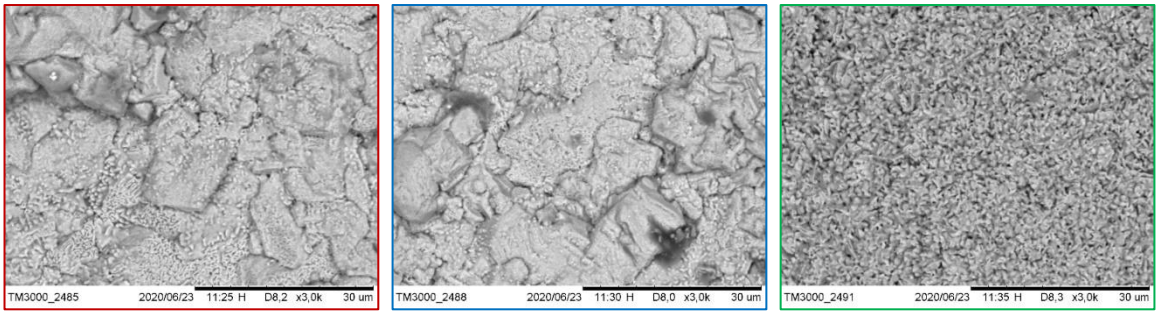

X3000

Figure 219: Test TII 7, Deposit surface at different current densities and magnifications.

TII 8 – Agar / Bone glue

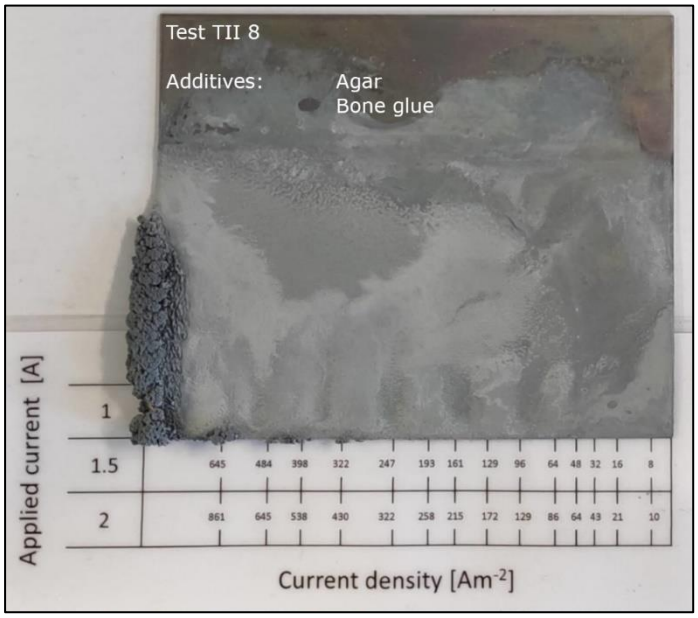

	Low	High
Adhesion	★★☆☆☆	

	Brittle	Ductile
Fracture	★★★★☆	

Figure 220: Test TII 8, Deposit appearance.

The combination of agar and bone glue was assayed in the TII8 test. The surface appears rough, Figure 220, with a fairly high amount of dendrites on the left edge. Adhesion was low while the fracture type was ductile. From surface analysis, Figure 221, a porous structure can be recognized at medium and low current densities while, at higher current densities, the deposit appears more compact.

Surface

300 A m^{-2}	200 A m^{-2}	100 A m^{-2}

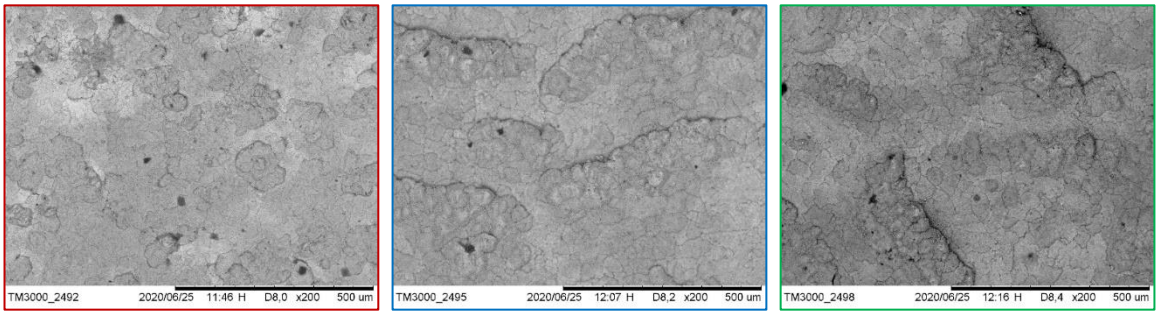

X200

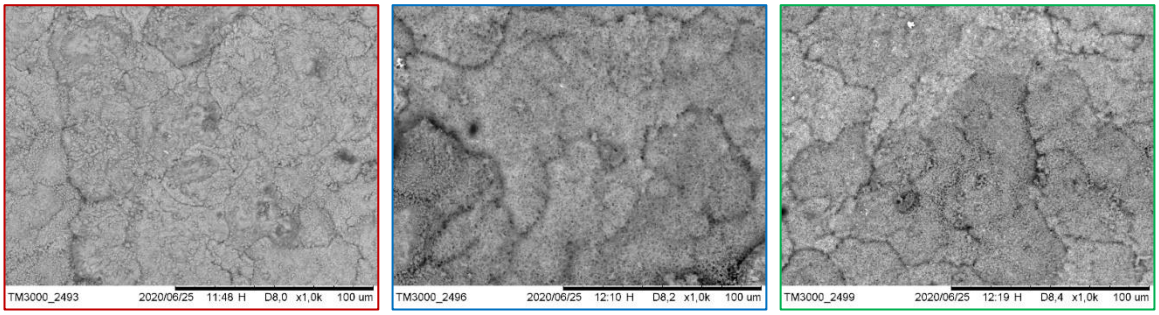

X1000

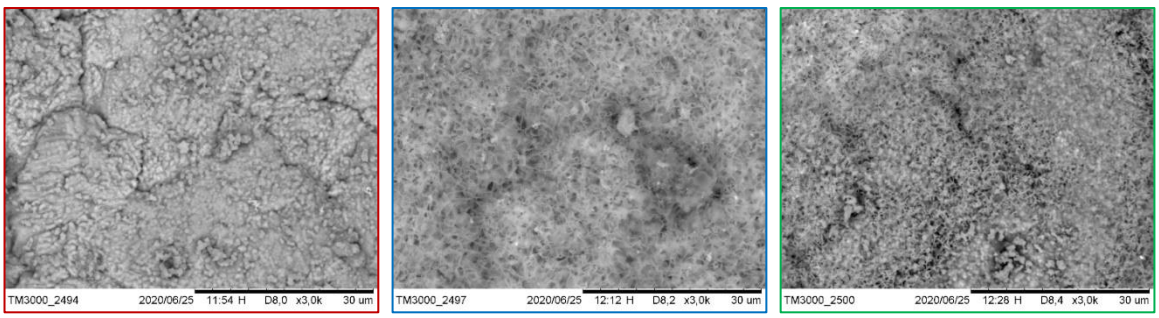

X3000

Figure 221: Test TII 8, Deposit surface at different current densities and magnifications.

TII 9 – Agar / Lignin sulfonate

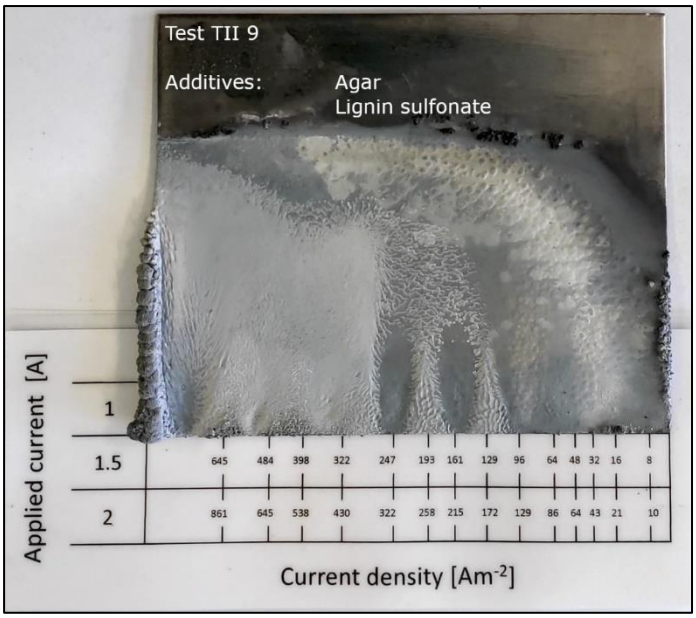

	Low	High
Adhesion	★★★★☆	

	Brittle	Ductile
Fracture	★★★☆☆	

Figure 222: Test TII 9, Deposit appearance.

TII9 test shows the effect of the combination of agar and lignin sulfonate. The deposit appears smooth with some rough areas, Figure 222, rounded dendrites are present on the left edge. Adhesion was high while the fracture type was somewhere between brittle and ductile. Surface magnification, Figure 223, reveals a porous deposit at the lowest current density that tends to become more compact at 200 A/m^2. Increasing the current density further, the structure changes completely; at 300 A/m^2 it becomes more contoured and compact.

Surface

300 A m^{-2}	200 A m^{-2}	100 A m^{-2}

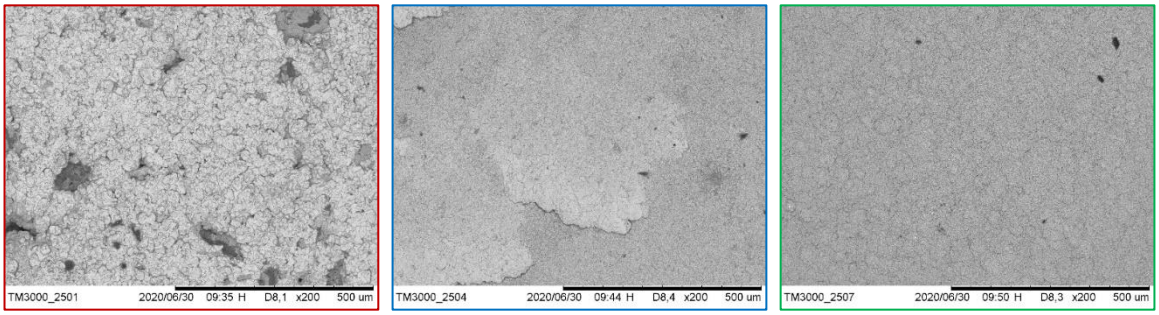

X200

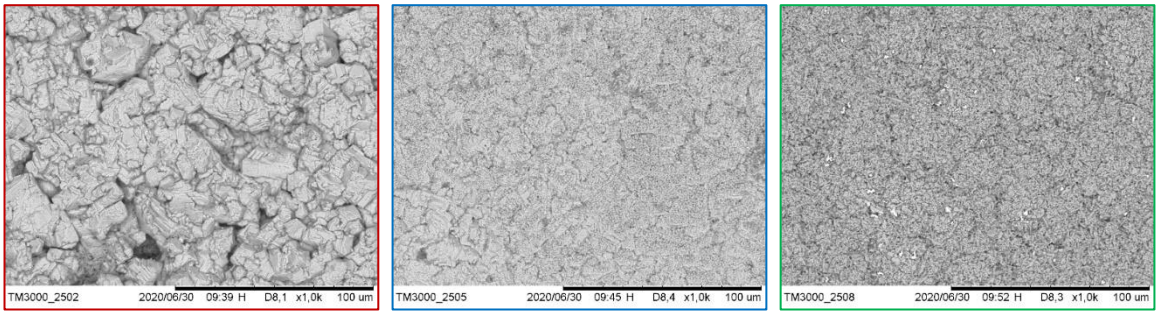

X1000

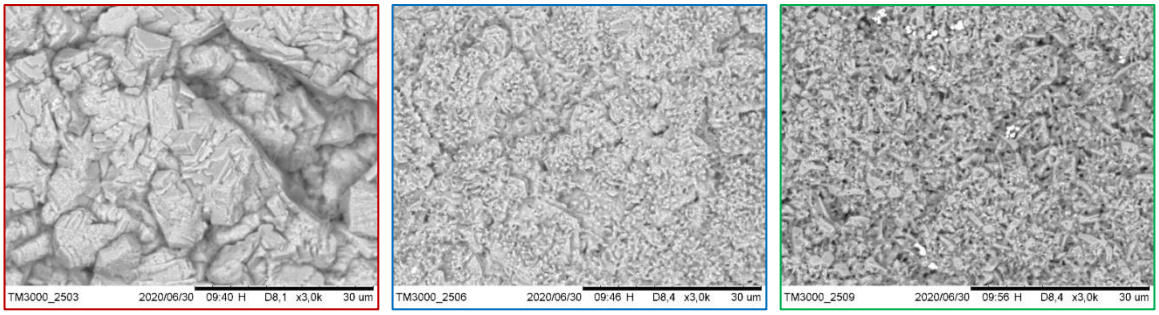

X3000

Figure 223: Test TII 9, Deposit surface at different current densities and magnifications.

TII 10 – Aesculus hippocastanum extract / Gum arabic

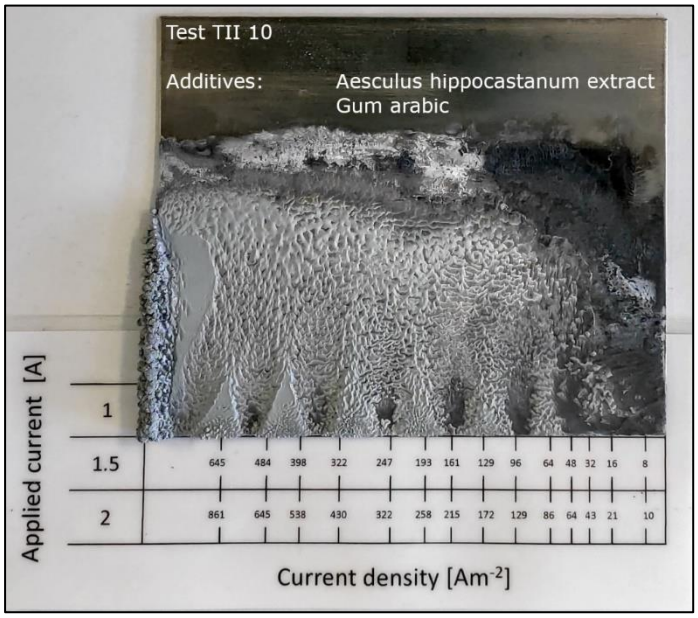

	Low	High
Adhesion	★★★☆☆	

	Brittle	Ductile
Fracture	★★★☆☆	

Figure 224: Test TII 10, Deposit appearance.

The TII10 test shows the effect of the combination of aesculus hippocastanum extract and gum arabic. As found in other tests, aesculus hippocastanum extract leads to a particular macro structure characterized by the presence of small "waves" on the overall surface of the deposit, Figure 224. A good amount of dendrites were present on the left edge of the deposit. Adhesion was average while the fracture type was somewhere between brittle and ductile.

Surface analysis shows lighter and darker areas, Figure 225, but the overall structure appears compact at each current density.

Surface

300 A m^{-2}	200 A m^{-2}	100 A m^{-2}

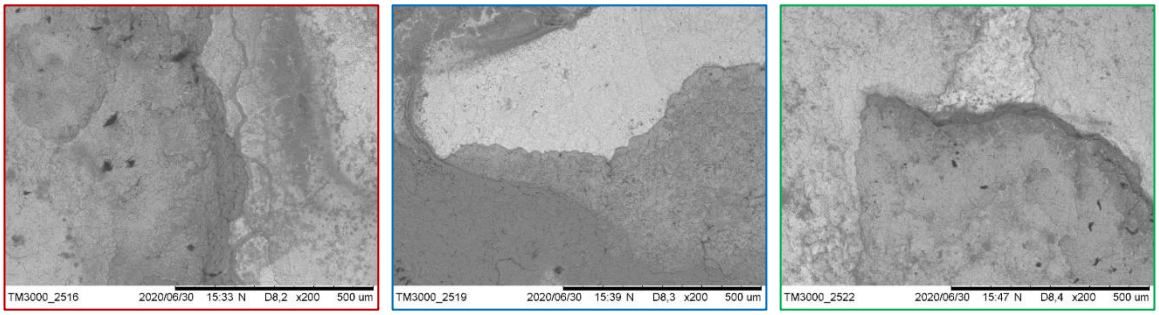

X200

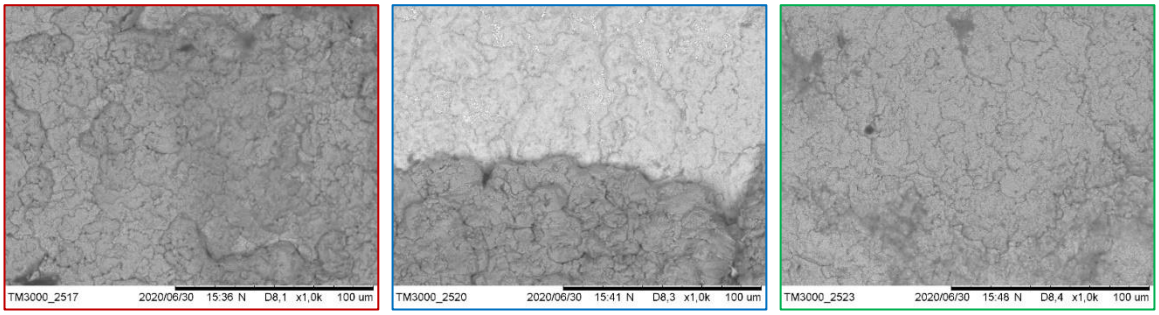

X1000

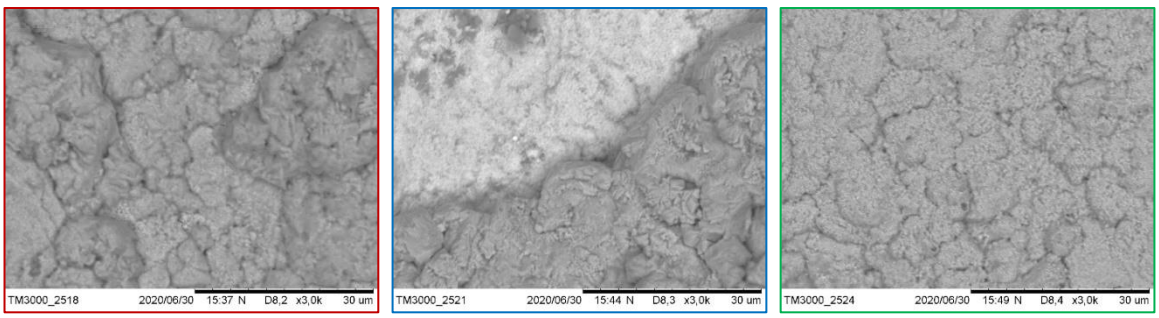

X3000

Figure 225: Test TII 10, Deposit surface at different current densities and magnifications.

TII 11 – Aesculus hippocastanum extract / Bone glue

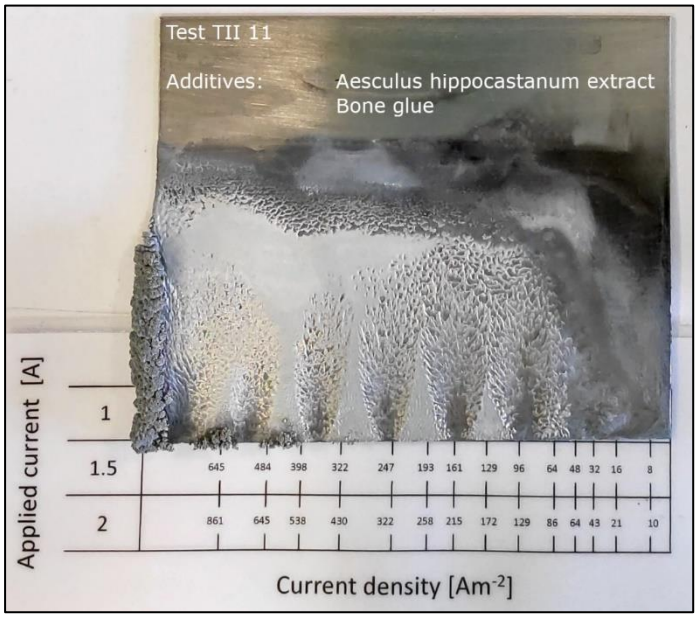

	Low	High
Adhesion	★★★★☆	

	Brittle	Ductile
Fracture	★★☆☆☆	

Figure 226: Test TII 11, Deposit appearance.

The combination of Aesculus hippocastanum extract and bone glue was tested in the TII11 test. The deposit exhibits the "wave" pattern already observed, Figure 226, but the surface is smooth. The left and lower left edges have a good amount of dendrites. Adhesion was high while the fracture type was quite brittle. Magnification of the surface shows a compact structure, Figure 227, consisting of distinguishable joined plates.

Surface

300 A m^{-2}	200 A m^{-2}	100 A m^{-2}

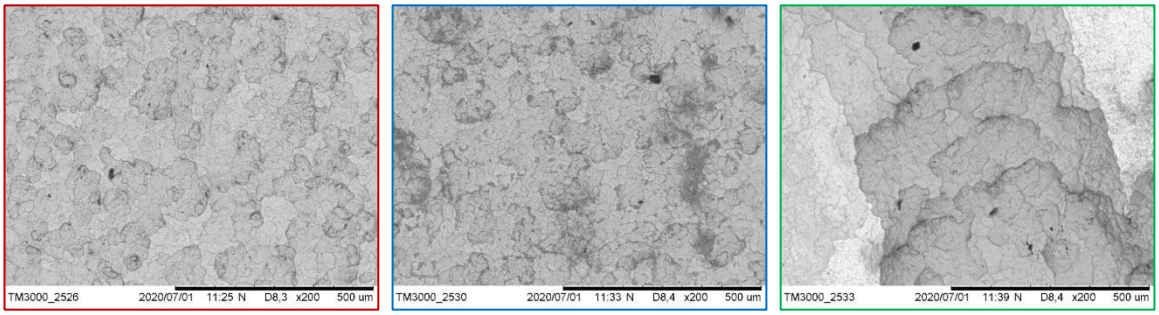

X200

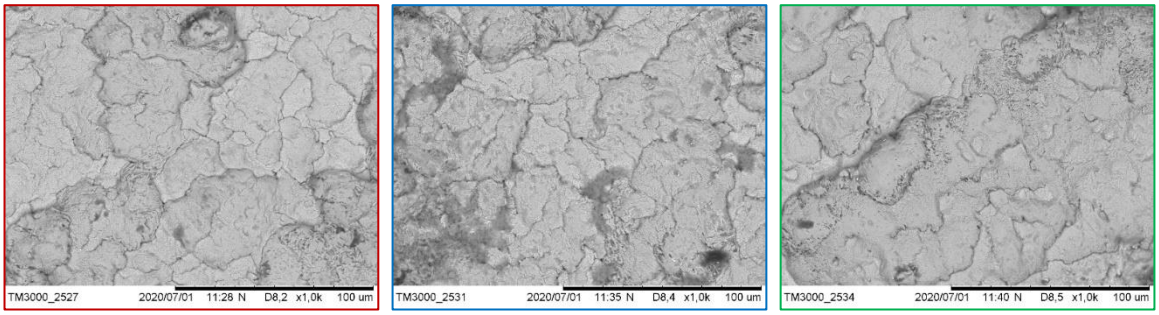

X1000

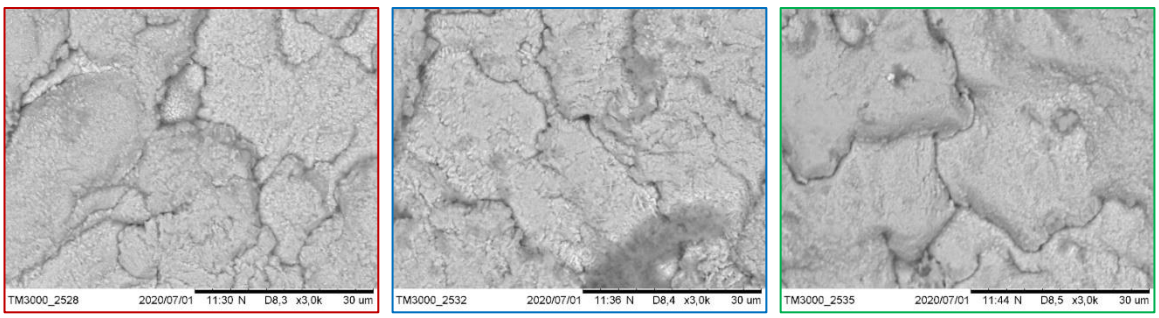

X3000

Figure 227: Test TII 11, Deposit surface at different current densities and magnifications.

TII 12 – Aesculus hippocastanum extract / Lignin sulfonate

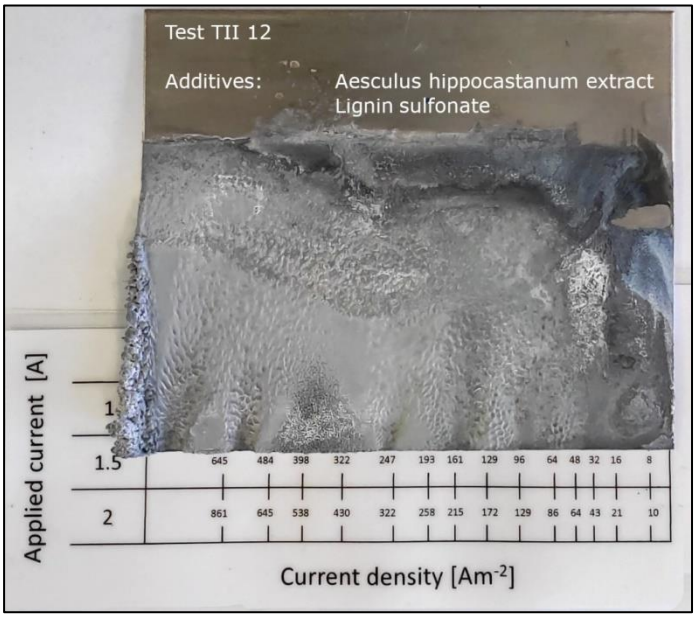

	Low	High
Adhesion	★★★★☆	

	Brittle	Ductile
Fracture	★★☆☆☆	

Figure 228: Test TII 12, Deposit appearance.

TII12 test shows the effect of aesculus hippocastanum extract and lignin sulfonate. The appearance of the deposit, Figure 228, shows the "wave" pattern, characteristic of hippocastanum extract, and an overall smooth deposit with some dendrites on the left edge and a floury deposit in the upper right corner. Adhesion, except for the upper right corner, was high while the fracture was brittle. Magnification of the surface shows a fairly compact lamellar structure, Figure 229.

Surface

300 A m^{-2}	200 A m^{-2}	100 A m^{-2}

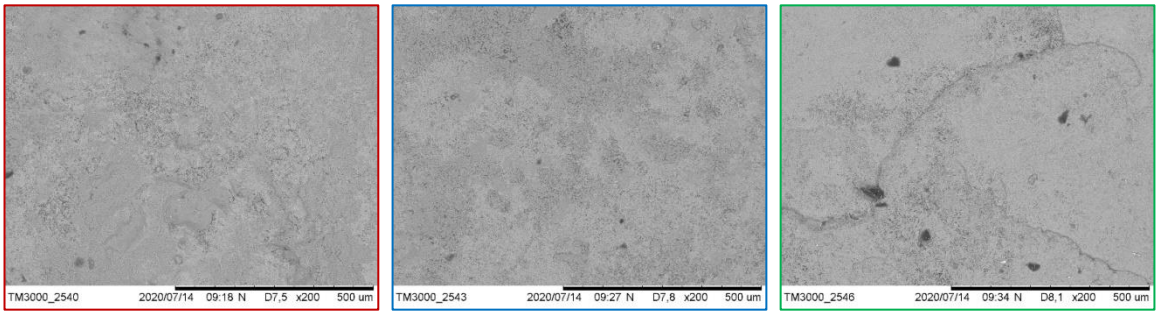

X200

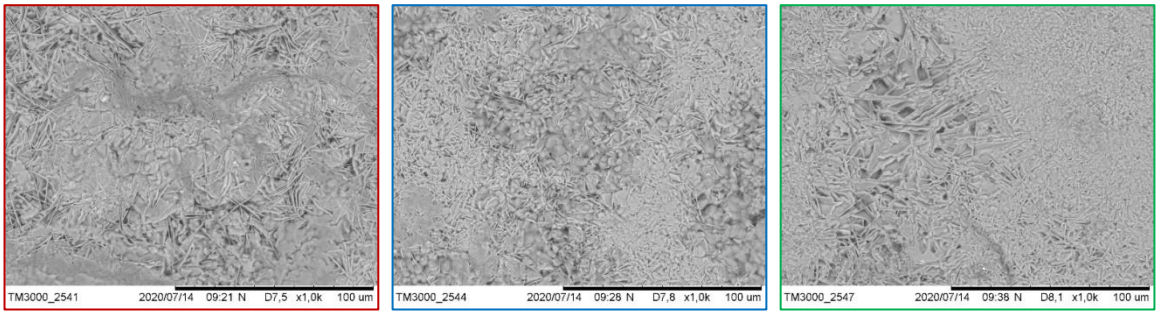

X1000

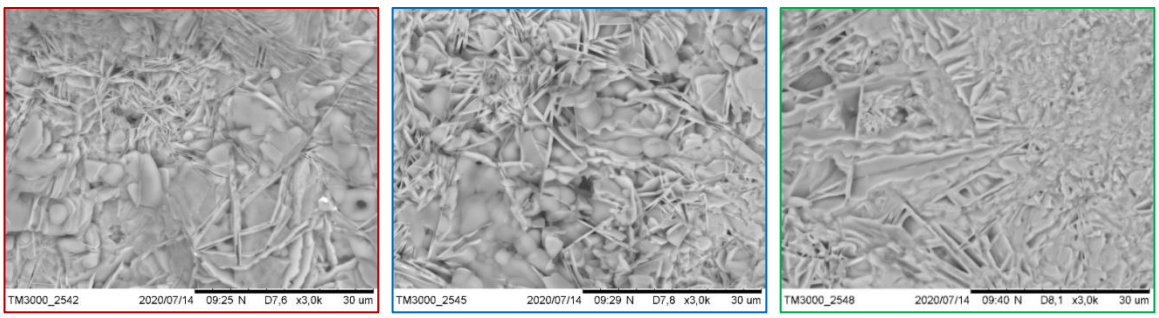

X3000

Figure 229: Test TII 12, Deposit surface at different current densities and magnifications.

TII 13 – Gum arabic / Bone glue

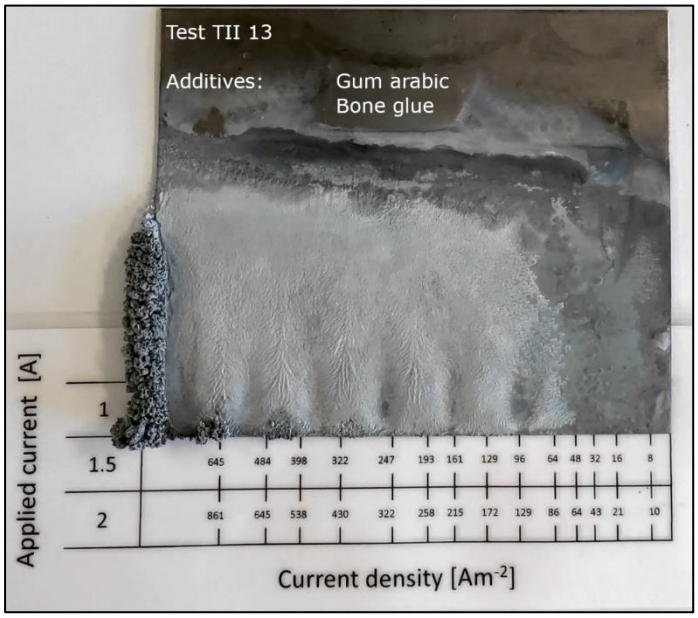

	Low	High
Adhesion	★★★★☆	

	Brittle	Ductile
Fracture	★★☆☆☆	

Figure 230: Test TII 13, Deposit appearance.

The effect of the combination of gum arabic and bone glue is shown in TII13 test. The deposit appears quite rough, Figure 230, and a good amount of dendrites are present on the left edge. Adhesion was high while the fracture type was brittle. Magnifications of the surface, Figure 231, show a blob like structure that is compact at maximum magnification.

Surface

300 A m^{-2}	200 A m^{-2}	100 A m^{-2}

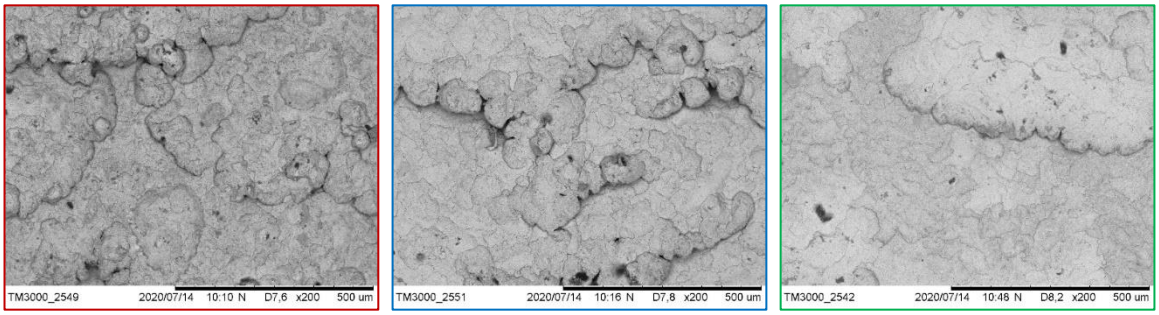

X200

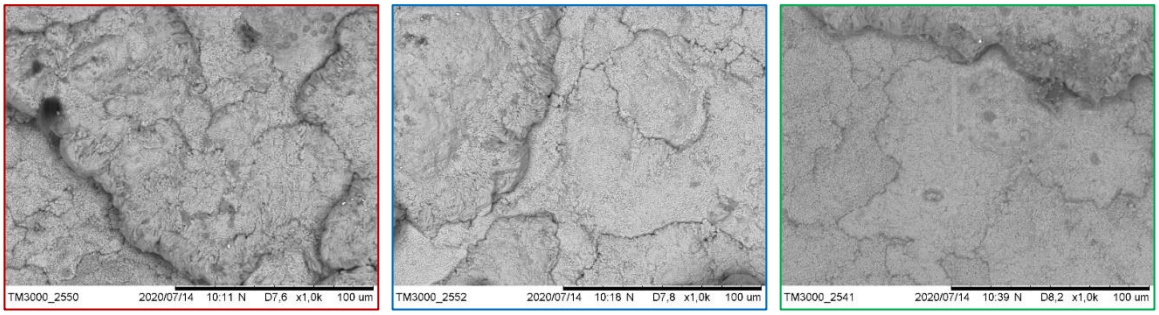

X1000

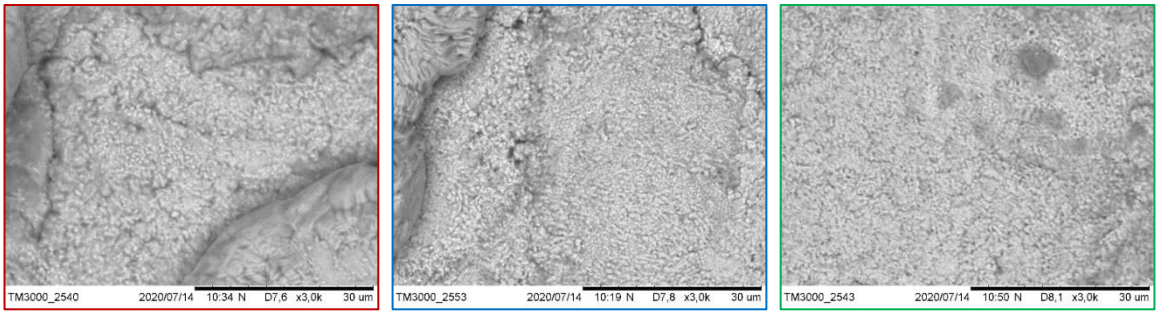

X3000

Figure 231: Test TII 13, Deposit surface at different current densities and magnifications.

TII 14 – Gum arabic / Ligningsulfonate

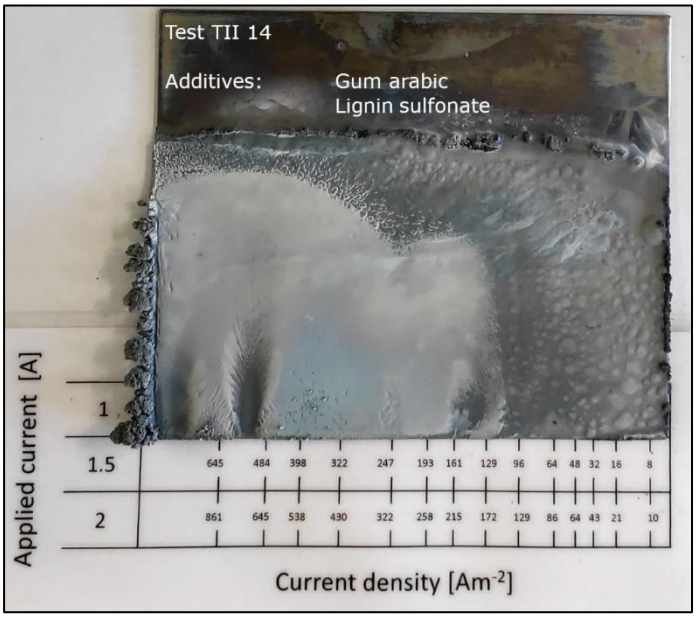

	Low	High
Adhesion	★★★☆☆	

	Brittle	Ductile
Fracture	★★☆☆☆	

Figure 232: Test TII 14, Deposit appearance.

Test TII 14 shows the effect of gum arabic and lignin sulfonate. The deposit appears very smooth in the middle and left side, dendrites are present in large quantity on the left edge while, on the opposite side, a small amount of such structures has formed, Figure 232. Adhesion was average while the fracture type was brittle. Surface analysis, Figure 233, reveals a porous structure at the lowest current density that becomes more more compact as the current density increases. At the highest current density, the deposit structure appears to be composed of many regularly shaped pieces.

Surface

300 A m^{-2}	200 A m^{-2}	100 A m^{-2}

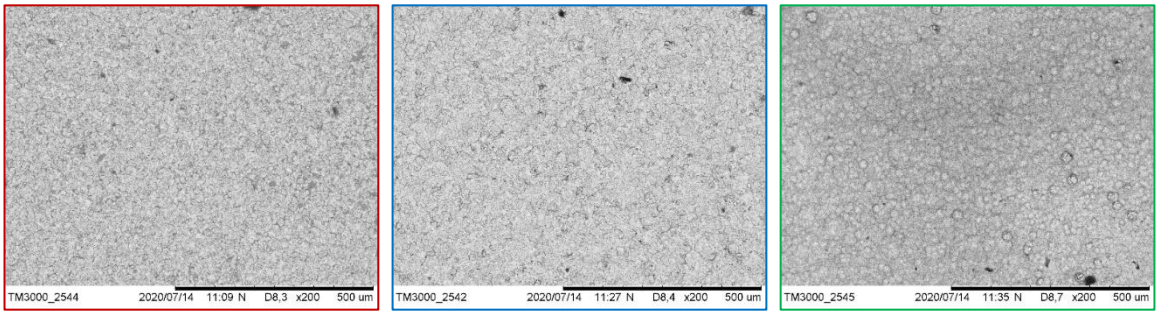

X200

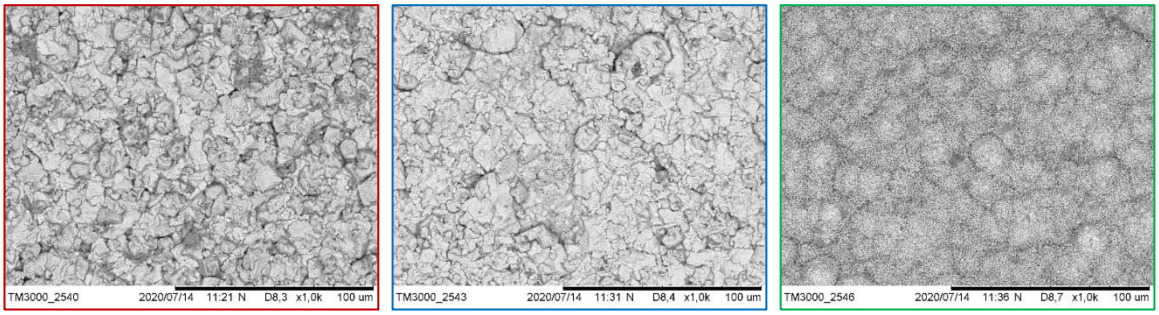

X1000

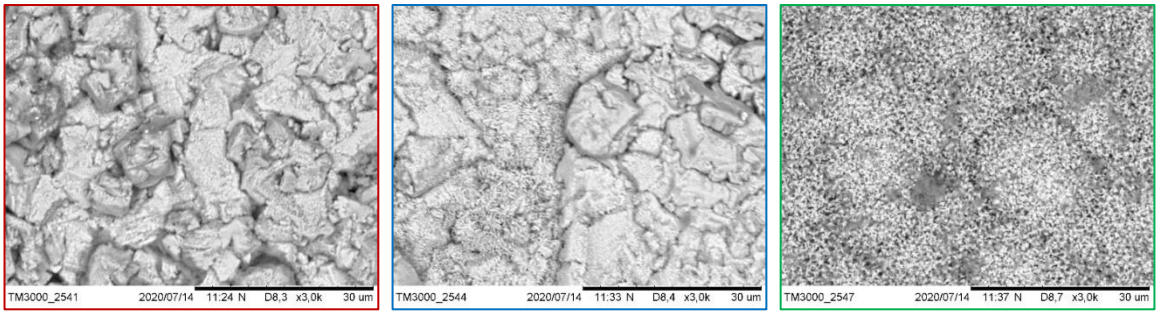

X3000

Figure 233: Test TII 14, Deposit surface at different current densities and magnifications.

TII 15 – Bone glue / Lignin sulfonate

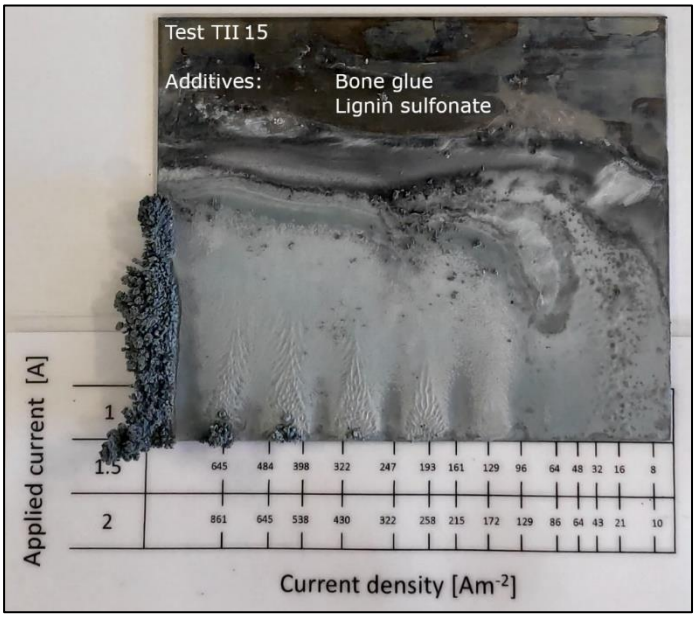

	Low	High
Adhesion	★★★☆☆	

	Brittle	Ductile
Fracture	★☆☆☆☆	

Figure 234: Test TII 15, Deposit appearance.

Test TII 15 shows the effect of the combination of bone glue and lignin sulfonate. The deposit appears smooth but covered with small dendrites, Figure 234. The left edge shows a large amount of dendrites. Adhesion was medium while the fracture type was very brittle. Surface magnifications, Figure 235, show a porous structure at 100 A/m^2 that becomes more compact at higher current densities. The deposit appears to be composed of overlapping blob-like areas that show no particular structure.

Surface

300 A m^{-2}	200 A m^{-2}	100 A m^{-2}

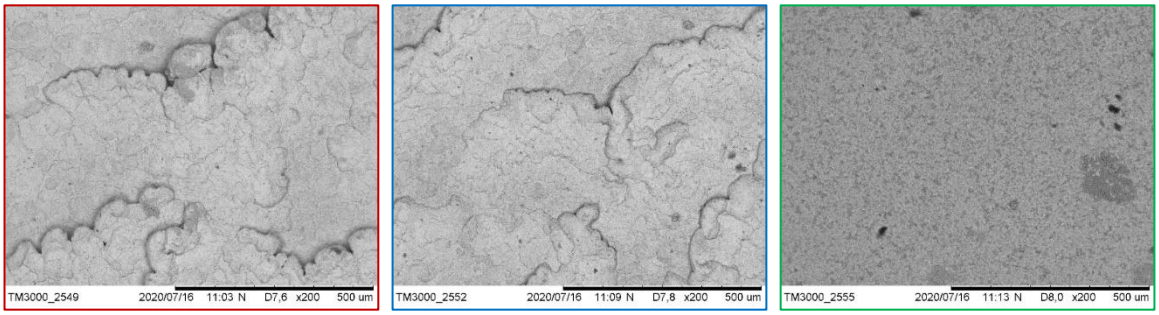

X200

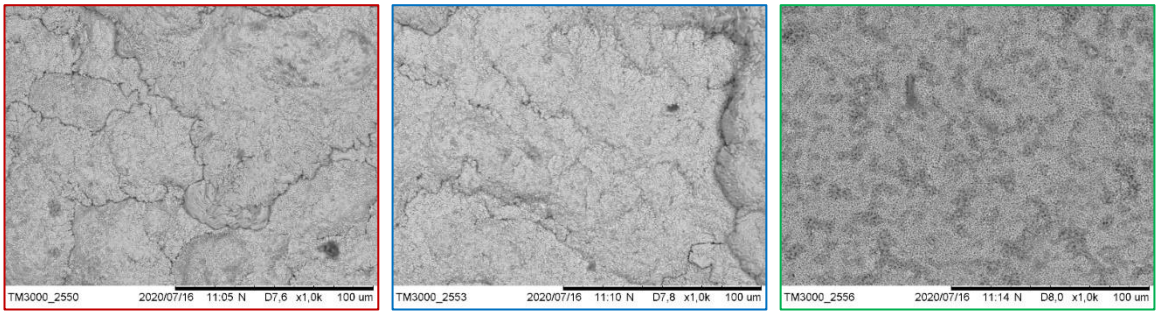

X1000

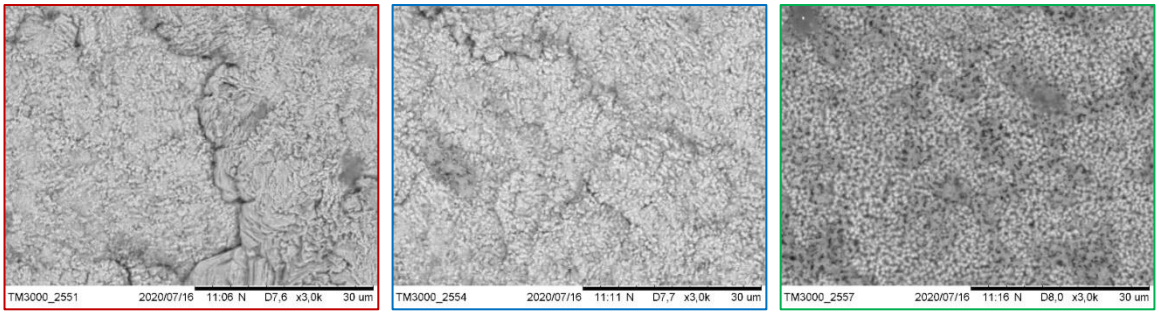

X3000

Figure 235: Test TII 15, Deposit surface at different current densities and magnifications.

Faradaic efficiency

Each deposit was rinsed with distilled water, air-dried, and weighed. Faradic efficiency was then calculated as follows:

$$W_{Theo} = \frac{MW\ I\ t}{nF}$$

$$Faradaic\ efficiency = \frac{W_{Exper}}{W_{Theo}} 100$$

Equation 16: Faradaic efficiency calculation: MW, zinc mass weight – I, current intensity (A)- t, time (s)- n, moles of electrons exchanged per mole of zinc- F, Coulomb constant- W_{Exper} , weight of the experimentally obtained zinc.

The calculated faradic efficiencies are shown in Figure 236; for all tests, they are in the range of 90-95%. A significant loss of efficiency was not observed for the tested additives combination.

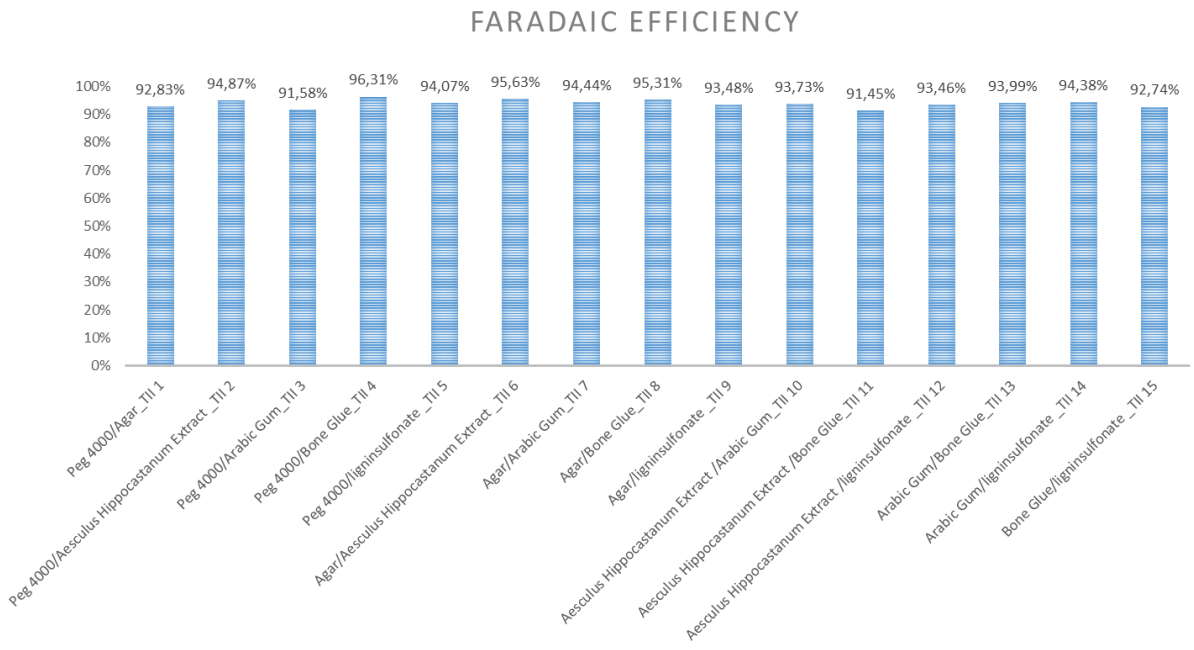

Figure 236: Faradaic efficiency.

Cell potential

The cell potential was recorded for the entire experiment and plotted in Figure 237. The baseline represents the average potential of an experiment conducted using an ammonium chloride solution containing zinc, 250 g/L and 10 g/L respectively, in the absence of additives. For each assay, the cell potential was calculated by averaging all values recorded during the individual experiment and compared to the baseline, Figure 238. This potential, compared to the baseline, can be attributed to the adsorption of additives on the cathode surface or their anodic or cathodic degradation.

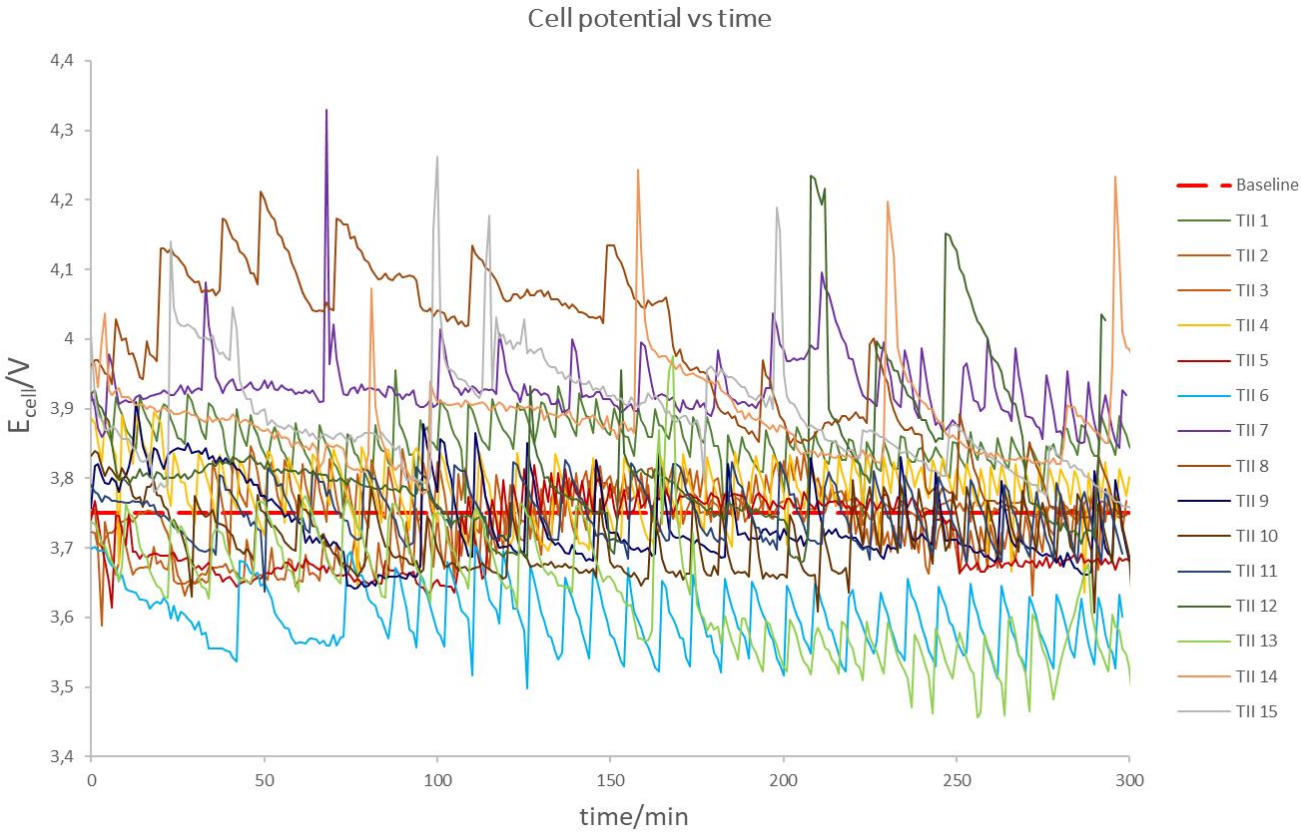

Figure 237: Cell potential and baseline.

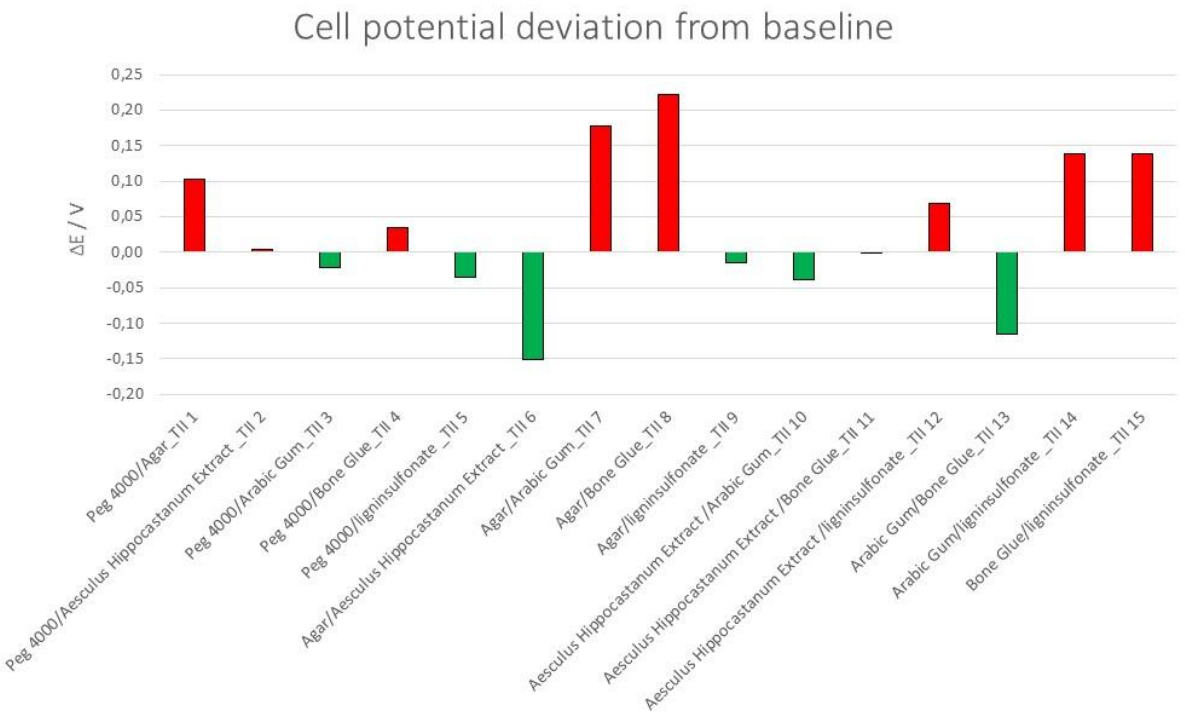

Figure 238: Cell potential deviation from baseline.

Current density

To assess the validity of Equation 15, four deposits were examined according to the procedure reported in section 0. Deposits were chosen for their amount of dendrites, from one with a small amount of dendrites (TII 2) to one with a high amount of such structure (TII 8). The experimentally obtained logarithmic equations for the TII 2-3-4-8 tests, compared with Hull's equation, are shown in Figure 239. At three current densities, 100, 200, and 300 A/m^2, the delta of Equation 15 was calculated and reported in Table 16 in percentage form. These results show good agreement between the experimentally obtained results and Equation 15, the difference between the two increases as the current density and the amount of dendrites increase. However, as far as this type of experimentation is concerned, the observed differences are considered minimal and a correction of the Hull cell ruler is not considered necessary.

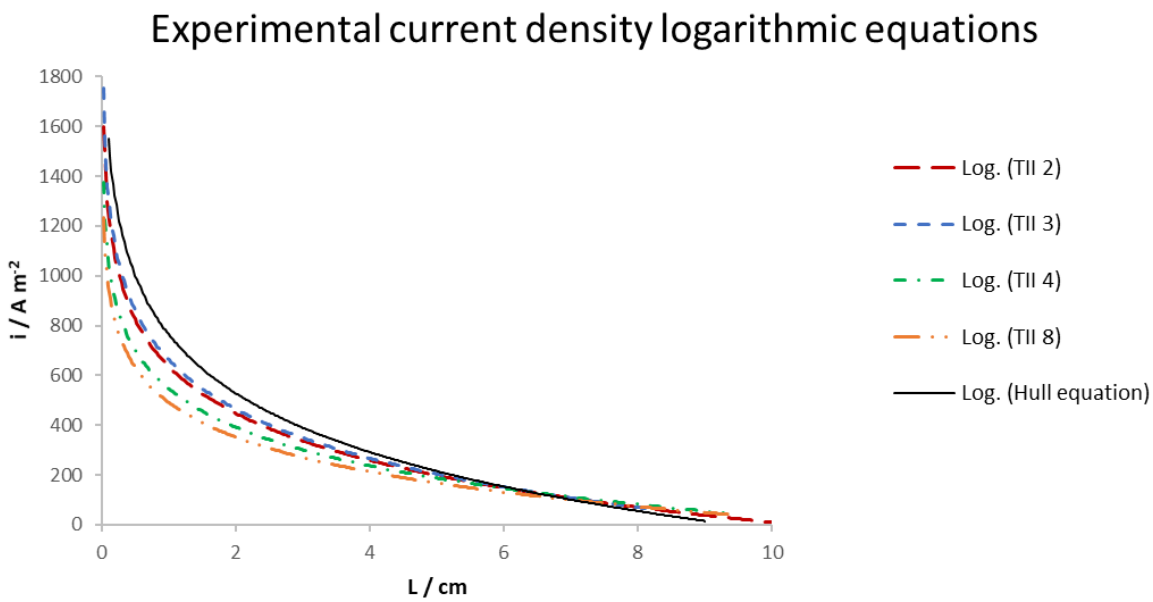

Figure 239: Current density logarithmic equations in function of L (distance from left edge) experimentally obtained (dotted lines) compared with hull equation (solid line).

Curent density delta (%) from Hull equation

	100 A/m²	**200 A/m²**	**300 A/m²**
TII 2	-1,96	-9,40	-11,87
TII 3	0,69	-5,95	-8,16
TII 4	4,89	-10,01	-14,98
TII 8	-8,57	-19,41	-23,02

Table 16: Current density delta percentage between experimental logarithmic equation and Hull equation.

Surface tension

Surface tension was measured by the stalagmometric method before and after each test. The surface tension of a 250 g/1 ammonium chloride solution at 25 °C was measured to be 82 dyne/cm while pure water is 72 dyne/cm; the presence of other substances (additives) could further change this parameter. Figure 240 shows the surface tension values measured before and after 5 hours of electrolysis; in some cases, the additives increased the surface tension of the electrolyte while in others they decreased it. After electrolysis in some cases the surface tension increased while in others it decreased. With such information it is difficult to tell if the additive was consumed or degraded into smaller molecules during the process, however, it is clear that the surface tension changes and this can be used as a monitoring parameter to keep additive concentrations in a certain range.

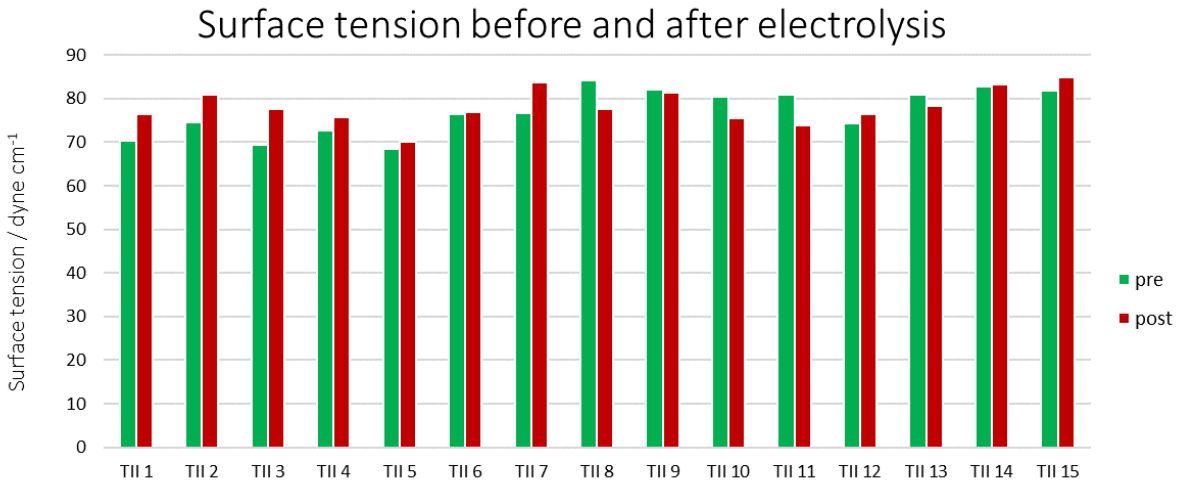

Figure 240: Surface tension (@25°C) of the electrolyte measured before and after 5 hours of electrolysis.

Conclusions

In this study, combinations of different additives were tested with the aim of finding the best performing pair in terms of deposit compactness. Many parameters such as cell potential, adhesion, fracture type, surface tension and faradic efficiency were checked simultaneously in order to define an as complete as possible a portrait of the additive pair. For all tested pairs, faradic efficiency was high, above 90%, and no significant decrease was observed. The cell potential varied between +200 and -150 mV compared to an

electrolysis in the absence of additives, implying that the presence of additives could increase or decrease current consumption. The surface tension was monitored before and after electrolysis, in many cases a variation was observed between the two measurements; with further information, this could be a used as a useful monitoring parameter to keep the additive concentration in a certain range avoiding accumulation or excessive depletion.

The theoretical Hull cell current distribution was verified and good agreement was found between the Hull equation and experimental data; deviation from the theoretical equation was observed to increase as dendrite formation increases. However, this deviation is small and the Hull cell ruler should not be changed and the standard Hull equation can be considered reliable.

The quality of the deposit, in terms of compactness, cannot be measured numerically. The quality was evaluated visually, considering the amount of dendrites and the magnification at the highest current density, the deposits obtained in the TII 6, TII 9, and TII 14 tests are the most promising. Therefore, the following additives involved in the above tests were selected for further investigation: agar, aesculus hippocastanum extract, lignin sulfonate, and gum arabic.

Electrodeposition additives for the EZINEX® process

Part III

Introduction

In the test report "Zinc electrodeposition: screening of additives", various additives were tested for zinc electrodeposition from ammonium chloride solutions. Each additive showed a different effect on the zinc deposit; one showed leveling characteristics, one promoted a compact deposit, one inhibited the growth of dendrites, and so on. From the analysis of the obtained deposits, six additives were selected and tested in combinations of 2 to take advantage of the effect of both additives to achieve the most compact deposit possible and without dendrites

According to results obtained from such tests, the most promising four additives were tested in mix of 3, 20 ppm each, to further exploit their influence on the zinc deposit; these are agar, aesculus hippocastanum extract, lignin sulfonate, and gum arabic.

Cell potential, adhesion, fracture type, structure, surface tension and faradaic efficiency were the parameters investigated in this experimentation.

TIII 1 – Agar / Aesculus hippocastanum extract / Ligninsulfonate

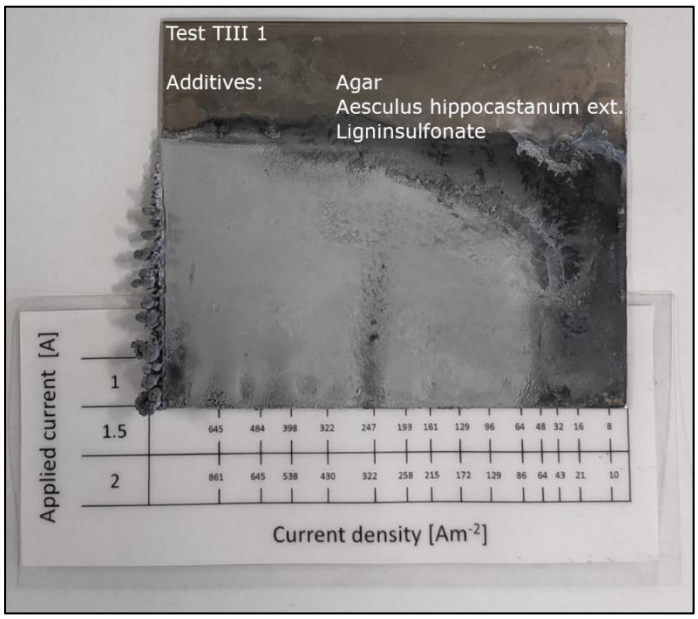

	Low	High
Adhesion	★★★★☆	

	Brittle	Ductile
Fracture	★★☆☆☆	

Figure 241: Test TIII 1, Deposit appearance.

The test TIII 1 was done using agar, aesculus hippocastanum extract, and ligninsulfonate, 20 ppm each. Figure 241 shows the appearance of the deposit, the overall surface was smooth with some dendrites on the left edge. The zinc plate was very adherent to the titanium substrate and the fracture was brittle. Analysis of the surface, Figure 243, reveals a porous structure that does not change too much as the current density increases.

Surface

300 A m^{-2}	200 A m^{-2}	100 A m^{-2}

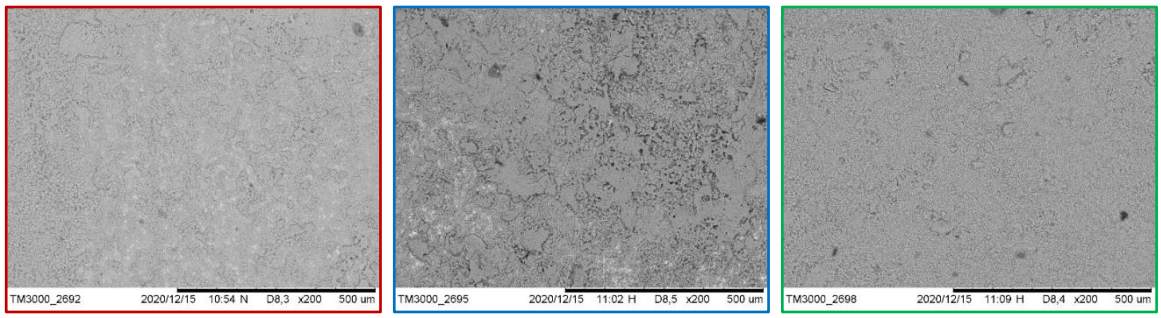

X200

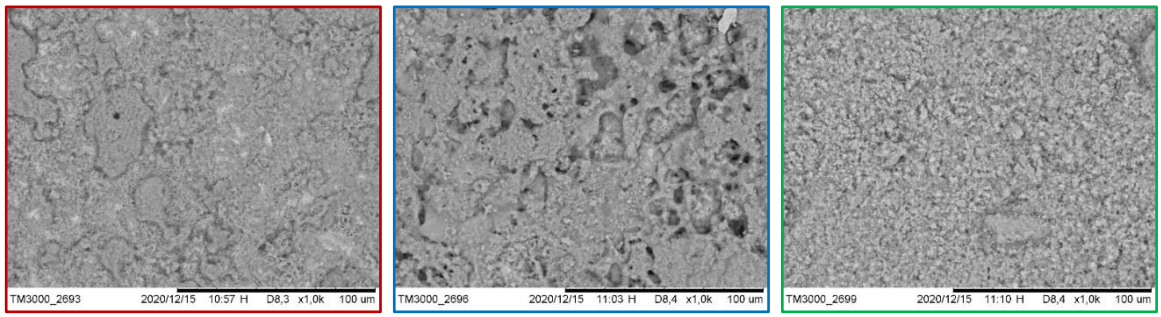

X1000

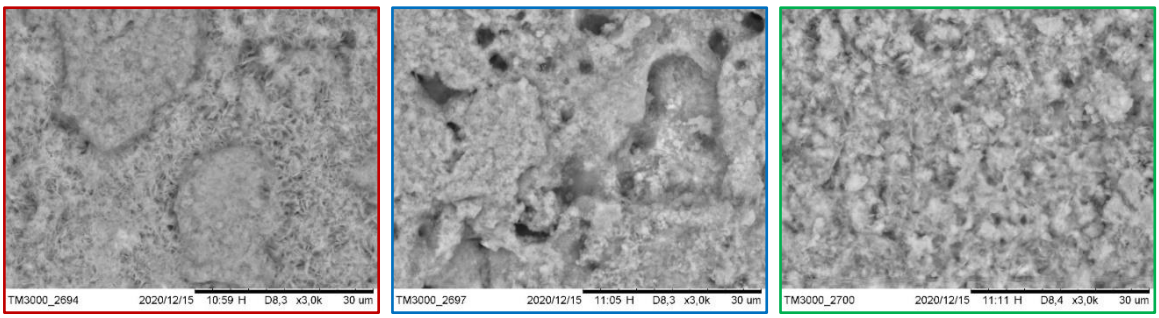

X3000

Figure 242: Test TIII 1, Deposit surface at different current densities and magnifications.

TIII 2 – Agar / Aesculus hippocastanum extract / Gum Arabic

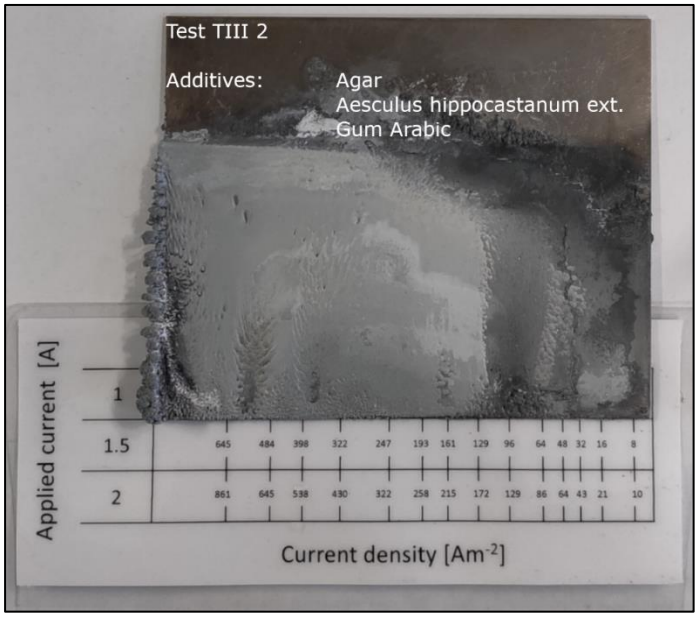

Low High

Adhesion ★★★☆☆

Brittle Ductile

Fracture ★★★☆☆

Figure 243: Test TIII 2, Deposit appearance.

The test TIII 2 was done using agar, aesculus hippocastanum extract, and gum arabic, 20 ppm each. The deposit appears smooth, Figure 243, with an obvious mark due to air sparging. Smooth dendrites are visible on the edge at high current density. Adhesion was medium, while the fracture type was halfway between brittle and ductile. Magnifications of the surface, Figure 244, reveal a compact deposit that resembles a grain-like structure. The different current densities do not appear to be particularly influential on the observed structure.

Surface

300 A m^{-2}	200 A m^{-2}	100 A m^{-2}

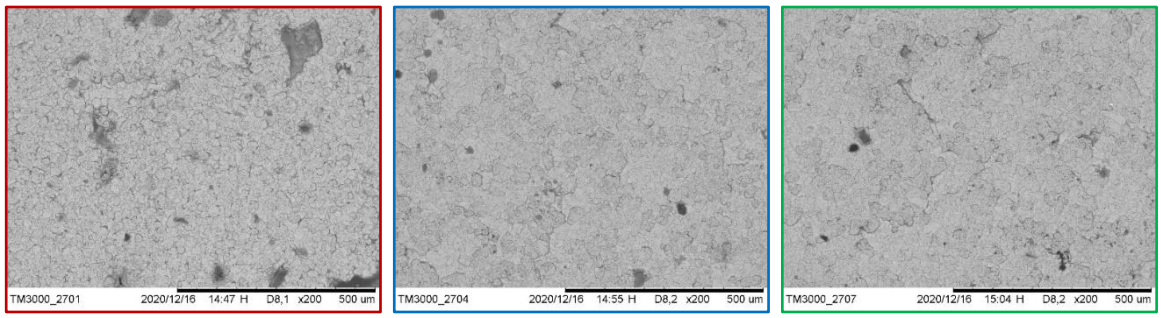

X200

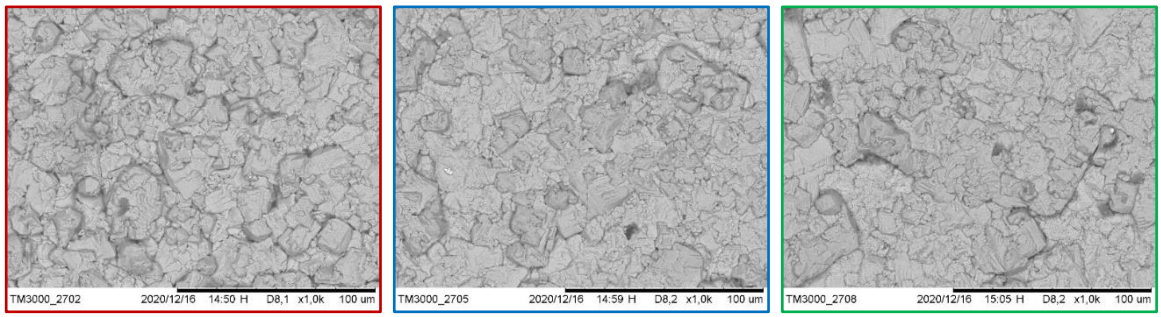

X1000

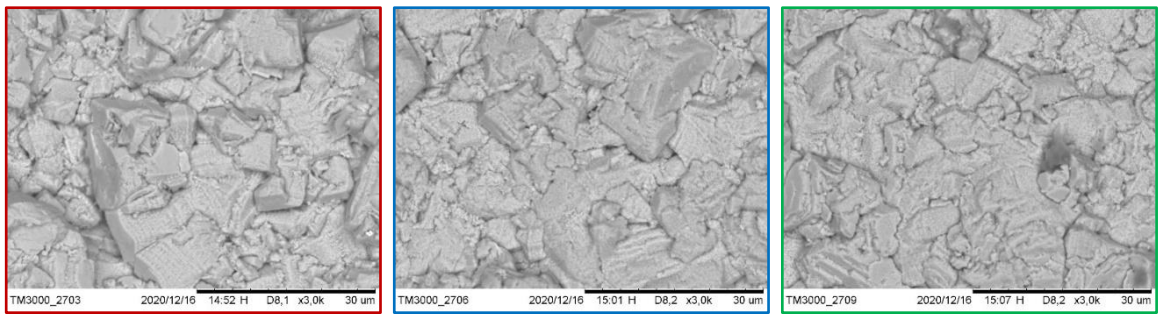

X3000

Figure 244: Test TIII 2, Deposit surface at different current densities and magnifications.

TIII 3 – Agar / Ligninsulfonate / Gum Arabic

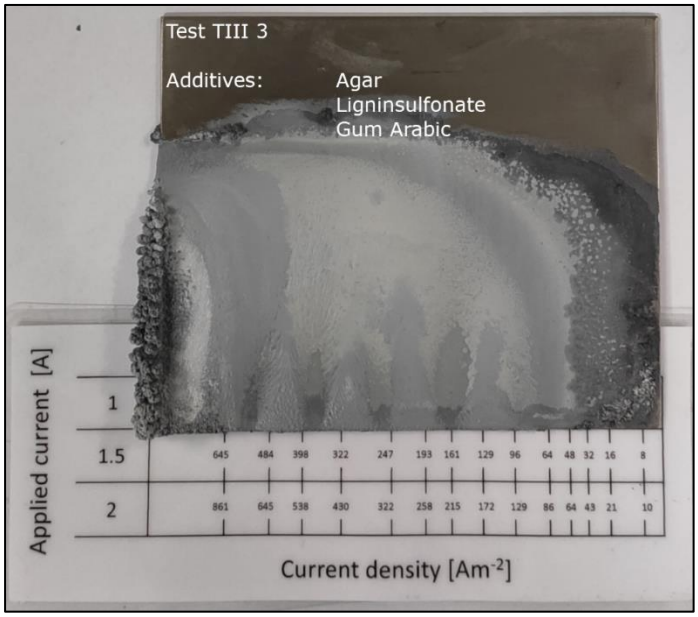

Low High

Adhesion ★★★★☆

Brittle Ductile

Fracture ★★★☆☆

Figure 245: Test TIII 3, Deposit appearance.

Figure 245 shows the zinc deposit obtained from the test TIII 3 in the presence of 20 ppm of agar, ligninsulfonate, and gum arabic. The deposit appears fairly smooth with sponge-like dendrites on the right edge. Adhesion of the deposit was good while the fracture type was halfway between brittle and ductile. Surface analysis, Figure 246, shows a porous structure at the lowest current density, which takes on a grain-like appearance as current density increases. However, even at 300 A/m^2, a porous structure is recognizable.

Surface

300 A m^{-2}	200 A m^{-2}	100 A m^{-2}

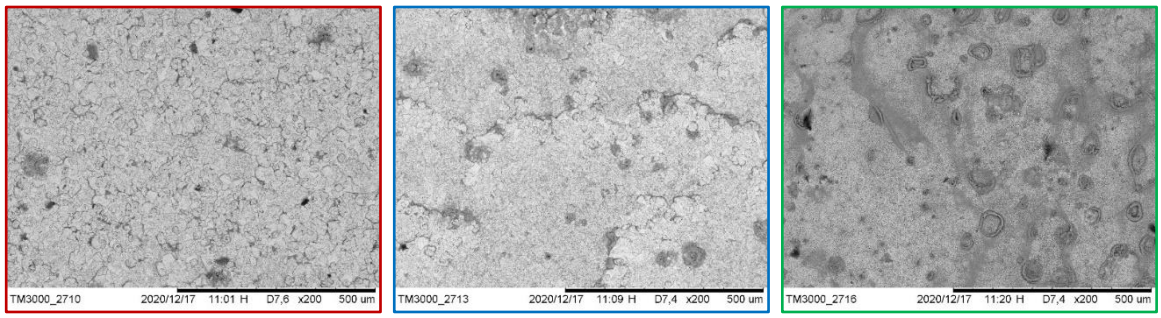

X200

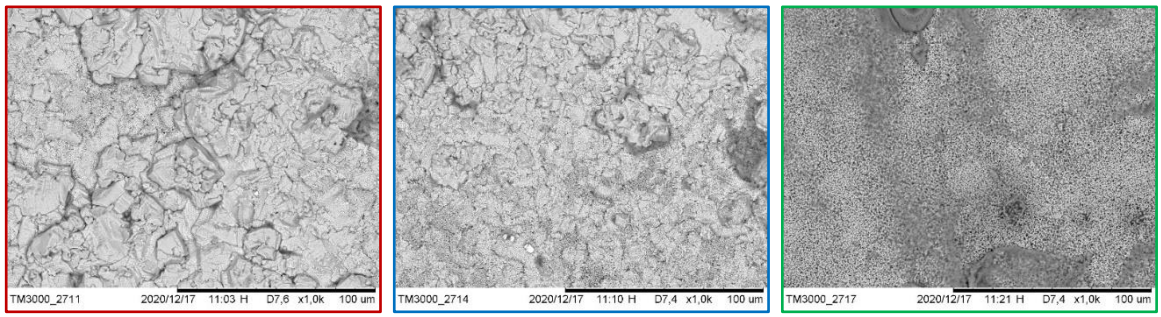

X1000

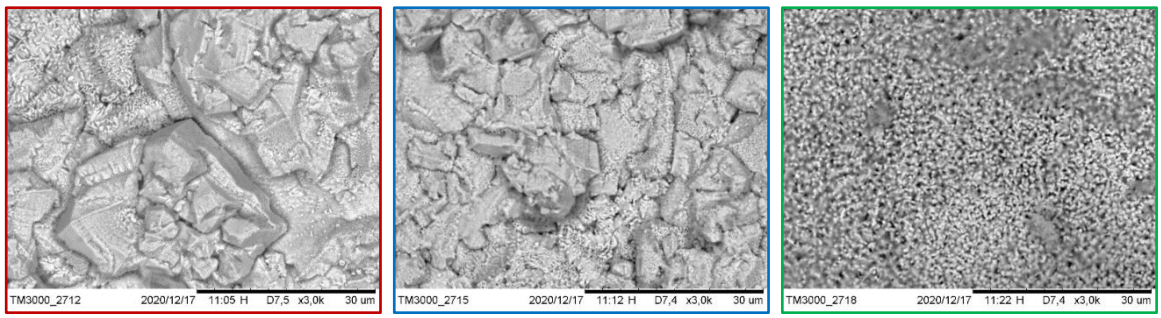

X3000

Figure 246: Test TIII 3, Deposit surface at different current densities and magnifications.

TIII 4 – Ligninsulfonate / Aesculus hippocastanum extract / Gum arabic

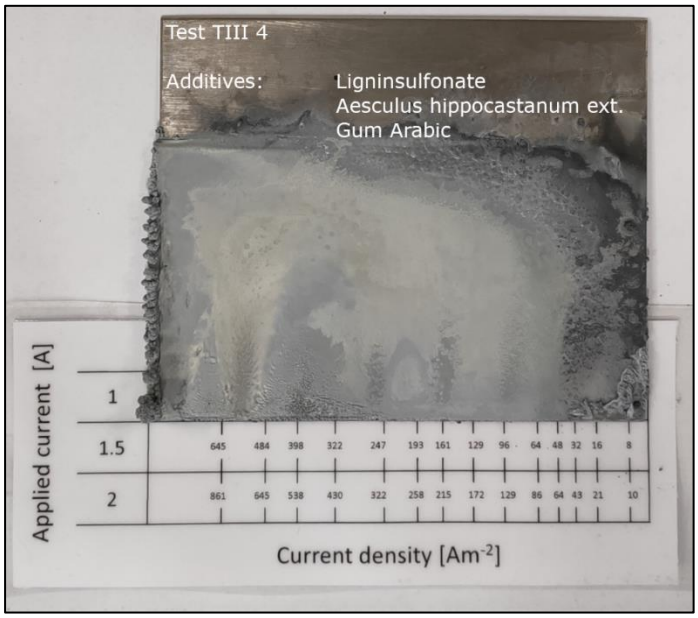

	Low	High
Adhesion	★★★★☆	

	Brittle	Ductile
Fracture	★★★☆☆	

Figure 247: Test TIII 4, Deposit appearance.

The test TIII 4 was done using ligninsulfonate, aesculus hippocastanum extract, and gum arabic, 20 ppm each. Figure 247 shows a fairly smooth surface with a small amount of dendrites on the left edge of the deposit. Adhesion was high while the fracture type was somewhere between brittle and ductile. Magnification of the surface, Figure 248, shows a grain-like structure with a porous morphology at the lowest current density, which tends to disappear completely as the current density increases.

Surface

300 A m^{-2}	200 A m^{-2}	100 A m^{-2}

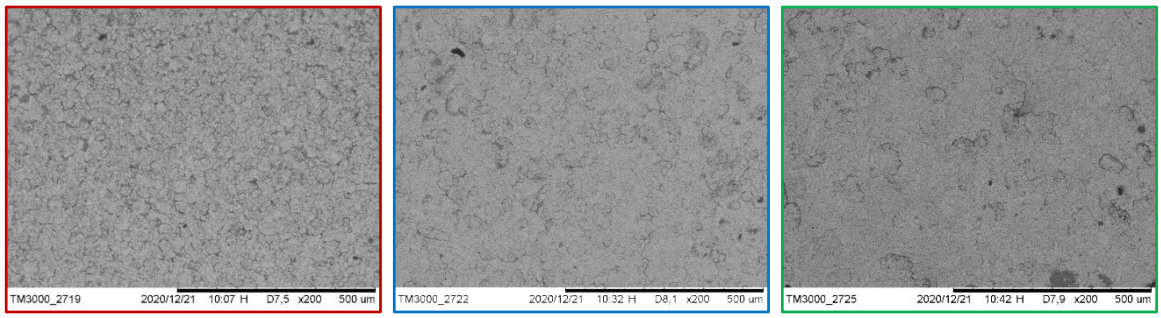

X200

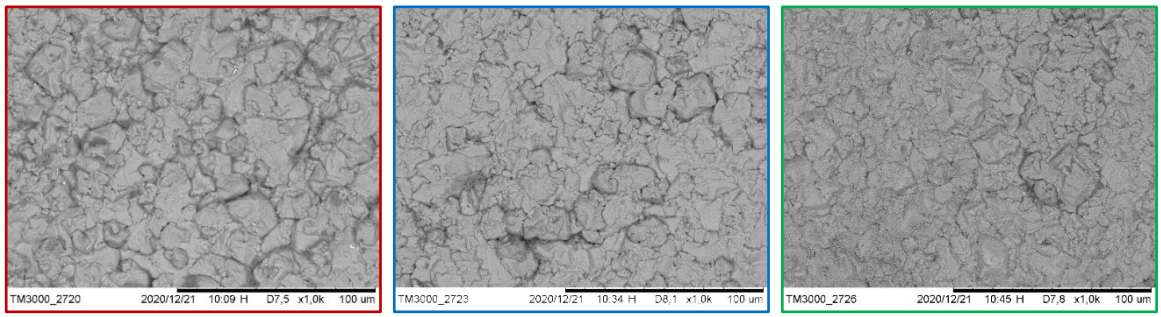

X1000

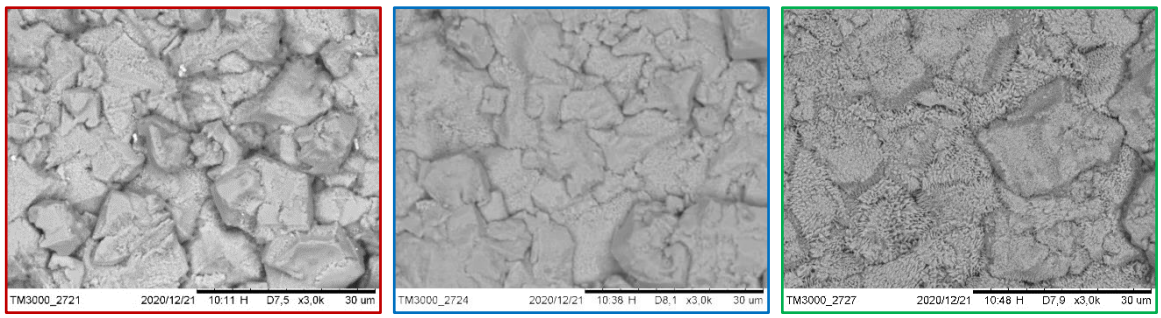

X3000

Figure 248 Test TIII 4, Deposit surface at different current densities and magnifications.

Faradaic efficiency

Calculated Faradaic efficiencies are reported in Figure 249; for all tests, they are the range 90-96%. A significant loss of efficiency was not observed for the tested additives mixture.

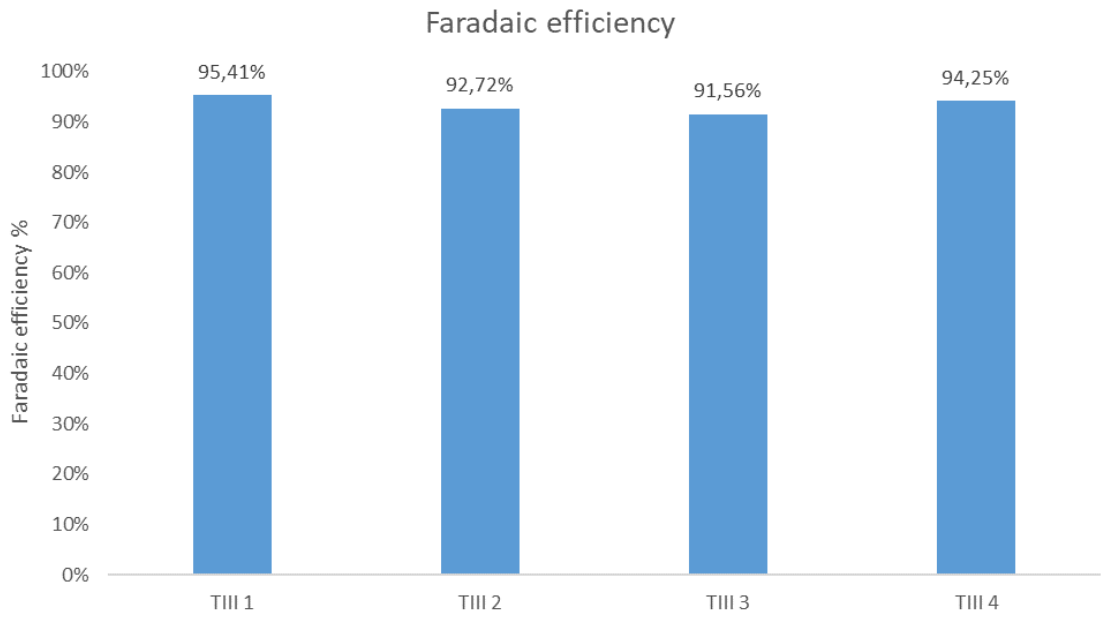

Figure 249: Faradaic efficiency.

Cell potential

The cell potential was recorded for the entire experiment and plotted in Figure 250. The test TIII 2 was on average 100 mV below the values recorded for the other tests. In the TIII 3, the cell potential dropped by 100 mV after 200 min, the reasons are unknown. Compared with the cell potential observed in the absence of additives, 3.750 V, the presence of additives tended to increase it, except in the TIII 2 assay.

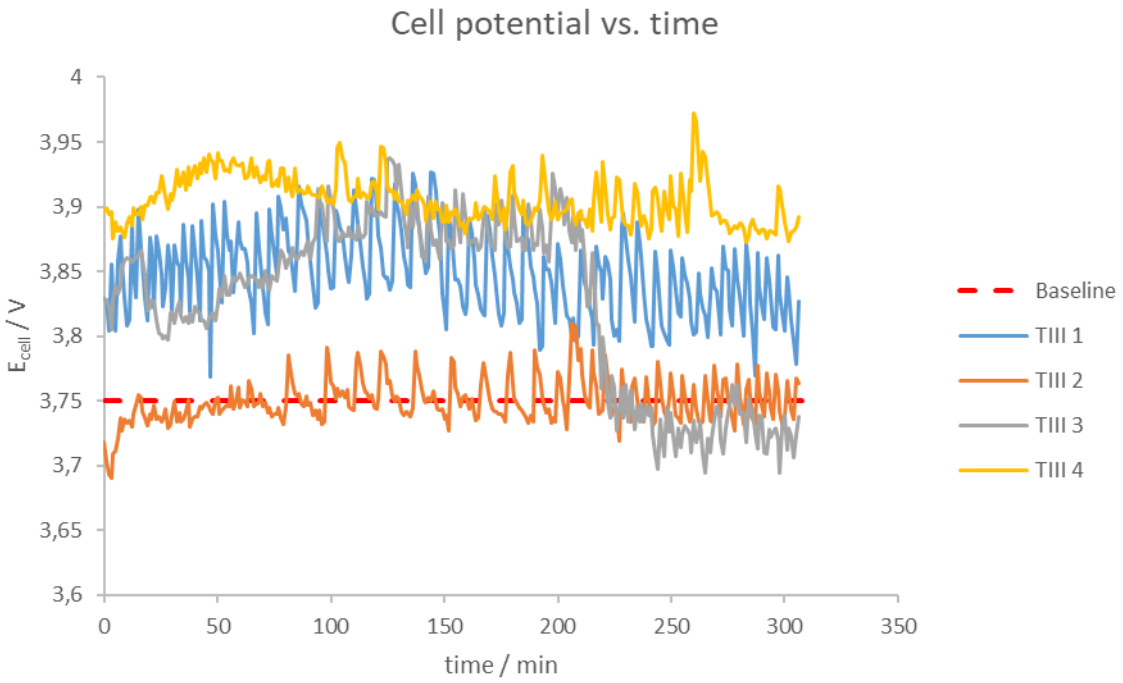

Figure 250: Cell potential and baseline.

Surface tension

Surface tension was measured by the stalagmometric method before and after each test, Figure 251. After electrolysis in some cases the surface tension increased while in others it decreased. With such information it is difficult to tell if the additive was consumed or degraded into smaller molecules during the process.

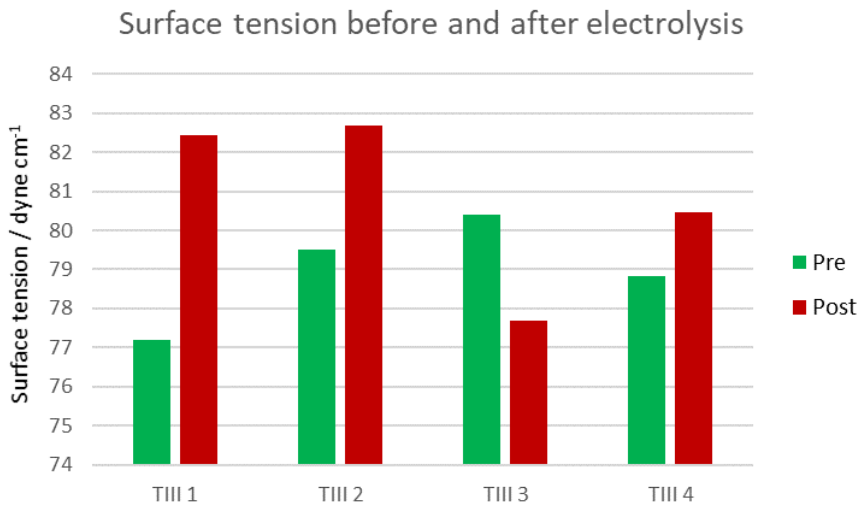

Figure 251: Surface tension (@25°C) of the electrolyte measured before and after 5 hours of electrolysis.

Conclusions

In this study, combinations of three different additives were tested with the aim of finding the best performing mixture in terms of deposit compactness. Many parameters such as cell potential, adhesion, fracture type, surface tension, and faradic efficiency were checked simultaneously in order to define an as complete as possible portrait of the additive mixture. For all tested mixtures, faradic efficiency was high, above 90%, and no significant decrease were observed. The cell potential, in most cases, was higher than that observed for electrolysis in the absence of additives implying that the presence of some additives will increase energy consumption. The surface tension was monitored before and after electrolysis, in many cases a variation was observed between the two measurements, however, it is too small to be used as a useful parameter to monitor the concentration of additives

Current distribution in the Hull cell, as reported in a previous report, was verified and good agreement was found between the theoretic equation and experimental data; deviations were observed to increase with increasing current density and dendrite formation. This deviation is small and the Hull cell and the current density equation can be considered reliable.

The quality of the deposit, in terms of compactness, cannot be measured numerically in reality, melt tests with relative quantification of slag should be done; the quality was then evaluated visually.

Compared to the previous report, the mixture of three additives produced better results in terms of deposit appearance. The best mixture of additives, from the point of view of compactness, was found to be the one tested in TIII 2; agar, aesculus hippocastanum, and gum arabic. In addition, the cell potential observed in the TIII 2 was very close to the cell potential of an electrolysis in the absence of additives, so the use of this additive mixture does not seem to increase the energy required by electrolysis.

The next step should be to test the mixture found under "pseudo-real" conditions which means continuous cycles of electrolysis and leaching for periods of time longer than 5 hours in order to evaluate the effects of aging and concentration.

References

1. Indian Bureau Of Mine. http://ibm.nic.in/.

2. Van Genderen, E., Wildnauer, M., Santero, N. & Sidi, N. A global life cycle assessment for primary zinc production. *International Journal of Life Cycle Assessment* (2016) doi:10.1007/s11367-016-1131-8.

3. ILZSG (2016) Monthly bulletin of the International Lead and Zinc Study Group 56(1):42–44.

4. Mohr, S., Giurco, D., Retamal, M., Mason, L. & Mudd, G. Global Projection of Lead-Zinc Supply from Known Resources. *Resources* **7**, 17 (2018).

5. Zinc processing | Britannica.com. https://www.britannica.com/technology/zinc-processing.

6. Zinc production & environmental impact. http://www.greenspec.co.uk/building-design/zinc-production-environmental-impact/.

7. Sofilić, T., Rastovčan-Mioč, A., Cerjan-Stefanović, Š., Novosel-Radović, V. & Jenko, M. Characterization of steel mill electric-arc furnace dust. *Journal of Hazardous Materials* (2004) doi:10.1016/j.jhazmat.2004.02.032.

8. Madias, J. Electric Furnace Steelmaking. in *Treatise on Process Metallurgy* (2014). doi:10.1016/B978-0-08-096988-6.00013-4.

9. Harris, William E. (1936), “The Waelz Process”, AIME Transactions, 121 Metallurgy of Lead and Zinc: 702–720. “The Waelz Process.”

10. Global industrial lead acid battery market expected to reach over US $13 billion says Technavio - Technavio. https://www.technavio.com/pressrelease/global-industrial-lead-acid-battery-market-expected-to-reach-over-us-13-billion-says.

11. Larsson, S., Bergbck, B., Eklund, M. & Lohm, U. HISTORICAL PRODUCTION AND USES OF LEAD. *Environmental Reviews* **7**, 53–60 (1999).

12. Boryczko, B., Hołda, A. & Kolenda, Z. Depletion of the non-renewable natural resource reserves in copper, zinc, lead and aluminium production. *Journal of Cleaner Production* (2014) doi:10.1016/j.jclepro.2014.01.093.

13. Leach, D. L. *et al.* Sediment-hosted lead-zinc deposits in earth history. *Economic*

Geology (2010) doi:10.2113/gsecongeo.105.3.593.

14. Dell, Ronald. & Rand, D. A. J. (David A. J. *Understanding batteries*. (Royal Society of Chemistry, 2001).

15. Uk, P. S. Coordinating Lead Authors. *Agriculture* (2007) doi:10.2753/JES1097-203X330403.

16. Guberman, D. E. Lead. *U.S. Geological Survey Minerals Yearbook—2012* (2015).

17. Lead Production & Statistics < Lead Facts | ILA - International Lead Association Website. https://www.ila-lead.org/lead-facts/lead-production--statistics.

18. Dudka, S. & Adriano, D. C. Environmental Impacts of Metal Ore Mining and Processing: A Review. *Journal of Environment Quality* (1997) doi:10.2134/jeq1997.00472425002600030003x.

19. Cohen, G. A. *LEAD: The Facts*. *Rescuing Justice and Equality* (2008).

20. Habashi, F. A short history of hydrometallurgy. in *Hydrometallurgy* (2005). doi:10.1016/j.hydromet.2004.01.008.

21. Rentz, O., für Umweltforschung, D.-F. I., Umweltbundesamt, Deutschland. & für Umwelt, N. und R. *Emission Control at Stationary Sources in the Federal Republic of Germany: Heavy metal emission control*. (French-German Institute for Environmental Research, University of Karlsruhe, 1996).

22. Pacific Environmental Services, Inc. Secondary Lead Processing.

23. EPA Lead Smelter Strategy Summary Report.

24. M. Olper: “Zinc Extraction from EAF Dust with the EZINEX® Process”. Working Party on Steel, Seminar on the Processing, Utilisation and disposal of Waste in Steel Industry, Eds United Nations Economic Commission for Europe, Balatonszèplak, Hungary, June 3-.

25. Maccagni, M. G. INDUTEC®/EZINEX® Integrate Process on Secondary Zinc-Bearing Materials. *Journal of Sustainable Metallurgy* **2**, 133–140 (2016).

26. US Patent N° 5.468.354, 21/11/1995.

27. US Patent N° 5.534.131, 09/07/1996.

28. Italian Patent Application N° MI2012A000579, 11/04/2012.

29. US Patent Application N° 14/513.192, 13/10/2014.

30. A.D. Zunkel, “Recovering Zinc and Lead from Electric Arc Furnace Dust: a Technology Status Report”, Fourth International Symposium on Recycling of

Metals and Engineered Materials, Eds D.L. Stewart Jr., J.C. Daley, R.L. Stephens, Pittsburgh, Pennsylvania, .

31. O. C. Ralston, “hydrometallurgy of lead”, Trans AIME 70.447-466 (1924), Discussion pp. 466-470.

32. R. G. Bowman, Handbook of non ferrous metals, 2nd ed, New York (1945).

33. G. D. Van Arsdale, Hydrometallurgy of base metals, McGraw-Hill, New York 1953.

34. Wang, C. *et al.* Characteristics of the reduction behavior of zinc ferrite and ammonia leaching after roasting. *International Journal of Minerals, Metallurgy and Materials* **27**, (2020).

35. Peters, E. The physical chemistry of hydrometallurgy. *In: International Symposium on Hydrometallurgy, AIME, NEW York, NY, USA.* (1973).

36. Andrea Grassi. Electrochemical study of hydrometallurgical processes based on ammonium chloride solutions. (2018).

37. Ossidazione e diagramma di Ellingham. http://www.ing.unitn.it/~colombo/Connettori/CAPITOLI/Appendice_ossidazione.html.

38. How lead is made - material, used, processing, product, industry, machine, Raw Materials. http://www.madehow.com/Volume-2/Lead.html.

39. https://xpssimplified.com/elements/manganese.php.

40. Ilton, E. S., Post, J. E., Heaney, P. J., Ling, F. T. & Kerisit, S. N. XPS determination of Mn oxidation states in Mn (hydr)oxides. *Applied Surface Science* **366**, (2016).

41. Tholkappiyan, R., Naveen, A. N., Vishista, K. & Hamed, F. Investigation on the electrochemical performance of hausmannite Mn_3O_4 nanoparticles by ultrasonic irradiation assisted co-precipitation method for supercapacitor electrodes. *Journal of Taibah University for Science* **12**, (2018).